TU

TECHNISCHE UNIVERSITÄT WIEN

DISSERTATION

Investigation of New High Magnetostrictive Materials

ausgeführt zum Zwecke der Erlangung des akademischen Grades eines Doktors der technischen Wissenschaften unter der Leitung von

Univ.Prof. Dr.techn. Roland Grössinger

E138

Institut für Festkörperphysik

eingereicht an der Technische Universität Wien

Fakultät für Physik

von

Nasir Mehmood

Matrikelnummer 0627516

Lorenz-Müller-Gasse 1A/5020

A-1200, Wien, Austria.

Wien, am Nov 2009   Unterschrift

Abstract

Low cost magnetostrictive materials that exhibit a large magnetostriction at low saturation field combined with a high mechanical strength and a good ductility are of great interest for applications in magnetomechanical sensors and actuators. Intermetallics based on the general formula 3d-metal (Fe, Co) + additives – up to 25% (such as Ga, Al, Ge, Pd or similar) are interesting candidates for new soft magnetic materials with a reasonable high magnetostriction. These alloys have a very similar phase diagram and crystallize in the A_2, B_2 or DO_3 structure. The idea here is that due the substitution with a nonmagnetic element the local symmetry is reduced which causes an increase of the magnetostriction.

The main focus of this thesis is on the investigation of magnetic and microstructural properties of magnetostrictive materials based on alloys between 3d-metal Fe and additives – up to 25%, such as Ga, Al, Ni and Co using different production routes as high frequency induction melting, severe plastic deformation (SPD), melt spinning, splat cooling and water quenching. Additionally Fe-Mn and Ni-Ga alloys were also investigated. In contrast to metallic systems, polymers composites and $CoFe_2O_4$ prepared with different routes were investigated with respect to magnetostriction in this thesis.

Structural properties lattice constant, crystallite size and texture were determined by using XRD analysis. Magnetic properties were measured using pulse field magnetometer or standard VSM. Magnetostriction measurements were performed either by using standard strain gauge method or capacitance cell methods.

Among different composition of Fe-Ga ribbons, with different quenching rates, $Fe_{82.5}Ga_{17.5}$ ribbon, melt spun at speed 15 m/s, has highest magnetostriction value of 116 ppm. In Fe-Ga rapidly quenched ribbons a strong dependence of magnetostriction on quenching rate was found. For $Fe_{81}Ga_{19}$ SPD bulk alloy magnetostriction values upto 67 ppm were measured. Slowly cooled bulk polycrystalline $Fe_{81}Al_{19}$ material has exhibit a magnetostriction value of 62 ppm. The magnetostriction in Fe-Al melt spun ribbons reached only values up to 30 ppm. The addition of Ga in Ni does not significantly enhance the magnetostriction and for higher values of Ga (up to 7%) addition magnetostriction decreases. The addition of Mn in Fe results in an increase in magnetostriction to -70 ppm, but requires higher field value (more than 5T) to reach saturation. The highest value of magnetostriction found in the $CoFe_2O_4$ ferrite prepared by combustion method, was -147 ppm.

Kurzfassung

Magnetostriktive Materialien, die bei niedrigem Magnetfeld eine hohe Magnetostriktion aufweisen, günstig in der Herstellung sind, dazu noch eine hohe mechanische Festigkeit und gute Duktilität besitzen, sind gute Kanditaten für industrielle Anwendungen als magnetomechanische Sensoren und Aktuatoren. Intermetallische Verbindungen, basierend auf der allgemeinen Formel 3d-Metall (Fe, Co) + Additiv (bis zu 25%, z.B. Ga, Al, Ge, Pd oder ähnliche) erfüllen diese Anforderungen recht gut. Diese Verbindungen haben alle recht ähnliche Phasendiagramme und kristalli sieren in der A_2, B_2 oder DO_3 Struktur. Die Idee diese Verbindung zu untersuchen basiert auf der Vorstellung dass die Reduktion der lokalen Symmetrie durch Substitution mit einem nicht-magnetischen Element vielleicht die Magnetostriktion erhöht.

Der Schwerpunkt dieser Arbeit liegt in der Untersuchung der magnetischen und mikrostrukturellen Eigenschaften von Fe-basierten magnetostriktiven Materialien, die auf unterschiedliche Arten (Hochfrequenzschmelzen, "severe plastic deformation" (SPD), "melt spinning", "splat cooling" and "water quenching") hergestellt wurden. Zusätzlich wurde die Magnetostriktion sowohl von Fe-Mn und Ni-Ga Verbindungen, als auch über verschiedene Herstellungsarten produziertes $CoFe_2O_4$ untersucht.

Strukturelle Eigenschaften, Gitterkonstanten, Kristallitgröße und Textur wurden über XRD Analyse bestimmt. Die Magnetischen Eigenschaften wurden entweder in einem Pulsfeldmagnetometer oder in einem Standard VSM festgestellt. Die Magnetostriktionsmessungen wurden entweder mit Dehnungsmess streifen oder in einer kapazitiven Zelle gemessen.

Bei der Untersuchung verschiedener Zusammensetzungen von Fe-Ga Bänder ("flakes") mit unterschiedlichen Abschreckraten wurde bei $Fe_{82.5}$ $Ga_{17.5}$ Bänder, das mit einer Abschreckgeschwindigkeit von 15 m/s gespritzt wurde, der höchste Magnetostriktionswert von 116 ppm gefunden. In der Probenserie "Fe-Ga rasch abgeschreckte Bänder wurde eine starke Abhängigkeit der Magnetostriktion mit der Abkühlrate festgestellt. Für "severe plastic deformed" $Fe_{81}Ga_{19}$ wurde eine Magnetostriktion von bis zu 67 ppm gemessen. Für langsam gekühltes polykristallines $Fe_{81}Al_{19}$ wurde eine Magnetostriktion von bis zu 62 ppm gefunden, wohingegen die Magnetostriktion der gespritzten Fe-Al Proben nur bis zu 30 ppm ergab. Die Probenserie Ni-Ga zeigte keine signifikante Verbesserung der Magnetostriktion, ab ca 7% Ga in Ni nahm die Magnetostriktion sogar ab. Die Fe-Mn Probenserie zeigte Magnetostriktionswerte bis ca. -70 ppm, man braucht aber ein Magnetfeld von mehr als 5T um die Proben zu sättigen. Der höchste Magnetostriktionswert (-147 ppm) in der $CoFe_2O_4$– Serie wurde an Proben festgestellt welche mit der "combustion method" hergestellt wurden.

Dedication

To my family

Acknowledgments

I am thankful to Almighty Allah for all His blessings and kindness. The writing of a dissertation can be a lonely and isolating experience, yet it is obviously not possible without the personal and practical support of numerous people. Thus my sincere gratitude goes to my parents, family, all my friends, and my companions for their love, support, and patience over the last few years. I would like to express my sincere appreciations and gratitude to my supervisor Prof. Dr. Roland Grössinger for his continuous guidance, encouragement and support during my study in the Institute of Solid State Physics at TU Wien. He always has patiently and gently kept me on track. His perpetual energy and enthusiasm in research had motivated all his advises, including me. In addition, he was always accessible and willing to help his students with their research. As a result, research life became smooth and rewarding for me.

This is a great opportunity to express my respect to Dr. Reiko Sato Turtelli has been always there to listen and give advice. I am deeply grateful to her for the long discussions that helped me sort out the technical details of my work. I am grateful to her for encouraging me to learn and to make more, better and faster.

I owe my deepest gratitude to Prof. Frank Kubel of the Institute of Chemical Technologies and Analytics of Vienna University of Technology and providing necessary help for structural characterization of the samples, many things would not have been possible without you.

Many people on the faculty and staff of the Institute for Solid State Physics assisted and encouraged me in various ways during my course of studies. I am especially grateful to Dr. Herbert Sassik, Dr. Michael Reissner, Dr. Herbert Müller, Dr. Andrey Prokofiev, Dr. Michael Mantler, Ing.Vladimira Piwetz, Adela-Vanda Peter, Peter Hundegger and Lahner Andreas their kind support and help for making samples and measurements of magnetic properties, magnetostriction and XRD etc. My special thanks to Dr. Saleh Muhammad, Dr. Van-Duong Giap, Markus Schönhart , Zahra Soltanmhammadi-Khayyat, Dip. Ing Martin Kriegisch, Michael Haas, Kamran Ali, Muhammd Atif, Nasir Mehboob, Rao Tahir Ali Khan, Tahir Ali and Lubuna Shafeek Beegum of the Institute of Solid State Physics for all their support and nice company.

I am indebted to Cristina Bormio Nunes of FAENQUIL Departamento de Engenharia de Materiais Lorenam, Brazil for providing the splat cooled samples and to Veronica Corral-Flores of Centro de Investigación en Materiales Avanzados Chihuahua, Mexico for the carbon fiber composites samples. I am grateful to Dr. Wolfgang Linert and Güliz Senbaşlar of Institute of Applied Synthetic Chemistry, TU Wien for providing necessary help and guidance for preparation of Ferrite samples and of Ijaz-ul-Mohsin of Institute of Chemical Technologies and Analytics of TU Wien for sintering Ferrite samples at high temperature . Thanks to RNDr. Gabriel Vlasák and Ing. Peter Švec of Institute of Physics, Slovak Academy of Sciences, Bratislava, Slovakia for the help and support for magnetostriction measurements on melt spun ribbons.

I am obliged to the Higher Education Commission of Pakistan for the financial means during the entire study period in Austria and to the Austrian Exchange Services OeÄD team for their sincere services all the way long.I am thankful to my parent organization for the grant of the study leave and sparing me for higher studies.

I wish to acknowledge the moral support to all HEC scholars network of supportive, forgiving, generous and loving friends without whom I could not have survived the process. I am fortunate to have friends like Asim Karim who always has extended his utmost help when needed at Pakistan.

Most importantly, none of this would have been possible without the love and patience of my family. My family members were all cooperating during this period, I wish to thank them all, especially to my brother Tariq Mehmood for taking care of all the matters at home. Finally I would like to extend my appreciations to my wife Rozeena, who was patient and kind enough to support and encourage me and to take very good care of our children Hifsah, Sohail and Asma.

Contents

List of Figures

List of Tables

19

Chapter 1

Motivation for This Work

Magnetostrictive materials are distinguished as materials that undergo a change in shape due to change in the magnetization state of the material, also experience an inverse effect where a magnetization changes causes a change of the local stress. Extensive work has been done to develop and use magnetostrictive materials for actuation and sensing devices after discovery of magnetostriction in Iron by James Joule's in 1842. Examples of magnetostrictive materials include the common ferromagnetic materials Fe, Ni and Co which have maximum magnetostrictive strain value up to 50 x 10^{-6} m/m. Additionally, high performance rare earth-Fe_2 alloys such as Terfenol-D ($Tb_{0.3}Dy_{0.7}Fe_2$) have been developed that generate "giant" magnetostrictive strains on the order of 1000 x10^{-6} [1] but this alloy has many restrictions such as its high cost, poor ductility, fracture resistance and very low value of tensile strength of 28 MPa [2] which limits its ability to withstand shock loads or operate in tension also it requires high magnetic fields for saturation. High material costs (e.g. about 3 ~ 23 \$/g of powder, depending on size) hinder large scale industrial applications. This means that one needs high magnetostrictive materials with low material costs which exhibit soft magnetic properties. Here, soft magnetic 3d based alloys without rare earths are very interesting candidates. In magnetostrictive materials the soft magnetic behavior is well described by a large parallel magnetostrictive susceptibility ($\chi_{\lambda parallel} = d_{\lambda parallel}/dH$). Desired characteristics for magnetostrictive materials are large values of magnetostriction at low saturation field, high mechanical strength, and good ductility, an ability to operate at high stress levels , higher operating temperatures and low cost. Due to the low cost, high magnetic moment and relatively good strength and good ductility that could be obtained from, Fe-based alloys without rare earth additions are the focus of the current research effort.

Substituting Fe by nonmagnetic Ga causes a dramatic increase of the magnetostriction. In 2001, Iron-Gallium alloys developed at the naval surface warfare center by Clark et al [3–5] appear to be promising materials for a variety of actuator and sensing applications. Single crystalline Fe-Ga exhibits joint magnetostriction up to ~450 ppm [6] under very low magnetic fields (~100 Oe) exhibiting a very small hysteresis, while demonstrating high tensile strength (~500 MPa) and limited dependence of magneto mechanical properties on temperatures between -20°C and 80°C [7–9]. The investigations found that magnetostriction values of 270 ppm [10] were reached in directionally solidified polycrystalline bulk Fe-Ga alloys.

It is clear that the structure, especially the disorder caused by the Ga substitution, plays an important role for the high magnetostriction found in single crystalline Fe-Ga alloys. This effect should become more evident when studying the magnetostriction on the materials produced by severe plastic deformation (SPD), splat cooling and rapidly quenching, where the short-range structural disorder should be larger . In this work, we investigated effect of severe plastic deformation (SPD) on magnetostriction of bulk $Fe_{81}Ga_{19}$ alloy. The values of magnetostriction rapidly quenched melt spun ribbons, already published are very contradictory e.g. for composition $Fe_{100-x}Ga_x$ ($15 \leq x \leq 30$), it is ranging from +98 ppm [11] to -3000 ppm [12].

Similarly to Ga, adding non magnetic Al into Fe also gives 5-fold rise in magnetostriction with up to 30% Al in single crystalline bulk Fe-Al alloys. There exist very detailed single crystal investigations on binary Fe-Al and magnetostriction value up to 95 ppm has been reported [13, 14]. Here for economical reasons Fe-Al alloys would be superior. Polycrystalline $Fe_{100-x}Al_x$ ($x = 15$, 19 and 25) samples were prepared and investigated for the influence of the structure and atomic ordering on the magnetostriction. For both alloy systems, the phase stabilization of the disordered bcc structure is the fundamental component to increase the magnetostriction of the materials. For $Fe_{81}Al_{19}$ melt spun ribbons of magnetostriction value -700 ppm was reported by Liu et al [15].

Because of very contradicting results in Fe-Ga ribbons and very high value in Fe-Al ribbons, magnetostriction measurements on these ribbons using a strain gauge method as well as a capacitance dilatometer has been performed, effect of quenching rates on magnetostriction and structural properties were also studied.

The cobalt ferrites are well known for its highest magnetostrictive coefficient 230 ppm has been obtained among the oxides-based magnetostrictive materials accompanied by a large strain derivative $(d\lambda/dH)_{max}$ of 1.3 x $10^{-9}A^{1}m$ and can be alternative of Galfenol (Fe-Ga) alloys because of lower costs as compared to metallic alloys, absence of eddy current losses and better corrosion resistance etc . Different sintering condition, preparation method entail the microstructure of the samples and consequently different maximum values of the magnetostriction coefficient . For specific application of stress sensors, the maximum strain derivative $(d\lambda/dH)_{max}$, which is related with stress sensitivity, is more important than the maximum value of the magnetostriction [16]. In the present work we produce polycrystalline $CoFe_2O_4$ powders by several techniques in order to obtain the highest possible magnetostriction together with high strain derivative, which may lead to a high magnetoelectric effect in composites. Additionally, investigations of the influence of different production methods on the structural and magnetic properties were performed. A systematic study also performed to understand the effect of processing conditions, annealing temperature and combustion rate on the magnetostrictive properties of $CoFe_2O_4$ produced by modified citrate sol gel method and combustion method. Such study can be used for optimizing the process parameter of magnetostrictive materials based on $CoFe_2O_4$.

Beside investigation of above mentioned materials we also investigated Ni-Ga, Fe-Mn, Sm-Fe alloys, polymer composites and steel pipeline samples.

Chapter 2

Physics of Magnetostriction and Magnetostrictive Materials

2.1 Magnetic Moment and Magnetic Dipole

According to classical electromagnetism, assuming current I around an infinitely small loop exhibiting an area A, as shown in Figure 2.1, the corresponding magnetic moment can be written as,
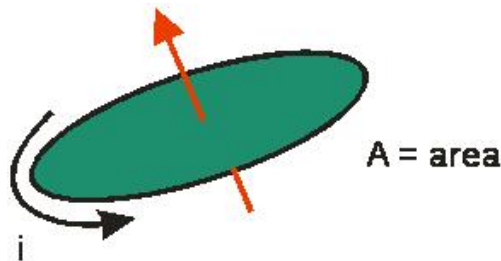
Figure 2.1: Magnetic moment according to classical magnetism.

$$dm = IdA \tag{2.1}$$

By summing up magnetic moments, for finite size of loop,

$$m = d \int m = I \int dA \tag{2.2}$$

Magnetic moment is measured in unit of $[Am^2]$, and the direction of vector is determined by right hand rule. The magnetic dipole is equal to a magnetic moment of a current loop in the limit of small area. The energy of magnetic moment m in the presence of induction B is given by,

$$E = \mu_0 m.H = \mu_0 mHCos\theta \tag{2.3}$$

Where θ is angle between moment m and external magnetic field H, μ_0 is permeability of free space having value 4π x 10^{-7} Henry /meter.

2.2   Intensity of Magnetization (*M*)

The total magnetic moment per unit volume is known as intensity of magnetization (M or J) and it is measured in $[Am^{-1}]$

$$M = \frac{m}{V} \tag{2.4}$$

Magnetic moment per unit mass, σ , is

$$\sigma = \frac{m}{mass} \tag{2.5}$$

and measured in $[Am^2/kg]$.

2.3   Magnetic Induction (*B*)

The response of material under the application of external magnetic field is known as magnetic induction or magnetic flux density and denoted by B , in vacuum it can be written as,

$$B = \mu_0 H \tag{2.6}$$

Inside material the relationship between B, M and H is given by,

$$B = \mu_0(H + M)......[Tesla, T] \tag{2.7}$$

In CGS system,

$$B = H + 4\pi M \tag{2.8}$$

2.4   Magnetic Susceptibility and Permeability

The ratio of magnetization (M) to magnetic field (H), is known as magnetic suscepti-bility (χ), it describes the response of magnetic material in the presence of magnetic field and can be used to describe the different classes of magnetic materials.

$$\chi = \frac{M}{H} \tag{2.9}$$

In case of magnetic induction can also be written as,

$$B = \mu_0(1 + \chi)H \tag{2.10}$$

$$= \mu_0\mu_r H \tag{2.11}$$

2.5 Classes of Magnetic Materials

2.5.1 Diamagnetism

Diamagnetic materials have only non magnetic atoms, all the orbital shells are filled and there are no unpaired electronic spins, magnetization induced by the field is very weak and is opposite to the field direction. The diamagnetic susceptibility is small and negative $\chi \approx -10^{-5}$. Examples of diamagnetism are copper (Cu), silver (Ag), gold (Au), bismuth (Bi) and beryllium (Be) [17].

2.5.2 Paramagnetism

In paramagnetic materials some of the atoms or ions in the material have a net magnetic moment due to unpaired electron spins in partially filled orbitals. For paramagnetic materials the susceptibility χ is small and positive and typically in the range of $\chi \approx 10^{-3}$ to 10^{-5}. The magnetization of a paramagnetic material is weak but the moments locally tend to align with a sufficient high applied magnetic field. This produces a magnetization in the material in the direction of the applied magnetic field. Aluminum (Al), platinum (Pt) and manganese (Mn) are paramagnetic materials [17].

2.5.3 Ferromagnetism

In certain solids, such as iron (Fe), nickel (Ni) and cobalt (Co), at room temperature, the moments in neighboring ions are strongly coupled (exchange coupling) and tend to align with each other. This alignment can lead to spontaneous magnetization in the material even in the absence of magnetic fields. The susceptibility for ferromagnetic materials is positive and can be as high as $\chi \approx 50$ to 10,000 [17], magnetic field induces very strong magnetization in ferromagnetic materials.

2.5.4 Ferrimagnetism

In ferrimagnets, the magnetic moments of antiprarallel ordered sublattices and are not equal and does not compensate each other which result in a net magnetic moment.
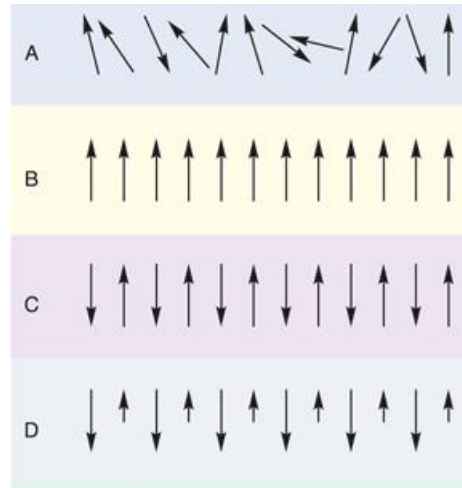
Figure 2.2: Types of magnetism: (A) paramagnetism (B) ferromagnetism (C) antiferromagnetism (D) ferrimagnetism (Credit and ©: Sigma-Aldrich).

$$M_A \neq M_B \tag{2.12}$$

$$M = M_A - M_B \neq 0.......for......T < Tc \tag{2.13}$$

Where M is total magnetization. Ferrimagnetics behaves similar as ferromagnetism. It exhibits all the hallmarks of ferromagnetic behavior spontaneous magnetization, curie temperatures, hysteresis, and remanence. Magnetite (Fe_3O_4) is a well known ferrimagnetic material.

2.5.5   Antiferromagnetism

In antiferromagnetic materials atomic moments are strictly anti-parallel ordered and equal in strength. Therefore they do not show any resulting magnetization. Antiferromagnetism is mainly found in transition metal oxides, halides etc (MnO, CoO, NiO) but also in intermetallic alloys like Fe-Mn or IrMn [18].

Figure 2.2 shows the spin alignment of paramagnetism, ferromagnetism, antiferromagnetism and ferrimagnetism.

2.6   Atomic Magnetism

According to the classical Bohr model of an atom as mentioned in Figure 2.3 , an electron is moving around a path enclosing an area $A = \pi r^2$ constitutes a current I,

$$I = \frac{-e\omega}{2\pi} \tag{2.14}$$

and magnetic moment,
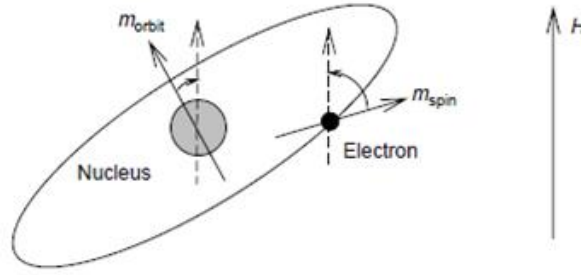
Figure 2.3: In highly magnetostrictive materials, the spin moment m_{spin} and orbital moment m_{orbit}orbit are strongly coupled. When the spin moment rotates to align with the external field H, the orbital moment rotates along with it and produces considerable lattice deformation [19].

$$m = \mu_0(I)A \tag{2.15}$$

Substituting I from equation 2.14 and $A = \pi r^2$ in the equation 2.15 magnetic moment can be expressed in terms of the radius, angular velocity and electron charge.

The angular momentum of the electron P, is quantized and is integral multiple of $\hbar$ (where $\hbar = \frac{h}{2\pi}$ and h = 6.63 x 10⁻³⁴Joule-sec is the plank constant), l is the orbital quantum number and can take integral value 0, ± 1, ± 2, etc.

$$P = m\omega r^2 = l\hbar \tag{2.16}$$

From equations 2.15 and 2.16, the orbital magnetic moment of the electron can be written as:

$$m = \frac{\mu_0 e\hbar}{2m}l = M_B l \tag{2.17}$$

Where M_B= 1.165x10^{-29} is known as Bohr magneton.

Equation 2.17 describes the orbital magnetic moment. However, there is another magnetic moment which arises from the intrinsic angular momentum of an electron associated with its spin. This can be expressed as $P = s\hbar$, where s = ±1/2 is the spin number for the electron.

In single atoms with multiple electrons, the sequence of filling of different orbitals with electrons is determined by Hund's rule [20]. This electronic configuration determines the total, i.e. spin+orbital, magnetic moment of the atom or ion, which in turn plays a significant role in determining the magnetic properties of the materials [21].

2.7 The Hysteresis Loop and Magnetic Properties

A hysteresis loop shows the link between the induced magnetic induction (B) or magnetization (M) and the magnetizing force (H). It is often referred to as the B-H or M -H loop, a M-H curve is shown in Figure 2.4.
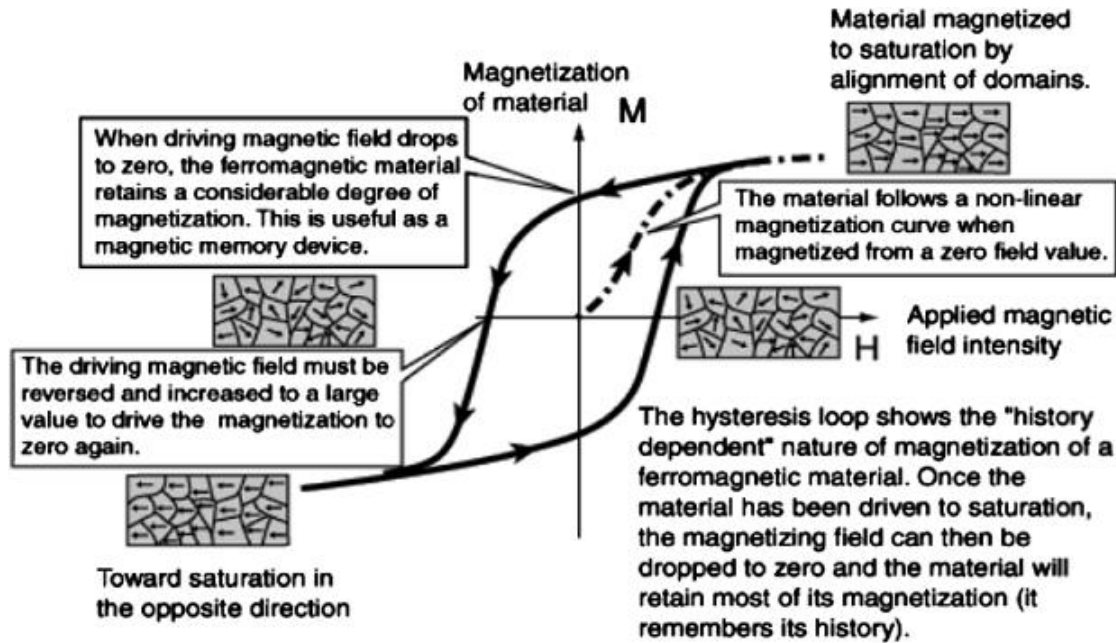
Figure 2.4: Magnetization curve [22].

The loop is generated by measuring the magnetization (M) of a ferromagnetic material while the field strength (H) is changed.

From the hysteresis loop, a number of primary magnetic properties of a material can be determined.

2.7.1 Saturation Magnetization (M_s)

The saturation magnetization is defined as the magnetization when all magnetic moments (spins) are aligned parallel to the external field. This is either achieved in a very high external field, or by extrapolating M against an infinite H (plotting M versus 1/H .... for H $\Rightarrow \infty$). This saturation magnetization is temperature dependent, and disappears completely above the curie temperature (T_c) where the ferromagnetic order changes into a paramagnetic state.

2.7.2 Remanence (M_r or B_r)

The magnetization that remains in a material when the external field is zero. The true remanence can only be determined in a magnetically closed system, where the demagnetizing factor is zero.

2.7.3 Coercivity (H_c)

The reverse magnetic field which is required to bring a magnetic material from the remanence state to zero magnetization ($_M$HC) or zero induction ($_B$HC). The magnetizing field has to be high enough in order to achieve saturation.

2.8 Curie Temperature (T_c)

At sufficiently high temperature, the thermal energy exceeds the exchange coupling energy between spins and breaks this alignment, leading to a paramagnetic state. The temperature at which this transition from ferromagnetic to paramagnetic state or vice versa occurs is known as the Curie temperature (T_c).

2.9 Magnetic Anisotropy

The energy which is necessary to magnetize a material in different directions is called magnetic anisotropy. There exist different kinds of magnetic anisotropies: shape anisotropy (depends on the shape of the sample), induced anisotropy (depends on heat treatment of the sample; with field or with stress) and the magnetocrystalline anisotropy (intrinsic effect of the material). It is experimentally observed that the magnetization vector tends to lie along certain crystallographic axes, the so-called easy axes, where the anisotropy has a minimum. An ideal magnetic isotropic material has no preferential direction for its magnetic moment in zero fields, while a magnetically anisotropic material will align its moment parallel to an easy axis.

2.9.1 Magnetocrystalline Anisotropy

In general the magnetocrystalline anisotropy is related to the involved elements as well as to the crystal symmetry of a material and this is known as magnetocrystalline anisotropy. The existence of magnetic anisotropy is demonstrated by the magnetization curves of ferromagnetic single crystals such as Fe and Ni in Figure 2.5.

Refer to Figure 2.5 for Iron (Fe)

> *<100>* is the easy direction of magnetization
>
> *<110>* is the intermediate direction of magnetization
>
> *<111>* is the hard direction of magnetization

When a magnetic field is applied to a ferromagnetic material the domain structure changes in such a way as to increase the magnetization parallel to the external field. This continues until the specimen is filled with favorably oriented domains. If the field is applied along an easy axis, the magnetization rapidly saturates. For other directions the magnetization process continues by rotating the magnetization vectors into the direction of the field
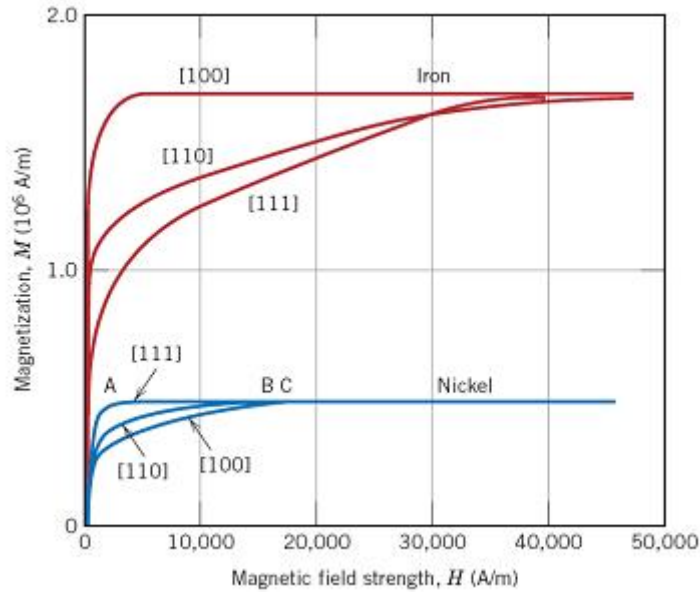
Figure 2.5: Magnetization curves for single crystals of iron and nickel. For both metals, a different curve was generated when the magnetic field was applied in each of [100], [110], and [111] crystallographic directions [23, 24].
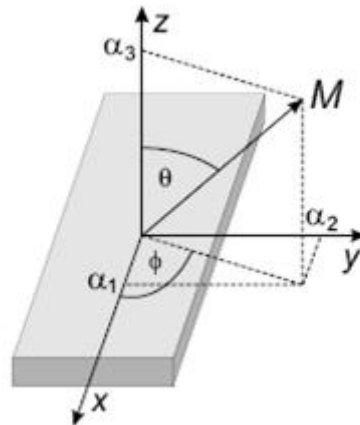
Figure 2.6: Definition of direction of cosines

until saturation is achieved. Thus the magnetization process generally involves domain wall motion followed by rotation.

Magnetic anisotropy energy is defined as the work required aligning the magnetization in a certain direction compared to that required for the easy direction. In quantifying the energy, it is customary to describe directions trigonometrically with a set of direction cosines which fulfills also the symmetry of the lattice. A phenomenological expression for the magnetocrystalline anisotropy of a cubic lattice may be derived from the spin-pair model as discussed in detail by Chikazumi [20]. Let α_1, α_2 and α_3 be the direction cosines between the magnetization vector and the principal axes as shown in Figure 2.6.

The magnetization direction $m = M/ \mid M \mid$ relative to the coordinate axes can be written in direction of cosines α_i as $m = (\alpha_1, \alpha_2, \alpha_3)$ with

$$\alpha_1 = sin\theta cos\phi \tag{2.18}$$

$$\alpha_2 = sin\theta sin\phi \tag{2.19}$$

$$\alpha_3 = sin\theta \tag{2.20}$$

These relation fulfill condition,

$$\alpha_1^2 + \alpha_2^2 + \alpha_3^2 = 1 \tag{2.21}$$

Using power series expansion of the components of magnetization magnetocrystalline energy per volume E_{cry} can be described as,

$$E_{\text{crys}} = E_0 + \sum_i b_i\alpha_i + \sum_{ij} b_{ij}\alpha_i\alpha_j + \sum_{ijk} b_{ijk}\alpha_i\alpha_j\alpha_k + \sum_{ijkl} b_{ijkl}\alpha_i\alpha_j\alpha_k\alpha_l + o(\alpha^5) \tag{2.22}$$

The terms $o(\alpha^5)$ with at least the fifth order in α are very small and can be neglected. There is no difference between oppositely magnetized systems and energy depends only on alignment. Since there is odd terms of α_i occur in the series expansion and expansion can be reduced to,

$$E_{\text{crys}} = E_0 + \sum_{ij} b_{ij}\alpha_i\alpha_j + \sum_{ijkl} b_{ijkl}\alpha_i\alpha_j\alpha_k\alpha_l \tag{2.23}$$

Using equation 2.23 energy density for different cubic, tetragonal and hexagonal systems can be written as, further mathematical details can be found in reference [25],

$$E_{\text{crys}}^{Cubic} = K_0 + K_1(\alpha_1^2\alpha_2^2 + \alpha_1^2\alpha_3^2 + \alpha_2^2\alpha_3^2) + K_2\alpha_1^2\alpha_2^2\alpha_3^2 + K_3(\alpha_1^2\alpha_2^2 + \alpha_1^2\alpha_3^2 + \alpha_2^2\alpha_3^2) \tag{2.24}$$

$$E_{\text{crys}}^{tetra} = K_0 + K_1cos^2\theta + K_2cos^4\theta + K_3sin^4\theta(sin^4\phi + cos^4\phi) \tag{2.25}$$

$$= K_0^{/} + K_1^{/}sin^2\theta + K_2^{/}sin^4\theta + K_3^{/}sin^4\theta cos4\phi \tag{2.26}$$

$$E_{\text{crys}}^{Cubic} = K_0 + K_1sin^2\theta + K_2sin^4\theta + K_3sin^6\theta + K_4sin^6\theta cos^6\theta cos\phi \tag{2.27}$$

1.9.1.1 Magnetocrystalline Anisotropy of Cubic Crystals

Using Figure 2.6 the magnetocrystalline anisotropy energy for different crystallographic direction of cubic system can be written as,

E100, [100] direction characterized by, for $\theta = 90°$ and $\phi = 0°$.

This result in, the $\alpha_1 = 0$, $\alpha_2 = \alpha_3 = 0$

E110, [110] direction characterized by, for $\theta = 90°$ and $\phi = 45°$.

This result in, the $\alpha_1 = \alpha_2 = 1/\sqrt{2}, \alpha_3 = 0$

E111, [110] direction characterized by, for $\theta = 90°$ and $\phi = 45°$.

This result in, the $\alpha_1 = \alpha_2 = \alpha_3 = 1/\sqrt{3}$

The energy density for cubic materials can be given as,

$$E_{crys}^{cubic} = K_0 + K_1(\alpha_1^2\alpha_2^2 + \alpha_1^2\alpha_3^2 + \alpha_2^2\alpha_3^2) + K_2\alpha_1^2\alpha_2^2\alpha_3^2 \tag{2.28}$$

Where α_1, α_2 and α_3 are the direction cosines (angle that magnetization vector makes with the crystalline axes) and K_0, K_1 and K_2 are the anisotropy constants. For most practical purposes K_1 and K_2 are the most important anisotropy constants. The corresponding energies can be obtained by inserting direction of cosines,

$$E_{100} = K_0 \tag{2.29}$$

$$E_{110} = K_0 + \frac{1}{4}K_1 \tag{2.30}$$

$$E_{111} = K_0 + \frac{1}{3}K_1 + \frac{1}{27}K_2 \tag{2.31}$$

2.9.2   Shape Anisotropy

Polycrystalline samples without a preferred orientation of the grains do not possess any average anisotropy. But, an overall isotropic behavior concerning the energy being needed to magnetize it along an arbitrary direction is only given for a spherical shape. If the sample is not spherical then one or more specific directions occur which represent easy magnetization axes which are solely caused by the shape. This phenomenon is known as shape anisotropy. Additionally, if the material consists of powder also the average shape of the grains contribute to shape anisotropy of the material.

2.9.3   Induced Magnetic Anisotropy

For magnetic alloys exhibiting a cubic crystal structure an unidirectional magnetic anisotropy can often be achieved by tempering in an external magnetic field. The external magnetic field orients the magnetization at high temperatures which must be below T_c.

During cool-down or rapid thermal quenching the high-temperature state is frozen out under retention of the oriented magnetization direction. Induced anisotropy as function of direction of cosines can be expressed as,

$$E_{ind}.1/aV = -F(\alpha_1^2\beta_1^2 + \alpha_2^2\beta_2^2 + \alpha_3^2\beta_3^2) - G(\alpha_1\alpha_2\beta_1\beta_2 + \alpha_2\alpha_3\beta_2\beta_3 + \alpha_1\alpha_3\beta_1\beta_3) \quad (2.32)$$

Where α_i, β_i being the direction cosines of magnetization during measurements and during annealing in an external magnetic field, respectively, *F* and *G* are material constant (a is binding energy constant and *V* is volume). For isotropic G = 2F, simple cubic G = 0, body-centered cubic F = 0 and face-centered cubic G=4F. For an isotropic system, we get

$$E_{ind}.1/aV = -F(\alpha_1\beta_1 + \alpha_2\beta_2 + \alpha_3\beta_3)^2 = -K.cos^2(\theta - \theta_{ann}) \quad (2.33)$$

With F = K being the anisotropy constant describing the induced magnetic anisotropy leading to a uniaxial alignment and $(\theta - \theta_{ann})$ being the angle between the magnetization during the measurement and during annealing.

The rearrangement of pairs of atoms does not only occur during annealing in an external magnetic field but also by plastic deformation. In this case this type of induced anisotropy is called roll-magnetic anisotropy.

2.9.4 Stress Anisotropy

In magnetic materials the inter-atomic distance can be influenced applying external stress which causes a rearrangement of the local direction of magnetization, this effect is known as stress anisotropy. Upon magnetization, crystal experiences a strain that can be measured as a function of applied field along the principal crystallographic axes. A magnetic material will therefore change its dimension when magnetized. The displacement in crystals influences the magnetic behavior vice versa. The magnetic properties can be altered by the magnetoelastic energy which are given by the magnetostriction and the elastic properties.

2.10 Magnetostriction

Magnetostriction is a small variation in dimension (length) of a material caused by an external magnetic field. Magnetostriction is an intrinsic property of all kind of materials. It can be divided into spontaneous magnetostriction and forced magnetostriction. The former is due to internal magnetic interaction of a sample, while the latter is due to magnetic interaction between the sample and externally applied magnetic field. It is roughly proportional to the magnitude of the magnetization.
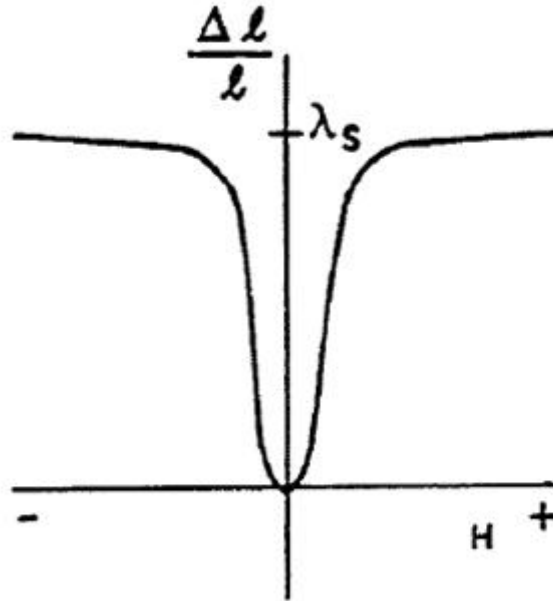
Figure 2.7: Relation between magnetic field and magnetostriction [26].

When Iron is cooled down from a high temperature through its Curie temperature (T_c), an anomalous isotropic thermal expansion is observed near the curie temperature. This slightly magnetic field-dependent anomaly associated with the magnetic ordering (of Fe or other magnetic substances) is called volume magnetostriction. The volume magnetostriction can be isotropic (amorphous materials) but also anisotropic depending on the crystal symmetry of a material. Now, if a magnetic field is applied to the magnetically ordered sample, an additional anisotropic deformation that stretches or shrinks the sample in the direction of the magnetic field is observed. This field-dependent phenomenon is called Joule magnetostriction; it is measured in microns per meter (μm/m) and denoted by λ . Figure 2.7 shows relation between magnetic field H and magnetostriction λ.

All materials are magnetostrictive up to certain extant, but this effect is more important in ferromagnetic and ferrimagnetic magnetic materials, where it is in range 10^{-5} as well as in iron (Fe) based amorphous alloys (40×10^{-6}) going up to 10^{-3} in rare earth metals, as compared to diamagnetic and paramagnetic materials .e.g. in Pd it is in the range of 10^{-8} at 10 kOe [27]. The existence of magnetostrictive effect was first discovered by J.P. Joule in 1842, when he was observing a sample of ferromagnetic materials, i.e. nickel (Ni) and iron (Fe) [28, 29].

2.10.1   Origin of Magnetostriction

Magnetostriction has its origin in a coupling between the direction of the orbital moment of an atom which describes the orientation (shape) of its anisotropic electron cloud, and the lattice i.e. spin-orbit coupling . When this orbital atomic magnetic moment (the
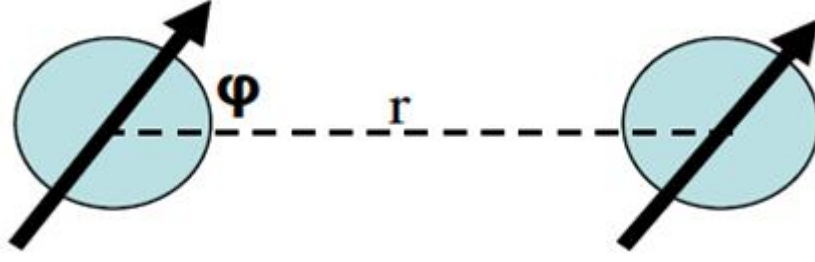
Figure 2.8: A spin pair with variable bond length, *r*, and angle φ, between parallel spin and bond.

dipole- dipole exchange energy) changes under external magnetic field (direction and/or magnitude), the distance and angle of dipole moment pair will spontaneously adjust to achieve a new slightly changed minimum energy. Accordingly the crystal will either change its volume or its symmetry to some finite strain such that a new equilibrium state will be reached. This effect is called magnetostriction (volume or shape magnetostriction).

2.10.2   Magnetostriction in Cubic Single Crystals

In single crystal the magnetostrictive strain induced by rotation of magnetization of magnetically saturated material depends upon the direction of measurements of strain and magnetization with respect to the different crystallic axes of the crystal. An expression for magnetostriction of a cubic lattice may be derived using a spin- pair model with variable bond length as shown in Figure 2.8 [20].

$$w(r, cos\varphi) = g(r) + l(r) \left(cos2 - \frac{1}{3} \right) + ... \tag{2.34}$$

The term g(r) in equation 2.34 is independent of the direction of magnetization and is the exchange interaction term. This expression plays important role in volume magnetostriction but does not contribute to the usual "linear" magnetostriction [20]. The second term $l(r) \left(cos2 - \frac{1}{3} \right)$ represents the dipole term and plays important role in determining the magnetostriction, λ_{100} or λ_{111}. Summing all nearest neighbor pair in cubic lattice, the total magnetoelastic energy can be expressed in term of strains $(\varepsilon_{xx}, \varepsilon_{yy}, \varepsilon_{zz}, \varepsilon_{xy}, \varepsilon_{yz}, \varepsilon_{zx})$ and orientation of magnetization $(\varepsilon_x, \varepsilon_y, \varepsilon_z)$ as:

$$\begin{aligned} E_{magnetoelastic} = &B_1 \left[\varepsilon_{xx} \left(\alpha_x^2 - \frac{1}{3} \right) + \varepsilon_{yy} \left(\alpha_y^2 - \frac{1}{3} \right) + \varepsilon_{zz} \left(\alpha_z^2 - \frac{1}{3} \right) \right] \\ &+ B_2 \left(\varepsilon_{xy} \alpha_x \alpha_y + \varepsilon_{yz} \alpha_y \alpha_z + \varepsilon_{zx} \alpha_z \alpha_x \right) \end{aligned} \tag{2.35}$$

The magnetoelastic energy is balance by the elastic energy that prevents crystal from being deformed without limit and can be expressed as,

$$E_{el}^{cubic} = \tfrac{1}{2}c_{11}\left(\varepsilon_{11}^2 + \varepsilon_{22}^2 + \varepsilon_{33}^2\right)$$
$$+c_{12}(\varepsilon_{11}\varepsilon_{22} + \varepsilon_{11}\varepsilon_{33} + \varepsilon_{22}\varepsilon_{33}) \qquad (2.36)$$
$$+\tfrac{1}{2}c_{44}\left(\varepsilon_{12}^2 + \varepsilon_{13}^2 + \varepsilon_{33}^2\right)$$

Where ε_{ij} represents deformation tensor and c_{ij} represents the elastic constant of the crystal.

Solving for minimization the sum of the magnetoelastic and elastic energies of magnetically saturated sample in equilibrium state

$$\frac{\partial\left(E_{elastic} + E_{magnetoelastic}\right)}{\partial\varepsilon_{ij}} = 0 \qquad (2.37)$$

If the direction of the magnetostriction in the measurements is characterized by the direction cosines β_i, then final expression for the elongation observed in cubic crystals due to these strains can be written as,

$$\tfrac{3}{2}\lambda = \tfrac{\triangle l}{l} = \tfrac{3}{2}\lambda_{100}\left(\alpha_x^2\beta_x^2 + \alpha_y^2\beta_y^2 + \alpha_z^2\beta_z^2 - \tfrac{1}{3}\right)$$
$$+3\lambda_{111}\left(\alpha_x\alpha_y\beta_x\beta_y + \alpha_x\alpha_z\beta_x\beta_z + \alpha_y\alpha_z\beta_y\beta_z\right) \qquad (2.38)$$

If direction of measurement is in [100] axis, i.e $\beta_x = 1, \beta_y = \beta_z = 0$. Then

$$\frac{\triangle l}{l} = \frac{3}{2}\lambda_{100}\left(\alpha_x^2 - \frac{1}{3}\right) \qquad (2.39)$$

Where λ_{100} change in length along [100], when magnetization is also in [100] direction. The maximum strain in this direction is,

$$\lambda_{\parallel} - \lambda_{\perp} = \frac{3}{2}\lambda_{100} \qquad (2.40)$$

This is accomplished by rotating the magnetization from perpendicular to parallel to the [100] axis, similarly for [111] measurement directions $\beta_x = \beta_y = \beta_z = 1/\sqrt{3}$ gives,

$$\lambda_{\parallel} - \lambda_{\perp} = \frac{3}{2}\lambda_{111} \qquad (2.41)$$

Were λ_{111} is length change along [111] when the magnetization is likewise along [111].

The magnetostriction measured in the [110] direction (λ_{110}) is dependent of λ_{100} and λ_{111}, and can be expressed as:

$$\lambda_{110} = \frac{1}{4}\lambda_{100} + \frac{3}{4}\lambda_{111} \qquad (2.42)$$

Figure 2.9 shows the λ_{100}, λ^{α} (volumetric) and λ_{111} strains mode of cube.

The relation between magnetostriction, elastic and magnetoelastic constants are:

$$\lambda_{100} = -\frac{2}{3}.\frac{B_1}{c_{11} - c_{12}} \qquad (2.43)$$
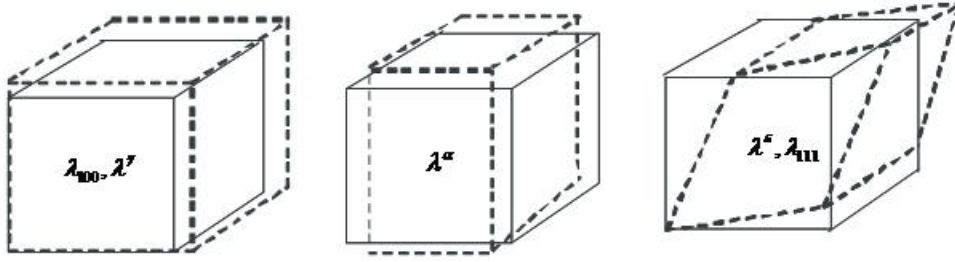
Figure 2.9: The strain modes of a cube [1].

$$\lambda_{111} = -\frac{1}{3} \cdot \frac{B_2}{c_{44}} \tag{2.44}$$

Volumetric distortion for cubic system can be written as,

$$\lambda^\alpha = \frac{B_0 + B_{1/3}}{c_{11} + 2c_{12}} \tag{2.45}$$

Where Where B_j represents magnetoelastic constant.

2.10.3 Magnetostriction in Hexagonal Single Crystals

For hexagonal symmetry elastic energy density can be written as,

$$\begin{aligned}
E_{el}^{hex} = {} & \tfrac{1}{2}c_{11}\left(\varepsilon_{11}^2 + \varepsilon_{22}^2\right) + \tfrac{1}{2}c_{33}\varepsilon_{33}^2 + c_{12}\varepsilon_{11}\varepsilon_{22} \\
& + c_{13}(\varepsilon_{11} + \varepsilon_{22})\varepsilon_{11} + \tfrac{1}{2}c_{44}(\varepsilon_{13}^2 + \varepsilon_{23}^2) + (c_{11} - c_{12})\,\varepsilon_{12}^2
\end{aligned} \tag{2.46}$$

The magnetostriction of hexagonal system is given by,

$$\begin{aligned}
\lambda = \tfrac{\triangle l}{l} = {} & \lambda_A \left((\alpha_1\beta_1 + \alpha_2\beta_2)^2 - (\alpha_1\beta_1 + \alpha_2\beta_2)\alpha_3\beta_3\right) \\
& + \lambda_B \left((1 - \alpha_3^2)(1 - \beta_3^2) - (\alpha_1\beta_1 + \alpha_2\beta_2)^2\right) \\
& + \lambda c \left(1 - \alpha_3^2\right)\beta_3^2 - (\alpha_1\beta_1 + \alpha_2\beta_2)\alpha_3\beta_3 \\
& + \lambda_D(\alpha_1\beta_1 + \alpha_2\beta_2)\alpha_3\beta
\end{aligned} \tag{2.47}$$

with,

$$\lambda_A + \lambda_B = \frac{2B_2 c_{13} - (2B_3 + B_1)\,c_{33}}{c_{33}(c_{11} + c_{12}) - 2c_{13}^2} \tag{2.48}$$

$$\lambda_A - \lambda_B = \frac{B_1}{(c_{11} - c_{22})} \tag{2.49}$$

$$\lambda_c = \frac{B_2(c_{11} + c_{12}) - (2B_3 + B_1)\,c_{13}}{c_{33}(c_{11} + c_{12}) - 2c_{13}^2} \tag{2.50}$$

$$4\lambda_D - (\lambda_A + \lambda_B + \lambda_c) = \frac{B_4}{c_{44}} \tag{2.51}$$
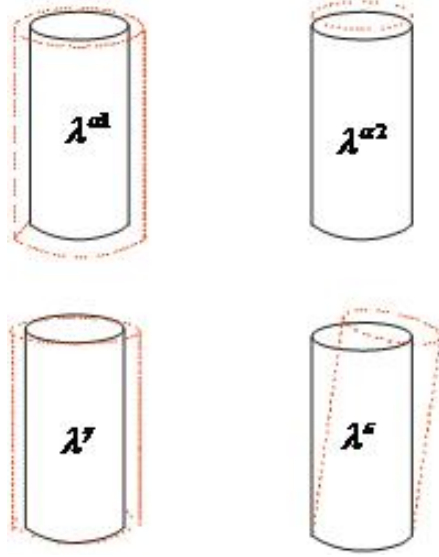
Figure 2.10: The symmetry modes for circular cylinder, hexagonal system [1].

2.10.4 Magnetostriction in Isotropic Materials

For an isotropic body i.e., amorphous or polycrystalline material, there is only one strain parameter, λ_s, and $\lambda_0 = \lambda_{100} = \lambda_{111} = \lambda_{110}$

$$\lambda_s(\theta) = \frac{\triangle l}{l} = \frac{3}{2}\lambda_s \left(cos^2\theta - \frac{1}{3} \right) \tag{2.52}$$

Where $\lambda_s(\theta)$ is the saturation magnetization at angle θ from the field and λ_s is saturation value in ideal demagnetized state and it is calculated from the difference between the maximum magnetostriction with field applied parallel to a certain direction and field applied perpendicular to the given direction. Substituting $\theta = 0°$ and $\theta = 90°$ in equation 2.52 ,

$$\lambda_\parallel - \lambda_\perp = \lambda_s + \frac{1}{2}\lambda_s = \frac{3}{2}\lambda_s \tag{2.53}$$

2.10.5 Saturation Magnetostriction in Polycrystalline Materials

In polycrystalline materials, the situation is more complex than in single crystals, because one has to relate the magnetostriction of the whole piece of material to the magnetoelastic and elastic properties of the individual grains. This problem cannot be solved by an averaging procedure. For this reason, it is assumed that the material is composed of a large number of domains with the strain uniform in all directions. It can be shown that, for a material in which no preferred grain orientation exists, for a cubic polycrystalline material the following expression can be found [20, 30, 31],

$$\lambda_s = \frac{2}{5}\lambda_{100} + \frac{3}{5}\lambda_{111} \tag{2.54}$$

Additionally useful definitions for a polycrystalline material are:
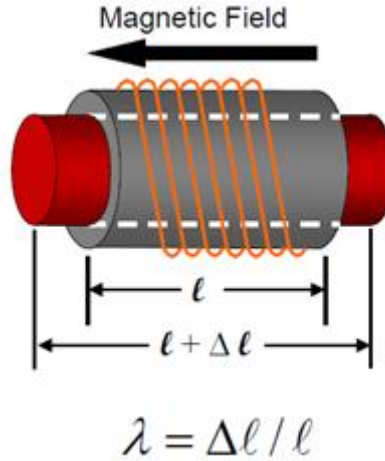
Figure 2.11: Joule Magnetostriction [33].

$\frac{\triangle l}{l}$ =Linear magnetostriction

$\frac{\triangle V}{V} = \lambda_{parallel} + 2\lambda_{perpendicular}$ =Volume magnetostriction

$\lambda_t = \lambda_\parallel - \lambda_\perp$ = Shape magnetostriction

$\lambda_\perp = \lambda_\parallel/2$=Isotropic material

2.11   Magnetostrictive Effects

In general, magnetostriction is reversible exchange between magnetic and mechanical energies [22]. Using this equivalence between magnetic and elastic states, magnetostrictive materials can be used for actuators and sensors application [32]. Several effects are now recognized as a consequence of magnetostriction.

2.11.1   Joule Effect

A rod of magnetic material of length L is shown in Figure 2.11, surrounded by a coil in such a way that magnetic field H is produced along the length of rod [19], on applying magnetic field length L of rod increases by small amount. The strain $\Delta L/L$ is called linear magnetostriction or Joule magnetostriction. This "linear magnetostriction" is generally used in sensors or actuators.

Joule effect is most commonly used magnetostrictive effect and it is the strain produced in direction of applied field. This effect is illustrated in Figure 2.12.

The magnetostrictive change with increasing magnetic field and saturates at value λ_s. If the magnetostrictive strain is positive, the effect is called positive magnetostriction, otherwise it is designated as negative magnetostriction.
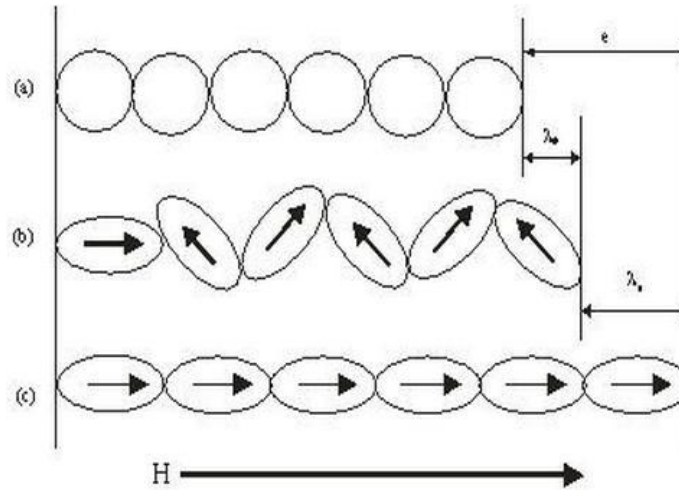
Figure 2.12: Schematics diagram illustrating the magnetostriction of ferromagnetic material (a) paramagnetic state above T_c ; (b) after it has been cooled through T_c; and (after it brought to saturation by a field H) [19].
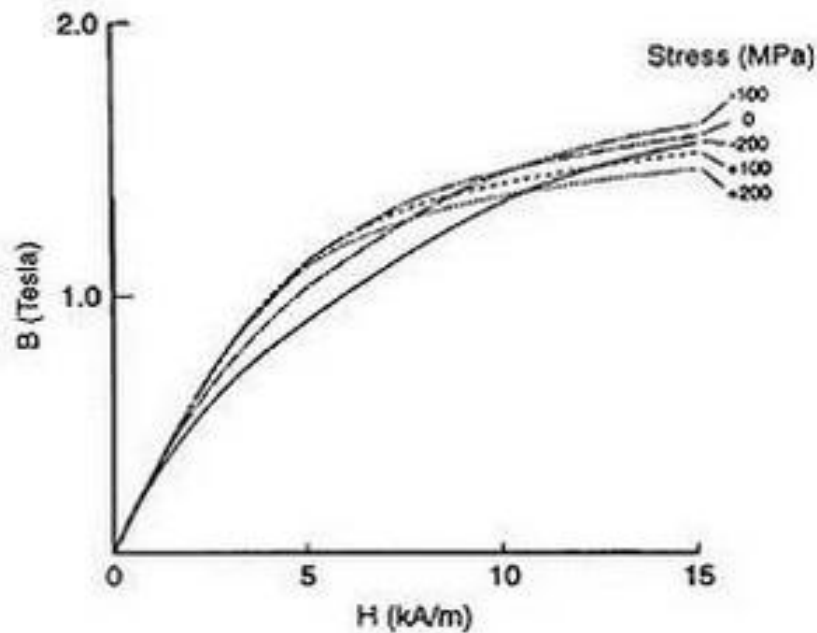
Figure 2.13: Effect of mechanical stress on the magnetization of ferromagnetic material [34].

2.11.2   Villari Effect

The Villari effect is inverse of the Joule magnetostriction and refers to the changes in magnetization of a magnetostrictive material in response to uni-axial stress [34]. The Villari effect is a reversible effect and also used in sensor applications [35]. Figure 2.13 shows the effect of mechanical stress on the magnetization of ferromagnetic material.

2.11.3 ΔE Effect

Young's modulus of materials changes on applying a magnetic field. The elasticity of magnetostrictive materials is composed of conventional stress-strain elasticity (E_0) arising from inter atomic forces and the magnetoelastic (E_s) contribution due to the rotation of magnetic moments and resulting strain which occur when a stress is applied. This is known as the ΔE effect and is quantified by $\Delta E = (E_s - E_0)/E_0$ [19].

2.11.4 Wiedemann Effect

A current-carrying ferromagnetic wire will produce a circular magnetic field in a plane perpendicular to the wire and the moments will align predominantly in the circumferential direction. When an axial magnetic field is applied, some of the moments align in a helical fashion creating a helical magnetic field. The twist observed in the wire is called the Wiedemann effect [19]. The physical background to this effect is similar to Joule effect, instead of pure tensile or compressive strains forming as a result of magnetic field, there is shear strain which results in a torsional displacement of ferromagnetic sample [22] .

2.11.5 Matteuci Effect

The inverse Wiedemann effect, known as the Matteuci effect, is the change in axial magnetization of a current carrying wire when it is twisted. Further details can be found in [36].

2.11.6 Magnetovolume (Barret) and Nagaoka-Honda Effect

In certain extreme operational conditions the volume of materials changes in response of magnetic field. This anomalous volume change is called the volume magnetostriction or Barret effect [35]. For instance, the fractional volume change is only 10^{-7} at a much larger field of 80 kA/m [22] . The inverse of the Barret effect, the Nagaoka-Honda effect, is the change in magnetic state caused by a hydrostatic pressure [37, 38]. However these variations are usually very small.

2.12 History of Magnetostrictive Materials

Magnetostrictive materials have been studied for a longtime. In 1842 James P Joule for the first time established the fact that ferromagnetic substance changes its length when magnetized and Iron was the very first material identified to be as magnetostrictive, shown in Figure 2.14 [28, 39].
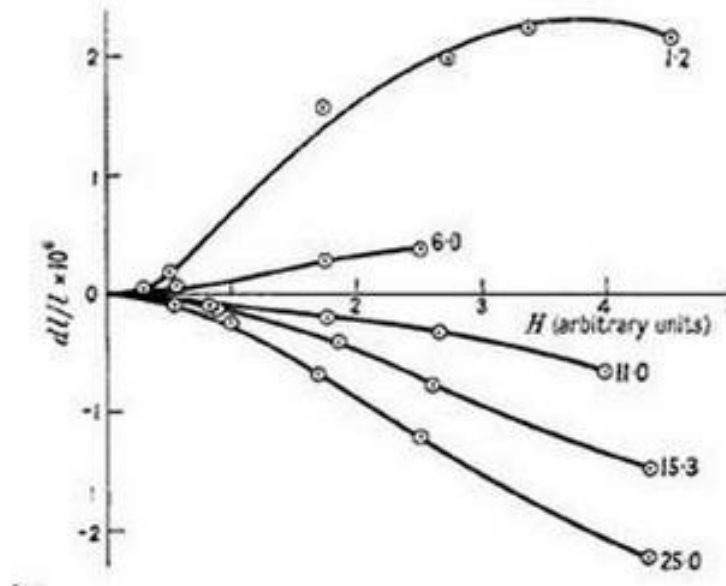
Figure 2.14: Joule original measurement of magnetostriction of Iron. The figure give applied tension in Kg. mm^{-2}.

Subsequently, nickel (Ni), cobalt (Co) and alloys of these materials were found to show magnetostrictive effects with quite small value of strains and variation in magnitude and sign from one material to other shown in Figure 2.15. During world war II one of the first practical applications of magnetostriction was of single crystal nickel having magnetostriction about 50 ppm to drive SONAR devices in echo location. Other early applications were telephone receivers, hydrophones, fog horns, oscillators, and torque sensors [19].

In 1963, largest-known magnetostriction in the rare-earth elements terbium (Tb) and dysprosium (Dy) were discovered. The strains in these elements were of the order of 10,000 × 10^{-6} at cryogenic temperatures and vanishes at room temperature due to low curie temperature 218 K [40] for terbium and 85K [41] for dysprosium. Using these materials as an actuator, at ambient temperature and above was impracticable.

This led the scientist to look for the materials that would work at room temperature, have large magnetostriction and require low magnetic field to attain maximum possible magnetostriction. In 1970 it was shown that by alloying rare earth (R) elements with 3d Iron (Fe), R-Fe$_2$ alloys (TbFe$_2$ and DyFe$_2$) gives huge magnetostriction even at room temperature. For example TbFe$_2$, DyFe$_2$ and SmFe$_2$ exhibit (3/2 λ_s) magnetostriction of 2630 × 10^{-6} , 650 × 10^{-6} and -2430 × 10^{-6} respectively [26]. However these R-Fe$_2$ alloys exhibit a very high value of magnetocrystalline anisotropies and requires large magnetic field, more than 2 MA/m to achieve saturation magnetostriction [19]. This poses technological limitations to use practically these materials, in actuators applications. Figure 2.16 shows room temperature magnetostriction of some rare earth-Fe$_2$ polycrystals.

However in 1980, A.E. Clark found that, fractional substitution of dysprosium (Dy) for terbium (Tb) in the TbFe$_2$ system considerably reduces the magnetocrystalline anisotropy.
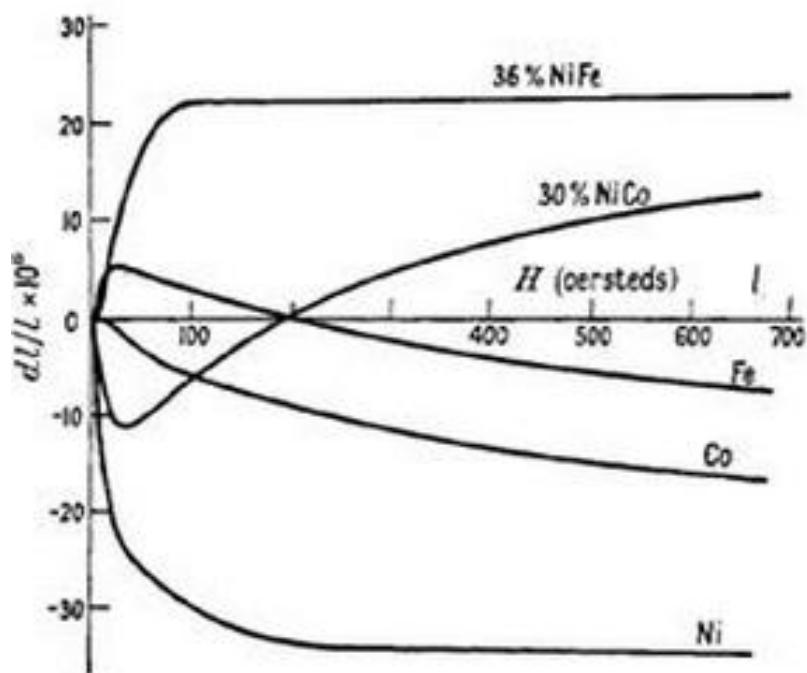
Figure 2.15: The magnetostriction of some common polycrystalline substances as a function of magnetic field strength [39].
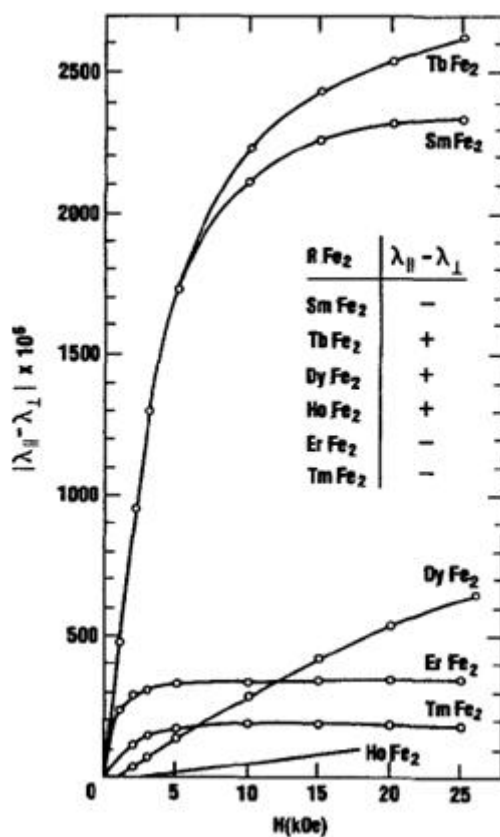
Figure 2.16: Room temperature magnetostriction of rare earth-Fe_2 polycrystals ($SmFe_2$, $TbFe_2$, $DyFe_2$, $ErFe_2$ and $TmFe_2$) [1].
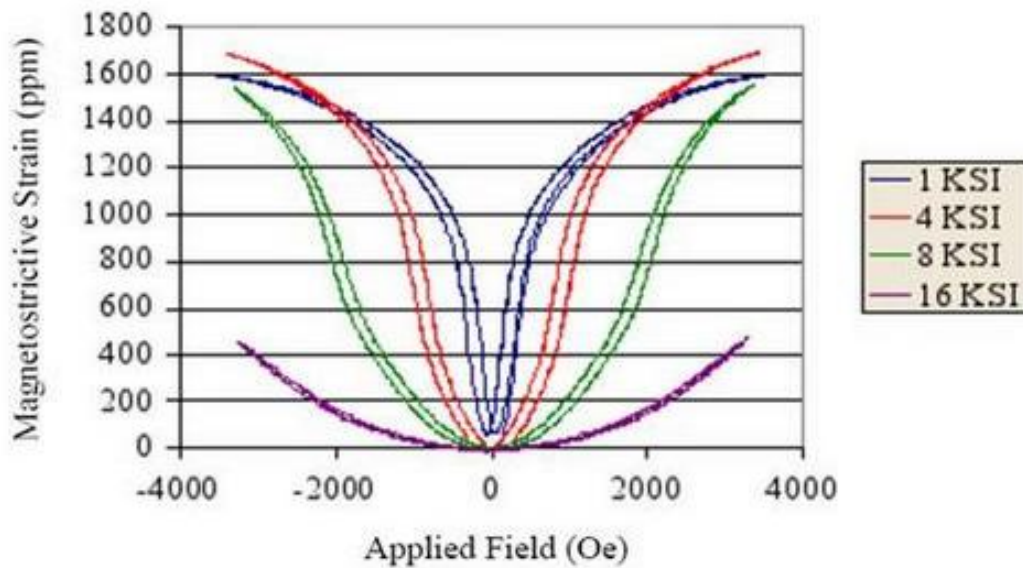
Figure 2.17: Magnetostriction of Terfenol-D at various fields (ETREMA Products, Inc.).

This lead to the development of the alloy $Tb_{0.27}\ Dy_{0.73}\ Fe_{1.9-1.95}$ commercially available since 1980 under the brand name Terfenol -D (Ter = terbium, Fe = iron, N = Naval, O = Ordnance, L = Laboratory, D = dysprosium).

The highest room temperature magnetostriction for Terfenol-D is $1{,}600 \times 10^{-6}$ at a reasonable saturation field of 0.16 MA/m [19] as shown in Figure 2.17.

In 1978, a new class of magnetostrictive material Metglas (metallic glass) based on amorphous metal was introduced. Metglas was produced by rapid cooling of iron, nickel, and cobalt alloys together with one or more of the elements silicon, boron, and phosphorus by making thin ribbons by melt spinning process. The higher value of coupling coefficient of Metglas (k > 0.92) makes them ideal for technological applications in sensor industry [38]. The best isotropic material is an iron rich metallic glass, Metglas® 2605 SC having composition $Fe_{81}B_{13.5}Si_{3.5}C_2$ produced by Allied Signals Inc. $Co_{75}Si_{15}B_{10}$ is also metallic glass with a negative magnetostriction which can be used also for force sensors applications. Table 2.1 contains some properties of Metglas® 2605C, electrical resistivity of this material is 20 times larger, which allows the application of these materials at high frequency with good efficiency.

In 2001, a new class of materials Iron-Gallium alloys (Galfenol) was developed at the naval warfare center by Clark et al [3, 5] . These alloys exhibit moderate magnetostriction up to ∼450 ppm at very low magnetic field shown in Figure 2.18 [6].

The effect of alloying iron (Fe) with Aluminum (Al) and Beryllium (Be) has also been studied [5, 43]. Fe-Ga and Fe-Al alloys show similar trends up to 25 at. % of Ga or Al. Fe-Be alloys, investigated up to 11 at. % Be, show magnetostriction similar to Fe-Ga, but the high toxicity of Be makes Fe-Be alloys difficult to handle. Moreover limited studies to

Properties (symbols)/ Units	Annealed Metglass 2605SC
Specific mass (ρ) /Kg.m^{-3}	7.320
Crystallization temperature /K	753
Thermal expansion coefficient (α_T) /10^{-6}.K^{-1}	5.9
Young modulus (Y^H) /GPa	25
Young modulus (Y^B)/ GPa	200
Vicker hardness under 50g /(Hv)	880
Tensile elastic limit /MPa	700
Thermal conductivity /W.m^{-1}.K^{-1}	9
Electrical resistivity (ρ_e) /$\mu\Omega$.m	1.35
Curie temperature (T_c) /K	643
Magnetic polarization ($J = \mu_0 M_s$)/ T	1.35 (H=80 A.m^{-1}) 1.61 (satn.)
Initial relative permeability (μ^τ_{33}/μ_0)	20,000 (80,000 at σ_{zz} = 1MPa)
Maximum relative permeability (μ^{max})	300,000
Magnetostriction coefficient (λ_s) /10^{-6}	30
Magnetomechanical coupling (k_{33}^{max})	0.97 (H = A.m^{-1})
Static magnetostrictivity (d_{33}^{max})/nm.A^{-1}	1,000

Table 2.1: Physical properties of Metglas 2605SC annealed ribbon [42].
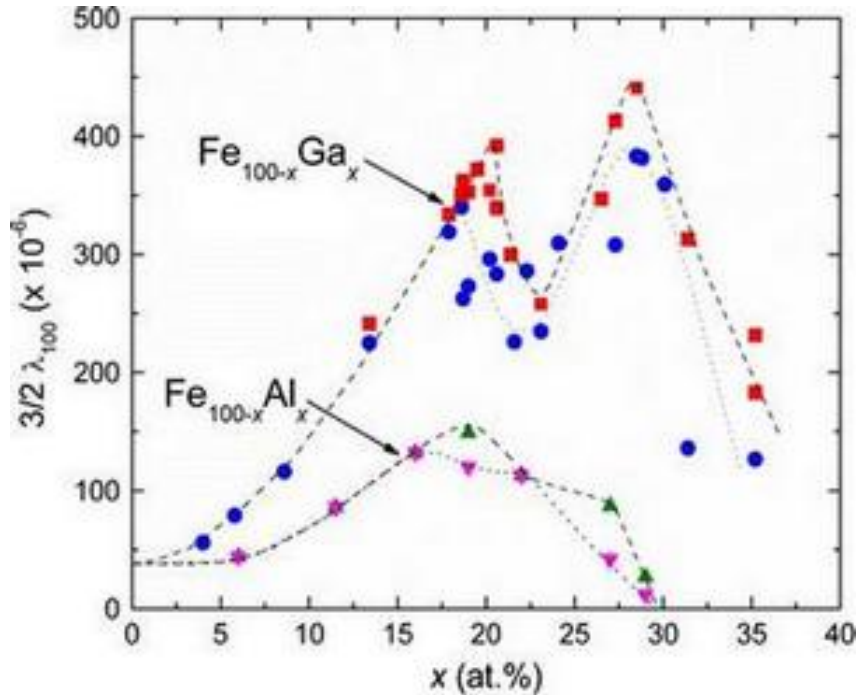
Figure 2.18: Magnetostriction constant (3/2) λ_{100} of Fe–Ga and Fe–Al alloys as a function of composition for two heat treated conditions. Samples were annealed in the A2 disordered bcc region and either slow cooled at a programmed rate of 600°/h (blue circles, Fe–Ga alloys; green triangles, Fe–Al alloys) or quenched into water at room temperature (red squares Fe–Ga alloys; magenta inverted triangles, Fe–Al alloys) [6].

	Terfenol-D	Galfenol	Iron	Nickel
Magneto-Mechanical Properties				
3/2 λ_s(μ strain)	1600~2400	150~420	-24	-66
Coupling Factor	0.7-0.8	0.69-0.76		
Hysteresis in λ-H and B-H curves	moderate	very low	low	low
Preferred plane for magnetostriction	<111>	<100>	<100>	<111>
Mechanical Properties				
Modulus of Elasticity (GPa)	25-35	65	200	207
Ultimate tensile strength (MPa)	28	500	250	140
Yield tensile strength (MPa)	28	500	250	140
Magnetic Properties				
Saturation magnetization (Tesla)	1	1.8	2.2	0.6
Relative permeability	2~8	60~360	150~5000	110~600
Magnetic field for 90% of λ_s(KA/m)	120	8		
Thermal properties				
Temperature dependence of λ	High	moderate		
Curie Temperature (°C)	357	675	1044	627
Other				
Raw material Cost ($/g)	0.5	0.08	0.014	
Crystallographic Structure	hexagonal	bcc	bcc	fcc
Electrical resistivity ($\mu\Omega$.cm)	60	120	8.9	6.4

Table 2.2: Comparison of the property between Terfenol-D, Galfenol, Iron and Nickel **[8, 26, 46]**.

date have shown that ternary alloys of Fe and Ga with nickel, molybdenum, tin, aluminum and cobalt do not considerably improve its magnetostrictive properties [6, 44, 45].

  Table 2.2 shows the property comparison of the properties between Terfenol-D, Galfenol, Iron and Nickel[1] [46].

---

[1]www.matweb.com

2.13   Applications of Magnetostrictive Materials

Magnetostrictive materials have two types of applications: actuators or sensors. Magnetostrictive based actuators have an electrical coil shaped in solenoid form around magnetostrictive rod. The coil transforms electrical energy into magnetic energy and a magnetostrictive rod convert the magnetic energy into mechanical energy. Design of magnetic circuit and driving coil are the important parameters for the optimization of magnetostrictive actuators.
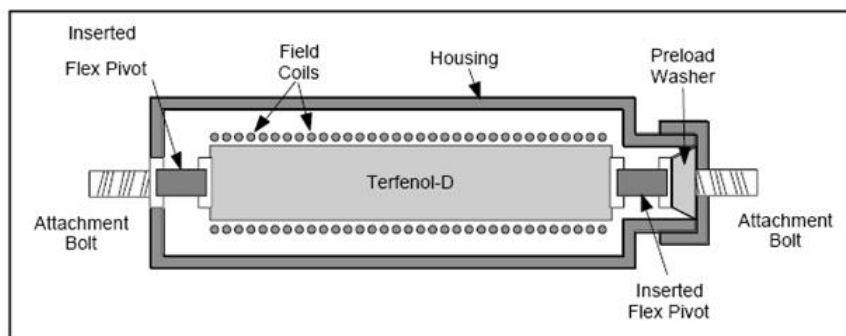
Figure 2.19: Standard actuator (Ref: Midé Technology Corporation, USA).

Magnetostrictive based sensor use a piece of magnetostrictive materials to convert mechanical strain into a changed magnetic permeability, reluctance and surrounding magnetic field of the material. A pick up coil, sensing coil, Hall probe or GMR probe can be used to measure this change of the magnetic state. Similar to the actuator a good circuit design is advantageous for sensor efficiency optimization.

After availability of Terfenol-D on commercial scales in mid of 1980s, many potential application of magnetostrictive materials were suggested , some of them are grouped as follows [26],

- Sound and vibration sources system

  - Magnetostrictive based Tonpilz transducers, ring transducers, flextensional transducers (by Asea Brown Boveri of Sweden) for acoustic transmission underwater SONARS, underwater information exchange, geophysical surveying, ocean tomography and mine clearance etc.

  - Sound sources using magnetostrictive transducer as broadband vibration sources are found in solid state speakers, laboratory and industrial shakers.

- Vibration control systems in infinitely soft vibration mode to control vibrating electrical machines and infinitely stiff modes to control the position of an object so that it is kept at fixed positions.

- High strain and force capability of magnetostrictive materials make them ideal for direct control in micromotional systems: diesel fuel engine injectors, laser optical scanning movie film pin registration and systems astronomical image stabilizing platforms.

- Non-direct motion control systems by applying magnetic field from a distance without wires to the magnetostrictive materials. Application includes linear motors, fast-response valve actuators fast servo valves, pumps and rotary motors.

- Material processing systems by direct interaction with magnetostrictive actuator or sound penetration. Ultrasonics high-frequency, high-power actuator used in medical, dental, petrochemical, sono-chemical applications includes :

    - Physical treatment such as ultrasonic cleaning, cell disruption and sterilization system, ultrasonic friction welding, emulsification, demulsifications, foaming systems, mixing, vibration and boundary layer control systems.

    - Chemical treatment such as petroleum production and processing, sonochmeistry process (i.e. chemical synthesis, emulsification breaking, catalysis, food processing)

- Electromechanical converter such as energy harvester system

- Sensor system includes various type compressive force, moment and torque non contact sensors.

2.14 Literature Review

2.14.1 Magnetostriction of Fe-Ga (Galfenol) Alloys

Body-centered cubic (bcc) Fe exhibits different sign of magnetostriction constants as: $\lambda_{100} = +20$ ppm and $\lambda_{111} = -16$ ppm at room temperature. This leads to a change of sign in the field dependence of the magnetostriction as well as to a strange behavior of the temperature dependence of λ in polycrystalline Fe [47,48]. Substituting Fe by nonmagnetic Si causes a decrease of the magnetostriction value, which is very helpful to reduce the losses in Fe–Si steels [49]. Generally it is expected that substituting the cubic magnetic Fe by small amounts of nonmagnetic elements causes a decrease of the magnetocrystalline anisotropy and a reduction of the magnetostrictive anomalies. However, Hall has shown that the addition of some nonmagnetic elements, such as V, Cr, and Al, strongly alters the anisotropy and enhances the magnetostriction [14, 50] . Therefore, substituting cubic 3d-metals like Fe or Ni by nonmagnetic elements like Ga or Al might be a new method to develop cheap and soft magnetic materials with high magnetostriction. Since few years it was realized that an essential increase of the magnetostriction of Fe could be achieved substituting small amounts of Fe by Ga [5,51–53]. In single-crystalline $Fe_{100-x}Ga_x$ between 17 and 19 at% Ga a maximum magnetostriction, which can reach values of 3/2 $\lambda_{100} \sim 400$ ppm at room temperature was found (See Figure 2.18).
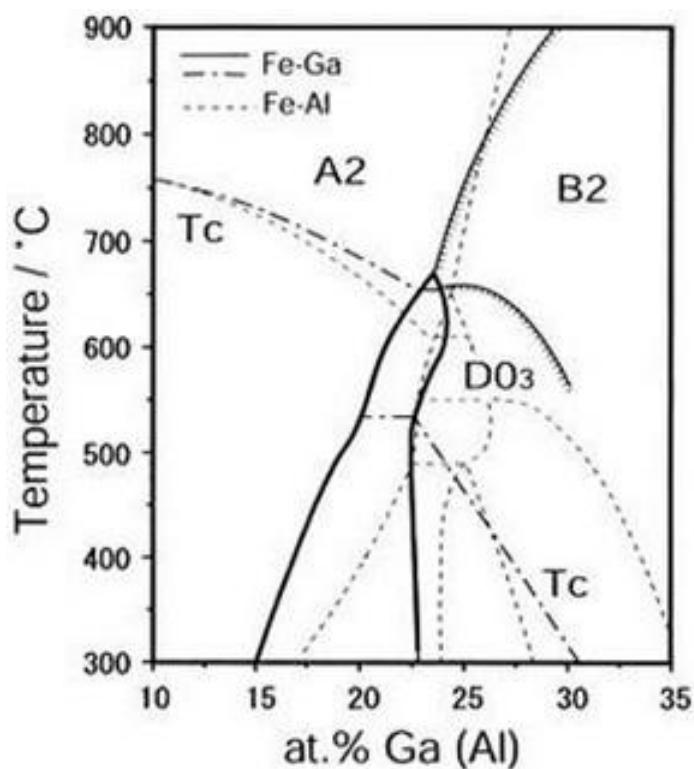
Figure 2.20: Metastable Fe–Ga phase diagram [52].

A second maximum exist close to 27 at% of Ga. These maxima depend strongly on the sample preparation [53]. Clark et al. have explained the main origin of high magnetostriction in 3d-based Fe–Ga alloys is the change of magnetoelastic energy due to the Ga substitution causing a lattice softening. The magnetostriction increase is explained by an increase of the magnetoelastic coupling constant due to short-range ordering between the Ga–Ga atoms in BCC α-iron (A_2 structure) with randomly substituted gallium atoms [5]. Measuring the elastic constants in Fe–Ga and calculating the magnetoelastic energy constants, a peak at 19% Ga is derived [53]. A further increase in gallium (Ga) substitution induces long-range ordering, which produces DO_3 and B_2 structures (Figure 2.20) that mitigate the magnetostriction [52].

2.14.2 Magnetostriction of Melt Spun Fe-Ga Ribbons

In recent years a large number of papers appeared reporting large and even "giant" magnetostriction values obtained on rapidly quenched melt-spun Fe-Ga ribbons. The reported magnetostriction values range from –3000 to + 1100 ppm [11, 54–56].

Figure 2.21 shows the magnetostriction measured on $Fe_{83}Ga_{17}$ ribbons with different thicknesses along the direction of the melt-spun ribbon length by a strain gauge, applying a magnetic field in the direction perpendicular to the ribbon [55].
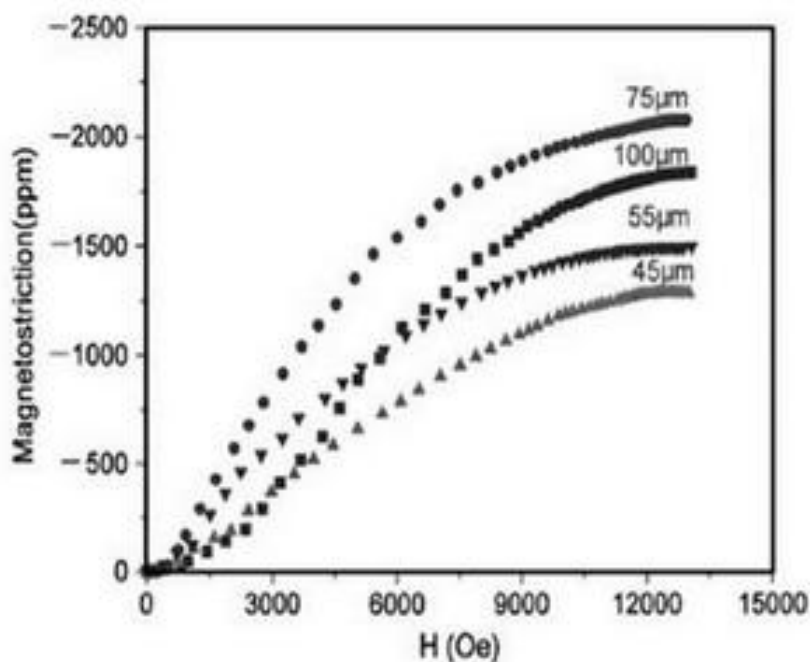
Figure 2.21: Magnetostriction behaviors measured for melt-spun ribbon $Fe_{83}Ga_{17}$ ribbons with various thicknesses [55].

"Giant" values ranging from -1300 ppm to +1100 ppm are reported in [57] for a $Fe_{85}Ga_{15}$ stacked ribbon sample (see Figure 2.22).

Figure 2.23 shows the magnetostriction measured on $Fe_{100-x}Ga_x$ (x = 16, 17, 19, 21) melt spun ribbons with along the direction of the melt-spun ribbon length by a strain gauge, applying a magnetic field in the direction perpendicular to the ribbon [56]. It is very important to note that "giant" magnetostrictions were obtained when measurements were performed using a strain gauge method in different geometries.

In a careful paper we investigated the possibility how such a "giant" magnetostriction can be achieved. It was shown that due to a large demagnetizing factor the ribbons tend to bend into the field direction thus causing an unrealistic high magnetostriction values. This means that in all cases were the field is applied perpendicular to the ribbon plane such effects has to be considered [58].
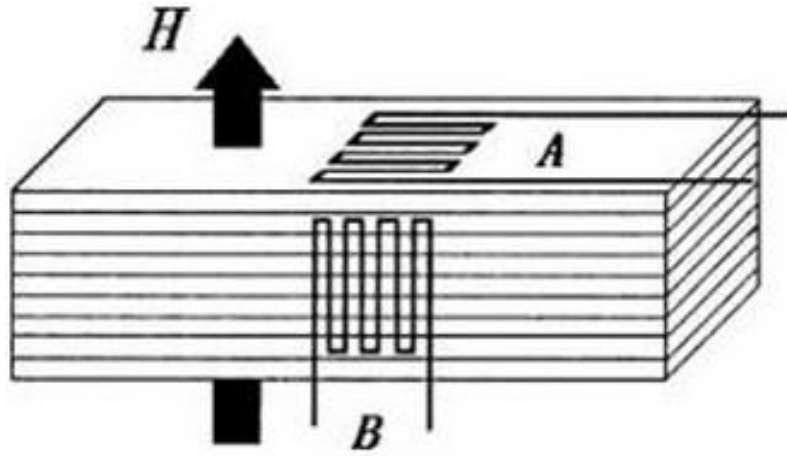
Figure 2.22: Stacked ribbons samples with the configuration of applied field and strain gauges [57].
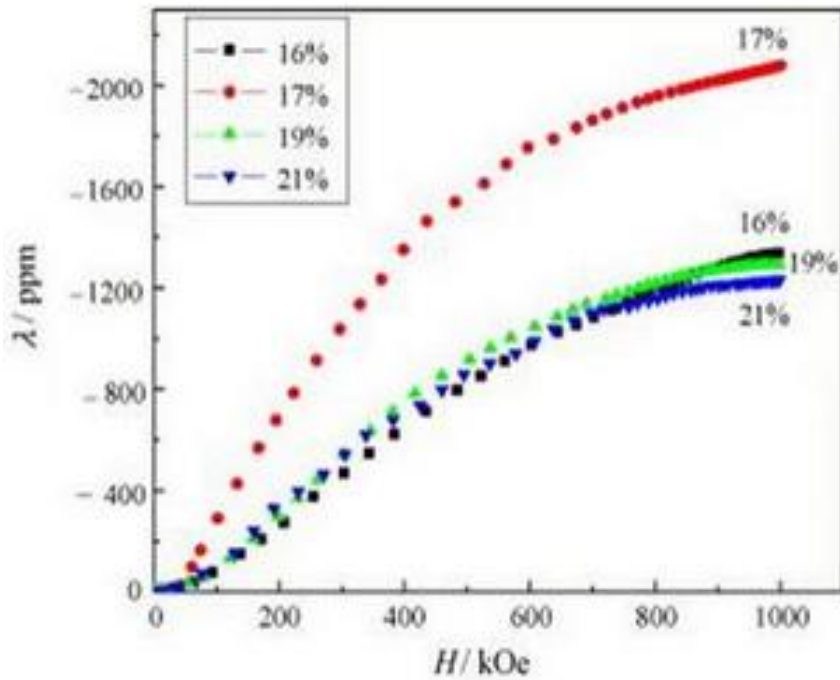
Figure 2.23: Magnetostriction of Fe-Ga ribbons with different Ga content [56].
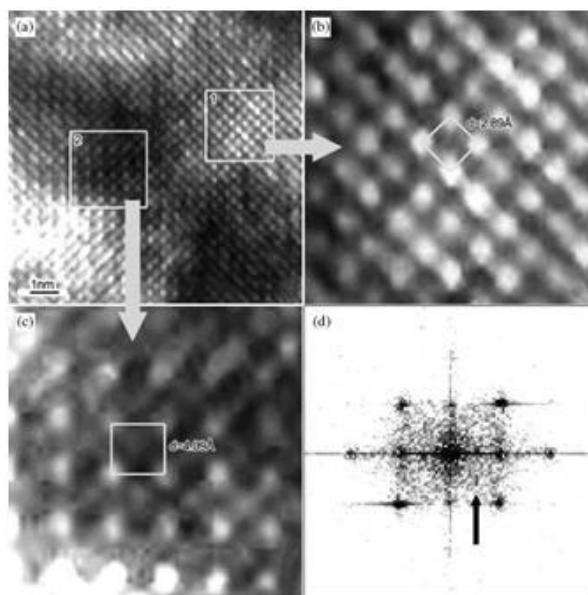
Figure 2.24: A typical high-resolution electron macrograph along [001] zone-axis direction, the structural features in the two boxes are apparently different; (b) TEM image with a larger magnification of box 1, showing a planar distance $d_1 = 2,89$ A; (c) TEM image showing the structural feature in the box 2, modified DO_3 structure of Fe–Ga with $d_2 = (2)^{1/2}.d_1 = 4,09$ A are recognized; (d) FFT pattern of area in box 2 showing the presence of weak super lattice spots [59].

These very high values were attributed to the appearance of a modified DO_3 structure together with Ga clusters, which are preferentially oriented with the ribbon normal due to the ribbon grain texture [15, 55, 56]. From HRTEM investigation, Zhang et al suggested the existence of Ga-rich clusters and DO_3 structure [56]. In similar XRD and TEM investigations made on $Fe_{85}Ga_{15}$ ribbon the existence of the DO_3 structure was also suggested – see Figure 2.24 [59].

However, investigations of the structure of melt-spun Fe-Ga with different concentrations of Ga were also reported [11]. There a DO_3 phase only for Ga concentration higher than 20 Ga at % was reported. For $Fe_{83}Ga_{17}$, only the disordered bcc phase was found, which shows some texture due to the melt spinning process. The rocking curve Figure 2.25 suggests that a texture is present and the [100] easy growth axis of bcc structure is tilted away from the ribbon normal as in Fe–Si alloys. It is interesting that only a magnetostriction of 130 ppm along the ribbon length was found in ref [59], however there a ferromagnetic resonance method was used to determine the saturation magnetostriction constant.

Recently, Pascarelli et al. investigated the local Fe–Ga atomic structure in highly magnetostrictive α $Fe_{80}Ga_{20}$ melt-spun ribbons using extended X-ray absorption fine structure (EXAFS) analysis at the Fe and Ga K-edges [60]. A careful X-ray diffraction (XRD) showed that this ribbon crystallizes in the A_2 phase. In this work, the presence of small Ga clusters could be excluded by EXAFS and X-ray absorption near edge structure (XANES), since no first shell Ga–Ga bonds were detected. However, EXAFS analysis of the second
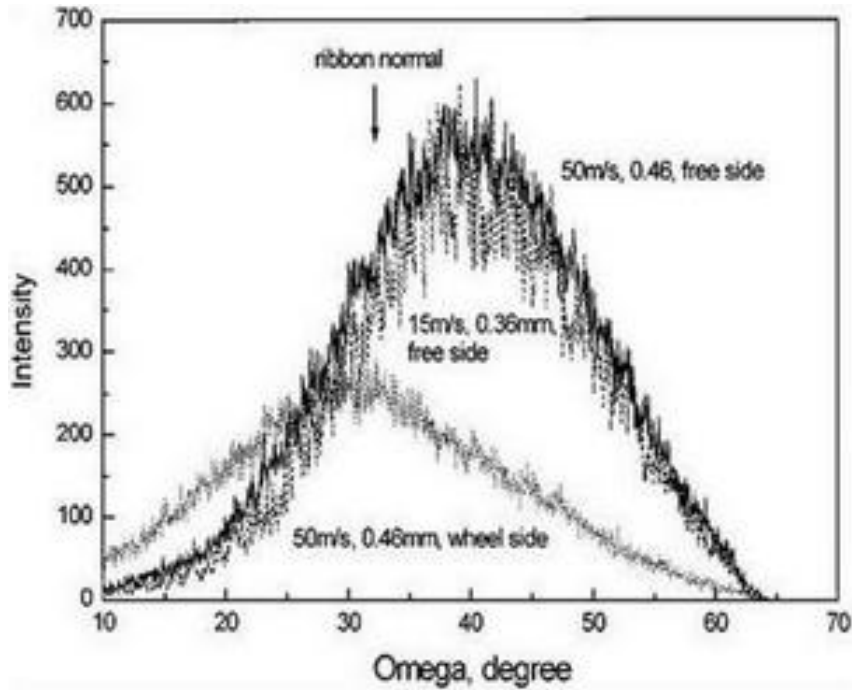
Figure 2.25: The (200) rocking curves of the free and wheel side of Fe Ga melt spun at 50 m/s, 0.46-mm O.D. and 15 m/s, 0.36-mm O.D. The ribbon normal is marked with an arrow (O.D = Orifice diameter) [59].

coordination shell around Ga clearly provides the evidence for the presence of one highly strained (+4%) Ga–Ga pair and five Ga–Fe pairs among the six crystallographically equivalent $< 100 >$ atomic pairs. This conclusion supports recent total energy calculations, which assign the large magnetostriction in these alloys to the strain caused by the rotation of the magnetization in the vicinity of such defects [61].

2.14.3 Magnetostriction in Fe-Al (Alfenol) Alloys

In the 60's decade, R. C. Hall showed that the addition of non-magnetic element Al in body centered cubic Fe resulted in a significant increase of the magnetostriction of pure Fe. He measured magnetostriction of Fe-Al single crystals in region of 6 to 30 atomic percent of Al at room temperatures and found that in $Fe_{100-x}Al_x$ single crystals λ_{100} increases with x, reaching near x = 19.2 a maximum value of 95 ppm depending upon atomic ordering [13, 50]. Leamy et al [62] measured room temperature magnetostriction of $Fe_{1-x}Al_x$ for x = 0.15-0.35, shown in Figure 2.26 and showed that shear modulus c_{11}-c_{12} decrease by nearly one half its iron value to minimum near x = 0.25 before increasing for larger x . The decreases in c_{11}-c_{12} vs. x in $Fe_{1-x}Al_x$ has been attributed to the transition from disordered α-Fe (bcc) to DO_3 or B_2 phases near x = 0.25 [62] .
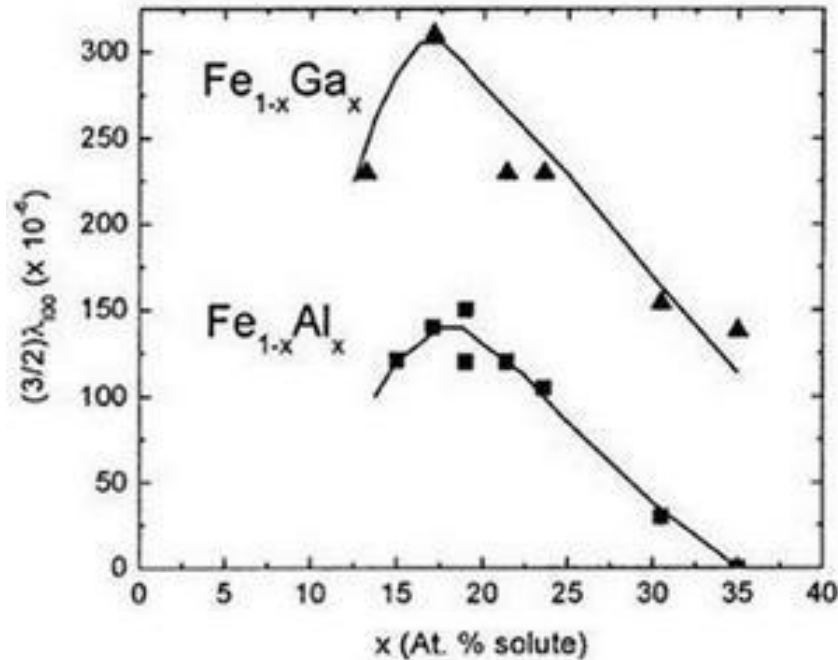
Figure 2.26: Saturation magnetostriction measured at room temperature for $Fe_{1-x}Al_x$ [5, 62].

In 1983 J.M Cook et al [63] measured magnetostriction of 25.24 at.% Al crystal and reported the $\lambda_{parallel}$ value 50 ppm along the [110] direction in the (001) plane, Figure 2.27 shows the measured magnetostriction values at 77 K and 296K.

Much more recently, Clark et al. [64] reported that the magnetostriction λ_{100} exhibits at 16.6 % Al a maximum value of about 130 ppm. Figures 2.30 and 2.31 , shows the saturation magnetostriction of $Fe_{1-x}Al_x$ for x = 14.1, 16.6, 21.5, 26.3 from 77 K to room temperature, magnetoelastic coupling (-b_{-1}) from 77 K to room temperature, comparison of (3/2) λ_{100} magnetostriction data of Fe-rich Fe–Al alloys and comparison of the magnetoelastic coupling, $-b_1$ for Fe-rich Fe–Al, Fe–Ga, and Fe–Be alloys respectively [64].
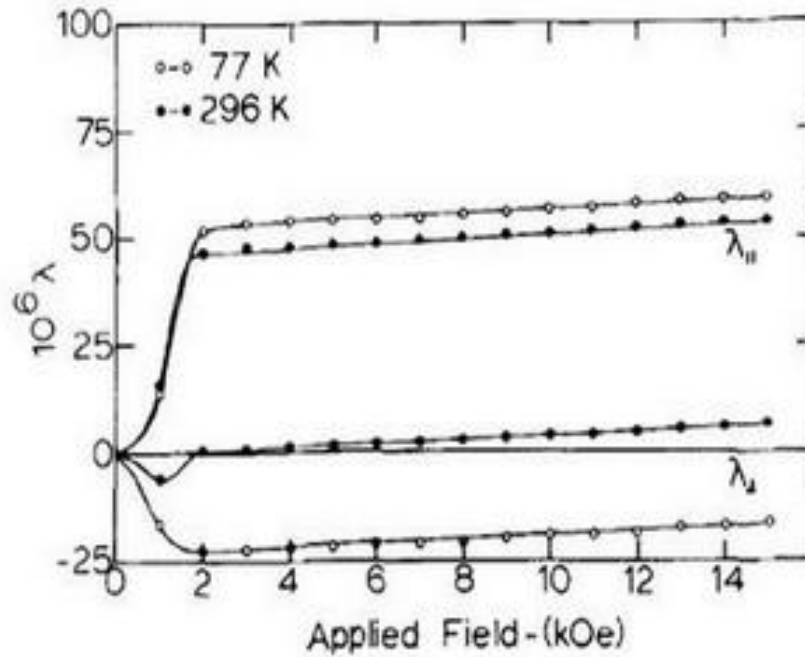
Figure 2.27: Magnetostriction of a 25.24 at. % Al crystal along crystal along the [110] direction as a function of applied magnetic field both parallel and perpendicular to the [110] direction at both 77 and 297K [63].
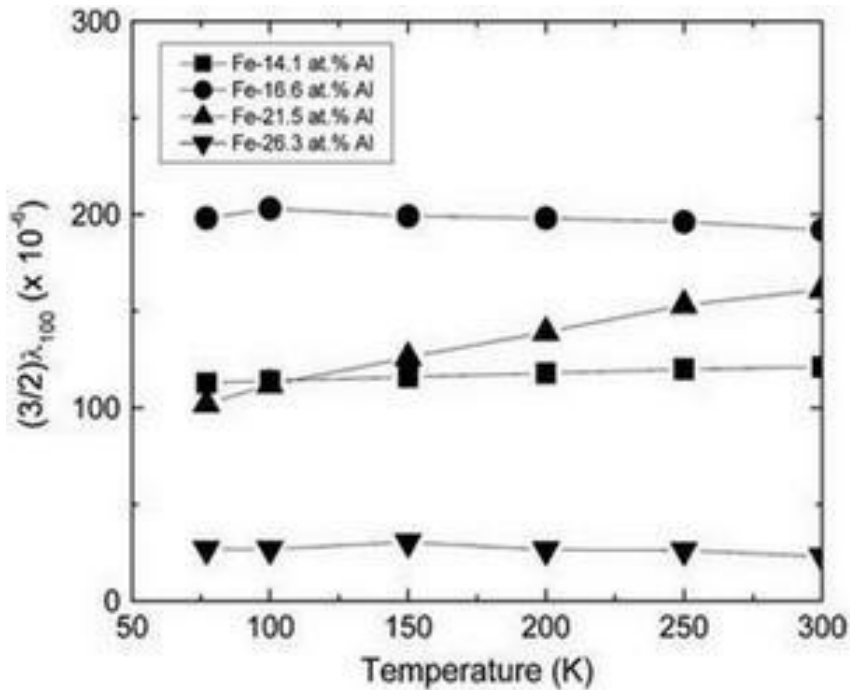
Figure 2.28: (3/2) λ_{100} for Fe-rich Fe–Al alloys from 77 K to RT [64].
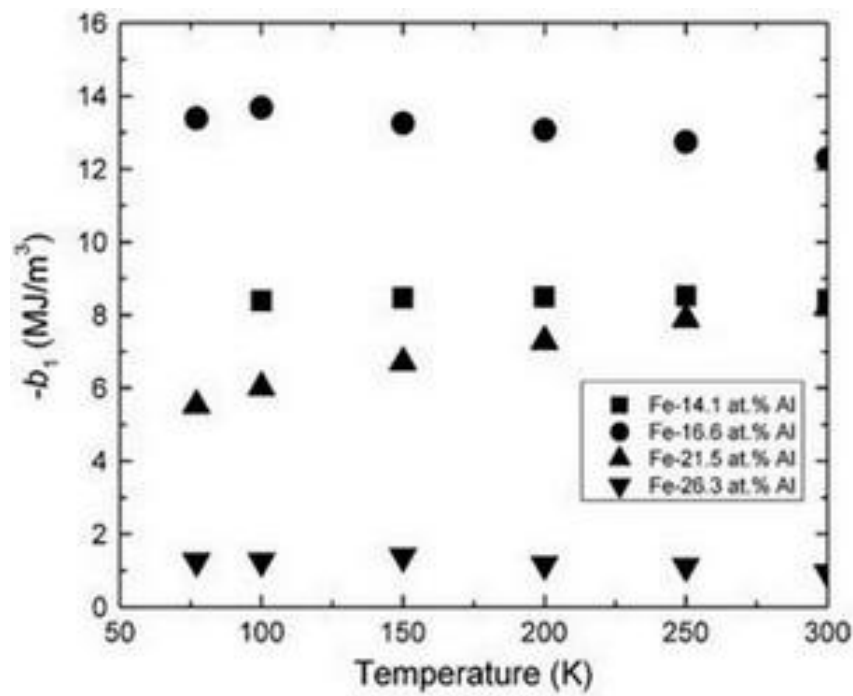
Figure 2.29: Magnetoelastic coupling, $-b_{-1}$, for Fe-rich Fe–Al alloys from 77 K to RT [64].
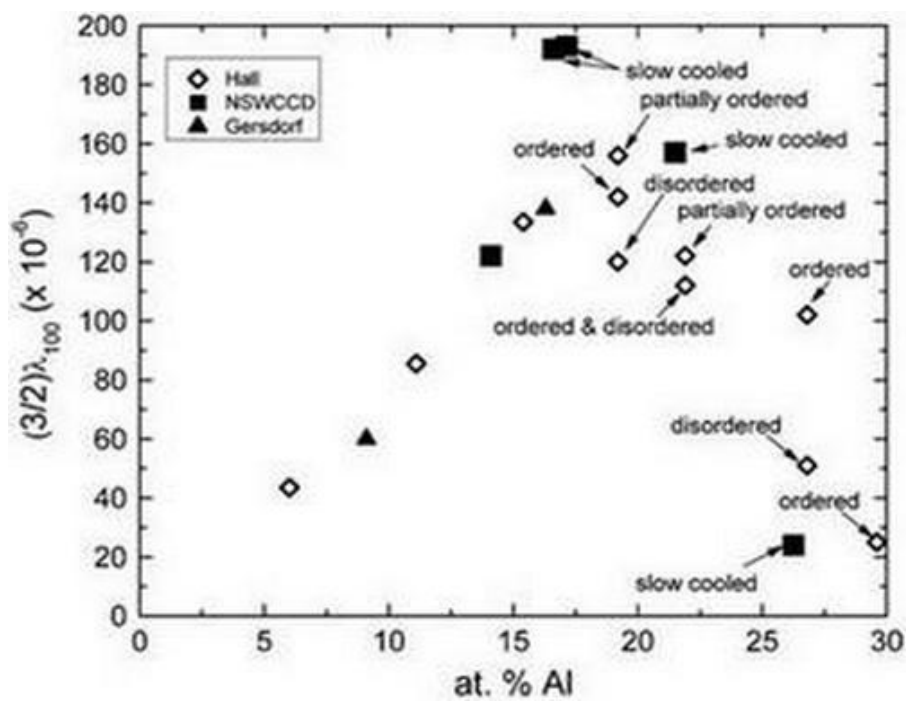
Figure 2.30: Comparison of $(3/2) \lambda_{100}$ magnetostriction data of Fe-rich Fe–Al alloys at RT from [14, 64, 65].
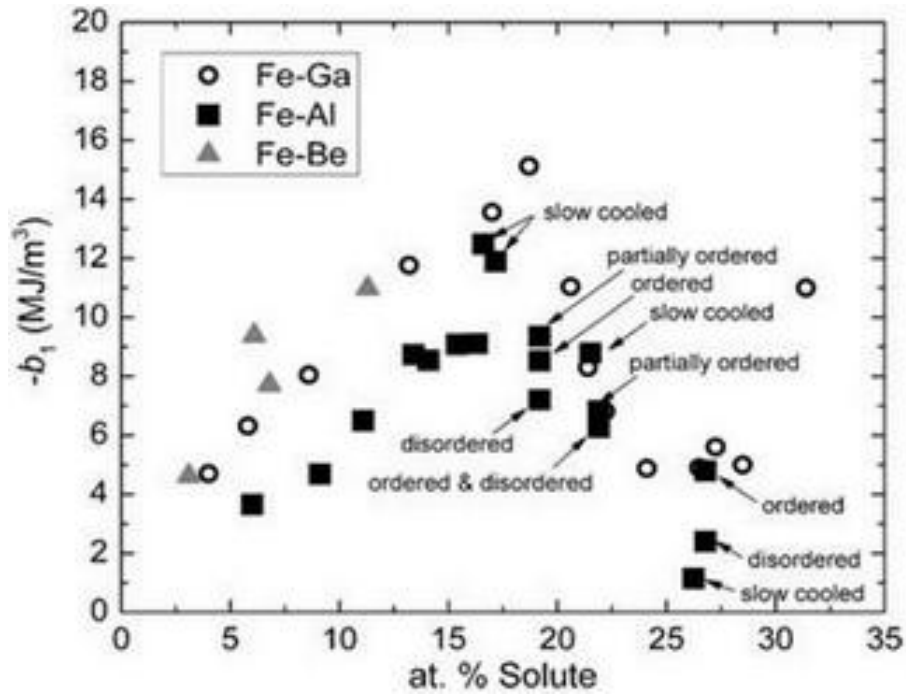
Figure 2.31: Comparison of the magnetoelastic coupling, $-b_1$, for Fe-rich Fe–Al, Fe–Ga, and Fe–Be alloy [64].

In the Fe-Al system, the highest value of magnetostriction was found also in the (100) direction for Al concentration around 19 at% Al, in which $(3/2) \lambda_{100}$ is $\sim$190 ppm at room temperature [64].

2.14.4   Magnetostriction in Fe-Al Melt Spun Ribbons

Liu et al. [15] measured the magnetostriction of rapidly quenched ribbons, melt spun at 12.5m/s and reported very high values up to -700 ppm for alloy $Fe_{100-x}Al_x$ (x = 19) and attributed this large magnetostriction more Al-Al pairs created by melt spinning at the optimized composition x = 19 and oriented by the (100) texture in ribbons, which enhances the magnetoelastic energy. Figure 2.32 shows the magnetostriction measured from the sample $Fe_{100-x}Al_x$ (x = 15, 17, 19, 21, 25 and 30) at $\theta = 90°$ and composition dependence of magnetostriction [15].
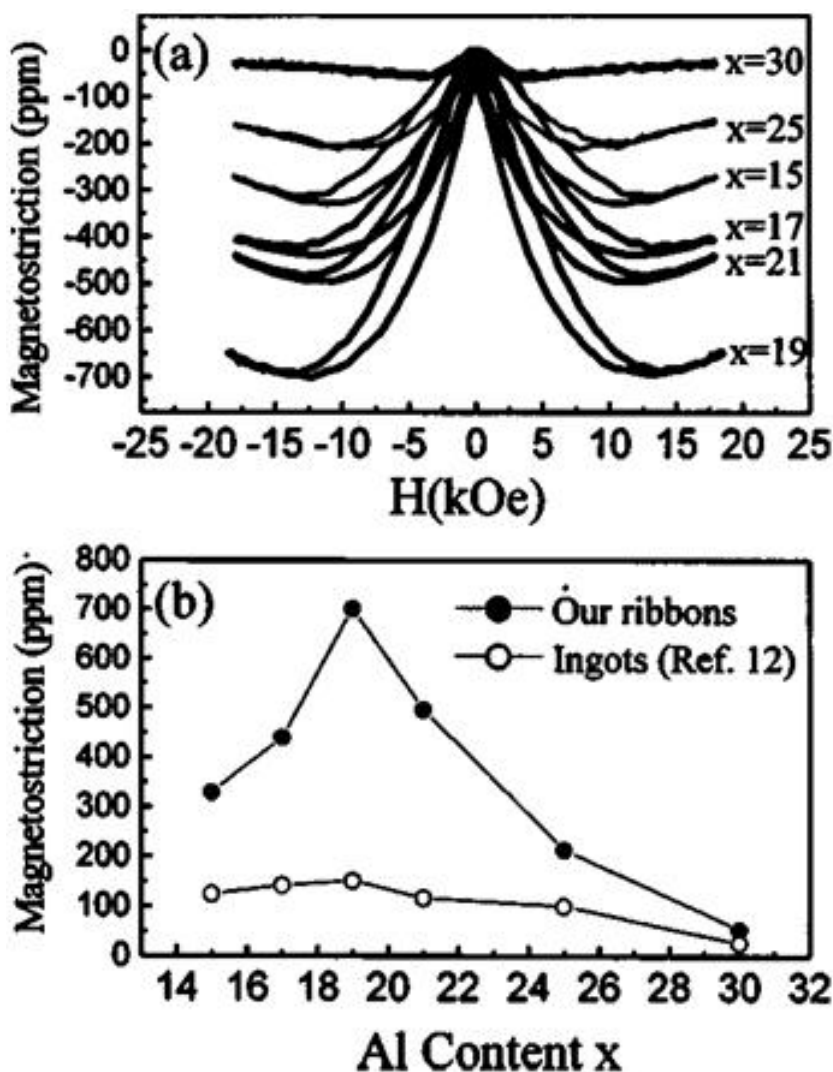
Figure 2.32: a) Magnetostriction measured from the samples $Fe_{100-x}Al_x$ (x = 15, 17, 19, 21, 25, and 30) at $\theta = 90°$; (b) composition dependencies of the magnetostriction [15, 62].

2.14.5   Magnetostriction in Cobalt Ferrite (Co Fe_2O_4)

Oxide based materials attracted engineering interest as non-metallic ferrimagnetic materials for applications at high frequencies where eddy currents have undesirable consequences in the usual metallic materials [66–68].

The spinels (named after well known mineral, spinel, $MgAl_2O_4$ or $MgO.Al_2O_3$) ferrite structure MFe_2O_4 (or AB_2O_4 or $A^{2+}(B^{2+}B^{3+})O_4$, where M refers to metal ions (Co^{2+}, Ni^{2+}, Fe^{2+}, Zn^{2+}, Cu^{2+} etc) can be described as a cubic closed pack arrangement of oxygen atoms with Me^{2+} and Fe^{3+} at two different crystallographic sites. These sites have tetrahedral and octahedral oxygen coordination (termed as A and B-sites, respectively), so the resulting local symmetries of both sites are different, shown in Figure 2.33 .The spinel structure contains two cation sites for metal cation occupancy. There are 8 A-sites in which the metal cations are tetrahedrally coordinated with oxygen, and 16 B-sites which possess octahedral coordination. When the A-sites are occupied by M^{2+}, cations and the B-sites are occupied by Fe^{3+}, cations, the ferrite is called a normal spinel. If the A-sites are completely occupied by Fe^{3+}, cations and the B-sites are randomly occupied by M^{2+}, and Fe^{3+}, cations, the structure is referred to as an inverse spinel. In most spinels, the cation distribution possesses an intermediate degree of inversion where both sites contain a fraction of the M^{2+}, and Fe^{3+}, cations. Magnetically, spinel ferrites display ferrimagnetic ordering. The magnetic moments of cations in the A and B-sites are aligned parallel with respect to one another. Between the A and B-sites the arrangement is anti-parallel and as there are twice as many B-sites as A-sites, there is a net moment of spins yielding ferrimagnetic ordering for the crystal. The choice of metal cation and the distribution of ions between the A and B-sites therefore, offer a tunable magnetic system [69] [70]. Magnetite Fe_3O_4, ferrites $NiFe_2O_4$ and $CoFe_2O_4$ have inversed spinel structure , having structure formula $Fe^{3+}[M^{2+}Fe^{3+}]O^{2-}_4$ where all Me^{2-} are in B-positions and Fe^{3-} ions are equally distributed between A and B-sites .

Cobalt ferrite, with a partially inverse spinel structure with cubic phase having space group Fd3m, is one of the most important and most abundant magnetic materials. As a conventional magnetic material, with a curie temperature (T_c) about 793 K, $CoFe_2O_4$ is well known to have large magnetic anisotropy, moderate saturation magnetization, remarkable chemical stability and a mechanical hardness, which make it a good candidate for the recording media. Cobalt ultrafine powders [71, 72] and films [73, 74] have attracted considerable attention for their wide range of technological applications such as transformer cores, recording heads, antenna rods, memory, ferrofluids, biomedical application, sensors, etc. [75, 76]

Recently, it has been shown that oxide-based materials, especially cobalt ferrite, could overcome some of the drawbacks of the alloy based magnetostrictive materials [77]. The important factors are the high corrosion resistance, better mechanical properties, higher
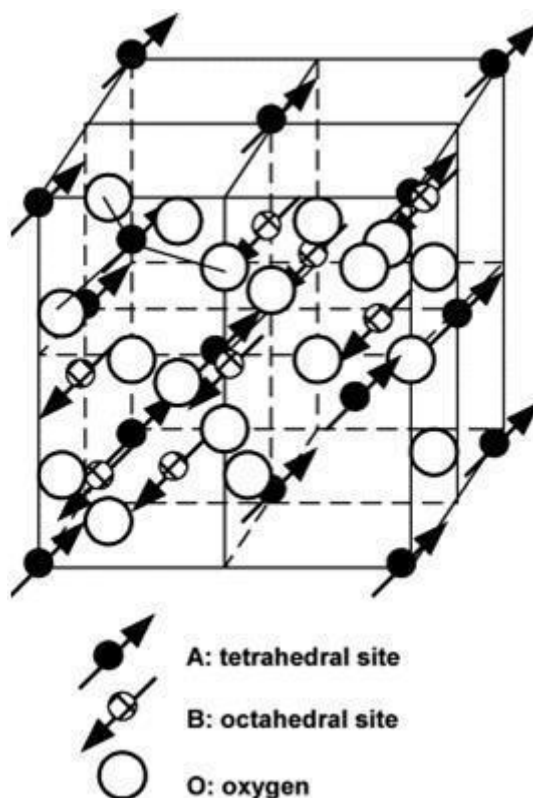
Figure 2.33: Schematic of a partial unit cell and ferrimagnetic ordering of spinel ferrite structure [69].

magnetostriction in the polycrystalline form and low cost as compared to the alloy based sensors. Although the magnetostrictive strains obtained at saturation are less for the polycrystalline cobalt ferrite when compared to single crystals of Terfenol, high values of the strains at low field strengths along with enhanced magnetomechanical coupling factor have been identified as the advantages of cobalt ferrite [77]. It is the slope of the magnetostriction or the piezomagnetic coefficient (dλ/dH) which determines the stress sensitivity of a material [17, 78]. For specific application of stress sensors, the maximum strain derivative (dλ/dH)$_{max}$, which is related with stress sensitivity, is more important than the maximum value of magnetostriction [16]. Apart from obtaining high magnitude of magnetostriction, the control of magnetostrictive hysteresis and the mechanical strength of the ferrite material are the two important concerns. Metal-bonded cobalt ferrite [79] and Mn-substituted cobalt ferrite [80], have been studied in order to enhance the corrosion resistance and the stress sensing properties. It has been shown that the substitution of Mn for Co as well as Fe can significantly alter the magnitude and enhance the low field slope of the magnetostriction of cobalt ferrite [81, 82]. Also, Mn substitution is effective in reducing the magnetomechanical hysteresis as compared to metal-bonded cobalt ferrite. The strain derivative is an order of magnitude greater than that of Terfenol based composites [83].

It is widely known that the sintered products derived from nanocrystalline ferrite powders exhibits improved magnetic permeability which depends on the microstructure, den-

Composition	Magnetostriction (ppm)
100 % $CoFe_2O_4$	-225
2/98vol % $Ag_{0.5}Ni_{0.5} + CoFe_2O_4$	-195
2/98vol % $Ag_{0.2}Ni_{0.5} + CoFe_2O_4$	-210
2/98vol % $Ag_{0.97}Ni_{0.03} + CoFe_2O_4$	-225
2/98vol % $Ag_{0.98}Ni_{0.02} + CoFe_2O_4$	-205

Table 2.3: Magnetostriction of $CoFe_2O_4$ and various compositions bonded with metals Ag and Ni [83].

sity, porosity, grain size etc., as compared to the materials sintered from the bulk counterparts [84, 85]. The maximum of magnetostriction coefficient is also influenced by the stoichiometry of cobalt ferrites and can be tuned substitution levels and sintering parameters [16].

At present, a variety of methods been developed to prepare cobalt ferrite. Sol-gel [86–89], citrate –gel [90] , micro-emulsion [91,92], polymer complex [93], co-precipitation [94–96] , hydrothermal method [97, 98], combustion method [99–102] and mechanical alloying [103] are the method that are used to prepare cobalt ferrite.

Cobalt ferrite has very rich history of research, up-to-date most of work done on the investigation of magnetic properties by changing the synthesis techniques and varying sintering condition. The work regarding magnetostrictive properties investigation cobalt ferrite is very limited.

In 1999 Y. Chen et al. [83] reported maximum magnetostriction value of pure sintered $CoFe_2O_4$ (produced by mechanical alloying method) of -225×10^{-6} and a small decrease of the magnetostriction coefficient, results shown in Table 2.3, in the composite samples obtained by addition of small amount of fine metal powders (Ag, Ni, Co) in order to increase the mechanical robustness.

In 2005, a study of Lo et al. [104] was dedicated to the possibility to improve the magnetostriction coefficient of $CoFe_2O_4$ samples by air annealing at 300 °C for 36 h. Lo et al prepared sintered polycrystalline cobalt ferrite by powder ceramic technique [105] and applied an external field parallel to the hard axis, the maximum magnetostriction measured along the hard axis at room temperature increased from 200×10^{-6} to 252×10^{-6} after annealing. The $(d\lambda/dH)_{max}$ increased from 1.5×10^{-9} to 3.9×10^{-9} A^{-1} m^{-1} . After annealing the maximum magnetostriction along the easy and hard axes increased by 20% and 26%, and the corresponding maximum strain derivative increased by 126% and 163% respectively under applying a field in the hard axis direction. This increase of the strain derivative is larger than that obtained by substitution Mn for Fe in cobalt ferrite [104].

Recent studies [105, 106] report the effect of substitution of Fe by Mn in $CoFe_{2-x}Mn_xO_4$ and showed that the incorporation of Mn leads to a decrease in the magnetostriction and Curie temperature. The maximum magnetostriction coefficients decrease drastically by
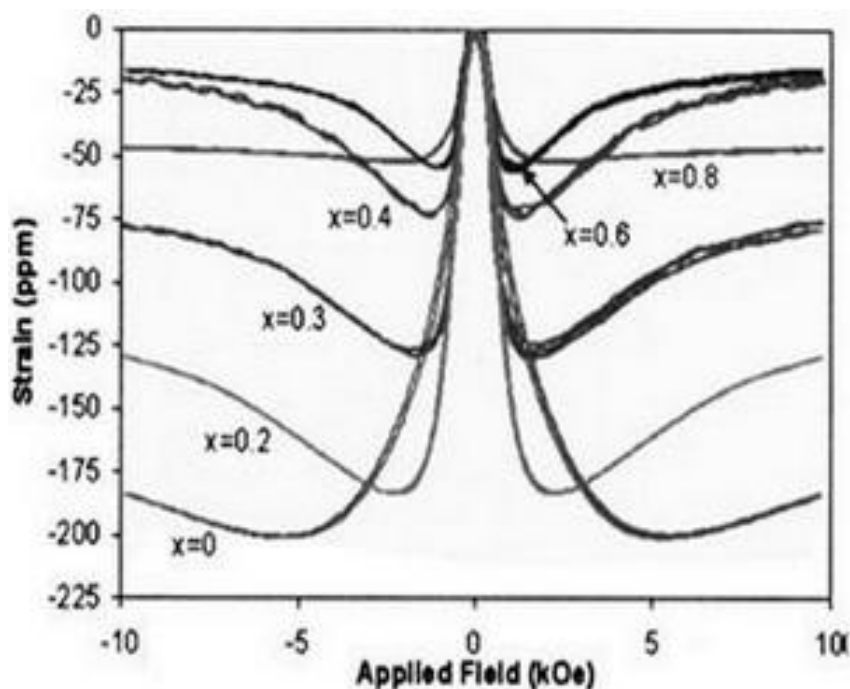
Figure 2.34: Magnetostriction curves for $CoFe_{2-x}Mn_xO_4$ [80].

Sample	X (%wt)	D(μm)	T_c(°C)	H_c(Oe)	M_s(emu/g)	$\lambda x(-10^{-6})$
S1	0	5.3	525	109	93	167
S2	0.3	12.3	480	108	96	144
S3	0.4	7.3	418	68	95	119
S4	0.5	6.9	355	45	77	73

Table 2.4: Doping level, average grain size, Curie temperature, coercive magnetic field, saturation magnetization and magnetostriction coefficient data of $CoMn_xFe_{2-x}O_4$

increasing the substitution level from 200×10^{-6} to 80×10^{-6} but the maximum stain derivative at low field for small amount of substitution (in fact x = 0.2 and 0.3) increases spectacularly shown in the Figure 2.34 . Table 2.4 also shows summarized results of the composition, average grain size, curie temperature, coercivity, saturation magnetization and magnetostriction for all the samples as were studied by O.Caltun et al [106].

The effect of substituting Fe and Co by Mn on the magnetostrictive properties of $Co_{1.2}Fe_{1.8}O_4$ has been also investigated [81]. A strong dependence of the magnetostriction on the Mn content is observed in both cases. The substitution of Co by Mn enhances the magnetostriction for small values of substitution in $Co_{1.2-x}Mn_xFe_{1.8}O_4$ whereas magnetostriction decreases continuously with increasing x in $Co_{1.2}Fe_{1.8-x}Mn_xO_4$. A two-fold increase in the initial slope $(d\lambda/dH)_{max}$ with large magnetostriction as compared to that of the unsubstituted compound is observed when small amounts of Co are replaced by Mn [81].

The curie temperature of $CoFe_2O_4$ can be adjusted over a substantial range by the substitution of Si and Co for Fe, and by varying the sintering condition [105]. In the last study,
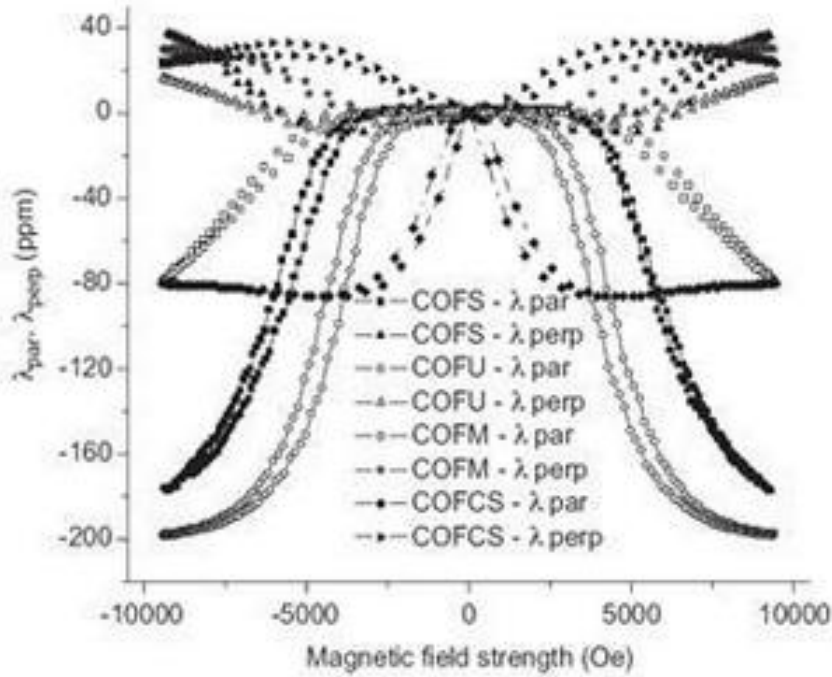
Figure 2.35: The magnetostriction curves at room temperature. Samples are sintered at 1275 °C..

the value of the maximum magnetostriction coefficient of pure cobalt ferrite was -94×10^{-6} and of the maximum strain derivative was 1×10^{-9} A^{-1} m^{-1}. In the case of $CoSi_{0.2}Fe_{1.8}O_4$ sample, a small amount of silicon substitution decreased the maximum magnetostriction coefficient to -90×110^{-6} and increased the maximum strain derivative to 4.5×10^{-9} A^{-1} m^{-1}.

More recently in 2008, O.Caltun et al [16] studied the influence of sintering temperature and the substitution level on the curie temperature and on the magnetostriction coefficients of cobalt ferrites sintered by conventional ceramic methods. The chemical composition of prepared sample was $CoFe_2O_4$ (COFS: stoichiometric), $Co_{0.8}Fe_{2.2}O_4$ (COFU: unstoichiometric), $CoFe_{1.8}Mn_{0.2}O_4$ (COFM: Mn substituted for Fe) and $Co_{1.3}Si_{0.3}Fe_{1.4}O_4$ (COFCS: Co and Si substituted for Fe) and sintering temperature was varied in three steps 1250°C, 1275°C and 1300°C respectively. The maximum value of parallel magnetostriction coefficient and maximum strain derivative corresponds to the COFM sample sintered at 1300°C. Figure 2.35 shows the parallel and perpendicular magnetostriction measured after sintering the samples at 1275°C. Small substitution of Mn increases the magnetostriction and magnetic properties of cobalt ferrite. On the other side Si and Co substitution for Fe in cobalt ferrite causes a decrease of the magnetic moment and parallel the magnetostriction coefficient diminishes in this case but the strain derivative reaches a very high value even at very low values of the applied magnetic field.

2.14.6   Miscellaneous Materials

2.14.6.1   Carbon Black Filled Polypropylene Composites

In 2003 Nai –Xiu et al [107] prepared carbon black (CB) filled polypropylene composites and measured a magnetostriction value of 115 ppm at parallel field of 3900A/m, which strongly dependent on magnetic intensity and on the time were the field is applied. Figure 2.36 shows variation of magnetostriction as a function of time applying different magnetic field intensity. Later in 2005 [108] they extended this work and measured the magnetostriction of polypropylene composite by adding carbon fiber (CF) to it, the measured values of magnetostriction after adding carbon fiber in polypropylene composites was very large i.e. 1163 ppm at 800KA/m comparable to Terfenol-D composites, the preeminent traditional magnetostrictive material . Figure 2.37 shows the variation of carbon fiber filled polypropylene composite as a function of time in parallel magnetic field. When the magnetic field is set to zero, the magnetostriction of composites does not return to zero short time but decreases continuously from a high value to zero over several hours and no magnetostrictive properties were observed in pure polypropylene composites. In this work no measurement were performed regarding measurement of magnetic hysteresis (MH) curve of similar samples.
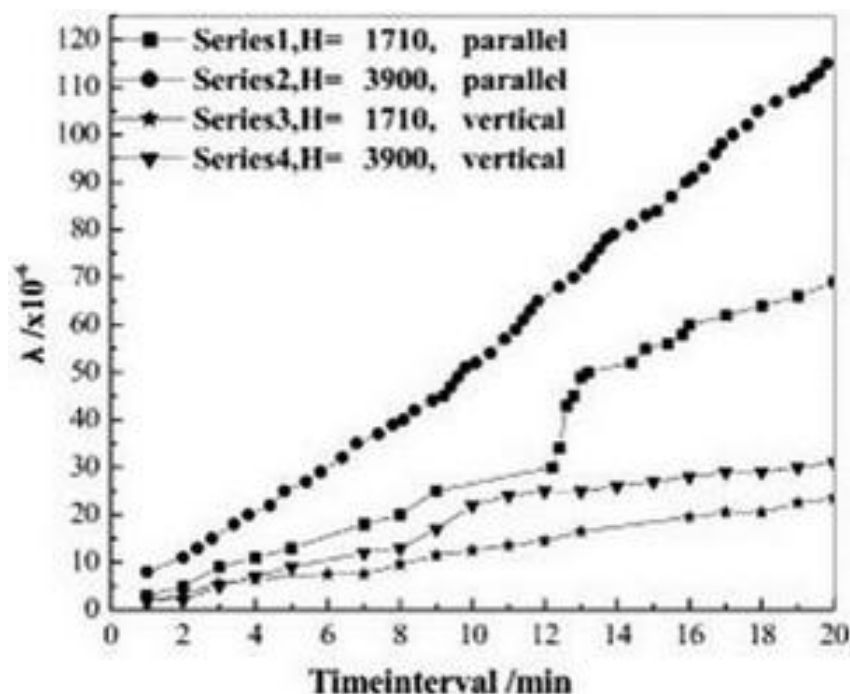
Figure 2.36: Variation of magnetostriction as a function of time interval with different MFI [107].
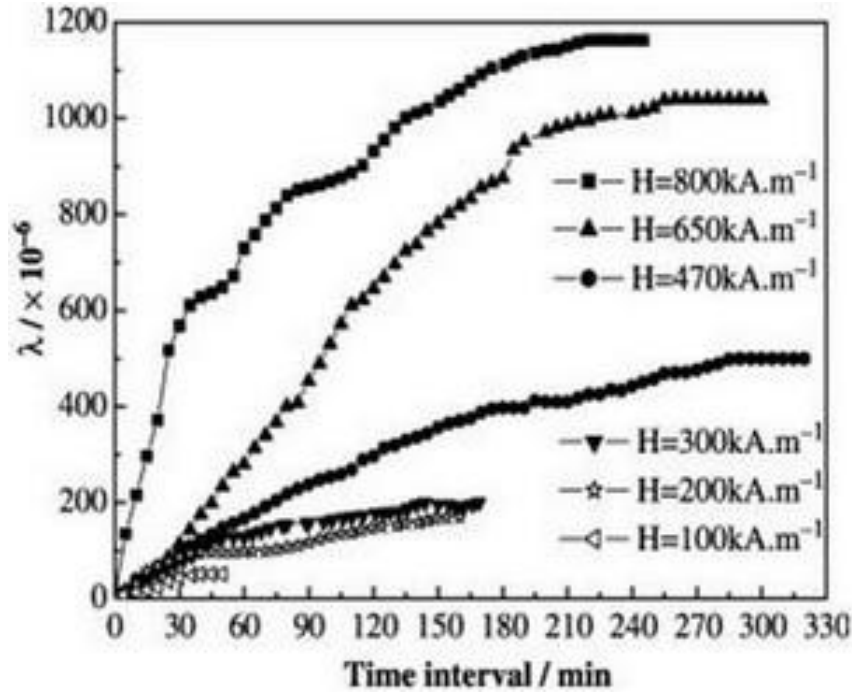
Figure 2.37: The variation of magnetostriction as a function of time interval in the parallel magnetic field [108].

2.14.6.2   Magnetostriction of Steel Samples

One way to investigate the residual stresses in steel which occur during the production due to plastic deformation is the study of the materials magnetic property [109]. Since steels are ferromagnetic materials we can use measurement of magnetic properties like hysteresis loop, domains, and magnetostriction to detect local stress areas, dislocations or scratches in steel components [110]. It is expected that the coercive force H_c increases proportional to the square root of the dislocation density ρ, and the initial susceptibility χ_i decreases with one over the square root of the dislocation density [111]. Due to the influence of the magneto-elastic energy $\lambda.\sigma$ (λ ... magnetostriction, σ .....local stress) the coercivity depends on the residual stresses. The stress dependence of the coercivity of a soft magnetic material can be simply described as,

$$H_c = \frac{\lambda \sigma}{\mu_s M_s} \tag{2.55}$$

Where M_s denotes the saturation magnetization. Body-centered cubic (bcc) Fe exhibits anisotropic magnetostriction constants of different signs $\lambda_{100} = 20$ ppm and $\lambda_{111} = -16$ ppm at room temperature. These considerations reveal that in (polycrystalline) steel a very complex situation determines the interplay between hysteresis parameters (domain walls) and dislocations or stresses. In a microstructural description the coercivity is determined by the mobility of domains and domain walls. Therefore, the ratio of the domain wall width (100–200 nm in soft Fe) to the dimensions of the local stress field is the most important

factor [112].

2.14.6.3 Magnetostriction of Fe-Mn Alloys

All types of order such as ferromagnetics and antiferromagnetic are magnetically ordered, however research and applications of antiferromagnetic materials are very limited. Peng et al. [113] performed magnetostrictive investigation on antiferromagnetic polycrystalline $Mn_{42}Fe_{58}$ and reported the maximum value of magnetostriction 169 ppm parallel to applied field of 1 Tesla and zero compressive stress. They also reported jumps in the magnetostriction curve when the sample was subjected to different compressive stress and reported very high value of magnetostriction such as -581 ppm, at the compressive stress of -1.52 MPa. However, the effect of defects, lattice orientation, magnetic domain configuration, and so on, on the magnetostriction has not been considered.
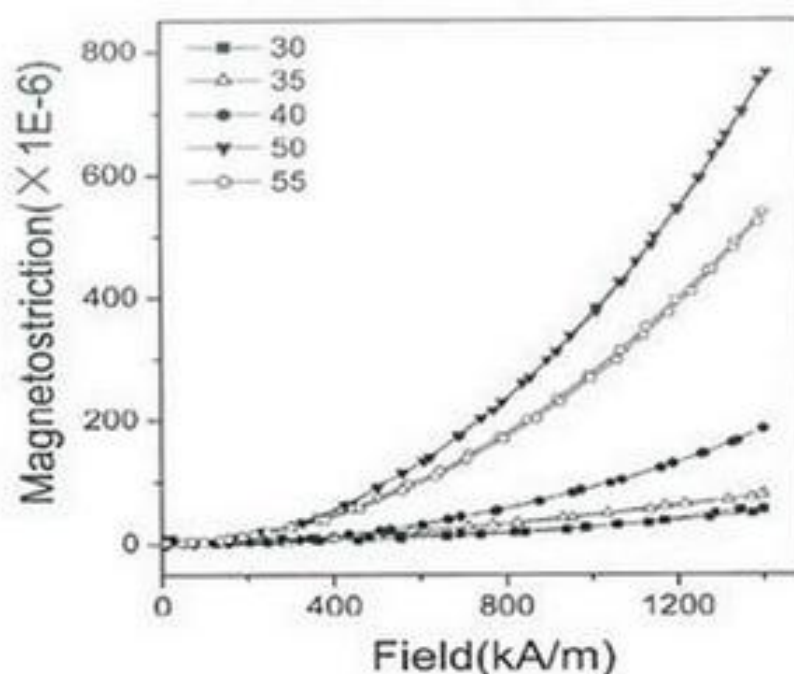
Figure 2.38: Magnetostriction curves of Mn_xFe_{100-x} (30 $\leq$ x $\leq$ 55) [114].

More recently Yan et al [114] investigated Mn_xFe_{100-x} (x = 30, 35, 40, 50, 55) up to a field of 1400 KA/m and reported a very high value of magnetostriction of 770 ppm for $Fe_{50}Mn_{50}$ alloy at maximum available magnetizing field and attributed this high vale as result of change of mixture of γ and ε phases within the γ phase . The 1400 kA/m was not enough to saturate the samples. With increasing Mn content, the Neel temperature of antiferromagnetic γ-Mn-Fe alloy increases but the temperature of martensitic transformation decreases , which can depress the transformation form γ to ε phase, which results in a decrease of the magnetostriction when x = 55). Figure 2.38 shows the magnetostriction curves of Mn_xFe_{100-x} (30 $\leq$ x $\leq$ 55).

Chapter 3

Experimental

3.1 Sample Preparation

3.1.1 Production of Polycrystalline Metallic Alloys

Production of polycrystalline metallic alloys ingot of the master alloys used in this work, were prepared from high purity (> 99.9 %) elements by using high-frequency induction melting (Hüttinger RF Generator, 30kW, 600 kHz) under Argon atmosphere in copper crucible, as shown in Figure 3.1. Each ingot was re-melted three to four times, to assure the homogeneity.

3.1.2 Nanocrystalline Samples by Severe Plastic Deformation (SPD)

High Pressure Torsion (HPT) machine available at Erich Schmid Institute of Materials Science, Austrian Academy of Sciences Department Materials Physics, University of Leoben is used to produce bulk nanocrystalline samples. Figure 3.2 shows the sketch of HPT tool. In principal a disc shaped sample is deformed by pure shear between two anvils
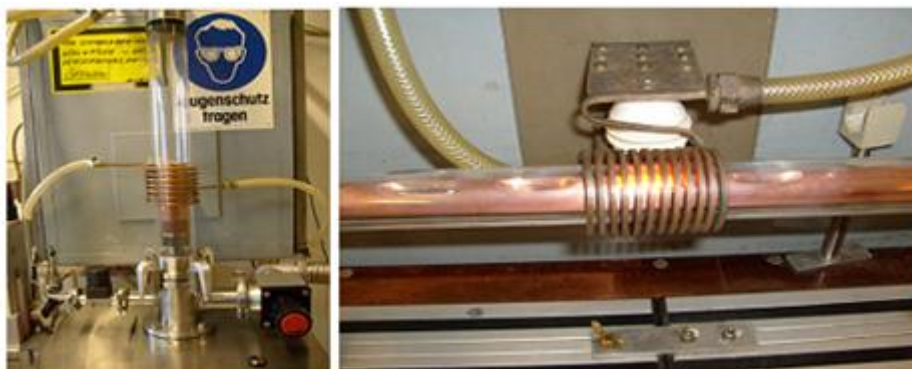
Figure 3.1: Set-up for the preparation of bulk metallic ingots Hukintiegel (left) and a water cooled Cu-boat (right) at TU Wien.
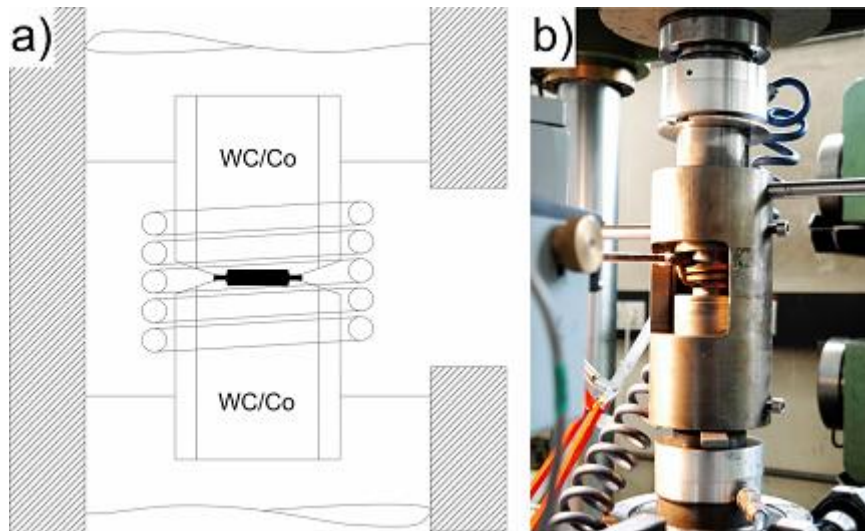
Figure 3.2: a) sketch and b) photograph of experimental setup [115].
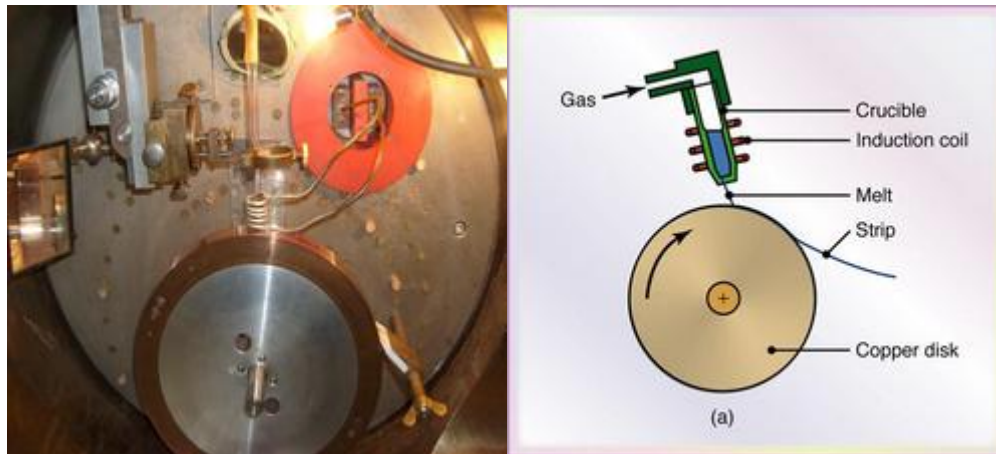
Figure 3.3: Set-up for the preparation of metallic ribbon (left) schematic representation of melt pouring on wheel (right).

that are rotating with respect to each other. The necessary torsion-momentum is provided by friction forces at contact areas anvil-material.

3.1.3   Production of Melt Spun Ribbons

The melt spun ribbon samples were prepared by melting the pieces of bulk ingots in quartz nozzle by RF generator and injecting the molten alloy with pressure 500 mbar on copper wheel of (dia 300 mm) rotating at velocities from 7–25 m/s through nozzle 0.80 mm orifice, keeping the distance of nozzle from wheel maintained at 0.30 mm. Figure 3.3 shows the setup for preparation of melt spun ribbons and schematics of melt pouring.
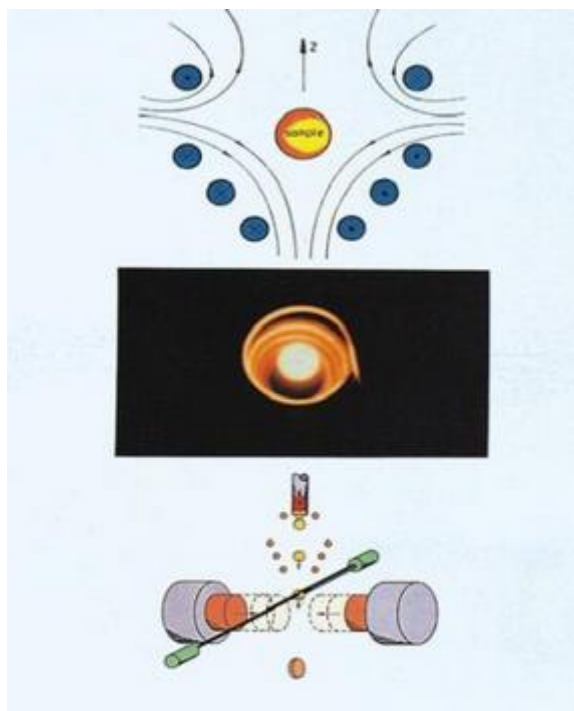
Figure 3.4: Splat cooling technique schematics.

3.1.4 Preparation Splat Cooled Foils

Splat cooling facility available at Escola de Engenharia Lorena, Universidade de Sao Paulo, Lorena-SP, Brazil was used to prepare the splat cooled samples. Some pieces of mass close to 100 mg were cut from the ingot of Fe-Ga alloy and re-melted to obtain small spherical samples.

These were then inserted into an Edmund Buhler splat-cooling apparatus, where the sample is levitated and melted inside an inductive coil. When the current to the coil was de-activated, the liquid fell through a laser detector that caused the drop to be pressed between two opposing copper plates, quenching it at a rate of about 10^6 Ks^{-1}. Figure 3.4[1] shows the schematics of splat cooling apparatus.

3.1.5 Heat Treatment of Samples

The samples were heat treated using high temperature box shaped and tubular shaped furnaces (Heraues HR170 and ROS 4/50) which works in the temperature range between room temperature and 1350°C for different durations. The heating speed is in the range of 10-20 °C/min.

The samples of Cobalt Ferrite prepared by combustion method were heat treated at 1450 °C for 10 minutes in Linn High Term GmbH furnace at heating rate 4 °C/min and cooling rate 20 °C/min.

---

[1]Edmund Bühler GmBH Lab Tec (http://www.edmund-buehler.de)

3.1.6   Sample Preparation of Cobalt Ferrite (CoFe$_2$O$_4$) [116]

3.1.6.1   Ball Milling Method (BM)

The starting raw materials were iron oxide (Fe$_2$O$_3$) and Cobalt oxide (CoO) powders. CoO and Fe$_2$O$_3$ powders were mixed with a molar ratio of 1:1 and then loaded together with 12mm diameter stainless steel grinding balls into a cylindrical hardened stainless steel vial. The ball to powder weight ratio was 10:1. The mechanical alloying was performed in a Spex 8000 high-energy vibratory mill.

3.1.6.2   Modified Citrate Gel Method (SG)

Iron nitrate (Fe (NO$_3$)$_3$.9H$_2$O) + cobalt nitrate (Co(NO$_3$)$_2$.6H$_2$O) + glycine (C$_2$H$_5$NO$_2$) were dissolved in 150 ml distilled water. The nitrates were used in stoichiometric amounts and the total metal concentration was 1 mol/l. The molar ratio between total metal ions and citric acid was 1. First, the starting mixture containing nitrates, citric acid and distilled water was mechanically stirred and heated in a plate at 80 °C then ammonia (NH$_3$ 25%) was added to adjust the pH of the solution to 6. After wards the plate was heated up to 200 °C keeping the stirring constantly until the water has been evaporated and forming a viscous gel. The ferrite powder formation was monitored keeping the heating in order to allow the dehydration and the atomic rearrangement to form cobalt ferrite powder.

3.1.6.3   Fluoride Modified Citrate Gel Method (MSG)

Similar to that technique described in 3.1.6.2, however in this case it was modified; the starting constituent components are different, that is, besides the components used in 3.1.6.2 ammonium fluoride NH$_4$F and 5 % more of Co in cobalt nitrate were added. The molar ratio between the oxide and NH$_4$F was 2 resulting as final product 5 mol%F in cobalt ferrite.

3.1.6.4   Combustion Method (CB)

This method is quite simple and fast because it does not involve the intermediate calcinating steps, that is, the stoichiometric amounts of cobalt and iron nitrates and glycine dissolved in distilled water were stirred and directly heated up to 200 °C on a plate, which boiled and thickened, after wards ignited producing a dry cobalt ferrite powder. Two moles of glycine per mole of metal ion was used.

3.1.6.5   Pressing of Ferrite Samples

The powders samples were pressed in to pellets using a hydrostatic pressure up to 5 Ton (with SPIRAL press max. capacity 30 Ton) having die diameter 5, 10, or 13 mm.

3.1.7   Carbon Fiber Polymeric Composites

A set of Carbon fiber filled polypropylenes/poly (butylene tereohtalate) composite (shown in Table 3.1) were prepared and their magnetic properties and magnetostriction were investigated. In all the cases, the amount of Carbon fibers was 25% volume fraction. Three different fibers were used, one was microfiber (6-7 micrometers in diameter) and two others were nanofibers, Pyrograf III (PR-19 and PR-24 grade PS)[2]. Additionally, some samples were prepared with 1 gram of cobalt ferrite, which was prepared by coprecipitation [95]. All the samples mixed in polypropylene to prepare the PP/CF composites. The samples were injection-moulded.

NAME	DESCRIPTION
PP	100 wt% polypropylene
PP-micro 58.8%	41.2 wt % polypropylene
	58.8 wt % carbon fiber (microfiber)
PP-1	97.3 wt% polypropylene
	2.7 wt% $CoFe_2O_4$
PP-nano19	60.7 wt% polypropylene
	39.3 wt % carbon fiber (nanofiber PR-19)
PP-nano24	60.7 wt% polypropylene
	39.3 wt % carbon fiber (nanofiber PR-24)
PP-micro-1	59.3 wt% polypropylene
	38.5 wt % carbon fiber (nanofiber PR-19)
	2.2 wt% $CoFe_2O_4$
PBT-nano19-1	74.65 wt% poly (butylene tereohtalate) 2
	24.88 wt % carbon fiber (nanofiber PR-19)
	0.47 wt % $CoFe_2O_4$

Table 3.1: Compositions in wt. % of polymeric composites

3.2   Samples Characterization

3.2.1   Samples Characterization

The structural characterization of the studied samples, including phase purity analysis, determination of grain size, crystallite size, texture and lattice parameter was carried out by means of X-ray diffraction by using PANalytical X'Pert PRO (XP-2), Siemens KF4 (Kristalloflex 4) and Siemens D5000 diffractometers, and by quantitatively analyzing the obtained data with Bruker AXS Rietveld program TOPAS.

---

[2]The specifications of these fibers can be found at http://www.apsci.com/ppi-pyro3.html

The average grain size of ferrite sample was also determined by using the Scherrer equation [117] for full-width at half maximum (FWHM) of the strongest reflection peak by using following equation,

$$t = k\lambda/\beta cos\theta \qquad (3.1)$$

Where t is the average crystallite size, K is Scherrer constant (for a value of 0.90 is used), λ is wavelength of X-rays. β is the integral breadth of a reflection (in radians 2θ) located at 2θ [3].

Crystallite size was calculated by Bruker AXS Rietveld program TOPAS from XRD patterns . Grain size and crystallite are not equivalent, grain can contain several crystallites.

3.2.2 Magnetic Domains Study

Topometrix Explorer magnetic force microscope (MFM) with Veeco "MESP" Cr-Co tip was used to observe domain structure of bulk Fe-Al samples keeping the distance between tip of probe and surface of the sample maintained at 50nm.

3.2.3 Microstructural Analysis

The Reichert-Jung Polyvar MET (maximum magnification 1500X) high resolution optical microscope was used for microstructural observation of Fe-Ga and Fe-Al samples. Scanning Electron Microscope JEOL JSM5410 was also used to measure the surface morphology of investigated samples. Chemical analysis was performed by the detection of characteristic X-rays by a Philips EDAX system.

3.2.4 Hysteresis Loop and Temperature Dependence of Magnetization

3.2.4.1 Vibrating Sample Magnetometer

Physical properties measurement properties system PPMS Q6000 (Quantum Design) with temperature range 1.9 K- 400 K with maximum field up to ± 9 Tesla with oscillating frequency 40 Hz and Pulse field magnetometer was used to measure hysteresis loop and temperature dependence of magnetization. Figure 3.5 shows the system diagram of vibrating sample magnetometer. Physical properties measurement system vibrating sample magnetometer (VSM) PPMS Q6000 (Quantum Design) available at TU Wien is shown in Figure 3.6.

---

[3]http://cnsm.kaist.ac.kr/vsm.html
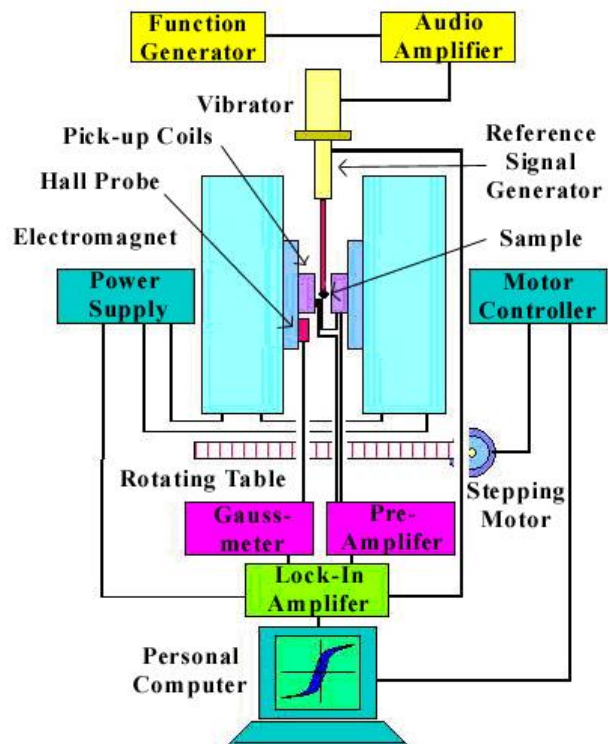
Figure 3.5: System diagram of vibrating sample magnetometer.

Figure 3.6: Physical properties measurement properties system vibrating sample magnetometer (VSM) PPMS Q6000 (Quantum Design) at TU Wien.
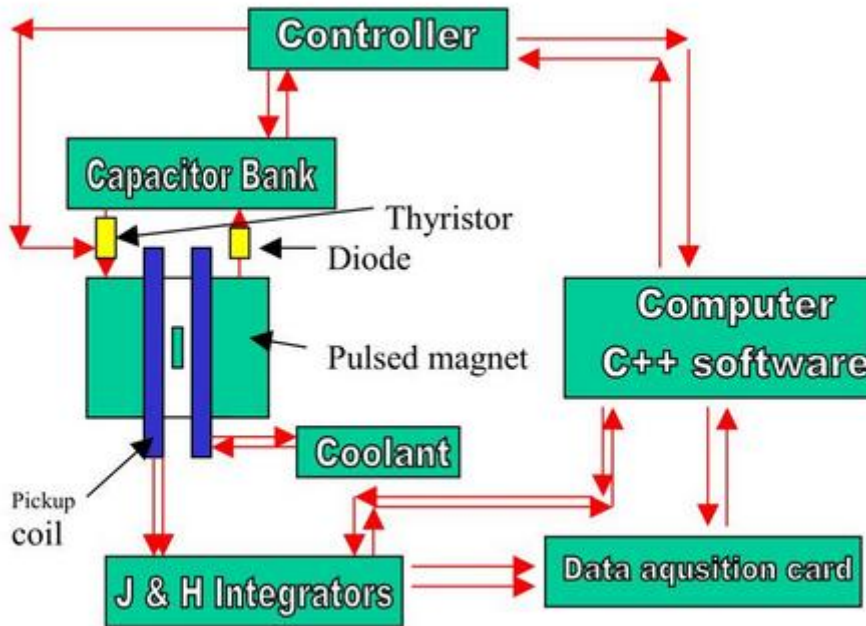
Figure 3.7: Block diagram of pulse field magnetometer [118].

3.2.4.2 Pulse Field Magnetometer

In addition to PPMS, Pulse Field magnetometer (Hirst Industrial system PFM11) that could charge a 22.5 kJ capacitor bank (C = 5 mF) to 3000 V in approximately 25 seconds using thyristors switch for measuring the hysteresis loop. The whole charging process of PFM, f/2f selection (40 ms and 57 ms) and the data acquisition is computer controlled using a Z80 microprocessor which is linked to the PC. The signal is integrated with a stable analogue integrator with selectable time constants. The signals are connected to a 14 bit 5M sample/s two channel ADC card from Datel (model: PCI-416N) directly in the computer. For the data handling a C++ based computer program was written.

The system is capable of accepting samples up to 30 mm diameter and 10 mm length within a $\pm$ 1 % pickup homogeneity range. The maximum field is 5 T. It is calibrated with an absolute error in H and M of $\pm$ 1.5 %. Figure 3.8 shows the PFM set available at TU Wien.

3.2.4.3 Magnetization Measurement of Steel Samples

The hysteresis measurements of steel (soft magnetic) samples were carried out on ring or frame shaped samples having a magnetically closed circuit. This allowed for an accurate determination of the coercivity. Figure 3.9 illustrates the corresponding sample geometry and the coil arrangement for these measurements. N_1 and N_2 represent the number of turns of the primary and the secondary coils. The thin legs were oriented parallel and perpendic-

Figure 3.8: Pulse field magnetometer at TU Wien.
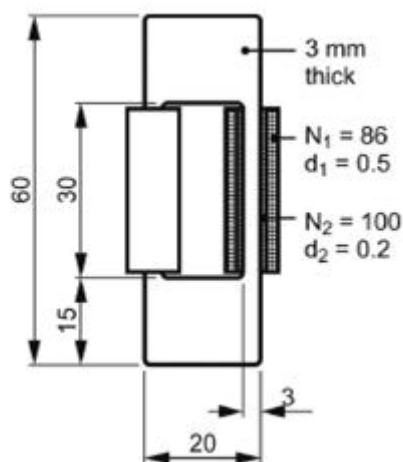
Figure 3.9: Sample geometry and coil arrangement for measuring the hysteresis loop of frame shaped samples. Samples denoted with "L" or "T" have the thin legs in parallel to the longitudinal or transversal direction, respectively.

ular to the pipe axis for the "L" and "T" samples, respectively. The connecting regions of the legs have a cross-section being five times larger than that of the legs itself. Therefore, the influence of these connecting regions on the measurements has been neglected.

(a) Illustration of strain gauge.

(b) Working principle of strain gauge.
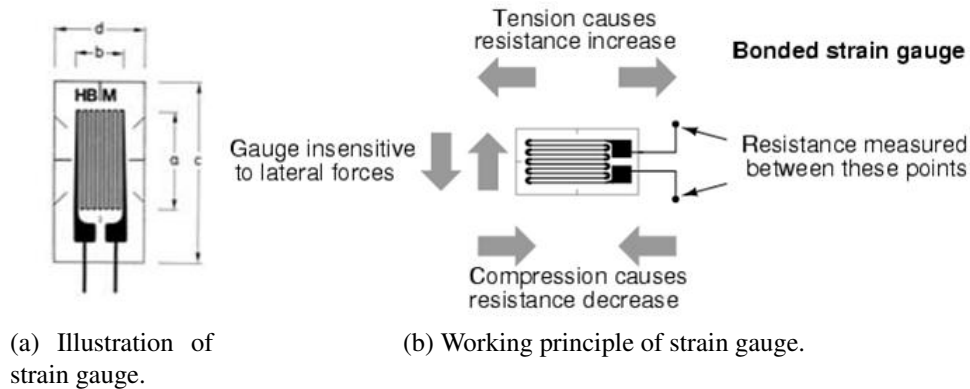
Figure 3.10: Illustration of strain gauge and working principle.

3.2.5 Magnetostriction Measurements

3.2.5.1 Strain Gauge Method

This is most commonly used direct method introduced by Goldman in 1947 and reviewed by Lee in 1979 having sensitivity $\pm 1 \times 10^{-6}$ is used to measure magnetostriction [119]. The Hottinger Baldwin Messtechnik GmbH (HBM) universal strain gauges types 1-LY$_{11}$-0.6/120 (120Ω, a = 0.6 mm, b = 1 mm, c = 5 mm, d = 3.2 mm maximum effective bridge supply voltage = 1.5 volt) and 1- LY$_{11}$-1.5/120 (120Ω, a = 1.5 mm, b = 1.2 mm, c = 6.5 mm, d = 4.27 mm maximum effective bridge supply voltage = 2.5 volt) are used to measure magnetostriction by gluing the strain gauge on the sample with cyanacrylate based HBM Z70 which is a single component, cold curing adhesive. For each measurement dummies are also used to reduce the influence of temperature and of magnetic field changes during the measurements. Figure 3.10 shows the illustration of strain gauge with one measuring grid and its working.

3.2.5.2 Capacitance Dilatometer Method

Tilting plate miniature capacitance dilatometer capable of measuring longitudinal and transverse magnetostriction in temperature range from 0.3 K to 300 K and sample size 1 $\times$ 1 $\times$ 1 mm^3 to 4 $\times$ 4 $\times$ 4 mm^3, schematic diagram shown in Figure 3.11 [120] . Static high magnetic fields up to $\pm$7T were produced by a superconducting magnet in a Helium cooled cryostat by using OXFORD PS120 superconducting magnets power supply. Temperature of the measurement system was controlled by using CONDUCTUS temperature controller model LTC 20. ANDEEN HAGERLING 2500A, 1 KHz Ultra precision capacitance bridge is used to measure the change in capacitance. Figure 3.12 shows the arrangement of dilatometer in temperature insert and the magnet system.

The change of the length of the sample after application of magnetic field is transmitted to sensitive AC capacitance Bridge through a mechanical system, capacitance of bridge is
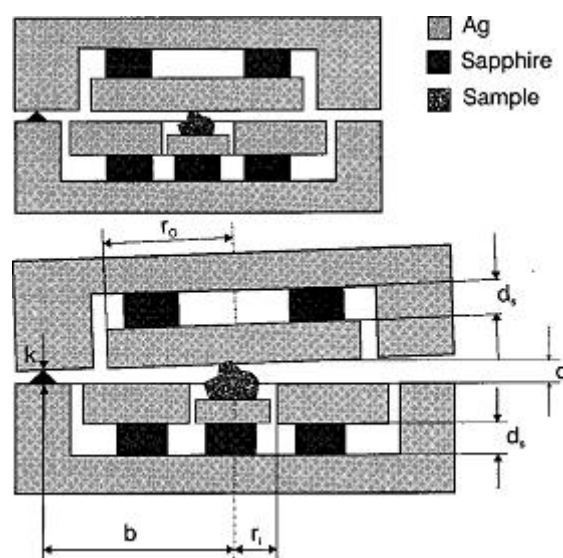
Figure 3.11: Schematic drawing of the capacitance dilatometer [120].
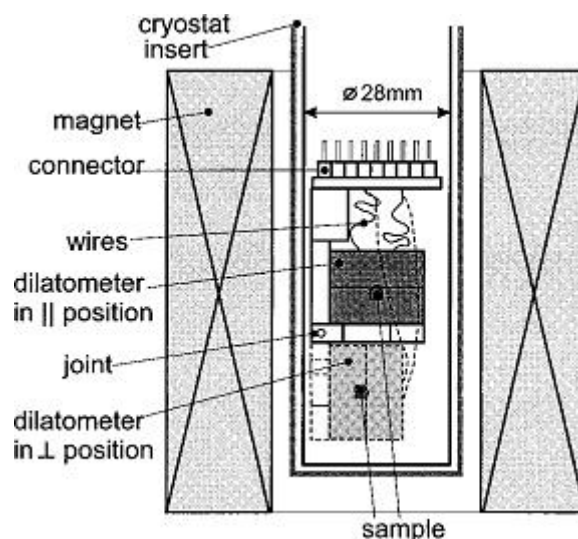
Figure 3.12: Arrangement of the dilatometer, temperature insert, and magnet system [120].

proportional to change of length and this change in dimension of samples is determined by software and computer attached to capacitance dilatometer system. The sensitivity of this method is in the range of $\pm 10^{-10}$.

A special capacitance device available at Institute of Physics, Slovak Academy of Sciences, Bratislava Slovakia shown in Figure 3.13 is used for direct measurement of magnetostrictions $\lambda_{\parallel}$ and $\lambda_{\perp}$ of melt spun ribbons. This device has high mechanical and thermal stability and sensitivity for determination of the changes of sample dimensions in the necessary intervals. Small changes in the sample dimensions $\triangle l$ ($6 \times 10^{-8} - 6 \times 10^{-4}$ mm) have to produce sufficiently high signal for sample diameter ~ 6 mm.

The design of the sample holder has been selected to ensure that a sample from the same material as the holder at H = 0 yields no measurable capacity changes with chang-
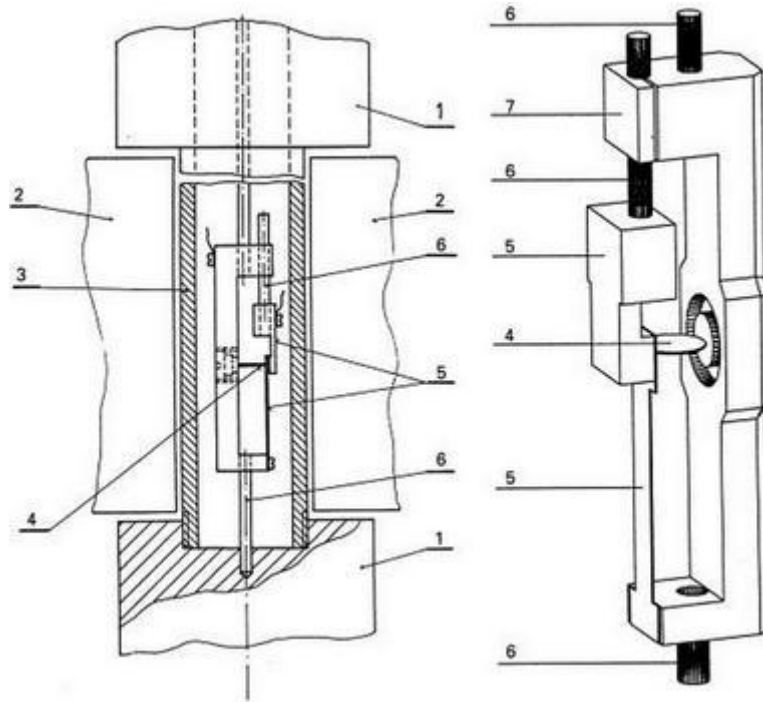
Figure 3.13: Device for λ measurement. (1) Cu block, (2) pole pieces, (3) Cu tube, (4) sample, (5) electrodes, (6) quartz tube, (7) assembly of capacitor electrodes and sample holder [121].

ing temperature. Samples (different from sample holder) dilate with temperature changes, leading to a change of the capacity. The entire measurement takes 1-3 min, the temperature stability has to conform to the desired measurement accuracy and to the magnitude of the measured magnetostriction. The desired stability is obtained by placing the sample/holder assembly inside a copper tube connected to two large copper thermal sinks. In stable thermal conditions of the environment ($\triangle T \Longrightarrow 0$) material with even very low values of $\lambda = 10^{-8}$ can be easily measured. The change of capacity is measured using the three terminal capacitance method by the capacitance bridge. The output signal from the bridge together with the value of the applied magnetic field is interfaced to a computer which controls the measurement conditions and stores the data [121].

Chapter 4

Results and Discussion

Part I

Magnetostriction Investigations in Bulk Materials

4.1 Bulk Fe-Ga Alloys

A set of six samples with composition $Fe_{81}Ga_{19}$ were made from bulk high frequency melted precursor ingots of $Fe_{81}Ga_{19}$ alloy with four samples having diameter 6 mm and 2 samples having diameter 8 mm to study the effects of severe plastic deformation on the magnetostriction values. These samples were severely plastic deformed (SPD) from very low shear rate $\varepsilon = 2$ to very high shear rate $\varepsilon = 35$ at room temperature and at 400°C as well, keeping one sample HPT-4 undeformed as a reference. Table 4.1 summarizes the parameter which were used to produce SPD samples.

Sample ID	Dia	T_{int}	T_{fin}	SPD Load	SPD Time	Shear Speed	Temp.	Shear Strain
		(mm)		(Ton)	(sec)	(rpm)	(°C)	(ε)
HPT-1	6	0.84	0.71	29	300	0.2	RT	35
HPT-2	6	0.87	0.70	29	72	0.2	RT	2
HPT-3	6	0.86	0.73	29	284	0.2	RT	8
HPT-4	6	0.71	Un-deformed					
HPT-5	8	0.88	0.77	40	54	0.2	400	2.2
HPT-6	8	0.94	0.69	40	907	0.2	400	35

Table 4.1: Severe plastic deformation parameters used to make $Fe_{81}Ga_{19}$ SPD samples.

4.1.1 XRD Data Analysis

Small discs having diameter 2.4 mm were cut from the each sample from deformed portion and analyzed for XRD. X-ray diffraction patterns of all the samples deformed with different shear rates are shown in Figure 4.1. In order to find lattice constant, crystallite size, texture and strain induced by SPD process, rietveld refinement was performed by Bruker Axis software TOPAS. Figure 4.2 shows plot of lattice constants (A°) and crystallite size (nm) as a function of shear strain. Similarly Figure 4.3 shows (110) texture and strain in in SPD samples as a function of shear strain. The undeformed sample also have additional (111) texture, having value of 0.40708. There exist no relationship between lattice constant and crystallite size with shear rate for the samples deformed at room temperature. For samples deformed at 400°C, the lattice constant and crystallite size decreases with increase of shear rate.
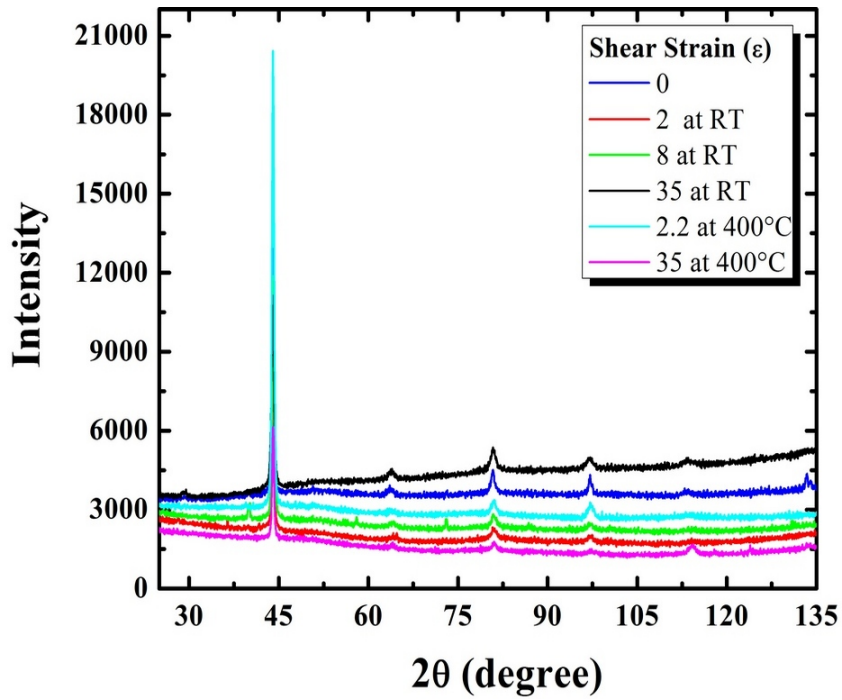
Figure 4.1: X-ray diffraction spectra (Cu- Kα radiation) of $Fe_{81}Ga_{19}$ samples deformed at different shear strains.
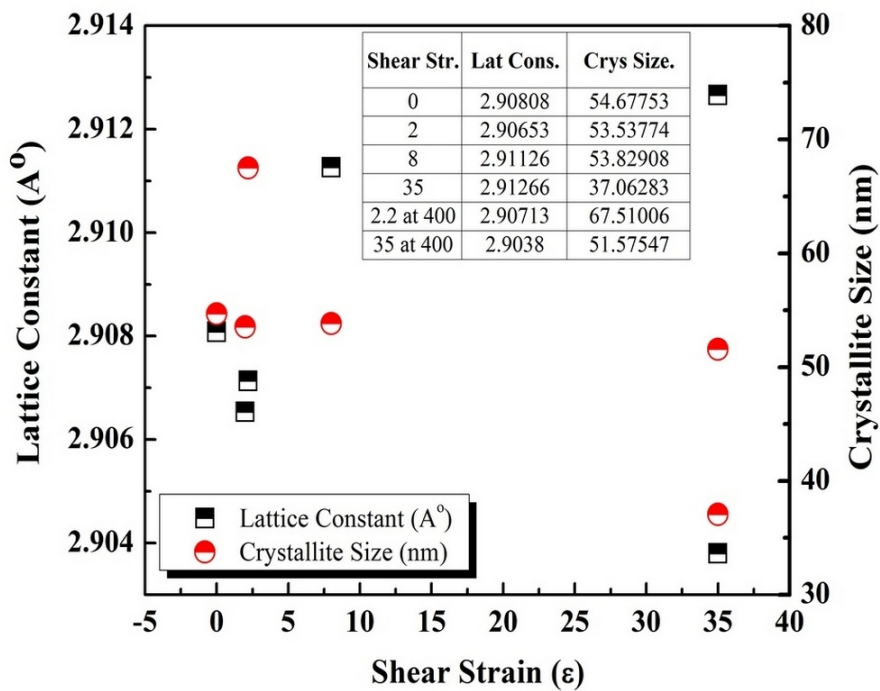
Figure 4.2: Lattice constants (A°) and crystallite size (nm) as a function of shear strain.
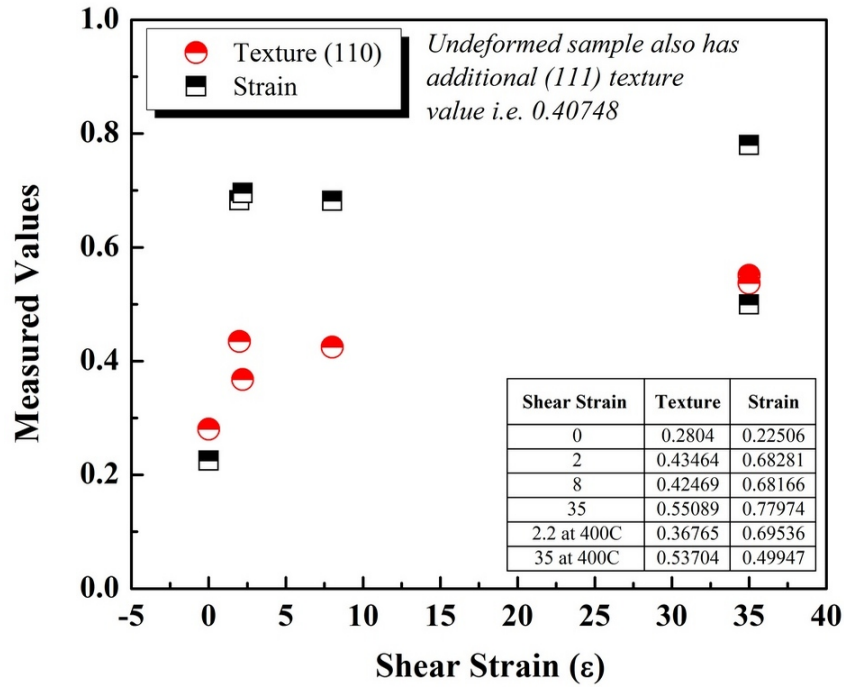
Figure 4.3: Texture (110) and strain in sample as a function of shear strain.

However one can see from Figure 4.3 for the samples deformed at room temperature the texture and strain increases with increase in shear strain. The difference between texture and strain value for the samples deformed at at shear rate $\varepsilon = 2$ and $\varepsilon = 8$ is not too large. For the samples deformed at temperature 400°C, texture value increases with increase in shear strain, while induce strain value decrease. These results shows that severe plastic deformation process clearly induces strain and texture in $Fe_{81}Ga_{19}$ alloy, which might result high value of magnetostriction.

Table 4.2 sums up the results calculated from XRD patterns.

Shear Strain (ε)	Lat. Const (A°)	Cryt. Size (nm)	Texture (110)	Induced Strain Value
0	2.90808	54.67753	0.2804	0.22506
2	2.90653	53.53774	0.43464	0.68281
8	2.91126	53.82908	0.42469	0.68166
35	2.91266	37.06283	0.55089	0.77974
2.2 at 400°C	2.90713	67.51006	0.36765	0.69536
35 at 400°C	2.90380	51.57547	0.53704	0.49947

Table 4.2: XRD measurements results of $Fe_{81}Ga_{19}$ deformed and un-deformed samples.
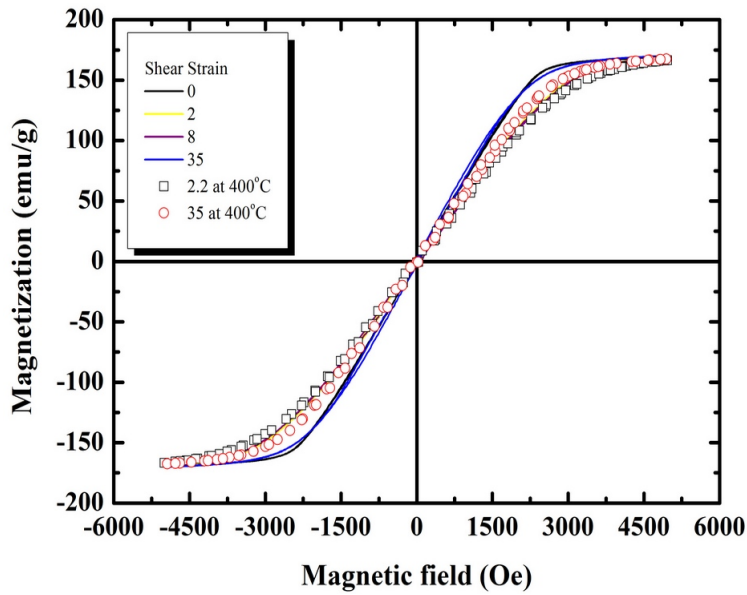
Figure 4.4: Magnetization curves measured on $Fe_{81}Ga_{19}$ samples.

4.1.2   Magnetization Measurements

Figure 4.4 shows the MH curves of $Fe_{81}Ga_{19}$ samples measured up to 5000 Oe. The saturation magnetization was found to be from 167 to 170 emu/g. The coercivity of samples (measured in open loop by VSM) increase with increases in shear rate due do induce stress and texture formed in the samples. Un-deformed sample has coercivity of 7 Oe, whereas the sample deformed at shear rate 35, has value of coercivity about 43 Oe. For samples deformed at 400°C the coercivity decrease with increase in shear rate (shown in Figure 4.5).

4.1.3   Magnetostriction Measurements

Figure 4.6 shows the magnetostriction measured on un-deformed $Fe_{81}Ga_{19}$ sample with strain gauge method. The magnetostriction was measured in two directions by bonding strain gauge at the center of sample to ensure the sample is isotropic and no preferential orientation or texture occurs.

Figure 4.8 shows the magnetostriction measured across the deformation direction on $Fe_{81}Ga_{19}$ sample severely plastic deformed at shear rate $\varepsilon = 35$ and Figure 4.10 shows the magnetostriction measured across the deformation direction of sample severely plastic deformed at shear rate $\varepsilon = 2$.

The magnetostriction was measured in two directions by bonding two separate strain gauges along the SPD direction and across the SPD direction as shown in Figure 4.7. λ_{par} represent the magnetostriction measured by applying magnetic field parallel to measuring grid (along the length of strain gauge) whereas λ_{per} represent the magnetostriction measured by applying magnetic field perpendicular to measuring grid (along the width of strain

Shear Str.	Hc (Oe)	Ms (emu/g)
0	6.6	168.27
2	27.25	169
8	37.82	168.97
35	42.62	170
2.2 at 400C	*45.15*	*166.92*
35 at 400C	*40.45*	*167.6*
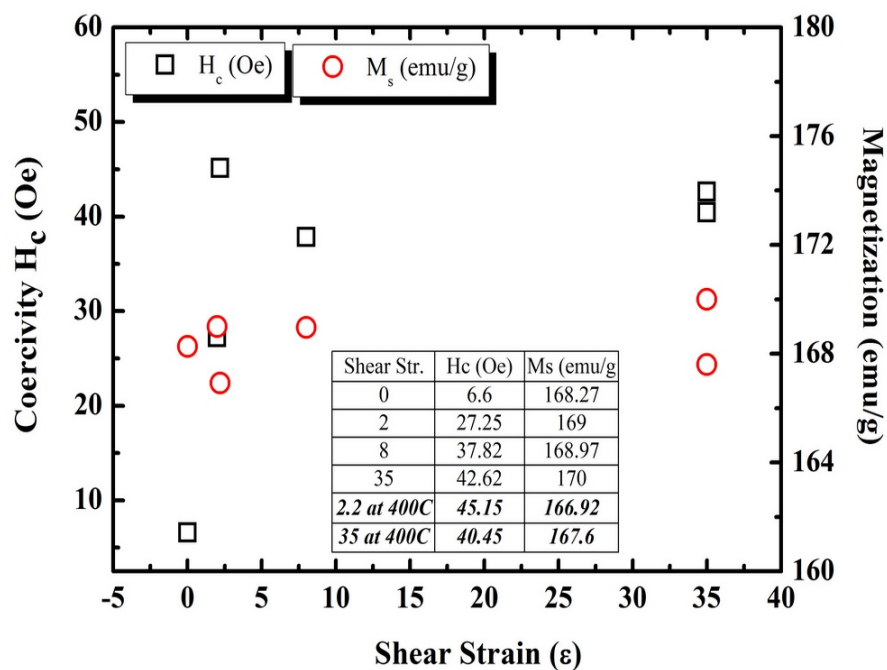
Figure 4.5: Magnetization (M_s) and Coercivity (H_c) of $Fe_{81}Ga_{19}$ SPD Samples.
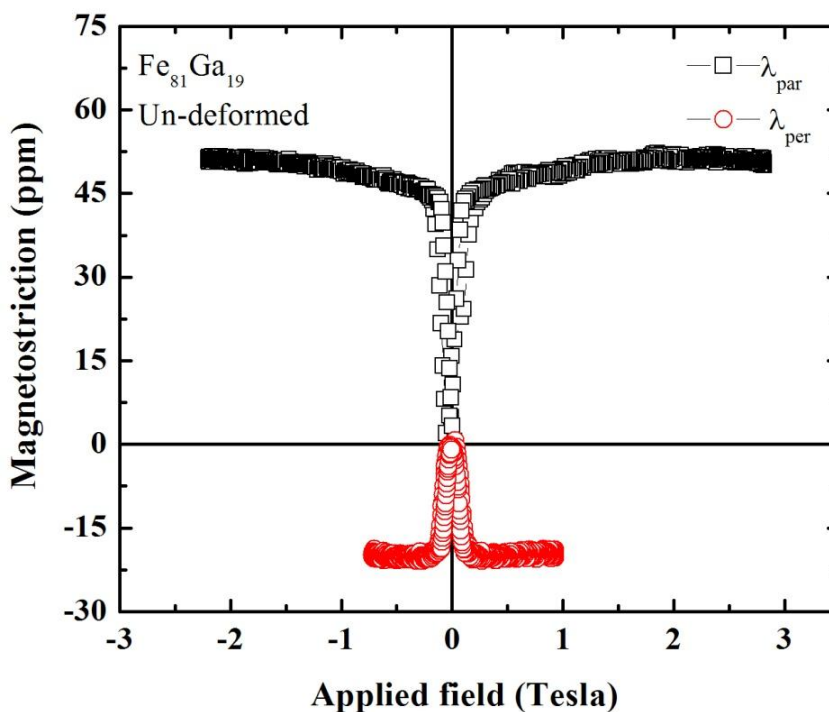
Figure 4.6: Parallel and perpendicular magnetostriction, λ_{par} and λ_{per}, of un-deformed bulk $Fe_{81}Ga_{19}$ strain-gauge at center of sample.
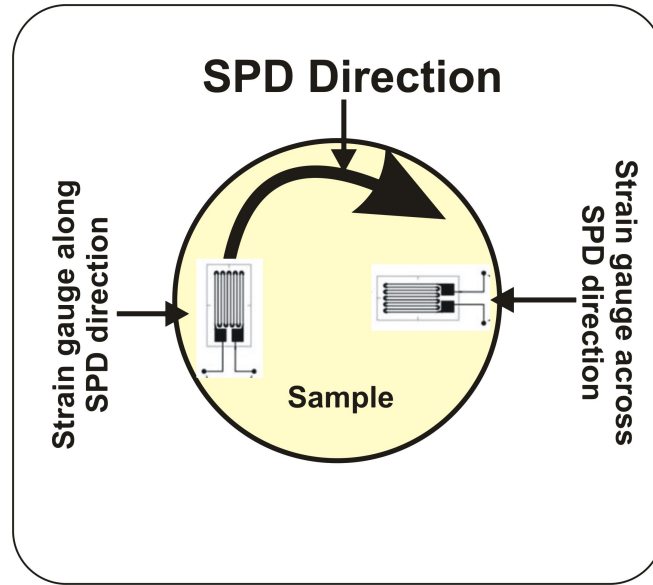
Figure 4.7: Strain gauge setup on the sample.
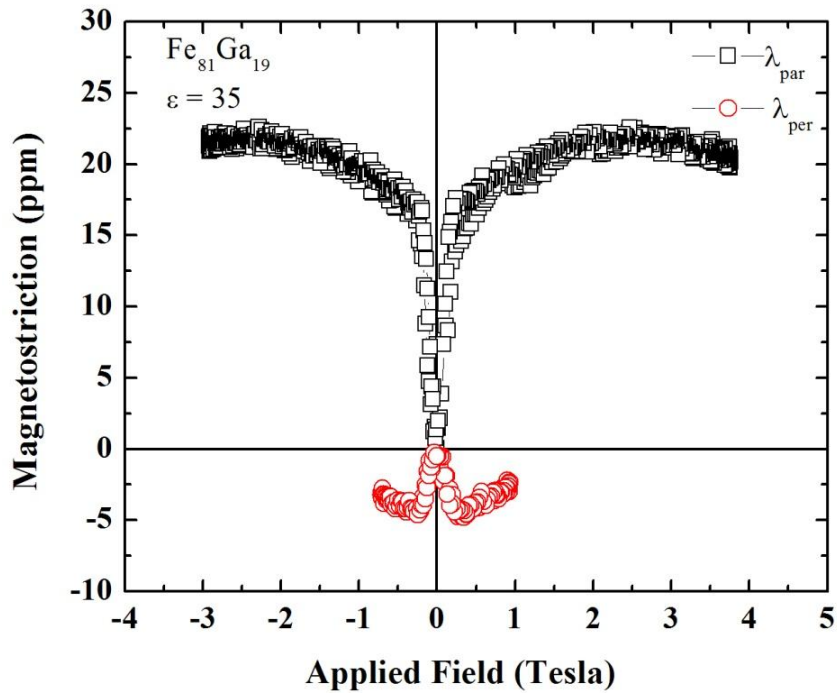
Figure 4.8: Parallel and perpendicular magnetostriction, , λ_{par} and λ_{per}, of severely plastic deformed $Fe_{81}Ga_{19}$ at shear rate $\varepsilon = 35$, across deformation direction.

gauge) as shown in Figure 4.9 .

Figures 4.11 and 4.12 shows the magnetostriction measured across deformation direction on $Fe_{81}Ga_{19}$ sample severely plastic deformed at shear rate $\varepsilon = 35$ and $\varepsilon = 2.2$ at high temperature 400°C.

The magnetostriction values measured of SPD sample are summarized in Table 4.3.
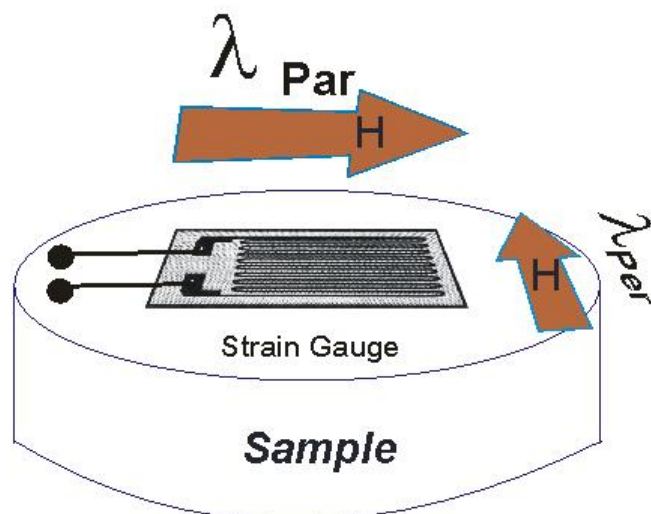
Figure 4.9: λ_{par} and λ_{per} measuring setup, of SPD samples.
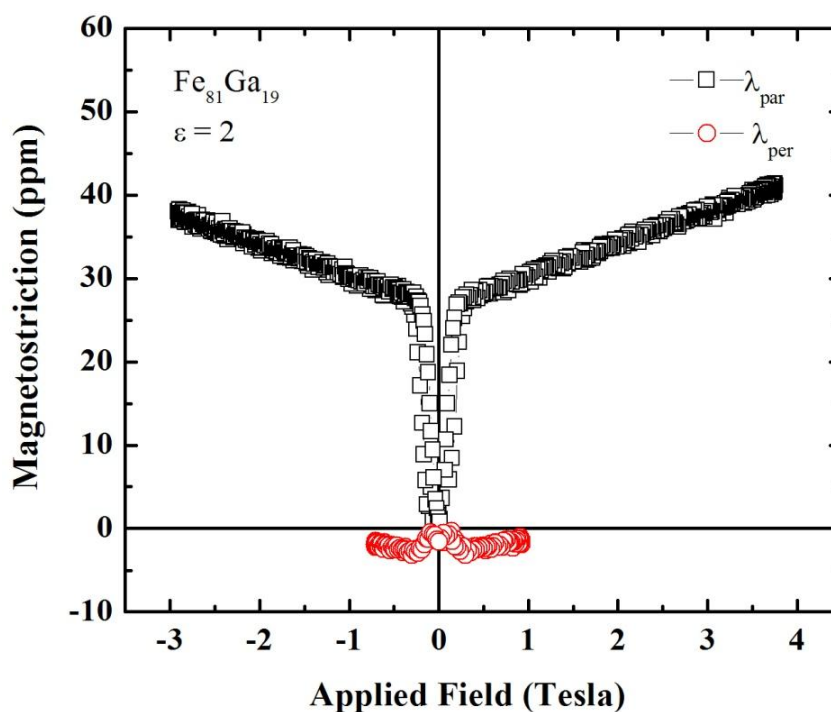
Figure 4.10: Parallel and perpendicular magnetostriction, , λ_{par} and λ_{per}, of severely plastic deformed $Fe_{81}Ga_{19}$ at shear rate $\varepsilon = 2$, across deformation direction.
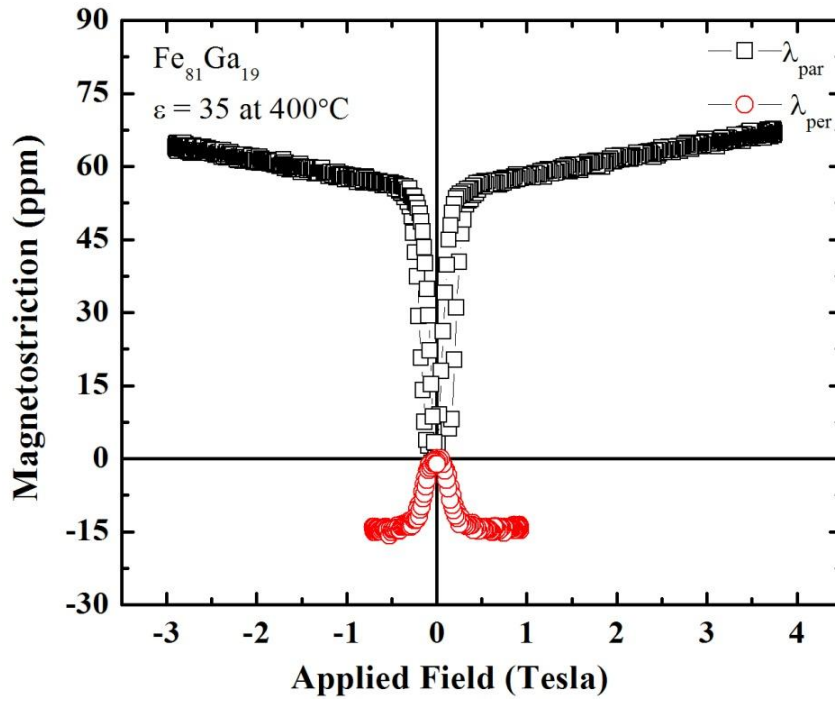
Figure 4.11: Parallel and perpendicular magnetostriction, , λ_{par} and λ_{per}, of severely plastic deformed $Fe_{81}Ga_{19}$ at shear rate $\varepsilon = 35$, at 400°C across deformation direction.
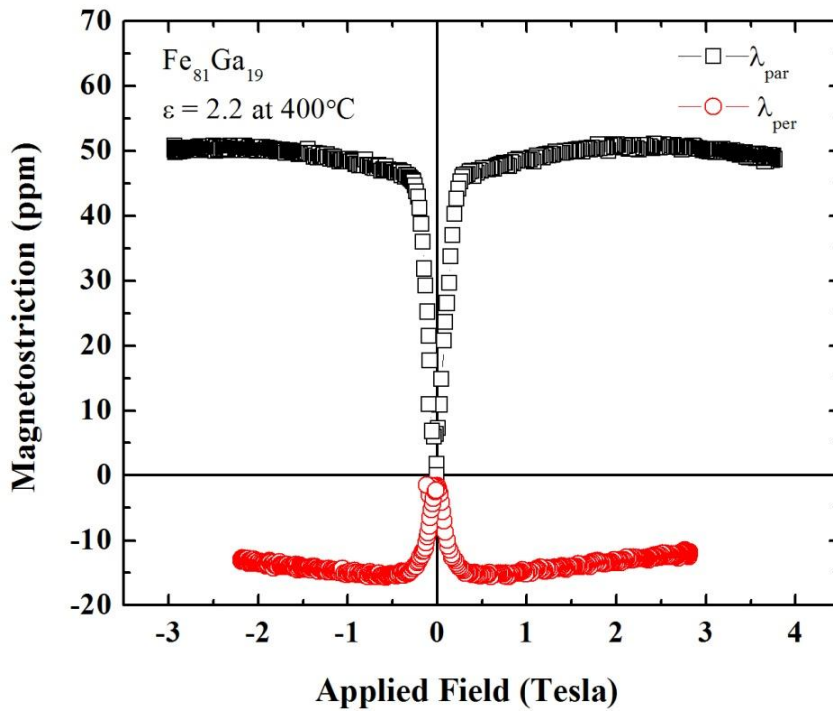
Figure 4.12: Parallel and perpendicular magnetostriction, , λ_{par} and λ_{per}, of severely plastic deformed $Fe_{81}Ga_{19}$ at shear rate $\varepsilon = 2.2$, at 400°C across deformation direction.

Sample ID	Shear Strain (ε)	Magnetostriction x10^{-6}(ppm)					
		Along SPD direction		Across SPD direction		Center of the sample	
		λ_{par}	λ_{per}	λ_{par}	λ_{per}	λ_{par}	λ_{per}
HPT-4	Un-deformed	-	-	-	-	53	-20
HPT-1	35	20	4	15	-2	-	-
HPT-2	8	12	-3	40	-3	-	-
HPT-3	2	12	-3	41	-3	-	-
HPT-5	35 (at 400°C)	25	-5	67	-15	50	-15
HPT-6	2.2 (at 400°C)	22	-5	50	-15		

Table 4.3: Magnetostriction values of un-deformed and severely plastic deformed $Fe_{81}Ga_{19}$ samples.

For shear rate $\varepsilon = 2$, 8 and 35, sample deformed at room temperature magnetostriction decreases. The magnetostriction of sample deformed at temperature 400°C increases from 53 ppm to 67 ppm. Magnetostriction values in perpendicular (across) direction of SPD are larger than parallel (along) to the SPD direction. The most important outcome of the above results was a decrease in the magnetostriction of SPD samples of $Fe_{81}Ga_{19}$ as compared to the coarse grained state. The difference can be attributed to several reasons. One of them is that the value of the applied magnetic field is low and not sufficient for the magnetization of a SPD sample up to the magnetization level of a coarse grained one. One can easily see this effect from the shape of magnetostriction curves for the samples deformed at room temperature for shear rate $\varepsilon = 2$ (shown in Figure 4.11), 8 and 35 (not shown).

4.2   Bulk Polycrystalline Fe-Al Alloys [122]

In the last years, the magnetostriction of Fe–x systems where x stays for nonmagnetic elements such as Ga, Al and Si had raised the interest of many research groups because of their potential use in low-cost sensor devices [5, 14, 64]. There exist very detailed single-crystal investigations on binary Fe–Al. In the Fe-Al system the highest value of magnetostriction was found also in (100) direction for Al concentration around 19 at % Al, which 3/2 λ_{100} is $\sim$190 ppm at room temperature [64]. Consequently the Fe-Ga and Fe-Al systems are interesting from a fundamental point of view as well as materials for magnetoelastic sensors. Here for economical reasons Fe-Al alloys would be superior. For both alloy systems, the phase stabilization of the disordered bcc structure is the fundamental component to increase the magnetostriction of the materials.

Polycrystalline $Fe_{100-x}Al_x$ (x = 15, 19 and 25) samples were high frequency melted, then annealed in vacuum at 1000 °C for 72 h. Afterward the bulk material was cooled either in a furnace (10°C/min.); or quenched directly in water, in order to investigate the influence of the structure and atomic ordering on the magnetostriction. The longitudinal and transverse magnetostriction measurements was performed on the as-cast and annealed samples.

4.2.1   Microstructure

Figure 4.13 shows as an example the microstructure of the bulk as cast $Fe_{81}Al_{19}$. The grains have dimensions of the order of 1000 μm = 1mm, but inside also smaller structures are visible. Also in heat treated and quenched material (Figure 4.14) very large grains were found, however smaller sub-structure was not detected.
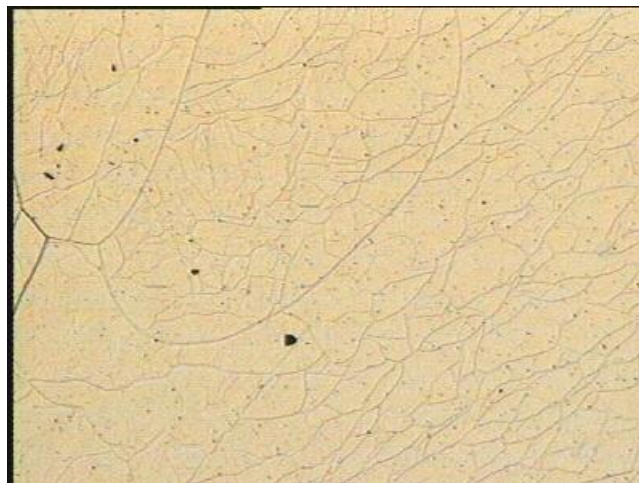
Figure 4.13: Microstructure of as-cast sample, with the same amplification shown in Figure 4.14.
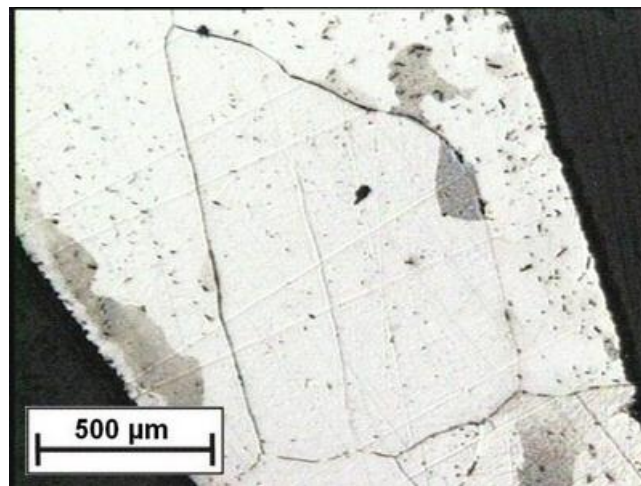
Figure 4.14: Microstructure of annealed (AN) sample.
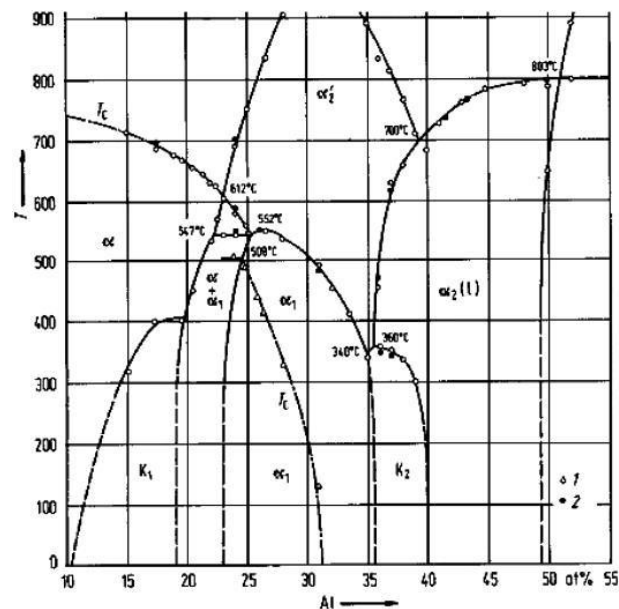
Figure 4.15: Fe-rich part of the phase diagram of the Fe–A1 alloys. (magnetic transformation). W. Kijster and T. Giidecke, Z. Metallkuide, 71 (1980)765.

4.2.2 XRD Data Analysis

According to the phase diagram (Figure 4.15) for an Al concentration of 15 at% only the disordered A_2 structure is expected, whereas for higher Al concentrations additional phases (such as B_2 and/or DO_3 structure) can be expected depending on heat treatment and processing conditions.

According to the X-ray diffraction patterns of the three as cast $Fe_{100-x}Al_x$ (x = 15, 19 and 25 at%) samples the following results are achieved: 15% Al: A_2 structure (space group Im3m), lattice constant = 2.90 x 10^{-10}m; 19 Al: A_2 structure, lattice constant = 2.90 x 10^{-10} m and 25 Al: 40% A_2 structure + 60% B_2 structure, lattice constant = 2.90 x 10^{-10}m. These results show that in this concentration range a lattice constant which is independent of the
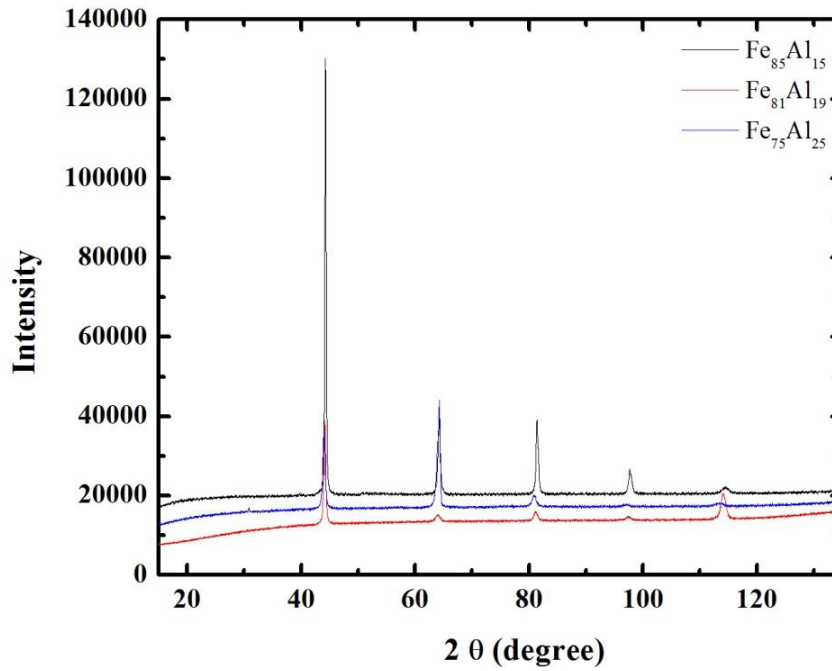
Figure 4.16: XRD pattern of $Fe_{85}Al_{15}$, $Fe_{81}Al_{19}$ and $Fe_{75}Al_{25}$.

Al substitution. The samples with x = 15 and 25% Al exhibit a strong texture. The intensity ratios of the XRD pattern of all as cast samples show (Figure 4.16) preferentially aligned grains.

4.2.3 Domain Structure

$Fe_{81}Al_{19}$ alloy was chosen for domain structure observation, because this alloy exhibits a higher magnetostriction, as will be shown later. Figure 4.17 shows as a comparison between the domain structure of AC, AN and Q samples of the $Fe_{81}Al_{19}$ alloy. The as-cast material shows very narrow domains (a typical stress pattern for high magnetostrictive materials). The heat-treated AN sample shows larger domains (which are within the grains) in two different orientated grains, whereas in the quenched sample the domains again become smaller (but larger than those of AC samples) due to an enhanced stress state.

4.2.4 Magnetization and Magnetostriction Measurements

Figure 4.18 shows the magnetization curves of all three samples at room temperature. The material is easy to saturate, the saturation magnetization decreases with increasing Al content from 198 emu/g (15 at% Al) to 153 emu/g (25 at% Al) – see Table 4.4.

Figures 4.20, 4.21 and 4.22 shows the room-temperature values of the longitudinal (λ_{long}) and transverse (λ_{trans}) magnetostrictions of the $Fe_{85}Al_{15}$, $Fe_{81}Al_{19}$ and $Fe_{75}Al_{25}$ alloys, respectively (measured according to setup shown in Figure 4.19) . For the $Fe_{85}Al_{15}$ alloy, considering the longitudinal magnetostriction the AC material gave the highest value,

Fe81Al19 - as-cast (bulk)

(a) AC

Fe81Al19 - annealed (bulk)   Fe81Al19 - quenched (bulk)

(b) AN   (c) Q
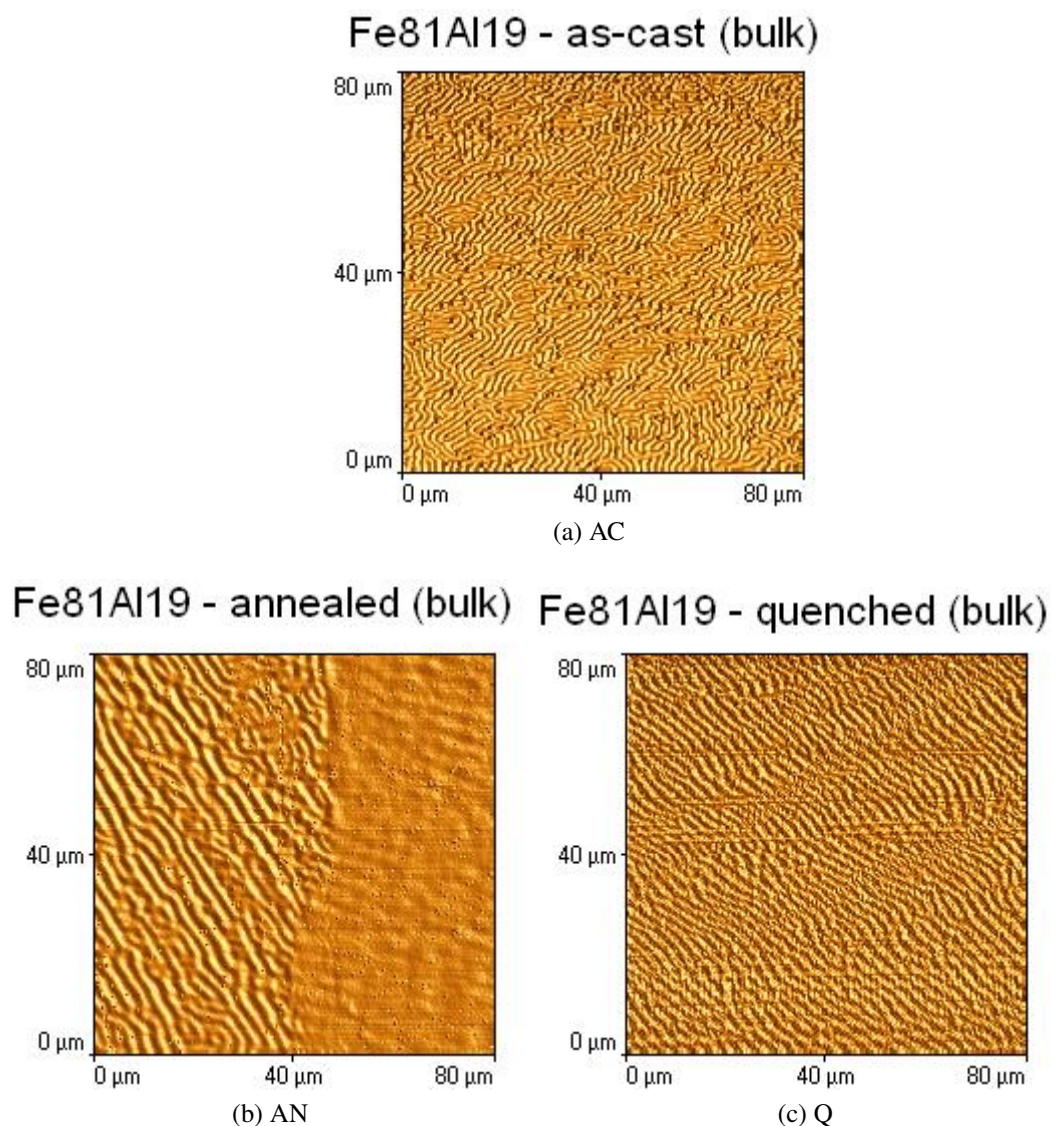
Figure 4.17: Domain structure of the AC, AN and Q samples.

which is about 43 ppm, followed by AN and Q samples. The magnetostriction measured in the transversal geometry behaves the other way: it increases starting from the as-cast state to the heat-treated state and thus to the quenched state.

The $Fe_{81}Al_{19}$ alloy behaves differently (see Figure 4.21). The longitudinal magnetostriction of the AC material gave the lowest value (20 ppm), whereas the AN sample exhibited the highest value (62 ppm), and Q sample exhibited $\lambda_{long} = 55$ ppm. These results are agreeing with the domain structure behavior, where the AN sample presents larger and more regular domains and almost relieved the internal stress. The magnetostriction measured in the transversal geometry decreases starting from the AN sample, becomes smaller in the as-cast state and goes further down in the quenched state.

For the $Fe_{75}Al_{25}$ alloy, which shows a mixture of ordered B_2 and disordered A_2 phases, the λ_{long} value is the lowest for the Q sample (25 ppm). The higher values such as 42 and 50 ppm were found, respectively, for the AC and AN samples. The magnetostriction
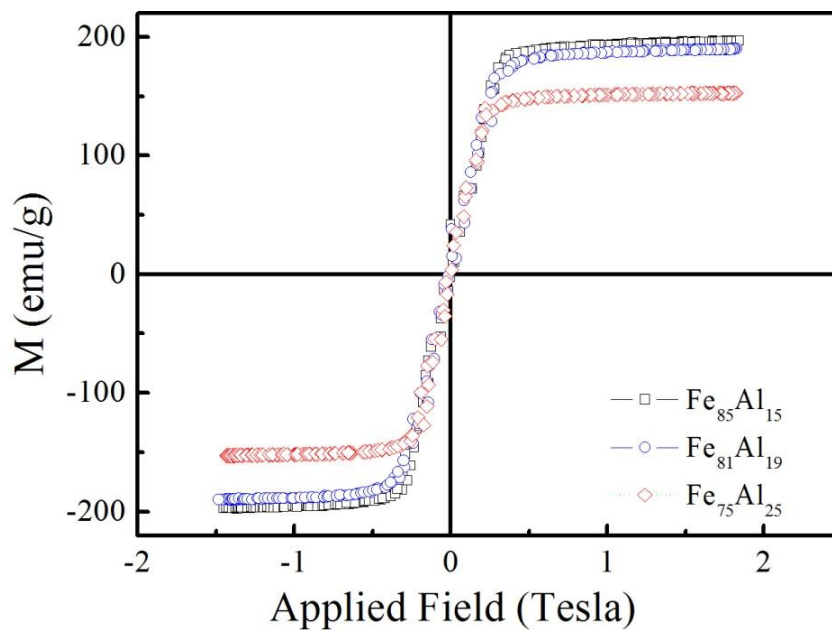
Figure 4.18: Magnetization curves measured on AC, AN and Q samples.
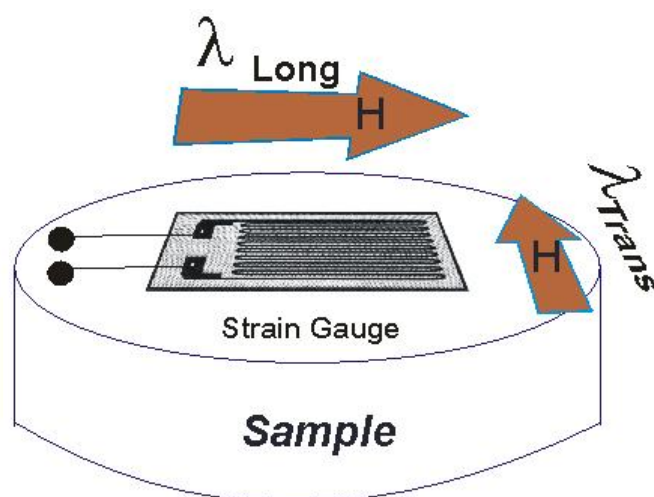
Figure 4.19: Longitudinal (Long) and Transverse (Trans) magnetostriction measurement setup.
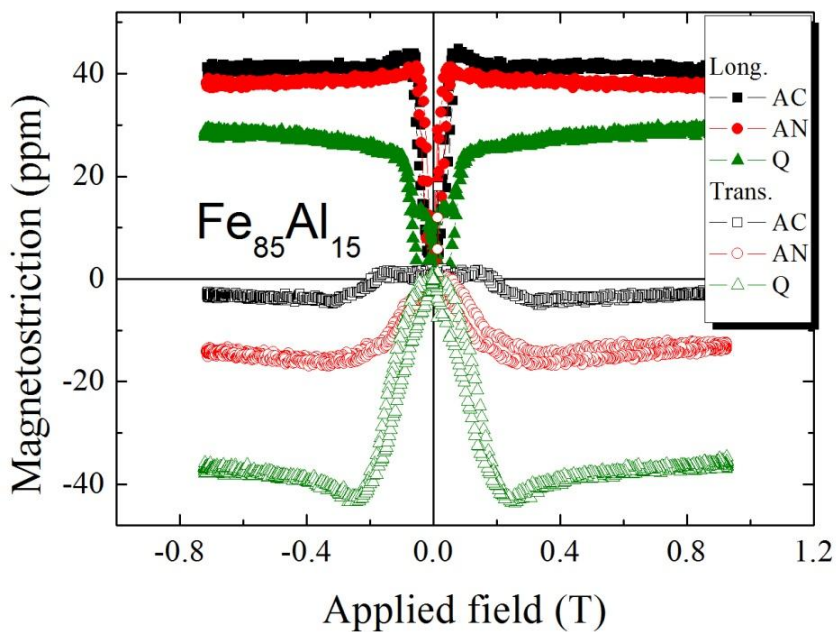
Figure 4.20: Longitudinal and transverse magnetostriction of $Fe_{85}Al_{15}$ measured in the AC, AN and Q samples.
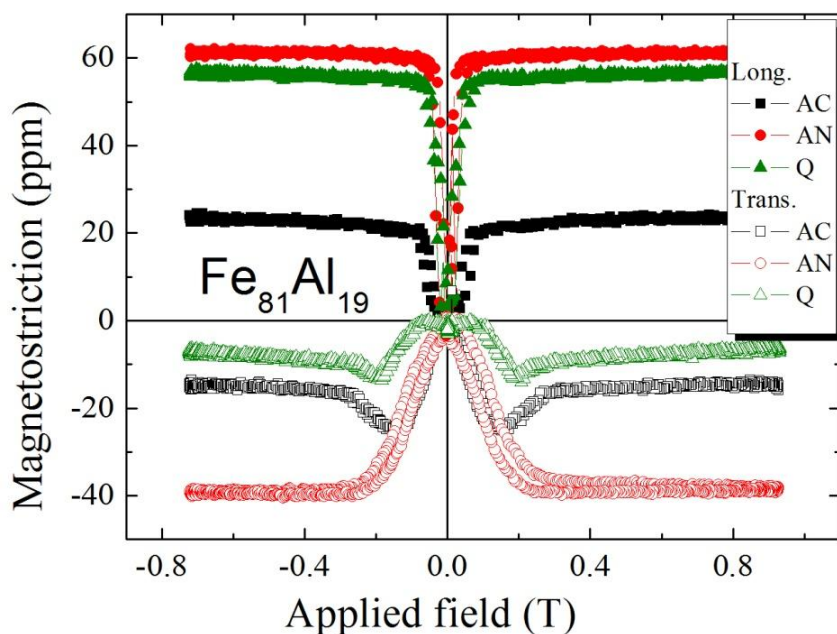
Figure 4.21: Longitudinal and transverse magnetostriction of $Fe_{81}Al_{19}$ measured in the as cast state, after annealing and after quenching.
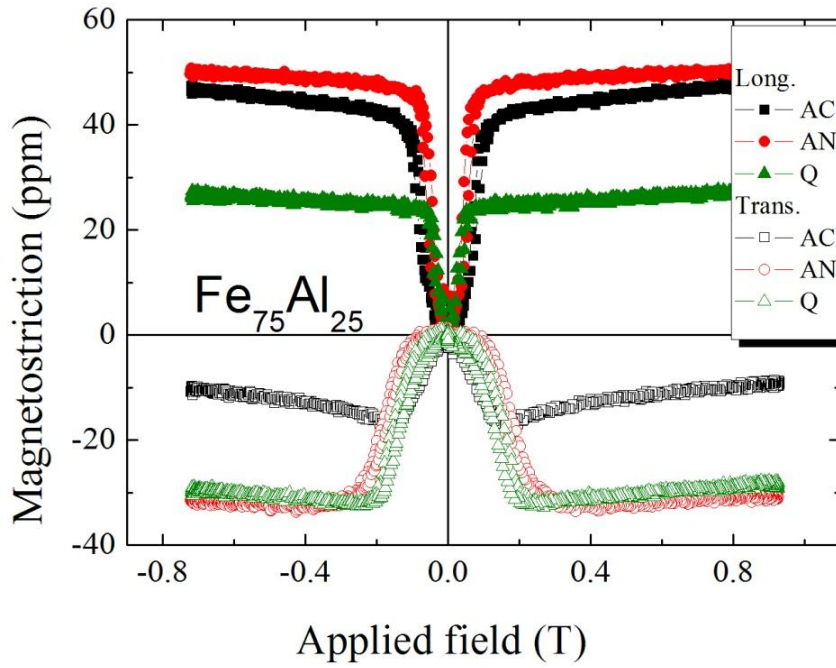
Figure 4.22: Longitudinal and transverse magnetostriction of $Fe_{75}Al_{25}$ measured in the as cast state, after annealing and after quenching.

Samples (at % Al)	M_S (emu/g)	λ_{long} (ppm)	λ_{trans} (ppm)	λ_{total} = λ_{long} - λ_{trans} (ppm)
15 AC		43	-4	47
15 AN	198	40	-14	54
15 Q		25	-42	67
19 AC		20	-24	44
19 AN	189	62	-37	99
19 Q		55	-13	68
25 AC		42	-17	59
25 AN	153	50	-33	83
25 Q		25	-32	57

Table 4.4: Saturation magnetization, longitudinal, transverse and total magnetostriction (at $\mu_0 H_{ext} = 0.3$ T) of $Fe_{100-x}Al_x$ in the AC, AN and Q samples.

measured in the transversal geometry decreases starting from the AN sample, becomes slightly smaller in the quenched state and goes further down in the as-cast state.

Magnetostriction in ferromagnetic polycrystalline isotropic materials is characterized by $\lambda_{long} = -2\lambda_{trans}$ and by the saturation magnetostriction, λ_s, determined by a phenomenological equation $(3/2)\lambda_s = \lambda_{long} - \lambda_{trans} = \lambda_{total}$. On the other hand, λ_s of an isotropic polycrystalline material can be calculate from the single crystal data by the well known equation $\lambda_s = 1/5 (2\lambda_{100}+3 \lambda_{111})$. To have hints of the influence of texturing or stresses in our samples, we determined the λ_s values from λ_{total} (see Table 4.4) and compared with λ_s calculated by the later equation, considering λ_{100} values from [64]. In Fe-Al alloys for the Al concentra-

tion between 15 and 25 at %, the contribution of λ_{111} can be neglected because its value is nearly zero [14]. The λ_{100} values of $Fe_{85}Al_{15}$, $Fe_{81}Al_{19}$ and $Fe_{75}Al_{25}$ from [64] are 120, 150 and 100 ppm, respectively, and corresponding calculated λ_s values are 32, 40 and 27 ppm, respectively. These λ_s values are always smaller than those λ_s found in our samples, indicating the existence of a texture and/or a disordered A_2 structure in our samples. Additionally, rarely the relation $\lambda_{long} = -2\lambda_{trans}$ was not obtained in our alloys. In Table 4.4 the most important results are summarized.

4.3   Fe-Mn Alloys

A set of Fe-Mn antiferromagnetic alloys samples was prepared by high frequency in-
duction melting having composition $Fe_{54}Mn_{56}$, $Fe_{53}Mn_{47}$ and $Fe_{51}Mn_{49}$. Magnetostriction
measurements were performed as shown in Figures 4.24, 4.25 and 4.26 (after annealing
for 1000°C/24 hrs and quenching) along (ALSD) and across (ACSD) the solidification
directions to make further investigation of results reported in ref [113, 114]. Table 4.5 sum-
marizes the magnetostriction measurement made on the all Fe-Mn samples (according to
setup shown in Figure 4.23).
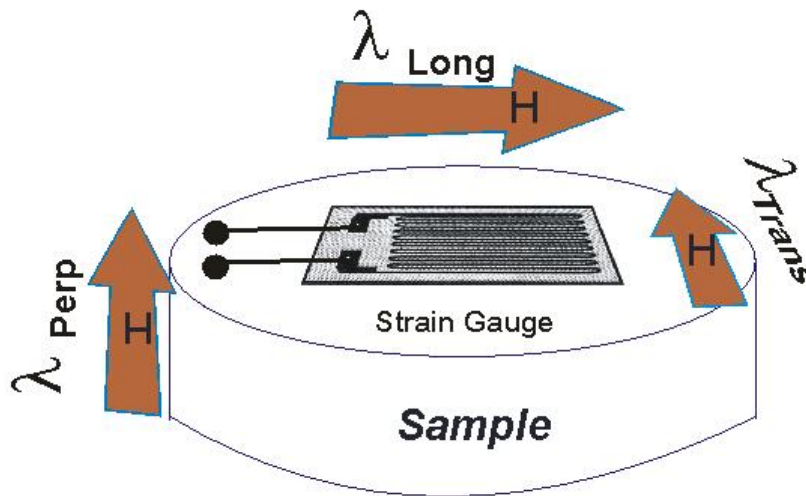
Figure 4.23: Longitudinal (Long) and Transverse (Trans) and Perpendicular (Perp) magne-
tostriction measurement setup.

Fe-Mn Alloy Composition	Heat Treatment Condition	Magnetostriction Measurement Direction	Magnetostriction (ppm)		
			λ H_{long}	λ H_{Trans}	λ H_{per}
$Fe_{54}Mn_{56}$	Annealed	ALSD	-49	-64	-40
$Fe_{53}Mn_{47}$	Annealed	ALSD	-42	-30	-67
$Fe_{53}Mn_{47}$	Quenched	ALSD	-52	-70	-25
$Fe_{53}Mn_{47}$	Quenched	ACSD	-56	-70	-40
$Fe_{51}Mn_{49}$	Annealed	ALSD	-44	-43	-38

Table 4.5: Magnetostriction results of Fe-Mn samples.

The maximum measured value of magnetostriction $\lambda_{perpendicular}$ was -70 ppm (~ 5 Tesla)
for the quenched sample having composition $Fe_{53}Mn_{47}$, which was same for both along
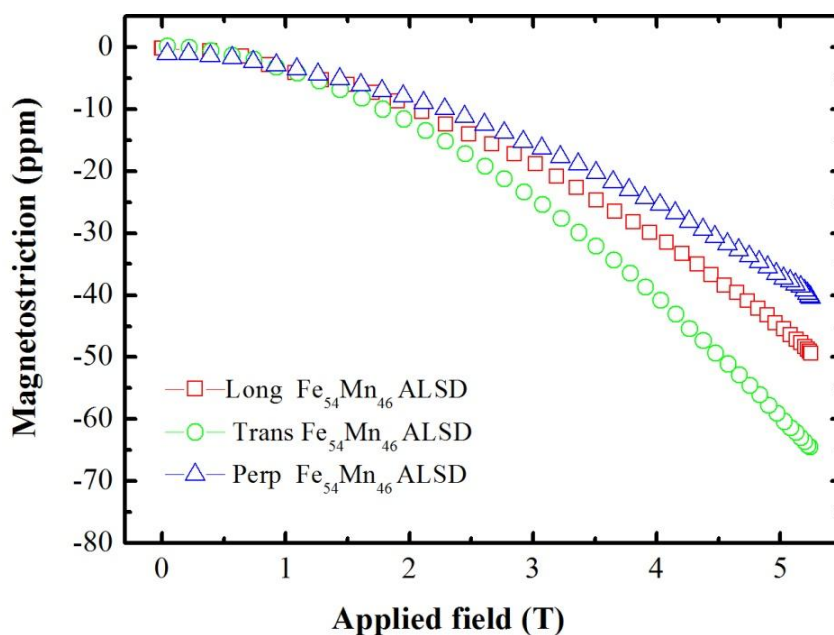
Figure 4.24: Magnetostriction of $Fe_{54}Mn_{56}$ along the solidification direction (ALSD) after annealing the samples at 1000°C for 24 hr by applying field parallel, transverse and perpendicular directions.
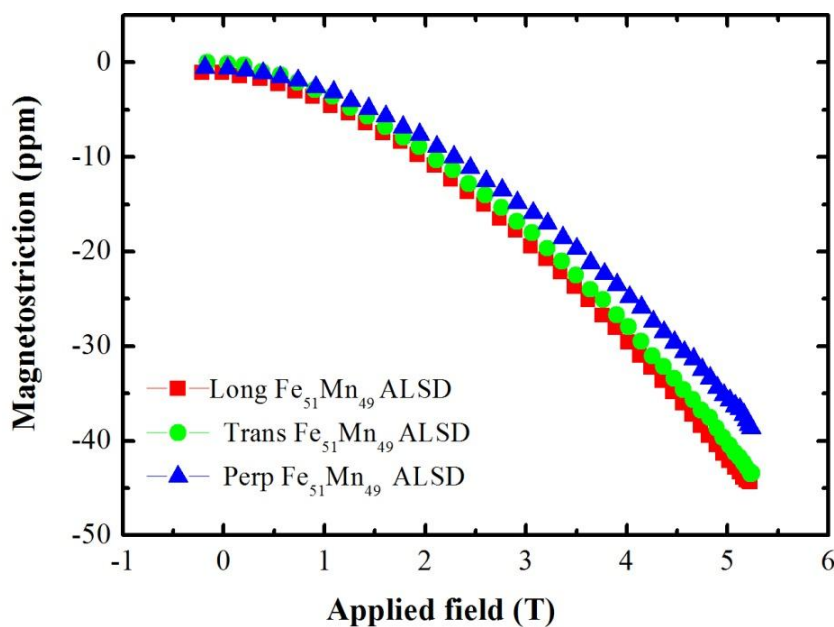
Figure 4.25: Magnetostriction of $Fe_{51}Mn_{49}$ along the solidification direction (ALSD) after annealing the samples at 1000°C for 24 hr by applying field parallel, transverse and perpendicular directions.
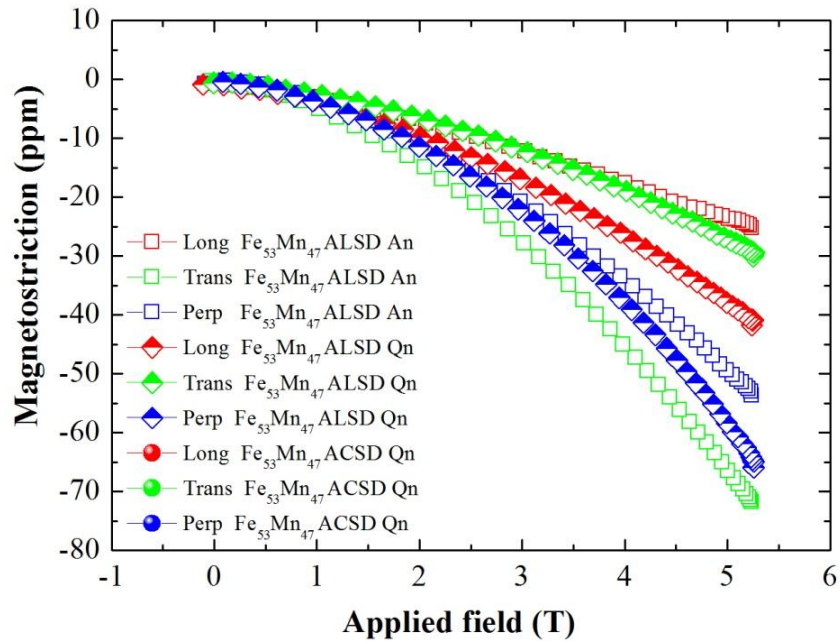
Figure 4.26: Magnetostriction of Fe$_{53}$Mn$_{47}$ along the solidification (ALSD) and across the solidification (ACSD) direction after annealing the samples at 1000°C for 24 hr and quenching by applying field parallel, transverse and perpendicular directions.
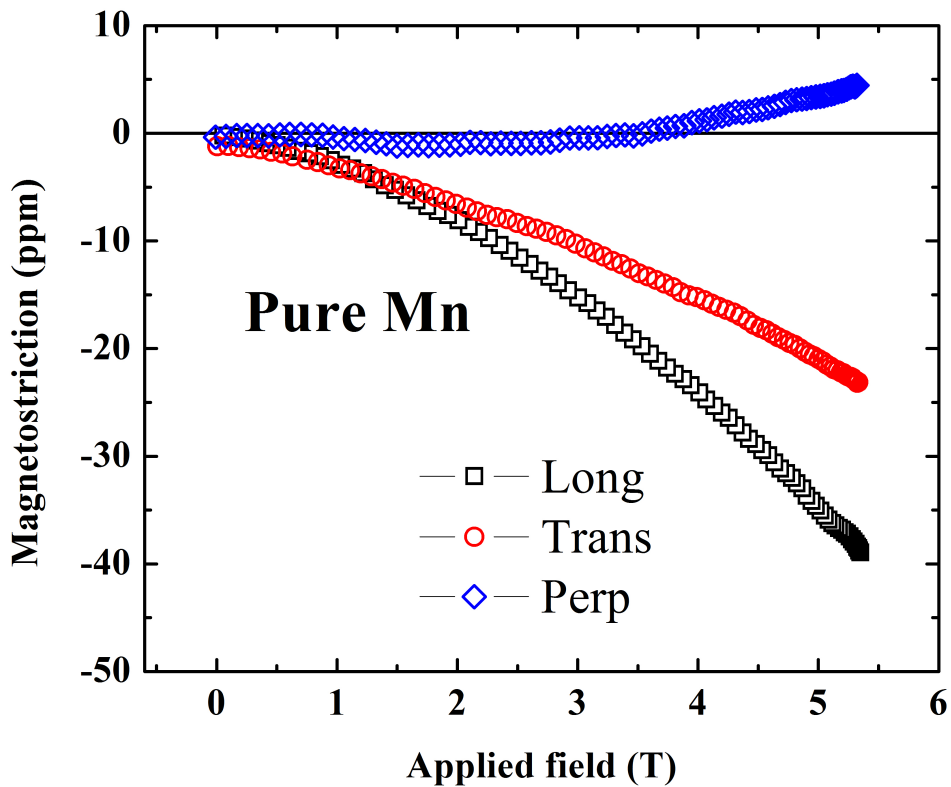
Figure 4.27: Magnetostriction of pure Mn.

and across the solidification direction of the sample. All the magnetostriction values measured are negative irrespective of heat treatment conditions and solidification direction. The samples were not saturated even field up to ~ 5 T. Figure 4.27 shows the magnetostriction measured on pure Mn. Pure Mn has longitudinal magnetostriction value of -40 ppm at $\sim$ 5 Tesla.

4.4   Sm-Fe Alloys

The cubic rare earth-Fe_2 compounds ($TbFe_2$, $SmFe_2$ and $DyFe_2$) have been extensively studied in last years because of their large magnetostriction at room temperature [26, 123]. $TbFe_2$-based compound "Terfenol" has already been commercially available and used in actuator applications [124]. Because of the high material cost of Tb, the of use of the "Terfenol" has been mostly limited to military or high-end applications. For a wide use of these high magnetostriction materials, $SmFe_2$ with its large saturation magnetostriction (λ_s = −1560 ppm) [1] and a relatively low material cost would be a preferable choice. $SmFe_2$ have a negative magnetostriction which is useful in applications requiring a large instantaneous compressive stress/strain. However properties of $SmFe_2$ inter-metallic alloys has not been so thoroughly investigated as Terfenol, because of the practical difficulties that are encountered when preparing the sample. The main problem centers on the high vapor pressure of Sm, which is 4 mbar at its own melting point (1072 °C) and over 400 mbar at the melting point of Fe. This inevitably results in severe Sm losses by volatilisation when $SmFe_2$ samples are prepared by fusing together the elemental components using conventional melting techniques [125].

However we produced polycrystalline $SmFe_2$ by induction melting furnace, the chemical composition of alloy was determined by electron probe microanalysis (EPMA) EDX technique. The as cast sample was not homogeneous and have different composition at different spots i.e. $SmFe_{2.3}$, $SmFe_{1.25}$ and $SmFe_9$.

Figure 4.28 shows the magnetostriction of dirty nominal $SmFe_2$ alloy measured by applying magnetic field in three different ways parallel to length of strain gauge (long), parallel to width of strain gauge (Trans) and applying field perpendicular to the thickness of sample (Perp) before heat treatment (according to setup shown in Figure 4.23). This shows that $SmFe_2$ based alloys even with less amount of Sm, even not single phase also have quite reasonable magnetostriction i.e. -500 ppm as compared to Terfenol and Galfenol alloys and can be useful for sensor and actuator applications.

The as cast sample was heat treated at 700°C for 132 hr under the vacuum with Ta-foil as getter material. XRD analysis of heat treated sample shows that the sample was pure single phase $SmFe_2$ having crystallite size of 21nm , lattice constant 7.426648A° and space group Fd3m.

Figure 4.29 shows the magnetostriction of $SmFe_2$ alloy after heat treatment. The measured value of magnetostriction for $SmFe_2$ heat treated sample was observed ∼-1040 ppm at magnetic field approx. 4 Tesla. Here $\lambda_{\text{long}} = -2\lambda_{\text{trans}}$ fits well.

The main problem here is only that $SmFe_2$ needs a rather high external field in order to develop the high magnetostriction which is a consequence of the high magnetocrystalline anisotropy of this material. Here steps to reduce the anisotropy - such as alloying or producing the material in a nanocrystalline state - are necessary in order to obtain a technically
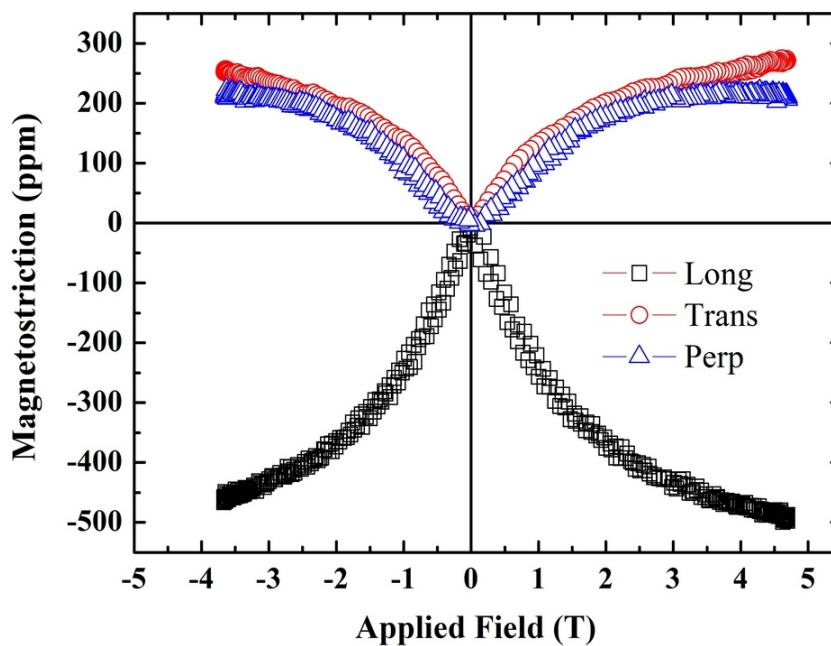
Figure 4.28: Magnetostriction of SmFe$_2$ (nominal) at room temperature before heat treatment.
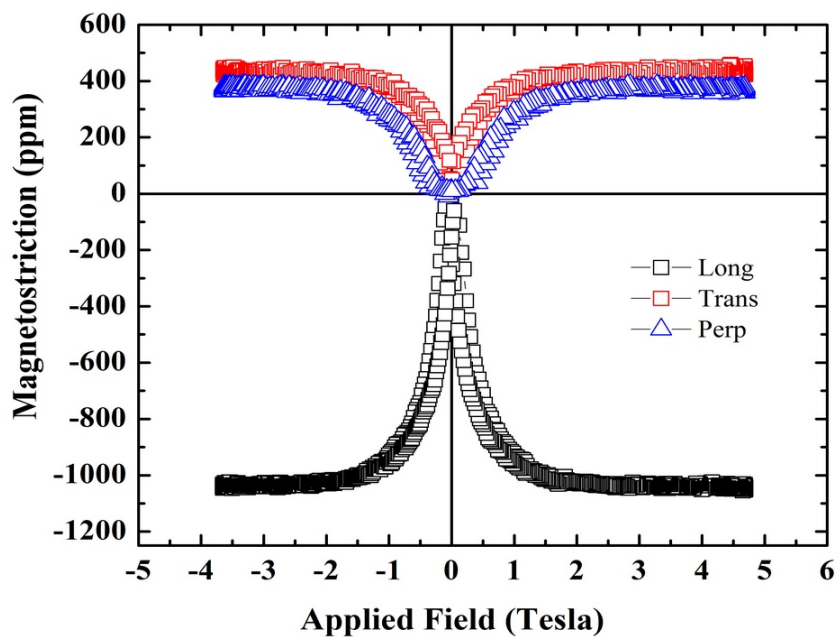
Figure 4.29: Magnetostriction of SmFe$_2$ alloy at room temperature, after heat treatment.

useful magnetostrictive material.

4.5 Ni-Ga Alloys

Keeping in view that addition of non magnetic V, Cr, Al and Ga in Fe and increase the magnetostriction of Iron as reported by Hall [14, 50] and Clark et al [5, 51–53] , we also made two samples of polycrystalline Ni-Ga alloys having composition $Ni_{98}Ga_2$ and $Ni_{93}Ga_7$ by conventional high frequency induction melting furnace technique to see effects addition of Ga in Ni. Figure 4.30 shows the magnetostriction (λ_{par}) of the $Ni_{98}Ga_2$, $Ni_{93}Ga_7$ and pure Nickel in as cast state. It can be seen that after addition of 2 % Ga the magnetostriction of Ni slightly increases about $\sim$ 4 ppm from -35 ppm to -39 ppm (measurement setup shown in Figure 4.46). By increasing Ga concentration to 7 at % the magnetostriction value of Ni decreases to -10 ppm.

The addition of Ga in Ni does not significantly enhance the magnetostriction and for higher values of Ga addition magnetostriction decreases. This shows that the magnetostriction of Ni behaves completely different by substituting with the nonmagnetic element Ga.
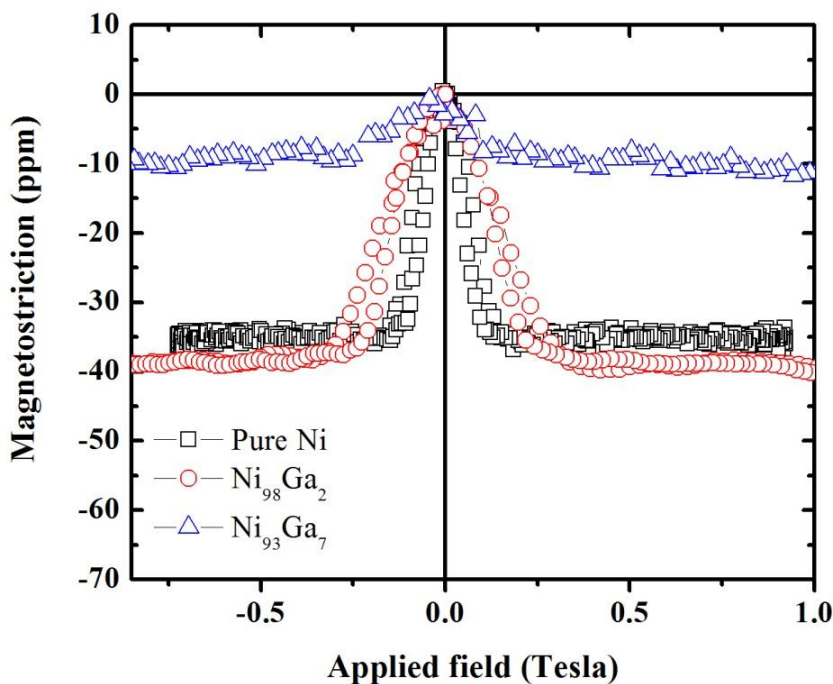
Figure 4.30: Magnetostriction (parallel) of pure Ni, $Ni_{98}Ga_2$ and $Ni_{93}Ga_7$ at room temperature.

4.6   Polymers Composites

In 2003 Nai –Xiu et al [107] reported magnetostriction value of 115 ppm at parallel field of 3900A/m of carbon black (CB) filled polypropylene composites and in 2005 they extended this work and measured the very large value of magnetostriction 1163 ppm at 800 KA/m comparable to Terfenol-D composites.
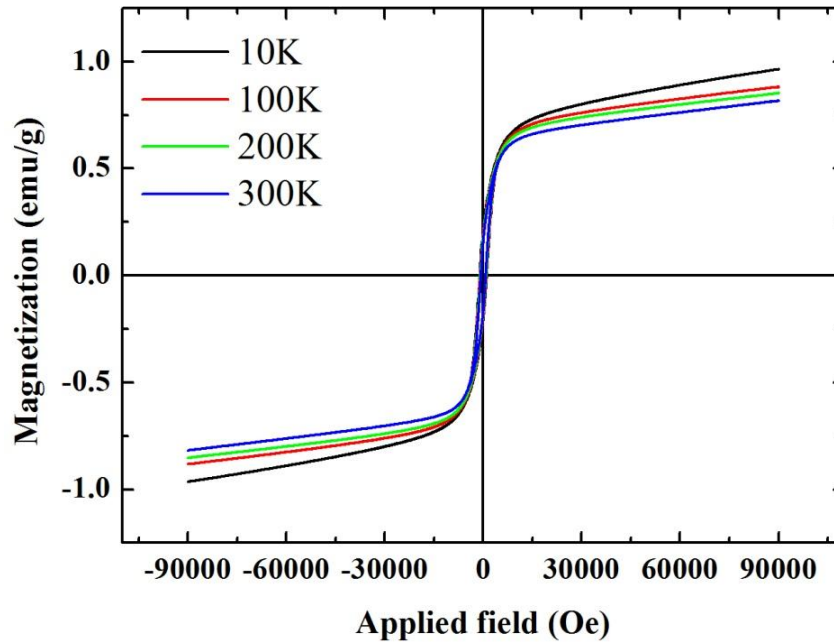
Figure 4.31: MH curve of PP-nano-19 at temperature 10K, 100K, 200K and 300K .
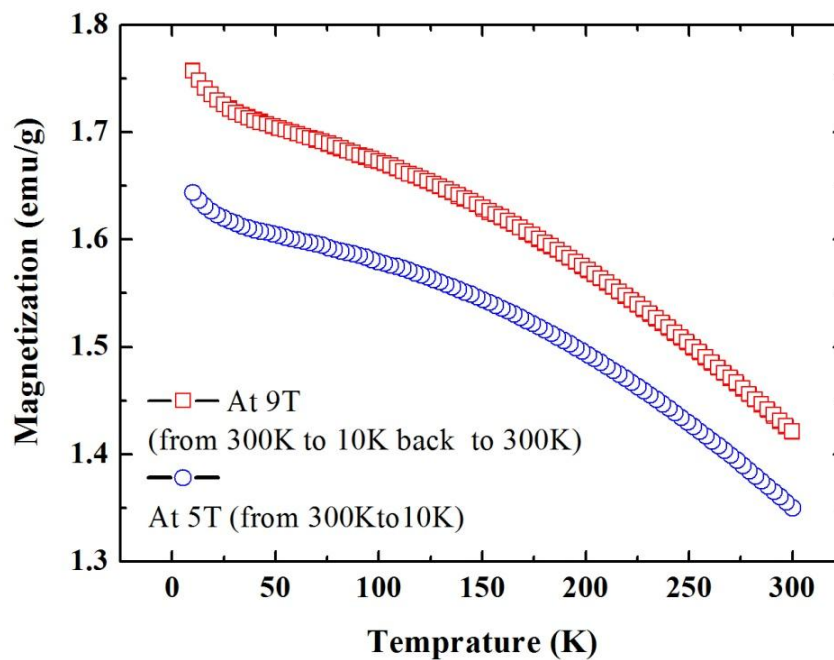
Figure 4.32: MT curve of PBT-nano19-1 at constants magnetic field 5T and 9T.

We also prepared carbon fiber based composites and investigated them magnetization and magnetostriction. Figure 4.31 shows the M-H curve measured up to 9 Tesla for the sample PP-nano19 having 60.7 wt% polypropylene and 39.3 wt % carbon fiber (nanofiber PR-19) at temperature 10K, 100K, 200K and 300K. The magnetization value of sample is very small, less than 1 emu/g. Same behavior can be seen from M-T curve measured at 5T and 9T of sample PBT-nano19-1 containing 74.65 wt% poly (butylene tereohtalate) 24.88wt % carbon fiber (nanofiber PR-19) 0.47 wt % $CoFe_2O_4$ as shown in Figure 4.32. In ref [107, 108] no magnetization values were reported. The samples PP1, PP-nano-24 also showed similar results.

All the samples PP1, PP-nano19, PP-nano24 and PBT- nano19-1 were also tested for magnetostriction by bonding strain gauge on the sample with HBM Z70 glue and applying magnetic field with Hirst pulse field magnetometer. These all samples showed zero magnetostriction which contrary to the values reported in ref [108] of similar type of samples in pulse field measurements.

4.7 Magnetic and Microstructural Investigation of Pipeline Steels [110]

Oil and gas pipelines are exhibit general a strong texture (due to the production process) which causes a magnetic anisotropy, with the magnetic easy axis in the axial direction of the pipe, along the length. In order to investigate the effects of stresses on hysteresis and other magnetic properties, pipeline steel samples X52, X56, and X60 were cut parallel (longitudinal or L-samples) as well as perpendicular (transversal or T-samples) to the pipe axis. From each steel type a cube of 10x10x10 mm^3 was cut to perform the microstructural investigation as well as the magnetostriction measurements.

4.7.1 Chemical Composition

The chemical compositions of the three steels under investigation were determined using the method included in the standard API-5L-2000 [126] as given in Table 4.6.

Elements	X-52	X-56	X-60
C	0.21	0.10	0.08
Mn	1.21	1.51	1.09
Si	0.05	0.31	0.26
P	0.021	0.014	0.010
S	0.019	0.002	0.004
Cr	0.02	0.03	0.01
Ni	0.02	0.02	0.02
V	0.00	0.00	0.08
Ti	0.00	0.02	0.00
Cu	0.05	0.01	0.30

Table 4.6: Chemical composition of three different pipeline steels under investigation.

4.7.2 Microstructure

The microstructure was investigated using a standard optical microscopy. As an example, Figure 4.33 depicts the typical microstructure in the longitudinal direction of all three studied steel samples. The steel X52 exhibits a distinctly visible texture (See Figure 4.33a) of ferrite/pearlite microstructure with both phases banding along the rolling direction. The texture is well visible. The mean planar grain diameter (d_m) was determined to be 22.5 μm.

The microstructure of the steels X56 and X60 consist also of ferrite/pearlite with incipient banding and d_m=11.5 μm. For X56 and X60 nearly the grain distribution indicates
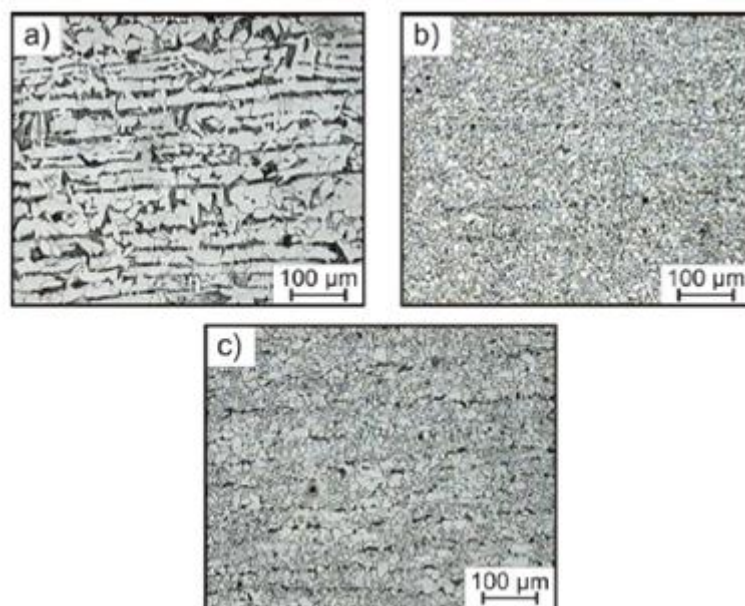
Figure 4.33: Microstructure of a longitudinal section of steel X-52 (a), X-56 (b) and X-60 (c).
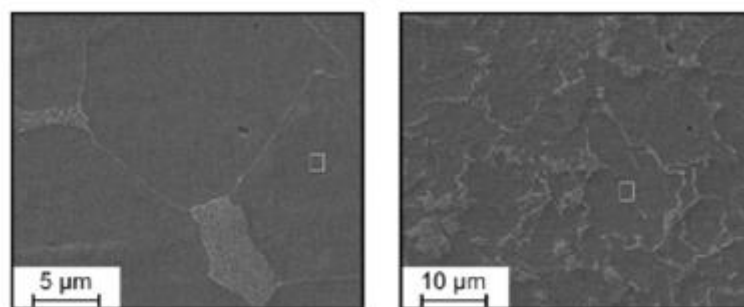
Figure 4.34: Comparison of Raster Electron microscopy image of the sample X52-L(left) and X56-L (right).

nearly no texture (See Figures 4.33 b,c). The inclusion level of sulphurs, aluminates, silicates and globular oxides from the three studied steels were determined using the method in the standard ASTM E 45 [127].

The microstructure as well as the local composition of grains was studied also using a raster electron microscope (Quanta 3D 200) with EDX. EDX gave local variations of the Mn as well as Si concentrations. EDX analysis revealed an in-homogeneous distribution of the additive elements. Especially carbon found at the gain boundaries. As an example Figure 4.34 depict a comparison of grain structure of the sample X52-L and X60-T.

Figure 4.35 compares a topological picture of the steel X52 as well as a domain structure as observed by the MFM. The domains have approximate width of 2μm, which is significantly smaller than the grain size, indicating the magnetic material with low coercivity.
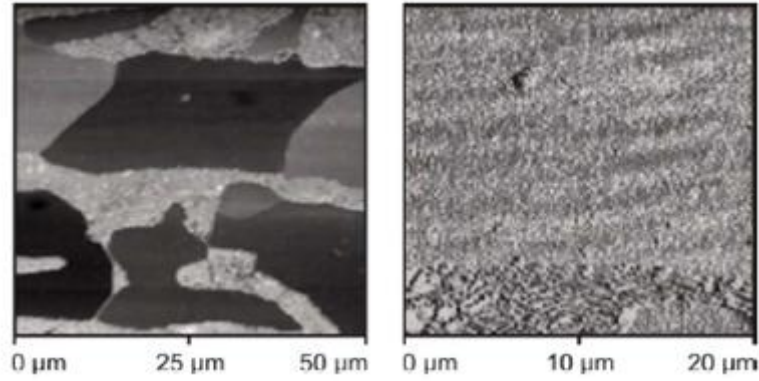
Figure 4.35: AFM (left) and MFM (right) picture of the steel X-52 - transversal direction.
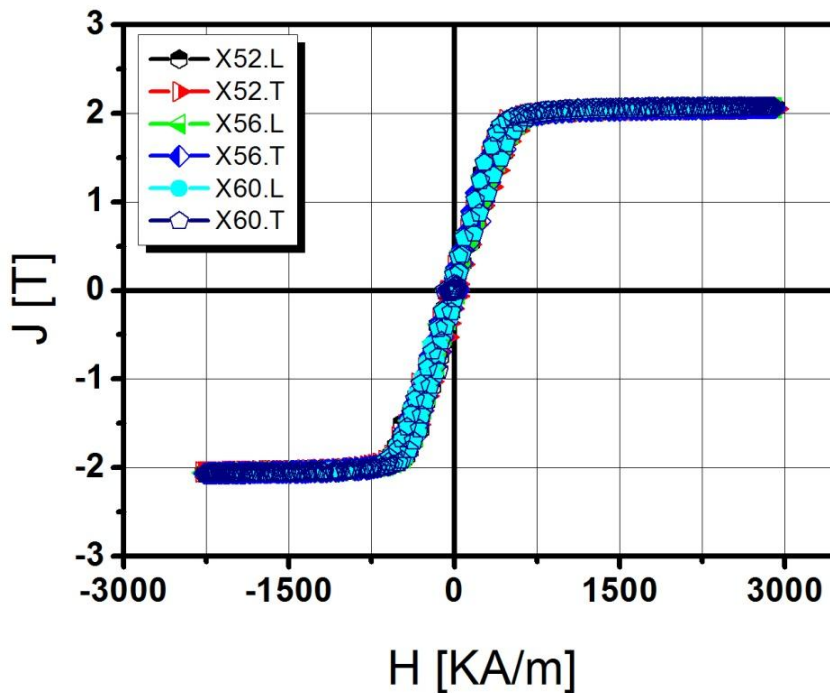
Figure 4.36: Room temperature hysteresis as performed on the steel samples X-52, X-56 and X-60.

4.7.3 Magnetic Measurements

4.7.3.1 Hysteresis

In order to determine the saturation polarization of the steel samples hysteresis measurements were performed with a Hirst pulsed field hysteresograph (measurement setup shown in Figures 3.7 and 3.8) applying a maximum field of 5T. These measurements were performed on the cubic samples. Figure 4.36 depicts the corresponding hysteresis loops.

For low fields the J(H) curve has a slope which is defined by the demagnetizing field of the sample which is roughly 550 kA/m for these cubes. Within the experimental error (± 0.01T) the saturation polarization for all steel samples is within 0.5% of the same value
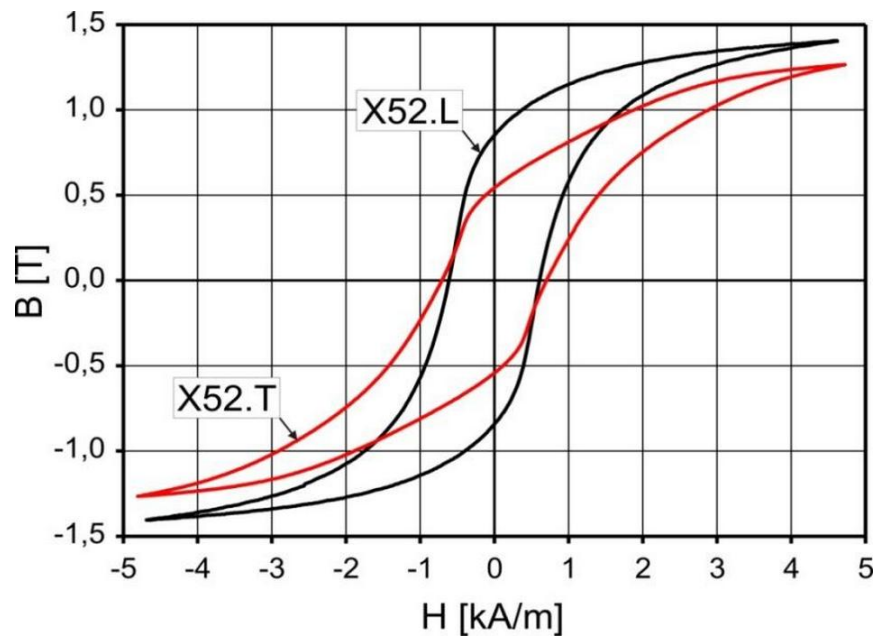
Figure 4.37: Hysteresis loops of X52-steel sample.
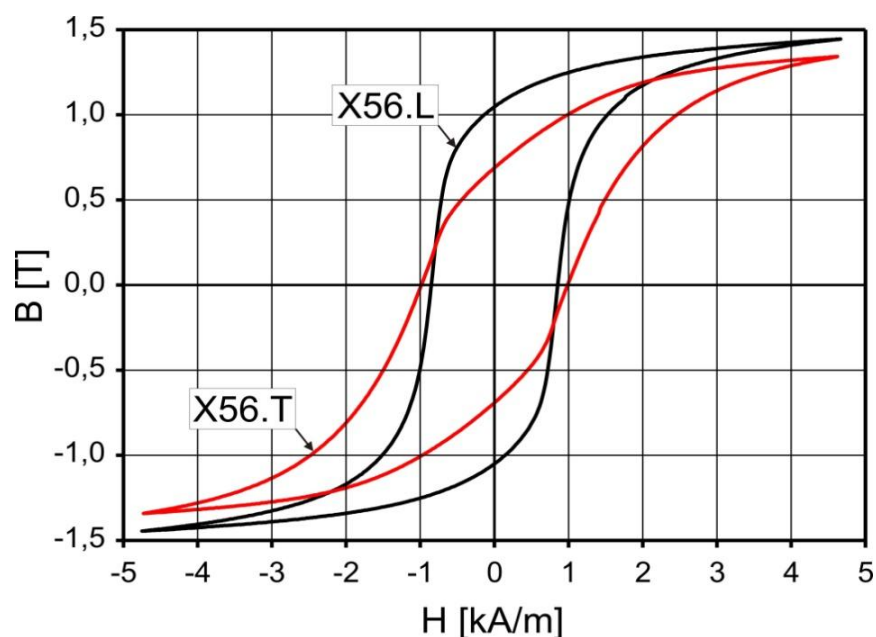
Figure 4.38: Hysteresis loops of X56-steel sample.

(2.07 T). It is 2% smaller than that of pure Fe, which agrees with the iron content of 98% of the steel samples. The hysteresis was measured in all three axis of the cube. However, due to the high demagnetizing factor no direction dependent differences were recognized. Figures 4.37, 4.38 and 4.39 compares the hysteresis loops of the longitudinal samples to the transversal ones measured according to the arrangement shown in Figure 3.9 in longitudinal ("L") and transversal ("T") direction at room temperature. The texture is most pronounced for the sample X-52 which is in agreement with the microstructure (see Figure 4.33).

Table 4.7 summarizes coercivity and remanence values (accuracy 1%) as obtained from
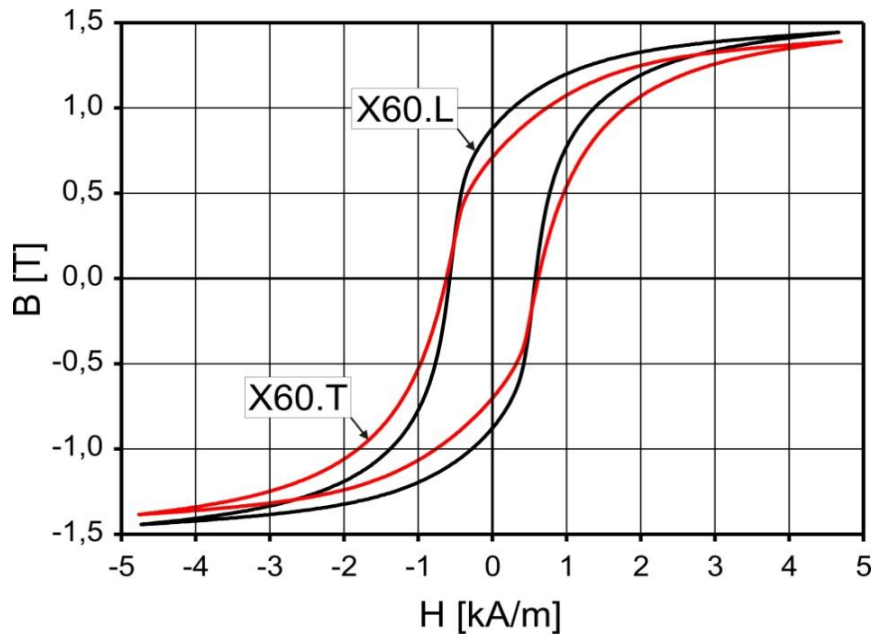
Figure 4.39: Hysteresis loops of X60-steel sample.

Steel	H_c(A/m)	J_r(T)
X-52L	614	0.85
X-52T	708	0.54
X-56L	855	1.05
X-52T	982	0.69
X-60L	578	0.88
X-60T	620	0.70

Table 4.7: Coercivity and remanence values as obtained from the pipeline Steel samples. L. . . longitudinal, T. . . ..transversal.

the hysteresis loop measurements of Figures 4.37, 4.38 and 4.39. The remanence values gained in parallel (L) and perpendicular (T) to the pipe axis differ strongly. The ratio of (remanent polarisation, saturation polarisation) is distinctly below the theoretical value of 0.75 for a cubic isotropic material. These facts strongly indicate the presence of a texture.

4.7.3.2 Magnetostriction

Figure 4.40 shows the longitudinal room temperature magnetostriction as measured on the samples X-52-L and X-52-T. The magnetostriction values are between 5 and 10 ppm being typical for polycrystalline Fe (measurement setup shown in Figure 4.46). The higher value of the magnetostriction in the transversal case may also explain the shape of hysteresis loop caused by magnetoelastic contribution. The magnetostriction curves for the sample X-56 show a nearly zero magnetostriction and also for the X-60 material a rather low magnetostriction value was found (see Figure 4.41). This behavior is in good agreement with the microstructure (see Figures 4.33 and 4.34) as well as with the shapes of
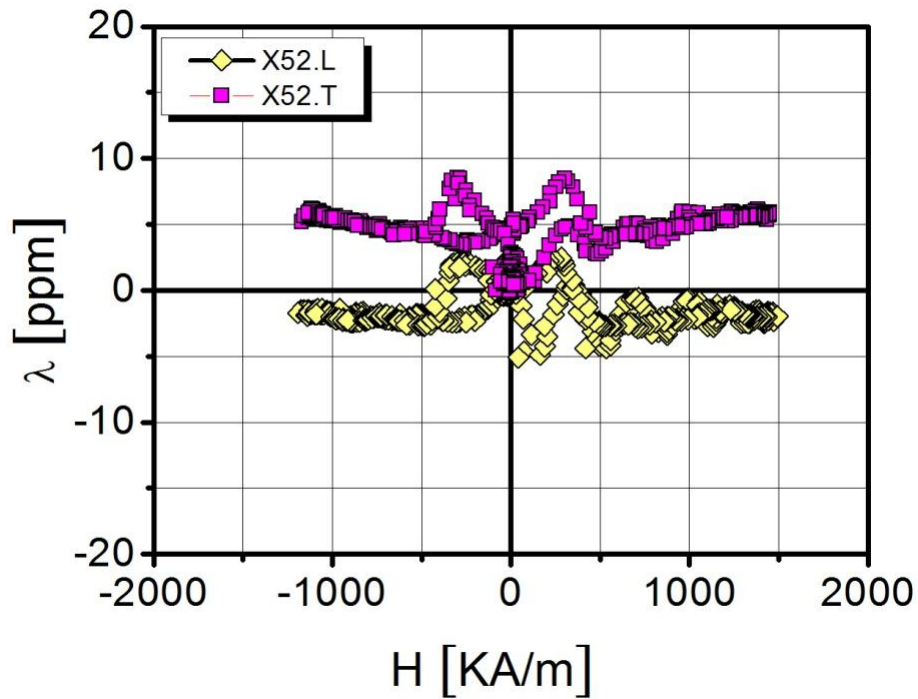
Figure 4.40: Longitudinal magnetostriction measured on the steel X-52-L and X-52-T at room temperature.

the hysteresis loops.
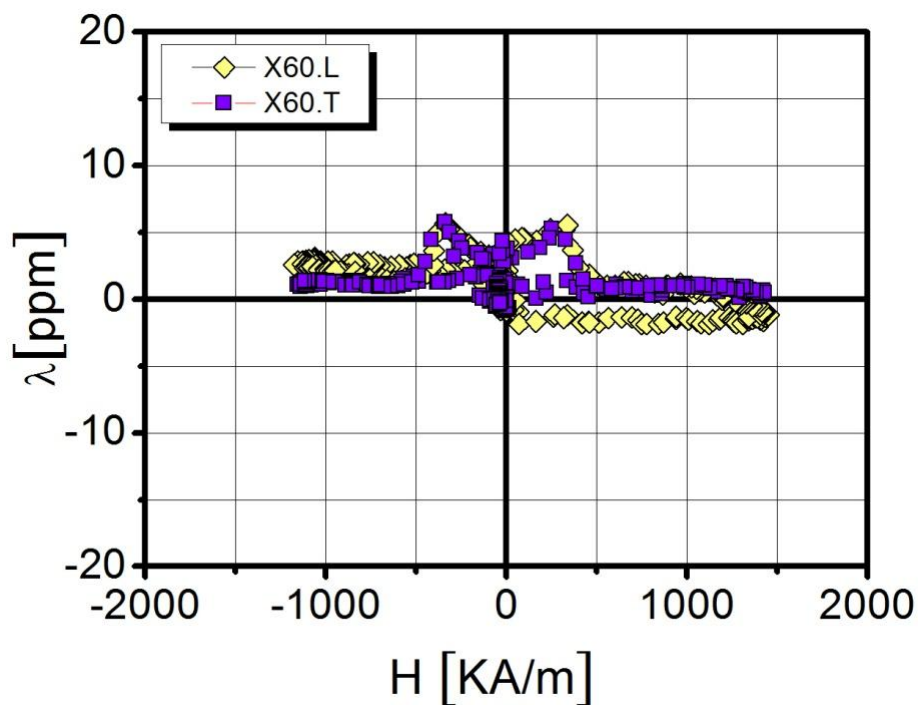
Figure 4.41: Longitudinal magnetostriction measured on the steel X-60-L and X-60-T at room temperature.

4.8   Cobalt Ferrite (CoFe$_2$O$_4$) [116]

Polycrystalline Co-ferrite was produced using different routes such as: ball milling, modified citrate-gel method, fluoride modified citrate-gel method and combustion method. All samples were afterward heat treated.

The purpose of the present work is to produce polycrystalline CoFe$_2$O$_4$ powders by several techniques in order to obtain the highest possible magnetostriction together with high strain derivative, which may lead to a high magneto electric effect in composites. Additionally, investigations of the influence of different production methods on the structural and magnetic properties were performed.

Figure 4.42 shows XRD patterns (Cu-Kα) of annealed Co-ferrite samples produced by the different methods. All samples showed sharp diffraction peaks where a Rietveld refinement gave generally a single-phase cubic inverse spinel structure of cobalt ferrite with a lattice constant close to 8.37x 10^{-10}m.
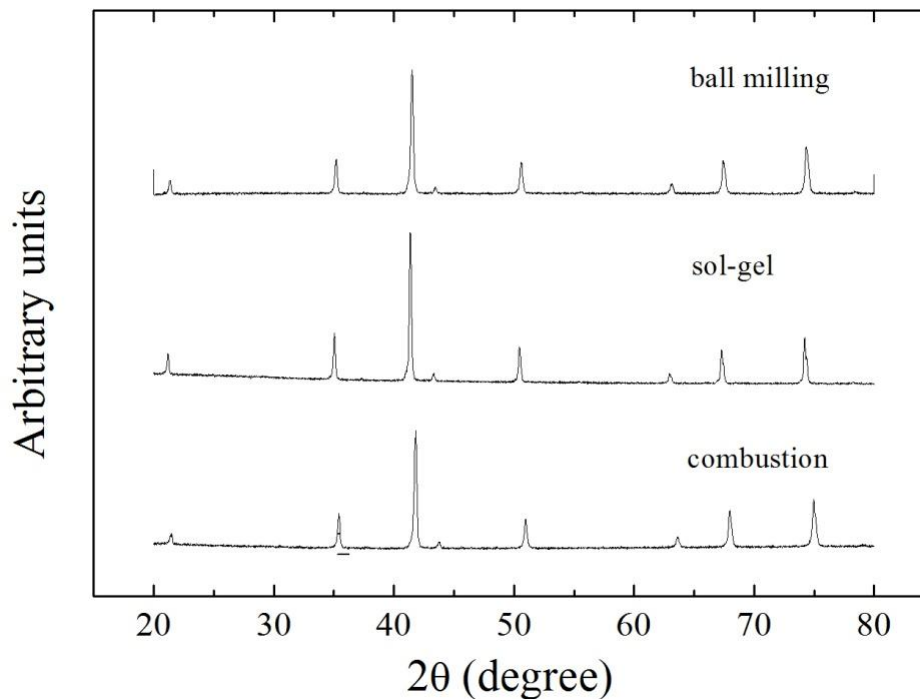
Figure 4.42: X-ray diffraction pattern of heat treated Co-ferrite produced by different methods.

The citrate-sol-gel method delivers a single phase CoFe$_2$O$_4$ pattern even in the as-produced state as well as after a heat treatment (1000°C, 5h), however for the samples produced by other methods, the spinel structure is formed only after annealing. The sample produced by fluoride modified citrate-gel method shows an impurity (about 7%) of CoO, the sample produced by the combustion method exhibit a significant lower lattice constant ($a_0 = 8.31$x10^{-10}m). The mean grain size of all annealed samples estimated by the fit procedure is 260 nm (BM2), 290 nm (CB) and 110 nm (FSG).
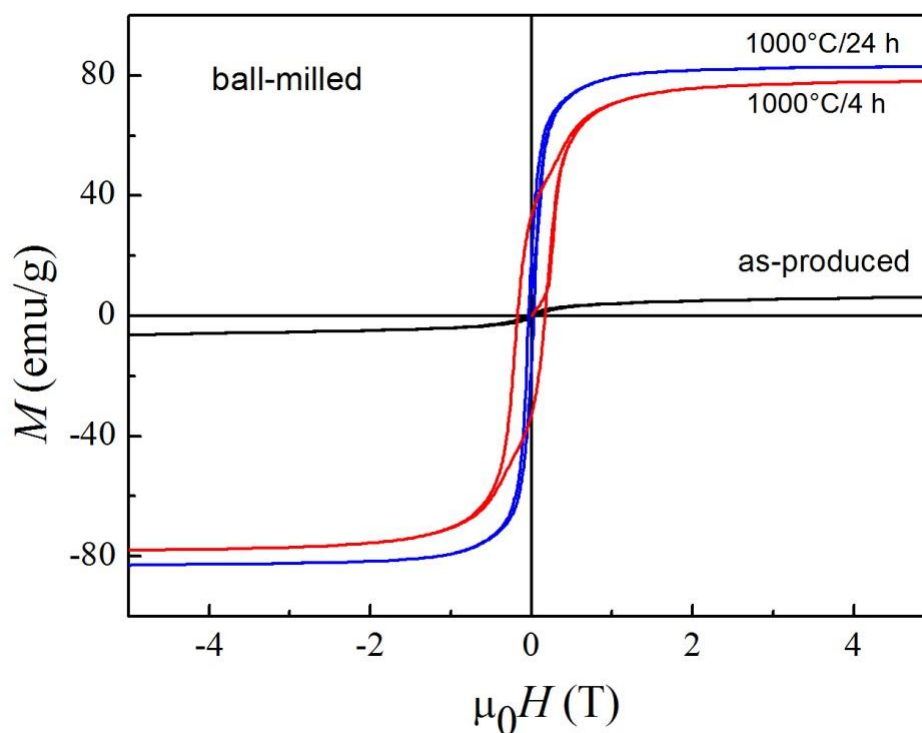
Figure 4.43: M(H) measured on BM samples in the as cast state, and after heat treatments (in air) at 1000°C for 4h and for 24h [128].

Room temperature hysteresis loops of the BM powders as-produced and after annealing at 1000 °C for 4 h and 24 h are shown in Figure 4.43.

The saturation magnetization (M$_S$) of the as-produced sample is as small as 6 emu/g and exhibits a coercivity (H$_C$) of about 450 Oe. The small saturation magnetization may be due to ferrimagnetic Fe$_2$O$_3$, which is well known to exhibit a low saturation magnetization. After a heat treatment at 1000 °C for 4 h, the coercivity, H$_c$, and the saturation magnetization, M$_s$, increase strongly. The values of H$_c$ and M$_s$ are 1700 Oe and 78 emu/g, respectively. However for the sample annealed at 1000°C for 24 h, the saturation magnetization increases up to 83 emu/g whereas the coercivity decreases to 322 Oe. The apparent difference in the values of M$_s$ and H$_c$ may be due to structural refinements as well as an increase of the grain size. The M$_s$ values correspond to the already well known saturation magnetization of pure Fe$_3$O$_4$. Figure 4.44 shows the room temperature hysteresis loops of Co-ferrite produced by different wet-chemical methods: SG, FSG and CB methods after the heat treatment described above.

Also here the achieved saturation magnetization is between 82 and 83 emu/g which is typical for pure Co-ferrite. Only the by combustion method produced material exhibit a significant lower magnetization value (61 emu/g). Figure 4.45 shows the low field behavior of the hysteresis loops, that is, the central part of the hysteresis loops shown in Figure 4.44. The corresponding coercivity values can be found in Table 4.8. The longitudinal magnetostriction, λ, measured at room temperature (measurement setup shown in Figure
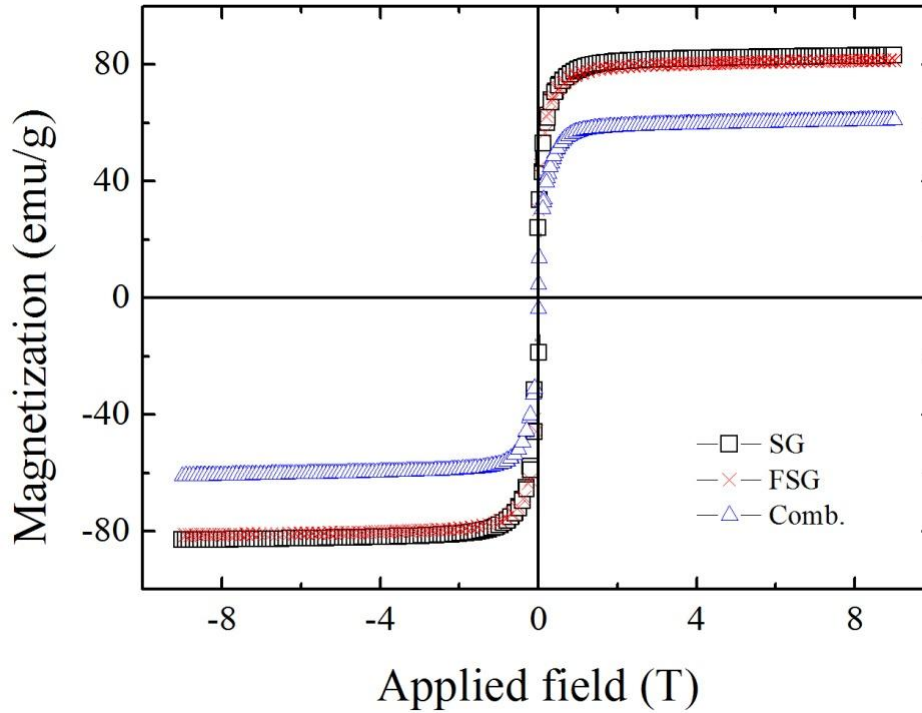
Figure 4.44: M(H) as measured on $CoFe_2O_4$ produced by: sol-gel, fluoride modified citrate-gel and combustion method; heat treatment: 1000°C/5h for SG, for FSG and Comb., respectively.

4.46) on annealed at 1000 °C for 4 and 24 h ball milled $CoFe_2O_4$ samples is shown in Figure 4.47 . The values of λ of these two samples are similar: 126 ppm and 122 ppm, respectively. However, as can be seen in the picture, the slope $d\lambda/dH$ becomes significantly larger after 24h of heat treatment. The $d\lambda/dH$ values are listed in Table 4.9.

Figure 4.48 shows the longitudinal magnetostriction (measurement setup shown in Figure 4.46) measured on the annealed samples produced by SG, FSG and CB methods after the heat treatment described above. Here the first two methods deliver typical magnetostriction value for Co-ferrites, whereas the magnetostriction of the sample produced by CB method gave a small λ (similar as M_s) of 30 ppm.

Sample	Annealing	M_s(emu/g)	H_c(Oe)
BM1	1000 °C/4h	77	1700
BM2	1000 °C/24h	83	320
SG	1000 °C/5h	83	530
FSG	1000 °C/5h	82	485

Table 4.8: Saturation magnetization and coercivity of the annealed BM, SG, FSG and CB samples.
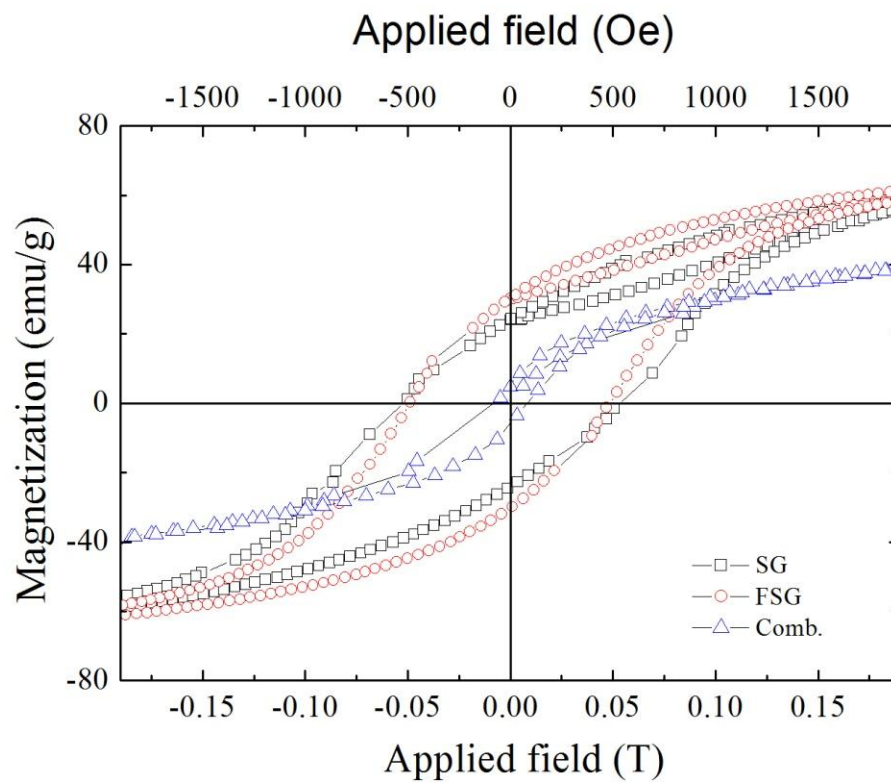
Figure 4.45: Central part of the hysteresis loops shown in Figure 4.44.
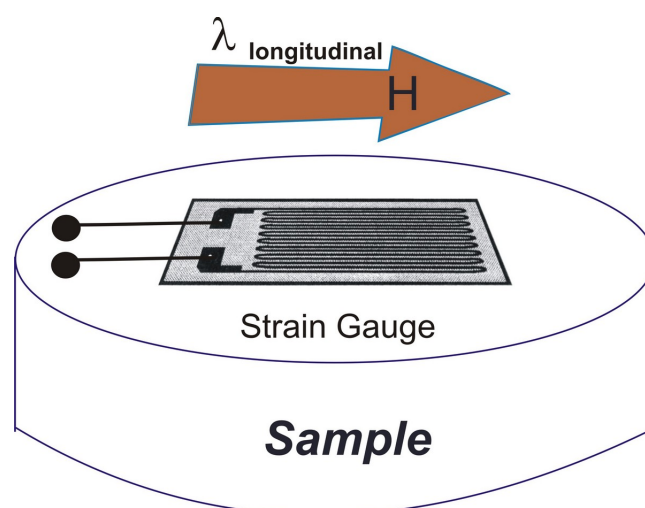
Figure 4.46: Longitudinal magnetostriction measurement set up.
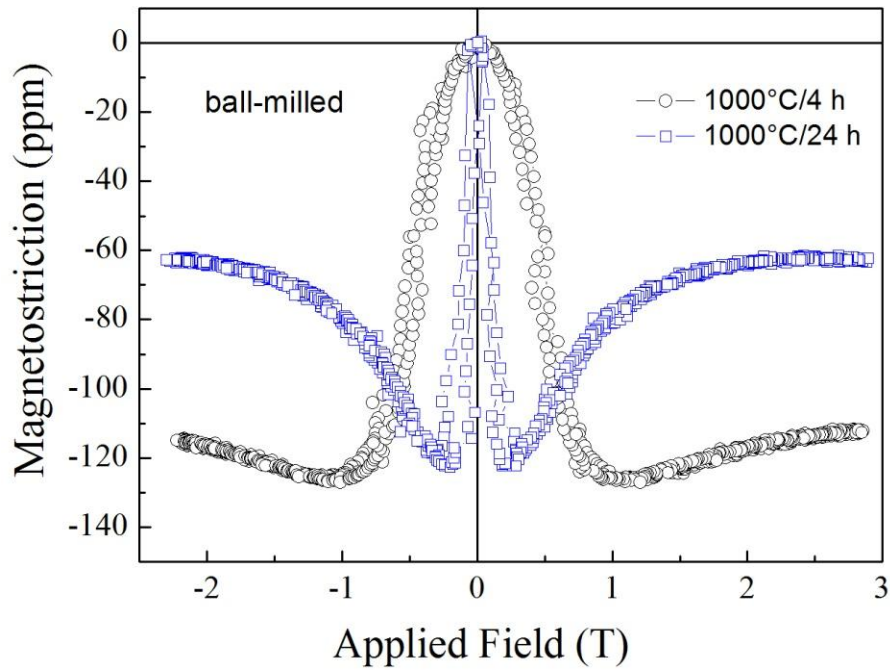
Figure 4.47: Linear magnetostriction measured on the ball milled samples annealed at 1000 °C for 4 and 24 h [128].
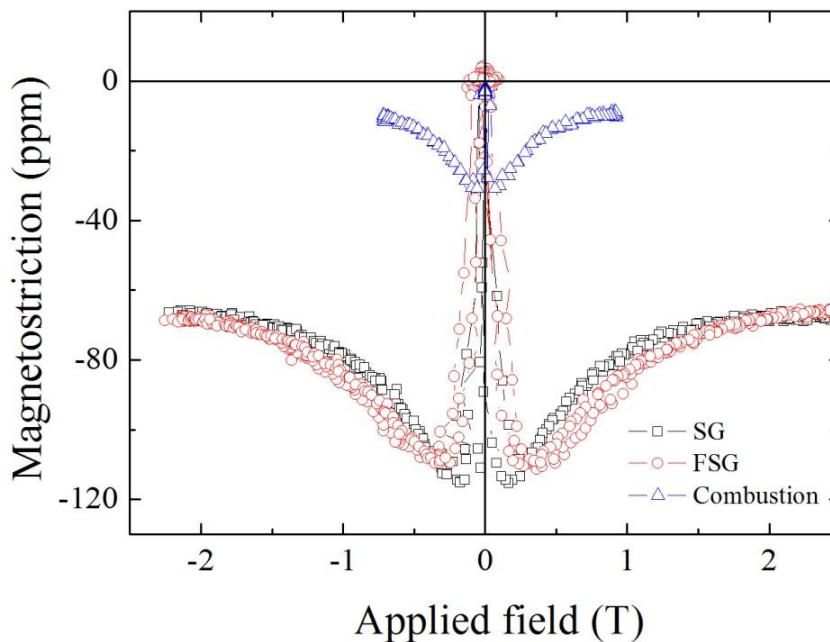
Figure 4.48: Linear magnetostriction measured on annealed samples produced by: SG, FSG and CB methods.

Sample	λ (ppm)	dλ/dH(ppm/T)	λ.dλ/dH (ppm^2/T)
BM1	126	126	15870
BM2	122	581	70876
SG	105	639	73472
FSG	110	319	36139
CB	30	375	11250

Table 4.9: Linear magnetostriction, dλ/dH and λ.dλ/dH of the annealed BM, SG, FSG and CB samples.

Table 4.8 summarizes the magnetic data and Table 4.9 the magnetostriction data as achieved for our samples of polycrystalline CoFe$_2$O$_4$ at room temperature. The values of dλ/dH determined between zero and the maximum value of magnetostriction as well as λ.dλ/dH are also listed in Table 4.9 because of their importance for the application as sensors and also in magnetoelectric composites.

4.9 Magnetostriction in Sol Gel Cobalt Ferrite as a Function of Annealing Temperature

A systematic study performed to understand the effect of processing conditions and annealing temperature on the magnetostrictive properties of $CoFe_2O_4$ produced by modified citrate sol gel method. Such study can be used for optimizing the process parameter of magnetostrictive materials based on Cobalt Ferrite.

4.9.1 Microstructure

Figures 4.49 and 4.50 shows the microstructures of the pellets annealed at 500°C and 1000°C for 5 hr in air at magnification scales i.e. 1 μm and 2 μm. Systematic microstructural changes are observed with increasing annealing temperature, Figure 4.53 shows variation of crystallite size as a function of annealing temperature. The samples sintered at 500°C show the presence of small particles in the form of agglomerates. The SEM micrographs show that the particle size increases drastically when the annealing temperature is 1000°C, ferrite particles are of uniform size with roughly spherical shape, some of them are found to be agglomerated. Larger pores are seen in the micrographs of the samples annealed at 1000°C, such increase in the porosity when sintered at higher temperatures has been observed in the case of other ferrites and this is due to the release of oxygen from the spinel lattice [129].

(a) 2μm   (b) 1μm
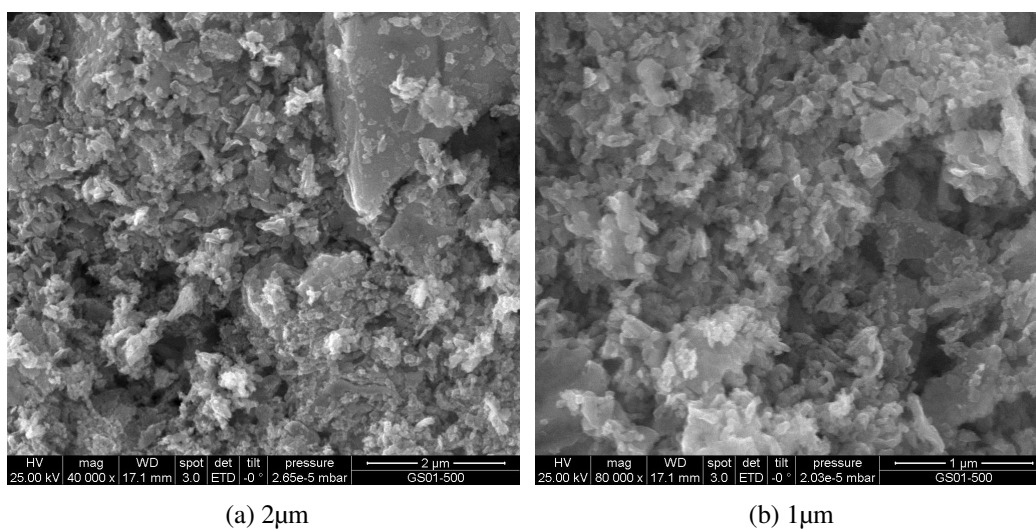
Figure 4.49: SEM micrographs of sol-gel $CoFe_2O_4$ sintered at 500°C/5hr in air at resolution 2μm and 1μm.

(a) 2μm

(b) 1μm
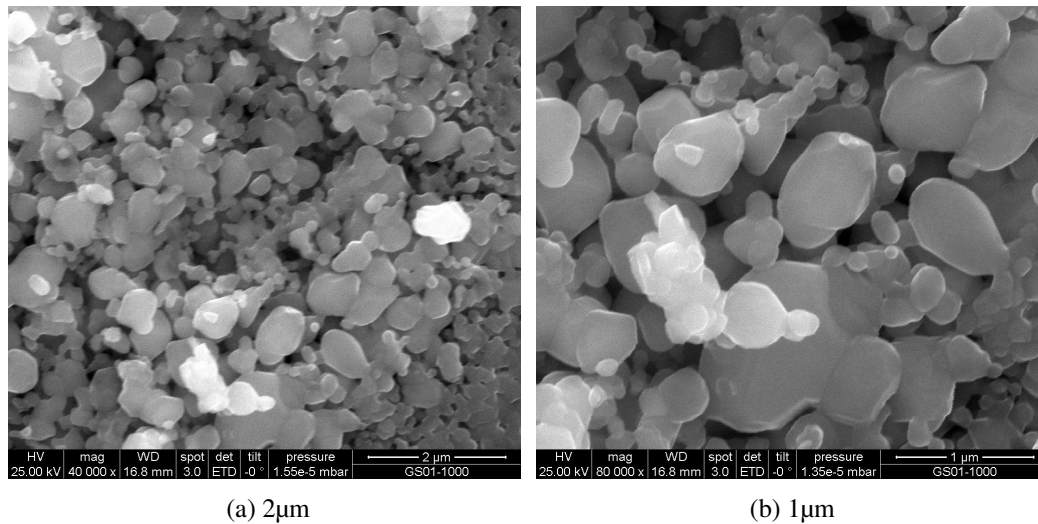
Figure 4.50: SEM micrographs of sol-gel CoFe$_2$O$_4$ sintered at 1000°C/5hr in air at resolution 2μm and 1μm.

4.9.2 XRD Data Analysis

The X-ray diffraction patterns of all the samples are shown in Figure 4.51. The XRD pattern of as synthesized particles shows very broad peaks, indicating the ultrafine nature and small crystallite size particles. The XRD of samples shows improvement in the sharpness and intensity of peaks with increasing annealing temperature.
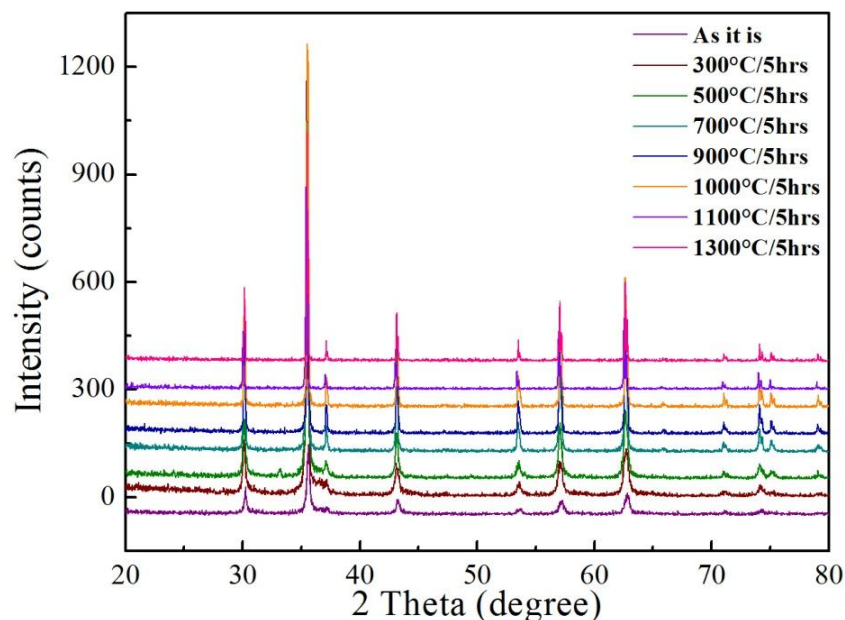
Figure 4.51: X-ray diffraction spectra (Cu- Kα radiation) of CoFe$_2$O$_4$, as prepared, sintered at 300°C, 500°C, 700°C, 900°C, 1000°C, 1100°C and 1300°C in air for 5 hr.

X-ray diffraction pattern was indexed by TOPAS program to in order to calculate di-
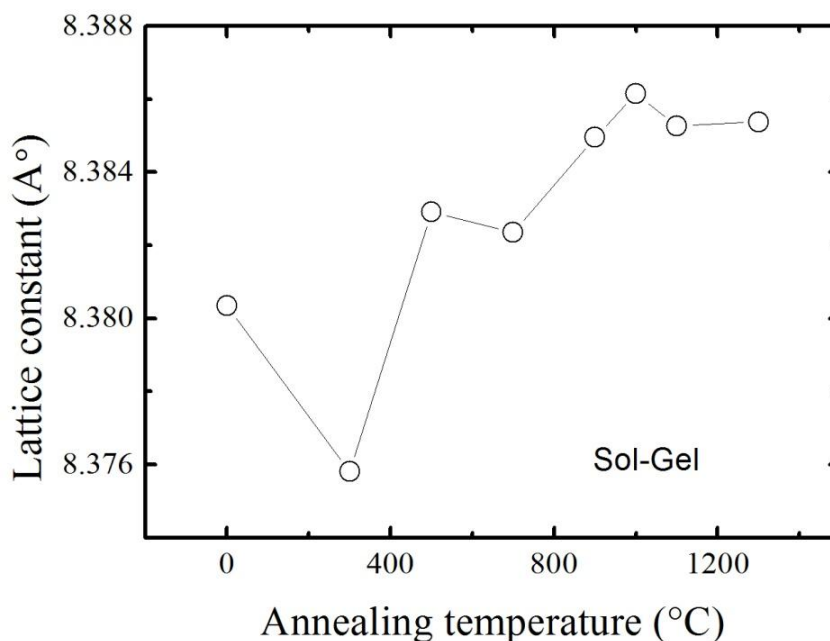
Figure 4.52: Variation of lattice constants (A°) as a function of annealing temperature.

mension of unit cell. Refinement of X-ray data shows that samples are composed of 100 % spinel structure, no additional peaks and impurity phases were found. Figure 4.52 shows the variation of lattice constants, as a function of annealing temperature. The lattice constant is found to be sensitive to the sintering temperature. This fact could be more easily seen from SEM images in Figures 4.49 and 4.50, the SEM image shows bulky aggregates of rough surface. On increasing sintering temperature, more regular, uniform particles developed. The lattice constant of sample sintered at 300°C decreases to value 8.37581A°, as compared to lattice constant 8.38035A° of as prepared sample, without annealing. For annealing temperature 500°C, 700°C, 900°C, 1000°C lattices constant shows almost linear increase as function a annealing temperature, whereas for 1100°C and 1300°C lattice constant becomes nearly constant i.e. 8.38527A° and 8.38538A° respectively (see Figure 4.52).

4.9.3   Magnetization and Magnetostriction Measurements

Figure 4.54 shows comparison of the room temperature magnetization curves of as prepared, annealed at 300°C, 500°C, 700°C, 900°C, 1000°C, 1100°C and 1300°C powders samples. The saturation magnetization of samples much improved from 61 emu/g of as prepared sample to 84 emu/g of sample annealed at 1300°C systematically. The saturation magnetization value $\sim$ 84 emu/g is comparable to the values reported in literature [130].

However there is continuous decrease in coercivity with increase of annealing temperature up to 1300°C (see Figure 4.57), this is due to increase of crystallite size, also can be seen from SEM micrographs. Figure 4.58 shows plot of coercivity H_c as function of
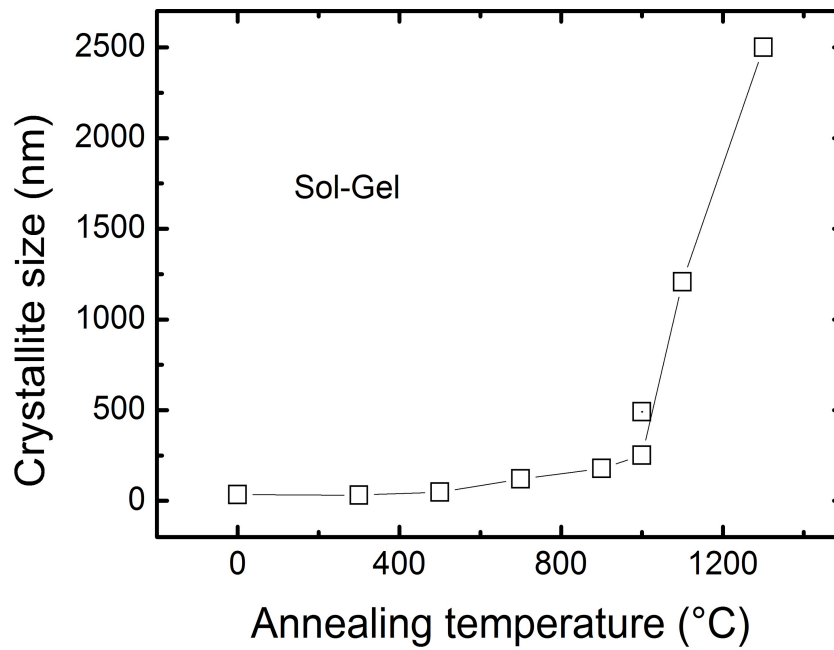
Figure 4.53: Crystallite size (nm) as a function of annealing temperature.
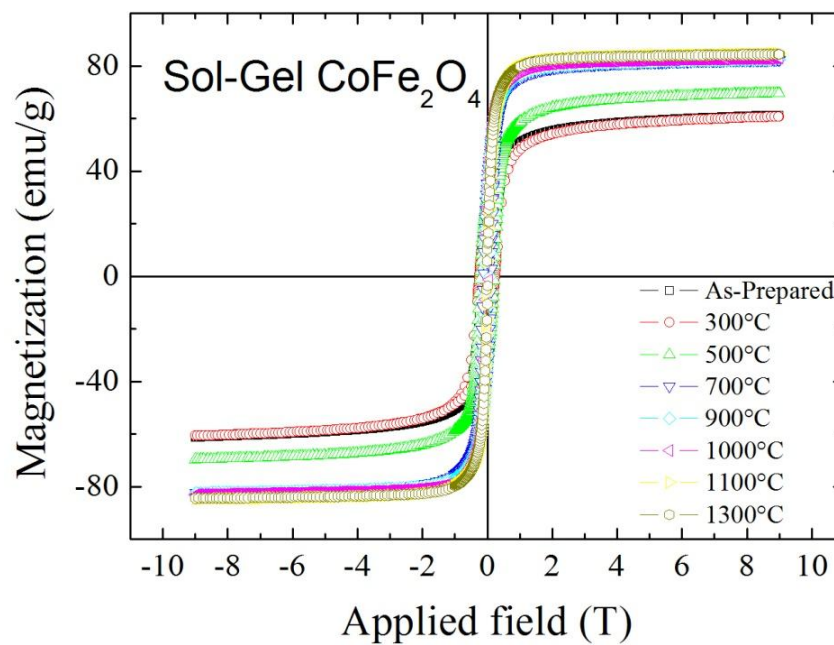
Figure 4.54: Hysteresis loop measured (at room temperature) of as prepared and the samples sintered at different temperatures.
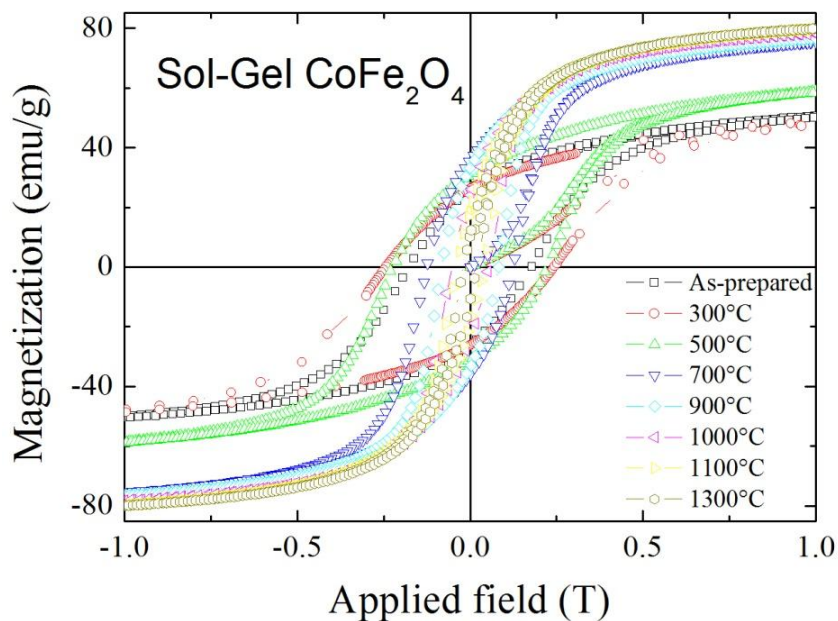
Figure 4.55: Central part of hysteresis loop, shown in Figure 4.54.
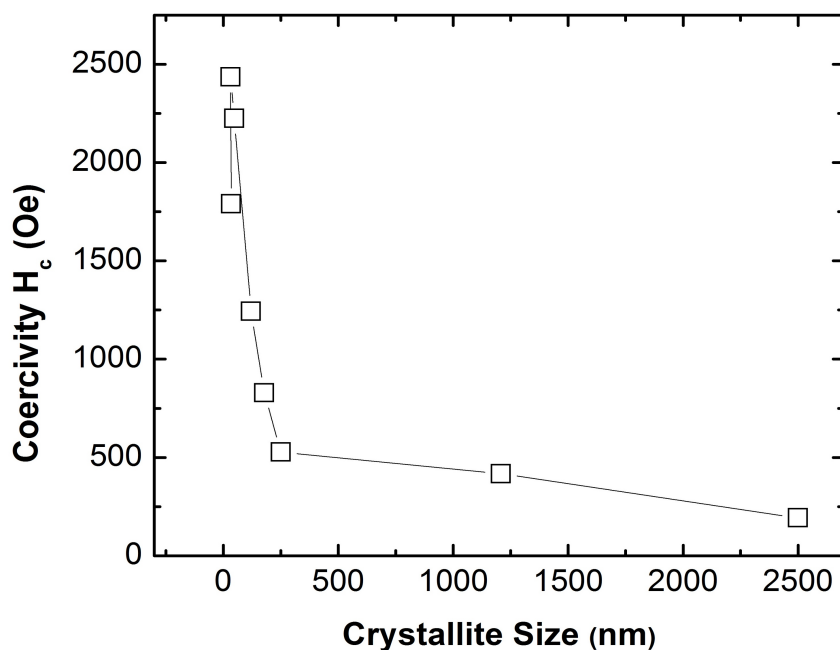
Figure 4.56: Coercivity (Hc) of as a function of crystallite size.

crystallite size.

Figure 4.58 shows plot of saturation magnetization M_s as function of crystallite size. Saturation magnetization increases significantly with crystallite size from 34 nm (61.3 emu/g) to 120 nm (82.4 emu/g) after this no significant change in magnetization observed in magnetization with increase of crystallite size 2500 nm (84.6 emu/g).

Figure 4.59 shows the magnetostriction as function of magnetic field measured up to maximum field 3 Tesla (measurement setup shown in Figure 4.46). It can be see the value
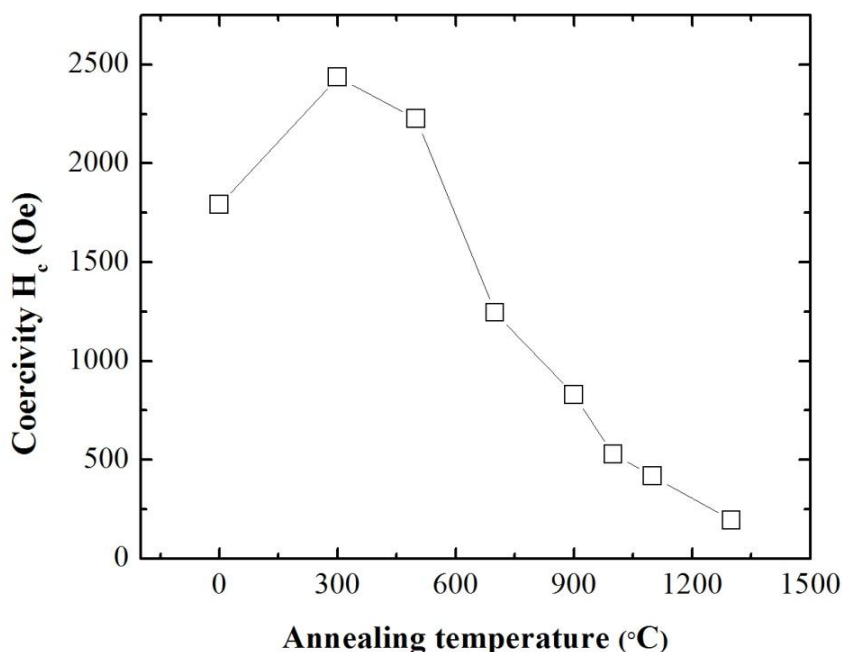
Figure 4.57: Coercivity (Hc) of as a function of annealing temperature.

of magnetostriction strongly depends on annealing temperature and increases consistently with increase in annealing temperature from 300°C to 1100°C. Maximum magnetostriction close to $\sim$-124 ppm is obtained for the sample annealed at 1100°C and decreases to lower value i.e.$\sim$-114 ppm with further increase in annealing temperature to 1300°C. In Figure 4.60 magnetostriction plotted as a function of crystallite size. Magnetostriction increases with increase in crystallite size and reach to maximum value 124 ppm at crystallite size 1.2 µm, after this for the sample annealed at 1300°C having crystallite size 2.5 µm magnetostriction decreases to 114 ppm. Similarly Figure 4.61 shows variation in magnetostriction with respect to lattice constant. The sample annealed at 1000°C having lattice constant (8.38615A°) and at 1100 °C having lattice constant (8.38527 A°) have 119 ppm and 124 ppm respectively. For the sample annealed at 1300 °C lattice constant slightly increases to the value 8.38538 A° as compared to the sample annealed at 1100 °C but at the overall magnetostriction value decreases 114 ppm, due to significant increase in crystallite size .

Figure 4.62 shows the plot of magnetostriction as function of coercivity, one can see that with increasing magnetostriction the coercivity increases almost linearly to the sample annealed up to at 1100 °C. This indicates that for these materials the magnetoelastic energy determines strongly the coercivity.

Table 4.10 summarizes the XRD analysis, magnetic and magnetostrictive properties of $CoFe_2O_4$ annealed at different temperature. A comparison of various parameter shows that the magnetostriction becomes highest when the saturation magnetization is larger, whereas the coercivity is found to decreasing with increase in crystallite size . However the relative change in magnetostriction of samples annealed at temperatures of 1000°C, 1100°C and
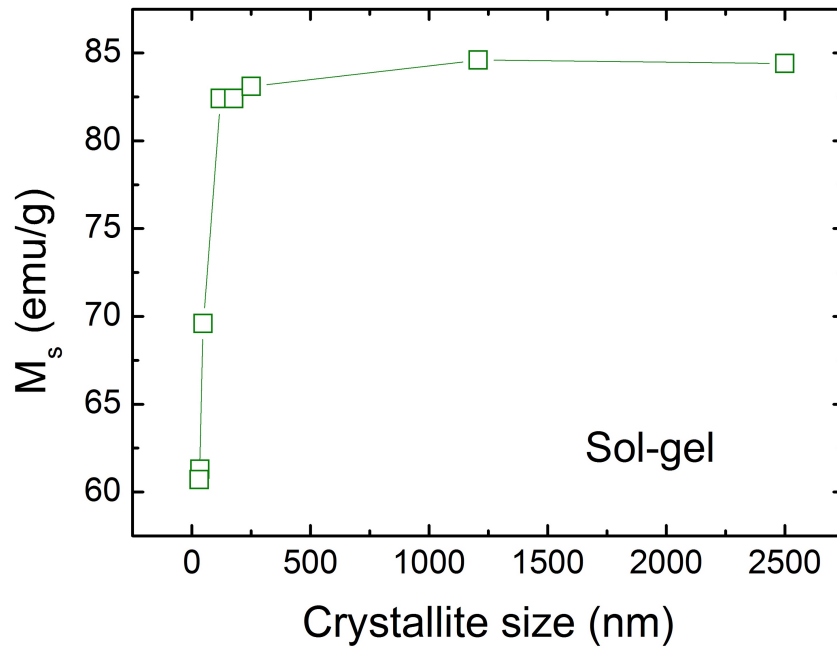
Figure 4.58: Room temperature magnetization (M) of as a function of crystallite size.
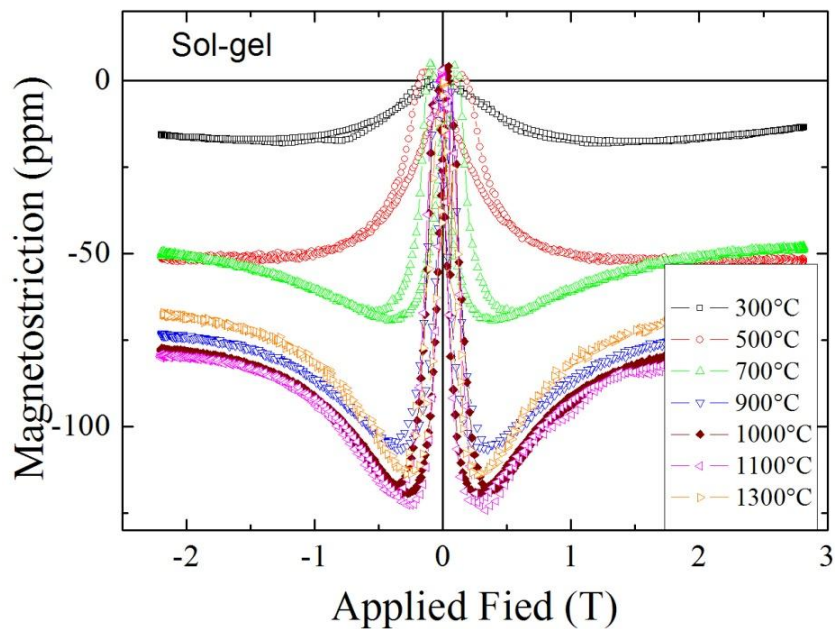
Figure 4.59: Comparison of linear magnetostriction of samples annealed at temperatures, 300°C, 500°C, 700°C, 900°C, 1100°C and 1300°C each for 5hr.
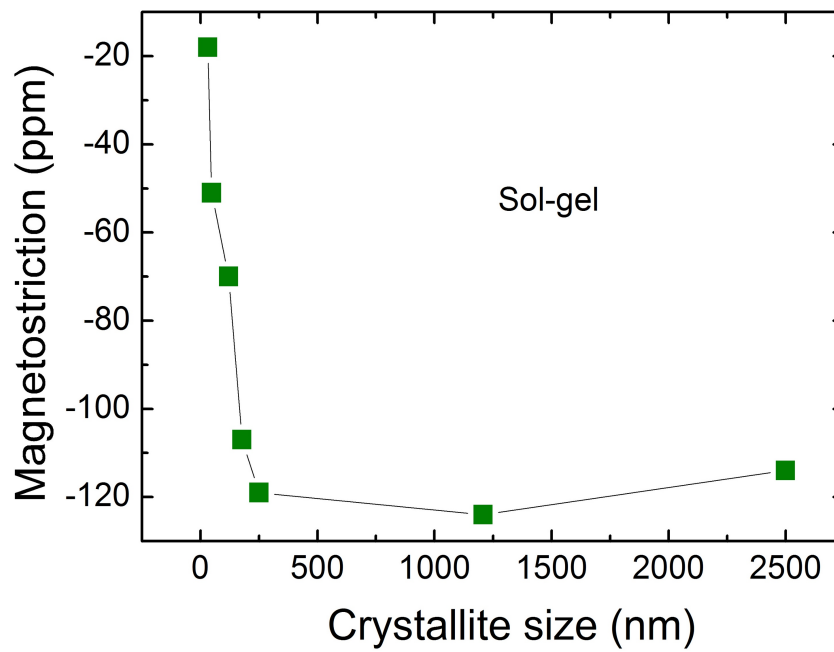
Figure 4.60: Linear magnetostriction as a function of crystallite size.
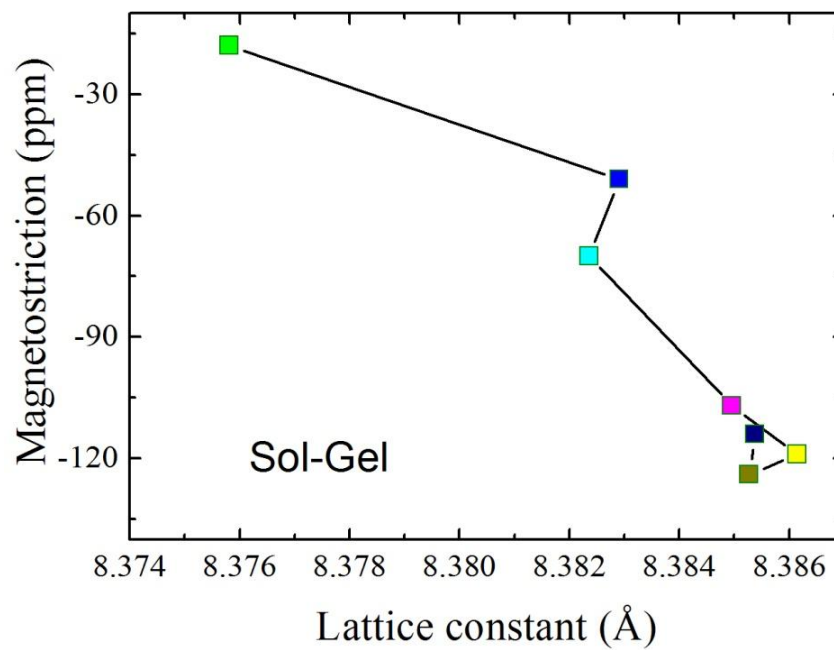
Figure 4.61: Linear magnetostriction as a function of lattice constant.
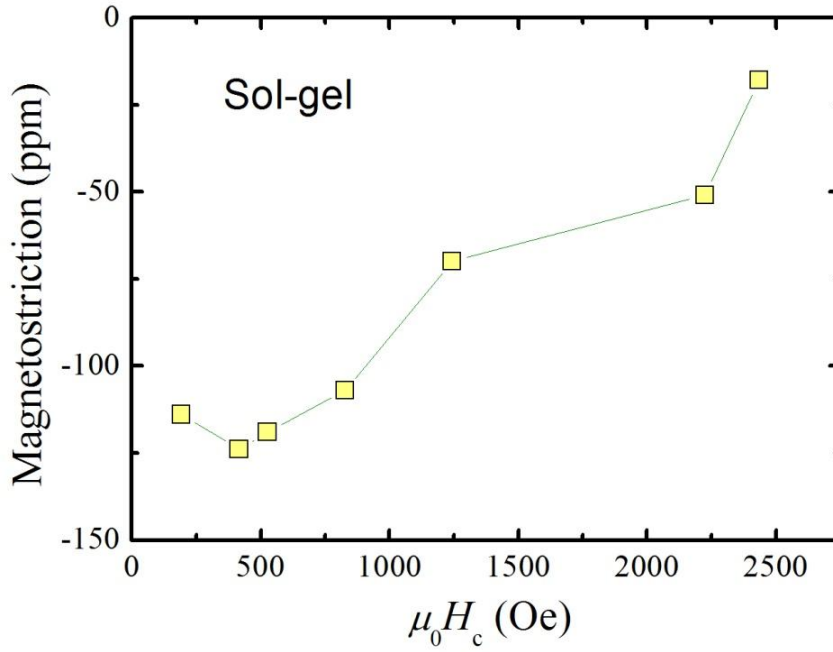
Figure 4.62: Linear magnetostriction as a function of coercivity.

Annealing Temperature (°C)	Lattice Constant (A°)	Crystallite Size (nm)	M_s (emu/g)	H_c (Oe)	$\lambda_{parallel}$ (ppm)
As it is	8.38035	34.1	61.3	1790	——
300	8.37581	31.5	60.7	2435	-18
500	8.38291	48	69.6	2225	-51
700	8.38236	121	82.4	1244	-70
900	8.38496	178	82.4	829	-107
1000	8.38615	251	83.1	527	-119
1100	8.38527	1208	84.6	417	-124
1300	8.38538	2500	84.4	193	-114

Table 4.10: Annealing temperature, lattice constant, crystallite size, magnetization, coercivity and magnetostriction parameter of sol-gel Cobalt Ferrite.

1300°C are not much large.

4.10   Magnetostriction in Cobalt Ferrite produced by Combustion Method as a Function of Burning Rate

Glycine (NH_2CH_2COOH) is considered to serve as fuel for the combustion reaction, being oxidized by nitrate ions [99]. The temperature reached in the combustion reaction has an important effect on the crystallite size of the powder resultants. By adjusting the glycine-to-nitrite ratio (G/N), we can control the reaction temperature, and thereby control the crystallite size of the $CoFe_2O_4$ powders which has huge effect on magnetic and magnetostrictive properties. A set of six samples were made with glycine to nitrate ratio 0.5:1, 1.0:1, 1.3:1, 1.5:1 and 2.0:1. In order to remove traces of residual organic compounds from as-prepared samples, all the samples were heat treated at 400°C for 2 h to decompose the residual substances completely. All the six powder samples were pressed in to the form of pellets and sintered at 1450 °C for 10 min, all the pellets were sintered under same conditions, with a heating rate of 4 °C/min and cooling rate of 20 °C/min [81]. Figure 4.63 shows the XRD patterns of the sintered pellets. A single phase spinel ferrite (space group Fd3m) is obtained after sintering all the pellets at 1450°C. There are no detectable traces of extra crystalline or amorphous phase found as it is clear from the absence of any additional reflections peak in the XRD patterns. The calculation lattice constant and crystallite size were performed on XRD data by using program TOPAS.
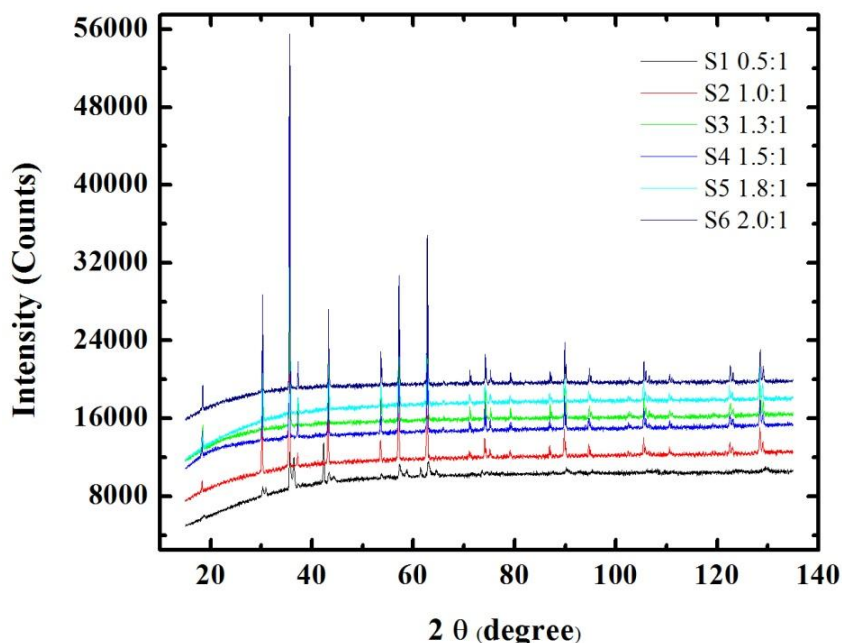
Figure 4.63: X-ray diffraction pattern (Cu- Kα radiation) of $CoFe_2O_4$, prepared by combustion method by varying glycine to nitrate ratio.

Figure 4.64 shows the crystallite size and lattice constant as a function of glycine used for preparing cobalt ferrite. The value of crystallite size increases with glycine contents up
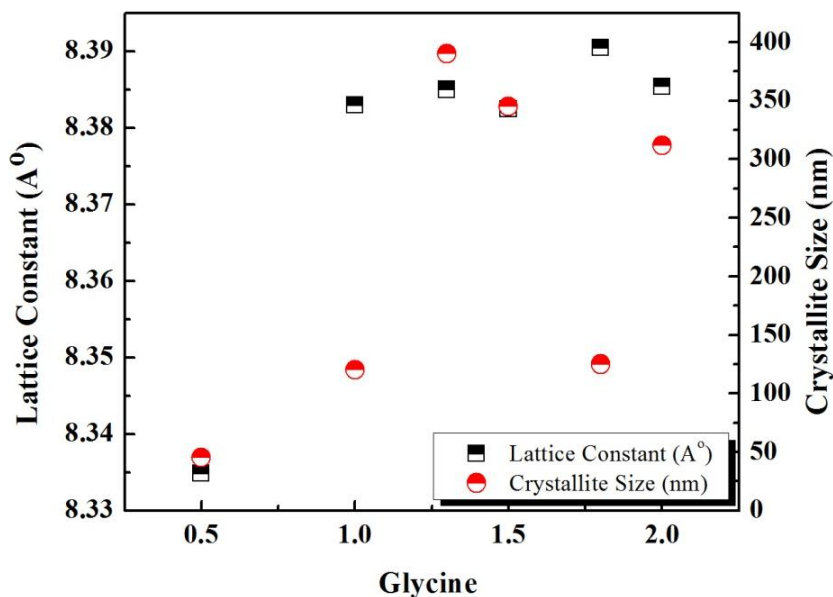
Figure 4.64: Lattice constant and crystallite size as a function of glycine used for synthesis of cobalt ferrite.

to 1.3 and then decreases for 1.5:1 and 1.8:1 and finally again increases for sample having G/N ratio 2.0:1.

Similarly with increase of glycine lattice constants increases with increase in glycine contents up to 1.3 and then decreases for 1.5:1 and increases to maximum value 8.39047A° at G/N ratio 1.8:1 and finally reaches to value 8.38537 A° after slight decrease for sample having G/N ratio 2.0:1, the variation in crystallite size and lattice constant as function of glycine content does not seen to be systematic.

Figure 4.65 shows the M-H curve of the measurements made at room temperature, whereas as Figure 4.66 shows the center part of MH loop to observe coercivity of the samples. The sample with G/N ratio 0.5:1 has saturation magnetization M_s about 51 emu/g , whereas for the remaining all the samples the saturation magnetization Ms is about 82∼84 emu/g and variation in glycine ratio has no significant effects on value of saturation magnetization.

Figure 4.67 shows plot of coercivity H_c as function of crystallite size. The coercivity of samples with G/N ratio 0.5:1,1:1 and 1.3:1 has linear relationship with crystallite size and increases with increase of crystallite size, whereas for G/N ratio 1.5:1, 1.8:1 and 2:1 it decreases and remains with in the range of 300∼400 Oe.

Figures 4.68, 4.69 and 4.70 shows the magnetostriction measured on all the sample in parallel, transverse and perpendicular to thickness of sample by strain gauge method.

Table 4.11 summarizes the lattice constant, crystallite size, magnetization, coercivity and magnetostriction and strain derivatives values measured on the all the samples with different G/N ratios.

The sample having G/N ratio 1.0:1 and 1.3:1 have maximum value of magnetostrictions
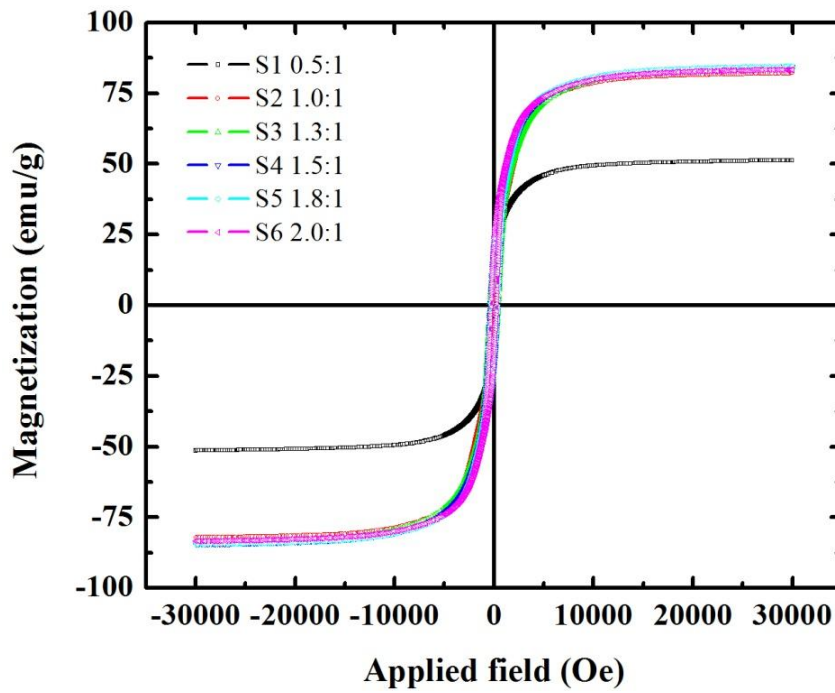
Figure 4.65: MH curve of $CoFe_2O_4$ of all samples with different nitrate-glycine ratio at room temperature.
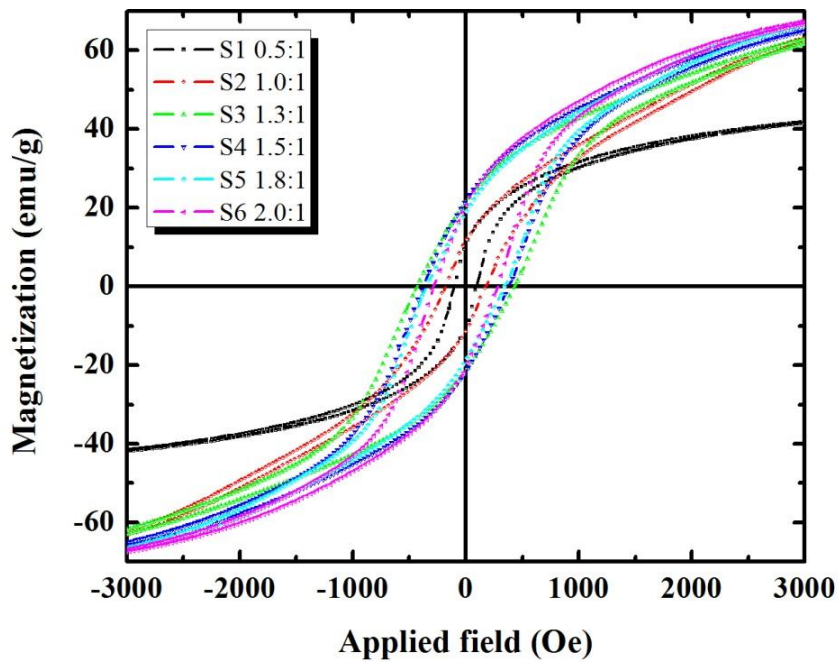
Figure 4.66: Coercivity of all samples (center part of curve shown in Figure 4.65).
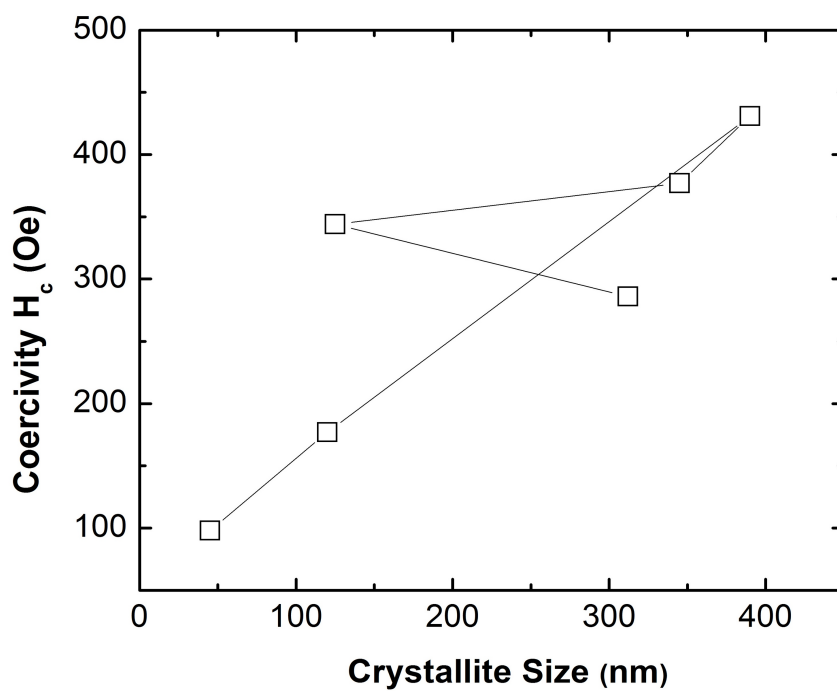
Figure 4.67: Coercivity (Hc) of as a function of crystallite size.
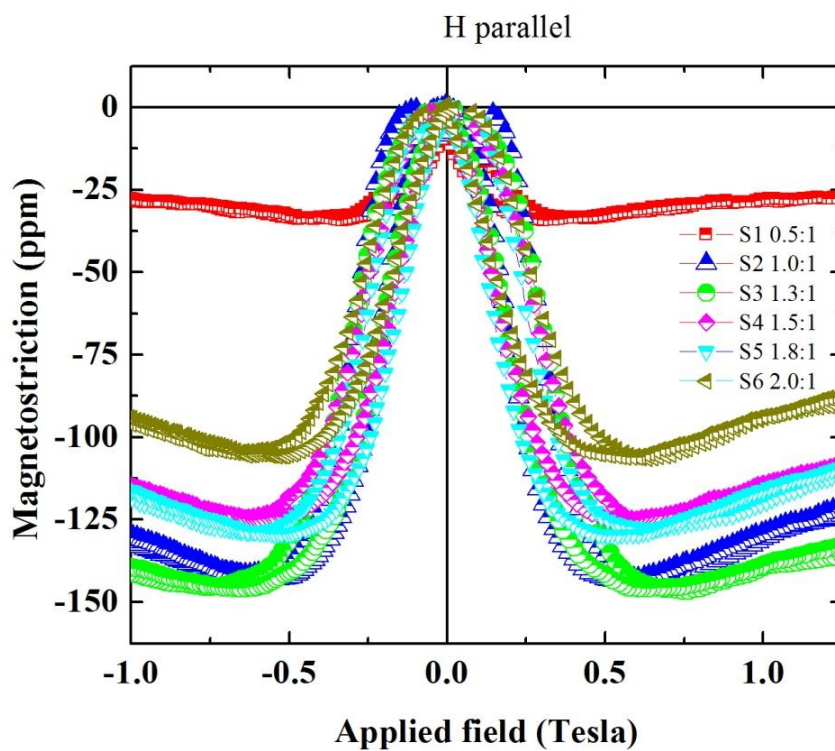
Figure 4.68: Linear magnetostriction (parallel to magnetic field) of all $CoFe_2O_4$ samples prepared with different glycine ratios.
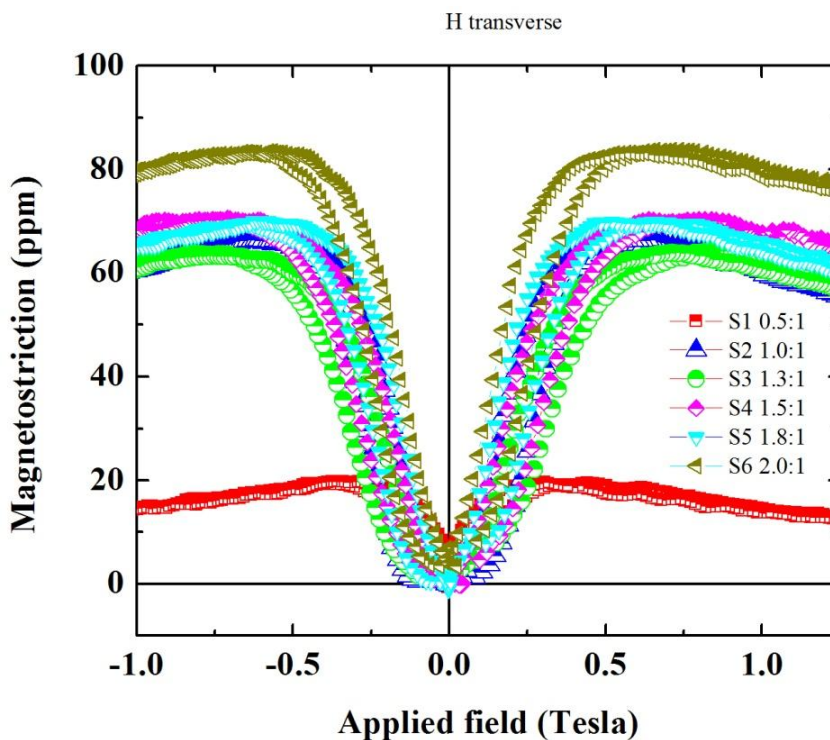
Figure 4.69: Magnetostriction (perpendicular to magnetic field) of all $CoFe_2O_4$ samples prepared with different glycine ratios.
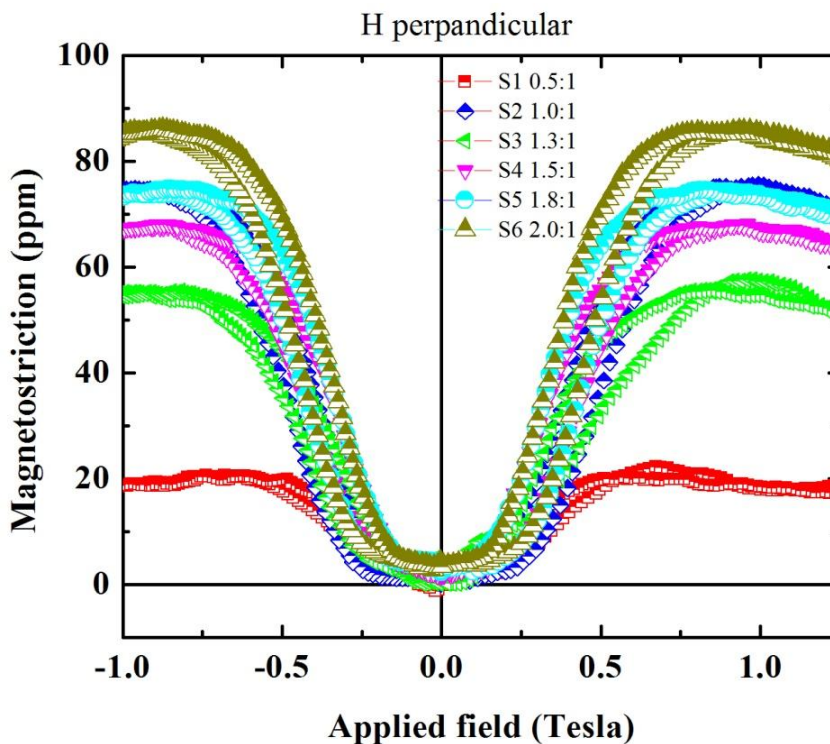
Figure 4.70: Magnetostriction (H perpendicular to the surface of sample) of all $CoFe_2O_4$ samples prepared with different glycine ratios.

Glycine to Nitrate Ratio	Lattice Const. (A°)	Cryst. Size (nm)	M_s (emu/g)	H_c (Oe)	Magnetostriction (ppm)			Strain Derivative $d\lambda/dH_{max}$ (ppm/T)
					λ_{parll}	λ_{trans}	λ_{per}	
0.5 :1	8.33485	45	51	98	-34	19	22	169
1.0 : 1	8.38294	120	82	177	-144	66	75	701
1.3 : 1	8.38499	390	84	431	-147	64	55	564
1.5 : 1	8.38245	345	84	377	-126	70	68	489
1.8 : 1	8.39047	125	84	344	-130	70	75	595
2.0 : 1	8.38537	312	83	286	-106	82	85	393

Table 4.11: Lattice constant, crystallite size, magnetization, coercivity and magnetostriction of the samples.

about -144 ppm and -147 ppm respectively, which is $\sim$ -50 ppm less then already reported -197 ppm for G/N ratio 2.0:1 in ref [81]. The strain derivative of sample with G/N ratio 1:1 is 701 ppm/T is very high as compared to the sample having G/N ratio 1.3:1, which is 564 ppm/T. The sample having G/N ratio 1:1 is has very good value of magnetostriction and strain derivatives and very useful for sensor applications.

Part II

Magnetostriction in Rapidly Quenched Alloys

4.11   Fe-Ga Alloys Melt Spun Ribbons and Splat Cooled Foils [58]

The structure, especially the disorder caused by the Ga substitution, plays an important role for the high magnetostriction found in single crystalline Fe-Ga alloys. This effect should become more evident studying the magnetostriction on rapidly quenched Fe-Ga alloys, where the short-range structural disorder should be larger. Melt spun rapid solidified Fe-Ga ribbons samples exhibits large magnetostriction and good ductility as compared to conventional bulk samples and has promising possibility as a new magnetic induced sensor/actuator materials [131].

We performed magnetostriction measurements on binary $Fe_{85}Ga_{15}$, $Fe_{80}Ga_{20}$, $Fe_{81}Ga_{19}$, ternary $Fe_{76}Ga_{15}Co_9$, $Fe_{78}Ga_{15}Ni_7$, $Fe_{80}Ga_{15}Al_5$ melt spun ribbons (rapidly quenched at wheel speed 12 m/s) and $Fe_{81}Ga_{19}$ splat cooled foils, using a strain gauge method as well as a capacitance dilatometer, from low temperature up to room temperature to investigate these materials for high magnetostriction.

4.11.1   Structural Characterization

4.11.1.1   Microstructure

Figure 4.71 (a,b) shows the microstructure of a $Fe_{85}Ga_{15}$ and $Fe_{80}Ga_{20}$ ribbon in solidification direction (ribbon thickness), where clearly column shaped particles are observed which are approximately perpendicular to the ribbon surface. The width of these column particles varies from 5 to 10 μm. This kind of structure was also observed in ternary $Fe_{76}Co_9Ga_{15}$ and $Fe_{78}Ni_7Ga_{15}$ ribbons as shown in Figure 4.72 (a,b) these particles are elongated along the direction of the ribbon with an average size of 2 to 3 of by 5 to 10 μm. It is interesting to note that each grain is composed by fine elongated particles which are oriented in the direction of the thickness of the ribbon, XRD spectra showed also a clear texture and the [100] easy growth axis of bcc structure is tilted away from the ribbon normal similar as was reported by S. F. Cheng in ref [11].

4.11.1.2   XRD Data Analysis

Figures 4.73 and 4.74 shows the XRD pattern of $Fe_{80}Ga_{20}$ ribbons. X-ray diffraction was measured from ribbon sides, the quenched side wheel and the unquenched side free, on several $Fe_{80}Ga_{20}$ ribbon samples in two different geometries: (1) fixed sample beam parallel to the ribbon and (2) rotating sample holder. The refined patterns show no deviation from the A_2 phase and no supplementary reflections were observed. The background function was refined by using a Chebychev polynomial. The refinements converged at RBragg values of 0.41% and 0.25%, respectively (the low values are related to the background in-

(a) Fe$_{85}$Ga$_{15}$
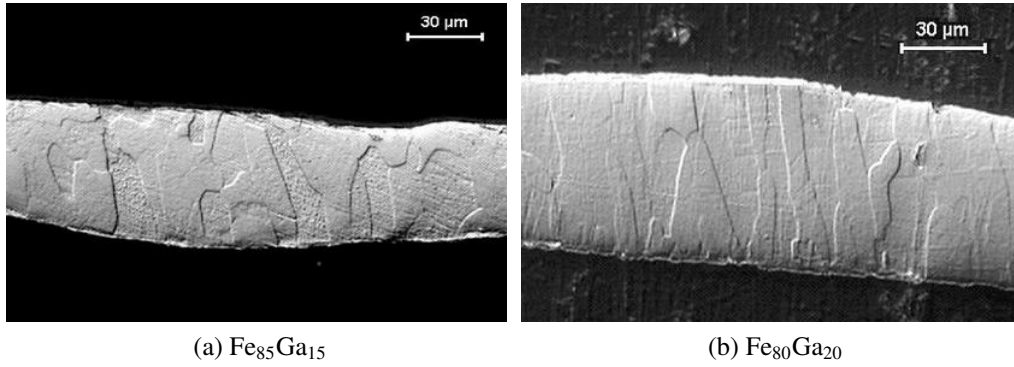
(b) Fe$_{80}$Ga$_{20}$

Figure 4.71: Images of cross-section (thickness) Fe$_{85}$Ga$_{15}$ and Fe$_{80}$Ga$_{20}$ ribbons melt spun at 10 m/sec.

(a) Fe$_{76}$Co$_9$Ga$_{15}$
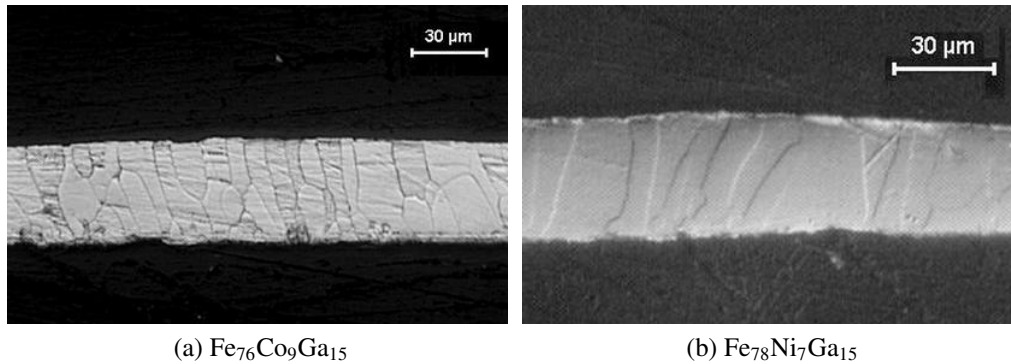
(b) Fe$_{78}$Ni$_7$Ga$_{15}$

Figure 4.72: Images of cross-section (thickness) Fe$_{76}$Co$_9$Ga$_{15}$ and Fe$_{78}$Ni$_7$Ga$_{15}$ ribbons melt spun at 10 m/sec.

tensity). For the wheel free side, the global agreement factors were Rexp: 1.18 (1.16); Rwp: 1.81 (1.77); Rp: 1.31 (1.27); and GOF: 1.54 (1.53), which confirm the models. Vibrational parameters Beq of 0.2 were assumed. Refinements on different lattice systems did not improve the model.

Lattice constants of 2.90604Å and 2.905423Å were found, respectively, for the wheel and free sides. The refined values agree with the 2.907Å given in literature [132]. The crystallite size was determined based on a Lorentzian size refinement following the Scherrer approach. The wheel and free sides of the ribbons where characterized by different average crystallite sizes: D = 159 ± 3 nm and D = 262 ± 8 nm, respectively. As expected, fast cooling gives rise to a smaller crystallite size. In all refinements, a pronounced texture model was used to obtain reasonable fits. For both ribbon sides, observed, refined, and difference patterns are given in Figures 4.73 and 4.74 , respectively, with and without applying a texture model. It can be seen that the two sides differ in texture. The wheel side shows mainly a primary (100) texture, refining to P = 0.650 ± 0.002 (P=1: untextured and P=0: fully textured sample) and a minor (211) texture, whereas the free side is affected by a stronger (100) texture (refining to P=0.478 ± 0.001), in addition to weak (211) and (031)
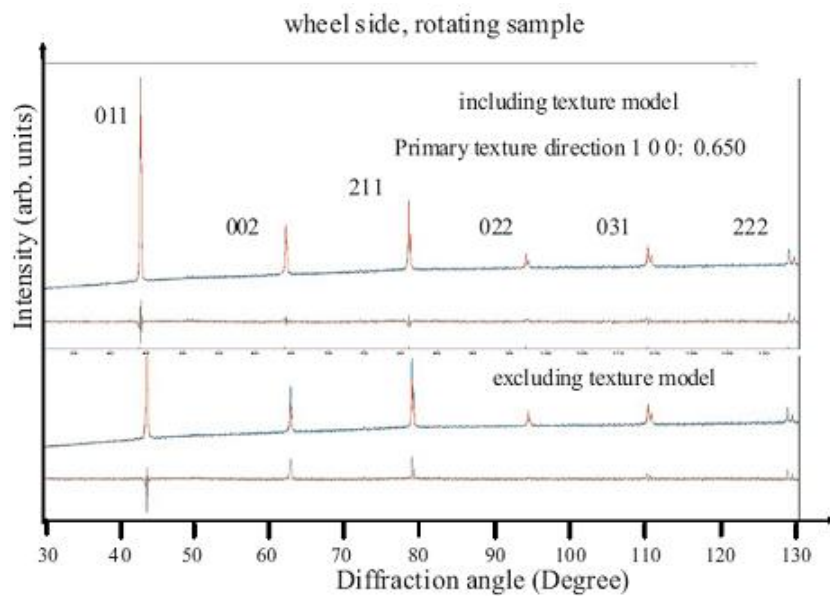
Figure 4.73: $Fe_{80}Ga_{20}$- Refined XRD pattern obtained on the wheel side with (top) and without (bottom) applying a textured model in the refinement: data (blue line), calculation (red line) and difference (gray line).
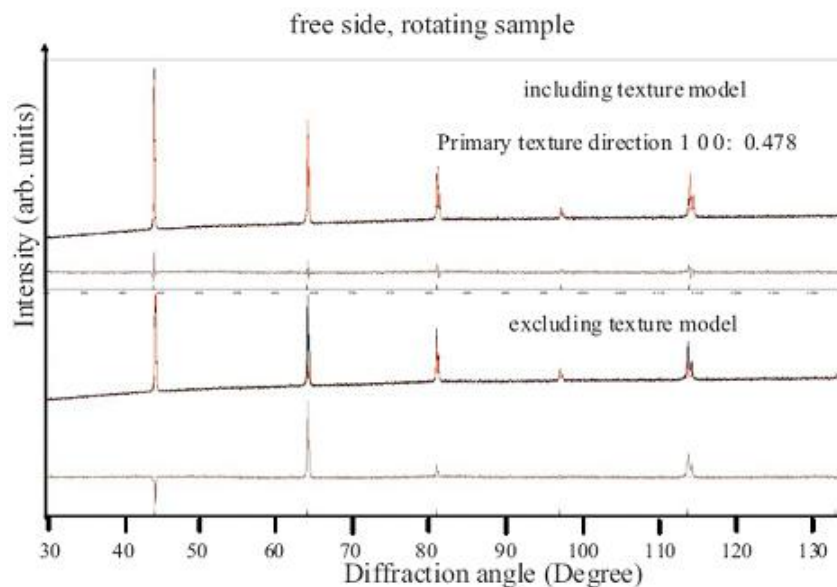
Figure 4.74: $Fe_{80}Ga_{20}$- Refined XRD pattern obtained on the free side of the ribbon with (top) and without (bottom) applying a textured model in the refinement: data (black line), calculation (red line) and difference (gray line).
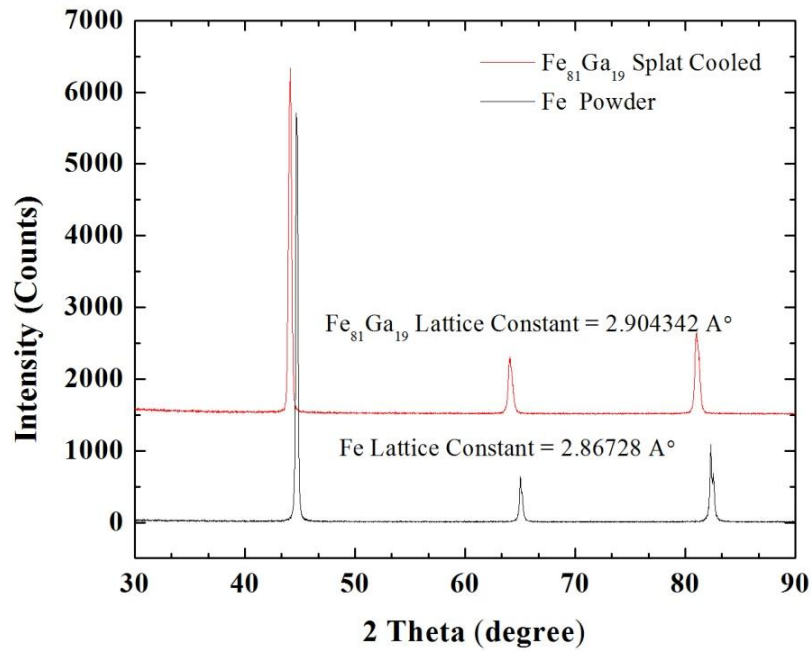
Figure 4.75: X-ray diffraction pattern of splat cooled $Fe_{81}Ga_{19}$ foil and pure iron.

texture contributions. The presence of texture effects on both sides is rather surprising but could be related to a mechanical compression on the copper wheel. This explanation would also be compatible with the lower degree of texture on the quenched side. The X-ray diffraction obtained from surfaces, free side and wheel side (the surface contact with copper wheel) of the ribbon showed that $Fe_{85}Ga_{15}$ exhibits single phase bcc disordered A_2 structure.

Figure 4.75 shows the XRD pattern of splat cooled $Fe_{81}Ga_{19}$ foil and pure iron with measured lattice constant 2.904342Å and 2.86728Å respectively the addition of Ga in Fe clearly indicates the increase of lattice constant of splat cooled $Fe_{81}Ga_{19}$ sample.

4.11.1.3   Magnetostriction Measurement

Figure 4.76 shows a typical magnetostriction measurement performed on $Fe_{80}Ga_{20}$ ribbon obtained at room temperature using the capacitance cell. The external field was applied in the ribbon plane and the magnetostriction was measured parallel to the thickness of the ribbon. We found a high positive magnetostriction of about 700 ppm, which is beyond any value obtained in polycrystalline bulk Fe-Ga. In this experiment, due to the here used geometry the bending of the sample should not play a role. Additionally, high magnetostriction values were found for the whole temperature range from 4.2 K up to 290 K. Figure 4.77 shows the temperature dependence of the magnetostriction obtained within this experiment, which detailed analysis of the strange temperature behavior is still under work. Using only one single ribbon as well as two ribbons put together without gluing them, gave similar results (see Figure 4.78).
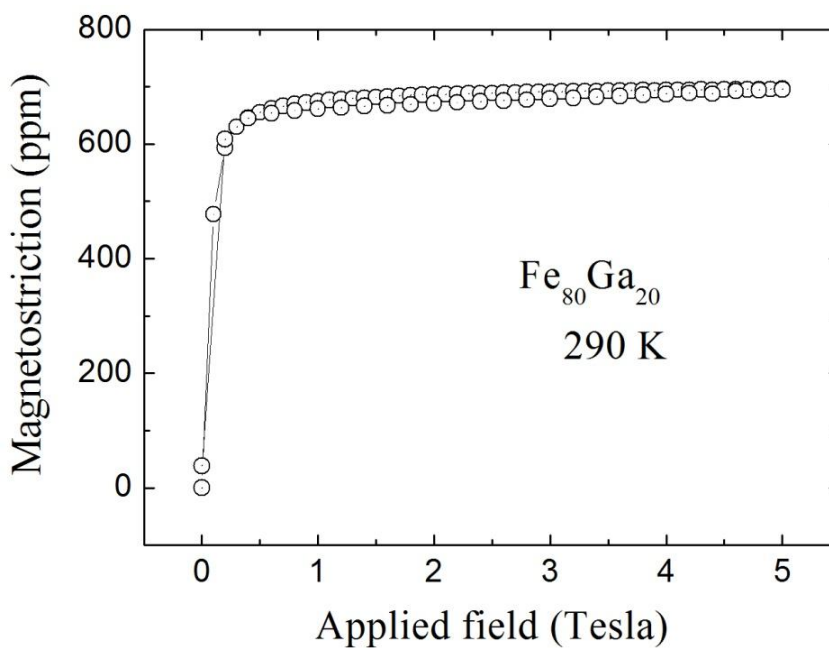
Figure 4.76: Magnetostriction, λ_{par} measured on $Fe_{80}Ga_{20}$ at room temperature measured in capacitance cell [133].
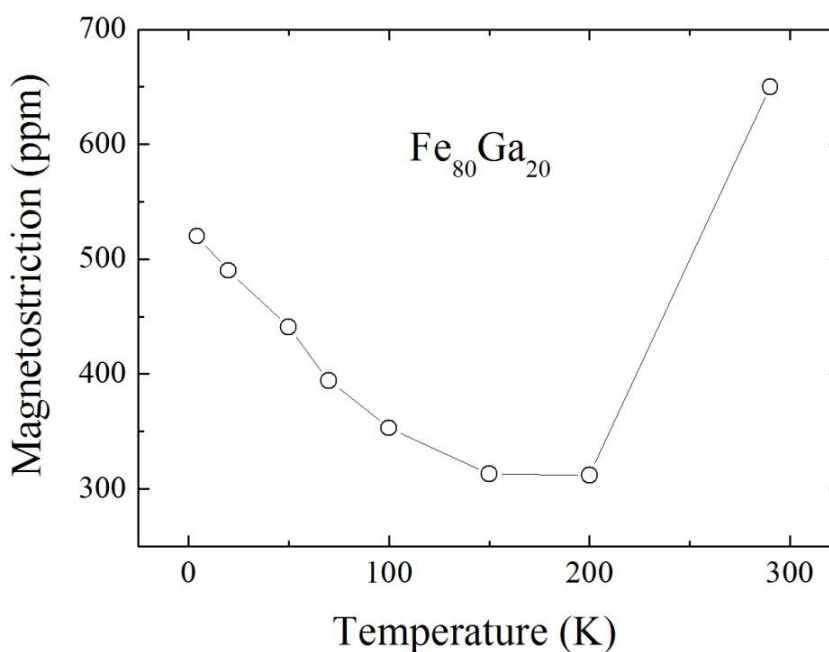
Figure 4.77: Temperature dependence of the magnetostrictions measured on single ribbon of $e_{80}Ga_{20}$ ribbon [133].
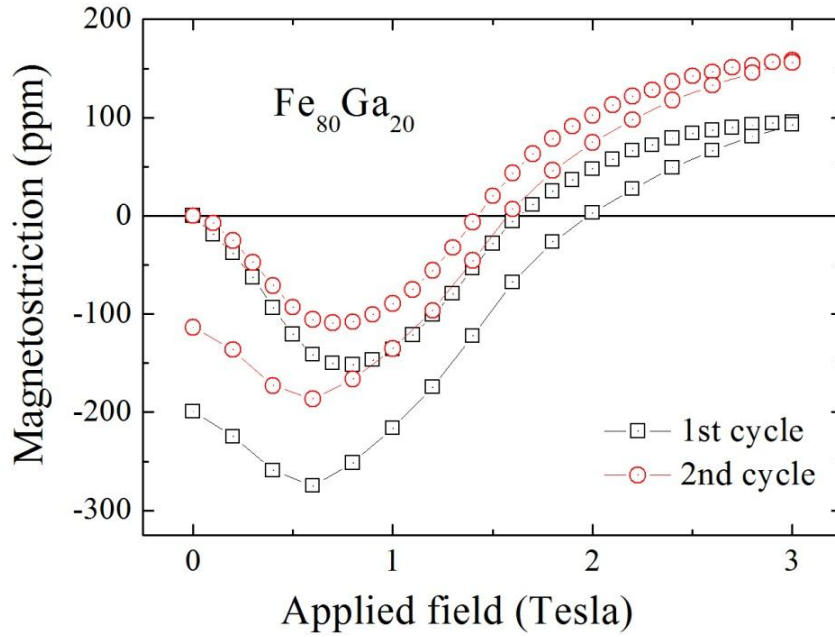
Figure 4.78: Two cycles of the magnetostrictions measurement carried out by means of capacitance cell on two glued $Fe_{80}Ga_{20}$ [133].
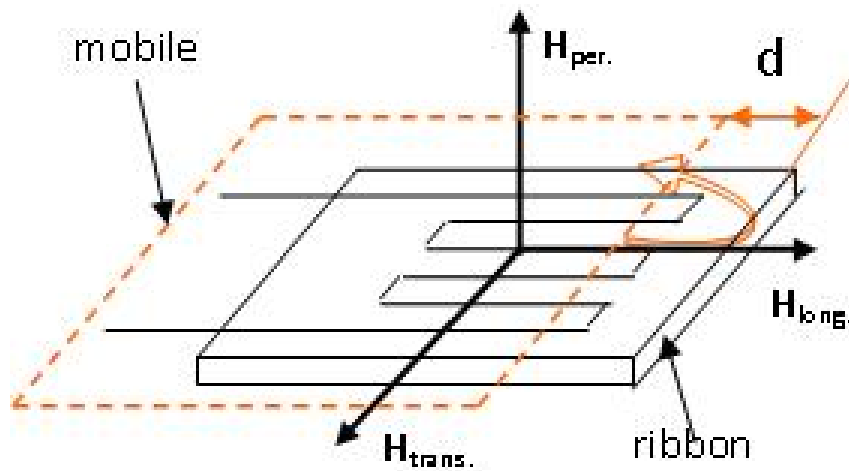
Figure 4.79: Possible orientations of the external field applied on the ribbons: H_{par}, H_{trans} and H_{long} with respect to the ribbon and the strain gauge on the ribbon.

On the other hand, significantly smaller magnetostriction values were found measuring two ribbons glued together (using strain gauge glue "Z70 from HBM"). In this case, the magnetostriction curve shows a large hysteresis, which is different for each cycle of measurement as show in Figure 4.78. These results show clearly the influence of glue, which may also induce stresses on the surface of ribbon.

Additionally magnetostriction measurements on a $Fe_{80}Ga_{20}$ ribbon and also on ribbons of different compositions were performed using the strain gauge method applying the field in different directions.
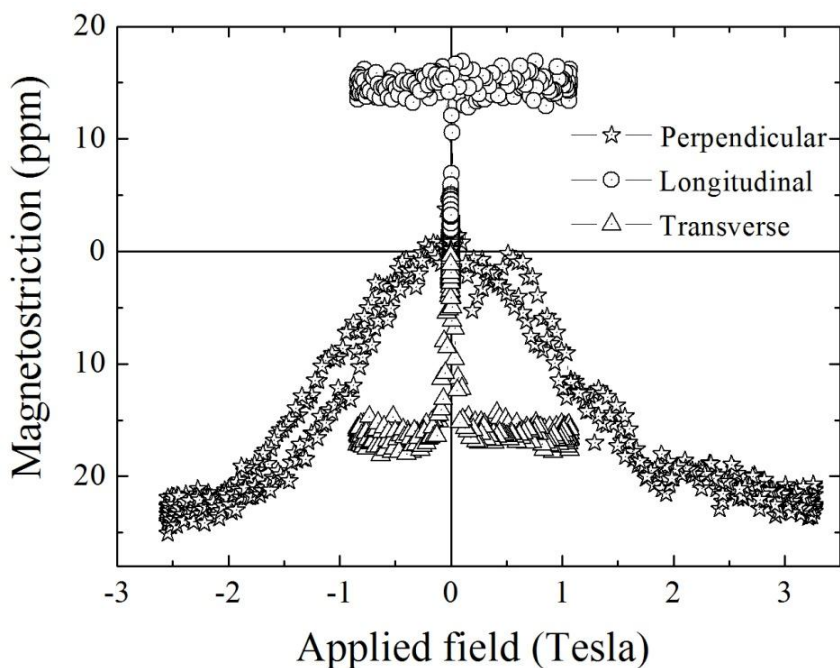
Figure 4.80: Magnetostriction measured on a $Fe_{80}Ga_{20}$ ribbon at room temperature with the strain gauge method, using the perpendicular, longitudinal and transversal geometry.

Figure 4.80 shows magnetostriction measurements on a $Fe_{80}Ga_{20}$ ribbon at room temperature using the perpendicular, longitudinal and transversal geometry. In this case the ribbon sample was completely fixed, i. e., d = 0 and glued on a thin plastic plate in order to prevent any mechanical movement.

The values obtained are rather low but still reasonable for polycrystalline bulk $Fe_{80}Ga_{20}$, however they are much smaller than those found by the capacitance technique on single ribbons without glue, but approaching to that value measured in glued sample. Similar results were found for $Fe_{81}Ga_{19}$ ribbons with different thickness. Figure 4.81 and Figure 4.82 shows the magnetostriction measured on $Fe_{81}Ga_{19}$ ribbons with thicknesses of 45 and 70 μm, respectively. For the thicker sample, larger perpendicular magnetostriction was found. Uncertain is here that the gluing of the thin ribbon on a plastic plate may hinder the magnetostrictive driven reduction of the sample.

Figure 4.83 shows magnetostriction measurements performed on a $Fe_{85}Ga_{15}$ ribbon. The perpendicular magnetostriction is a little bit larger than those of the former samples, however a negative magnetostriction for the longitudinal geometry was found.

Magnetostriction investigations using the strain gauge technique were also made on Fe-Ga foils made by splat cooling with thicknesses of 40 and 87 μm, as shown in Figure 4.84 (87 μm not shown here). No significant difference of magnetostriction was found due to thickness of the samples with respect to each other and as compared to the magnetostriction of ribbons produced by melt spinning technique.

Magnetostriction investigations using the strain gauge technique were also made on Fe-
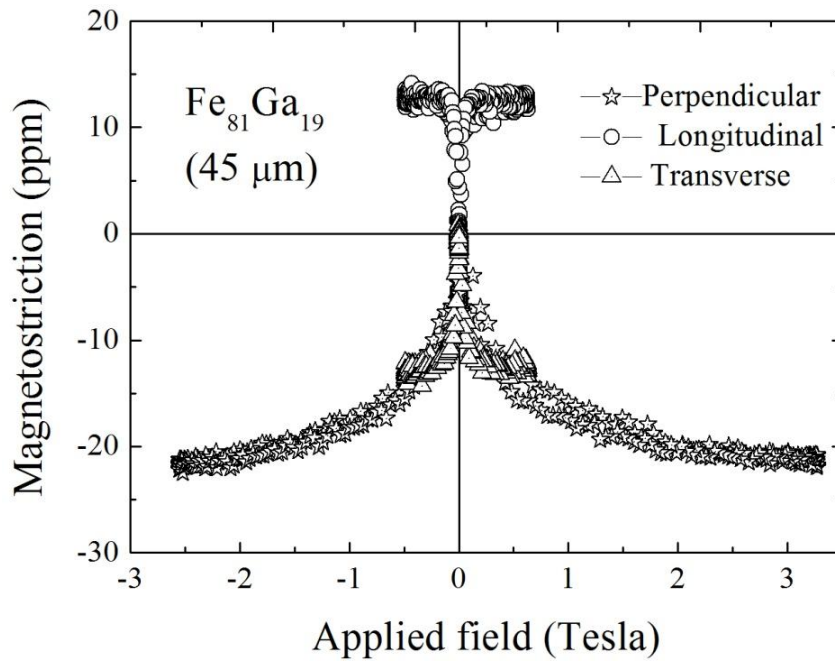
Figure 4.81: Magnetostriction measured on the $Fe_{81}Ga_{19}$ ribbon (thickness 45 μm) measured with the strain gauge method.
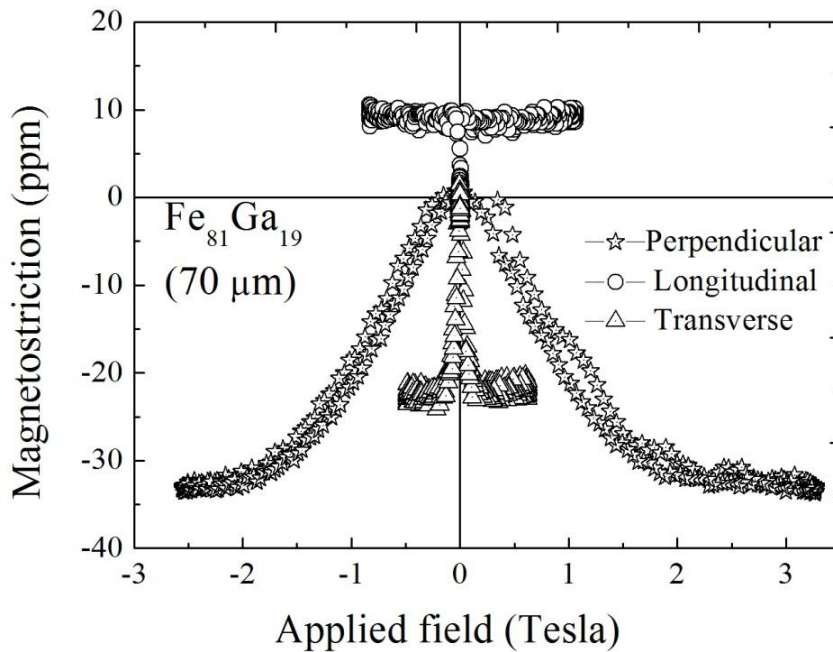
Figure 4.82: Magnetostriction measured on a $Fe_{81}Ga_{19}$ ribbon (thickness 70 μm) measured with the strain gauge method
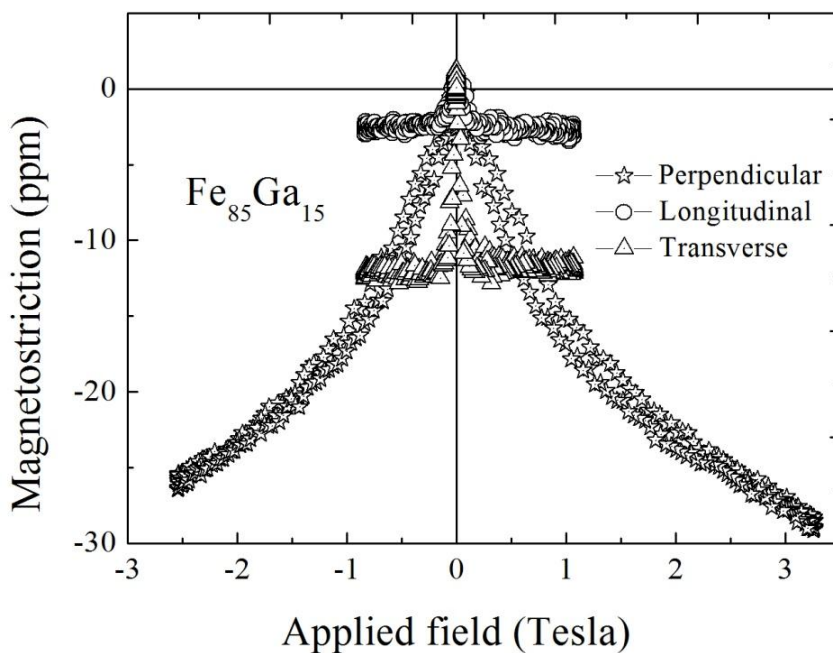
Figure 4.83: Magnetostriction of a $Fe_{85}Ga_{15}$ ribbon measured with the strain gauge method.
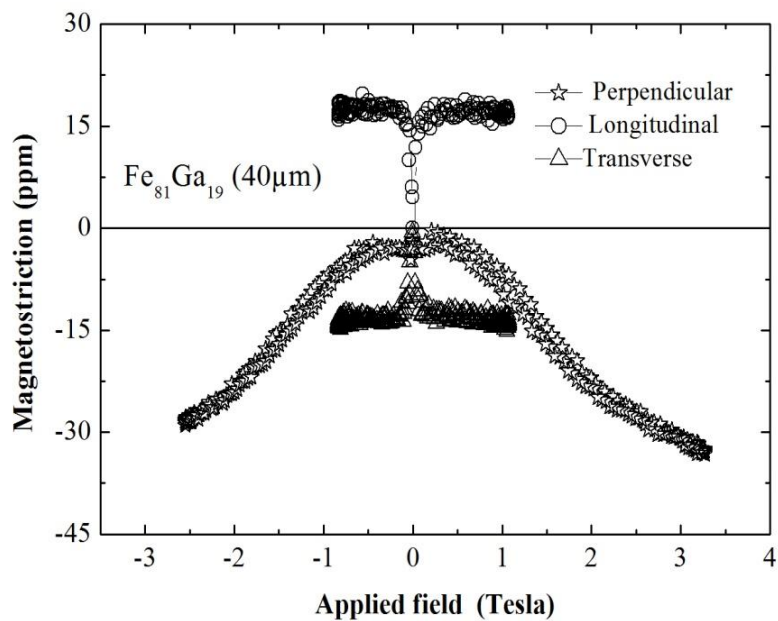
Figure 4.84: Magnetostrictions measured on the splat cooled $Fe_{81}Ga_{19}$ foil (40 μm).
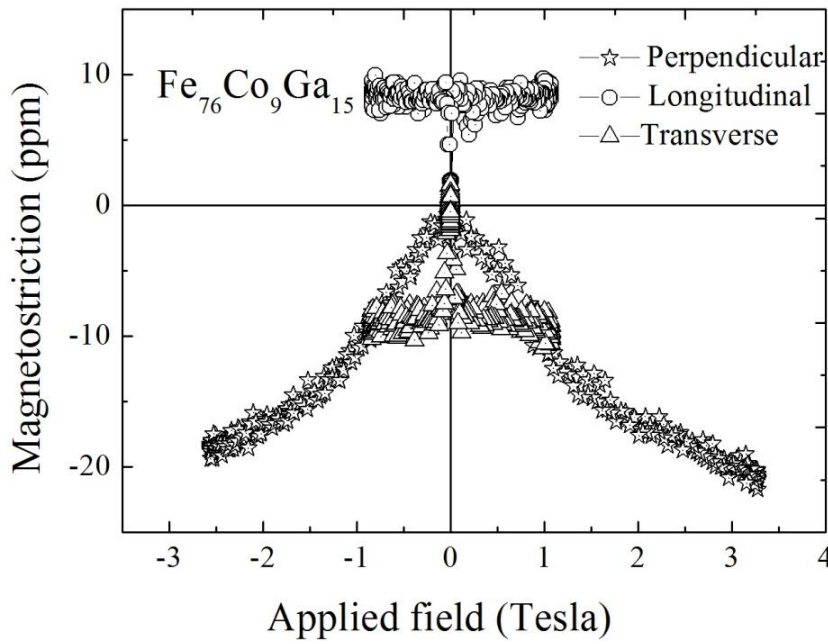
Figure 4.85: Magnetostriction of $Fe_{76}Co_9Ga_{15}$ measured with a strain gauge.
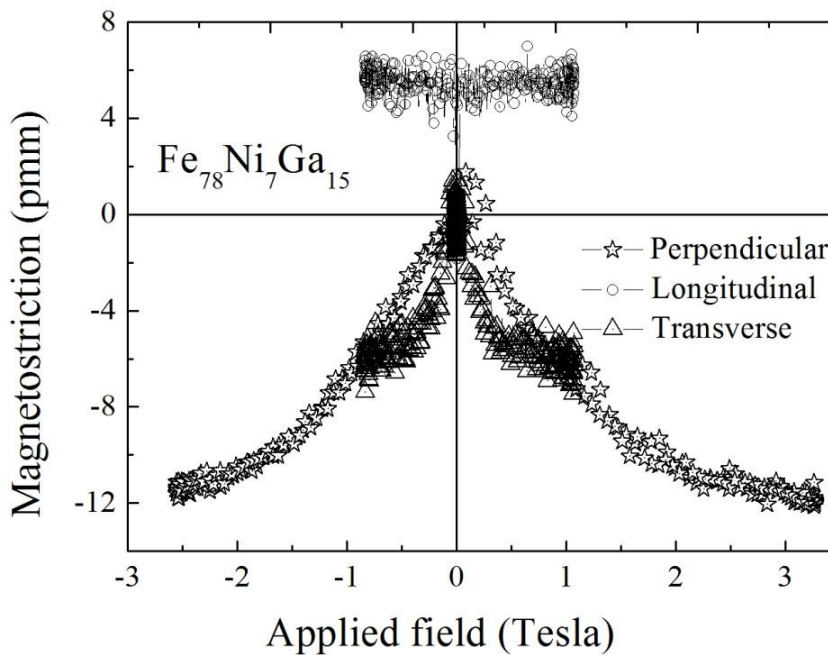
Figure 4.86: Magnetostrictions measured on the $Fe_{78}Ni_7Ga_{15}$ ribbon.

Ga ribbons where Fe were partially substituted by Co, Ni or Al (see Figures 4.85, 4.86 and 4.87 respectively). For all three substitutions, a reduction (in comparison with that obtained in $Fe_{85}Ga_{15}$) of the perpendicular magnetostriction was detected.

To investigate the possible effect of glue on the stain gauge method, additional measurements were performed on stacked 5 pieces of $Fe_{76}Co_9Ga_{15}$ ribbons without being glued on the plastic plate. The results are shown in Figure 4.88, similar values of longitudinal and transverse magnetostriction to those obtained for a single ribbon (see Figure 4.85) were
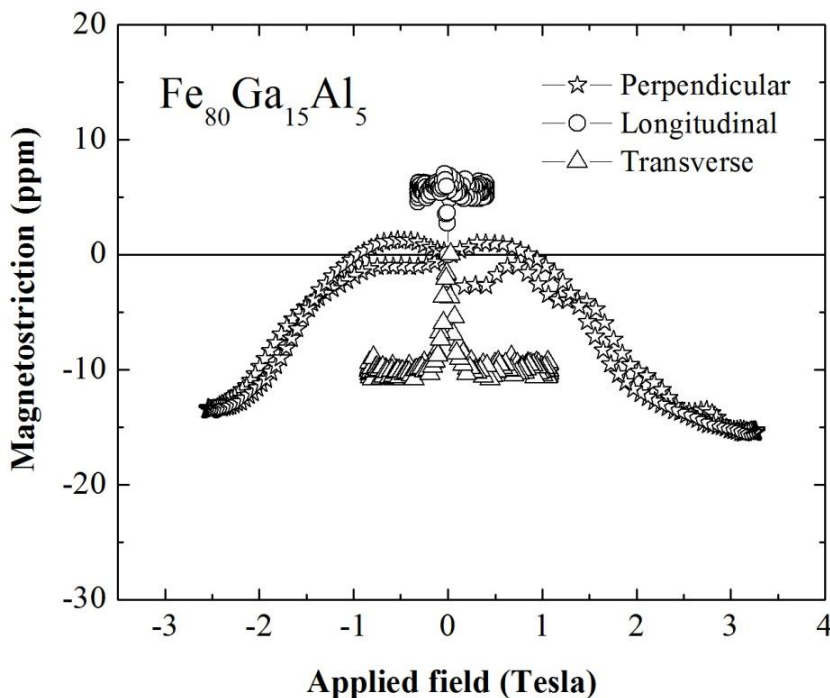
Figure 4.87: Magnetostrictions measured on the $Fe_{80}Ga_{15}A_{l5}$ ribbon.
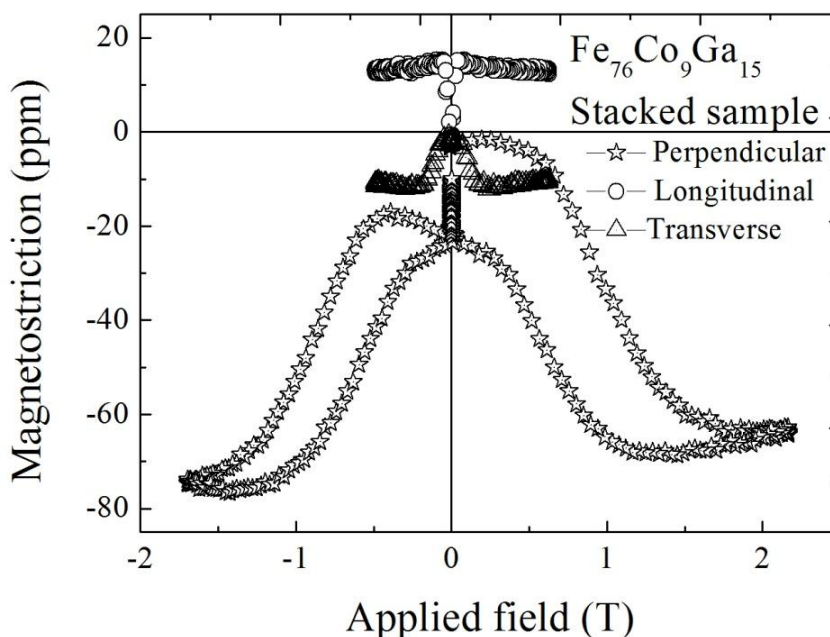
Figure 4.88: The longitudinal, transverse and perpendicular magnetostrictions measured on the stacked ribbons sample of $Fe_{76}Co_9Ga_{15}$.

found, however, similar as in the capacitance cell experiment for the glued sample (see Figure 4.78), the perpendicular magnetostriction presents an irreversibility in the curve of the field dependence of the magnetostriction.

In order to check the feasibility of these measurements, similar experiments were performed using a pure polycrystalline Fe foil exhibiting a thickness of 25 μm (from Good
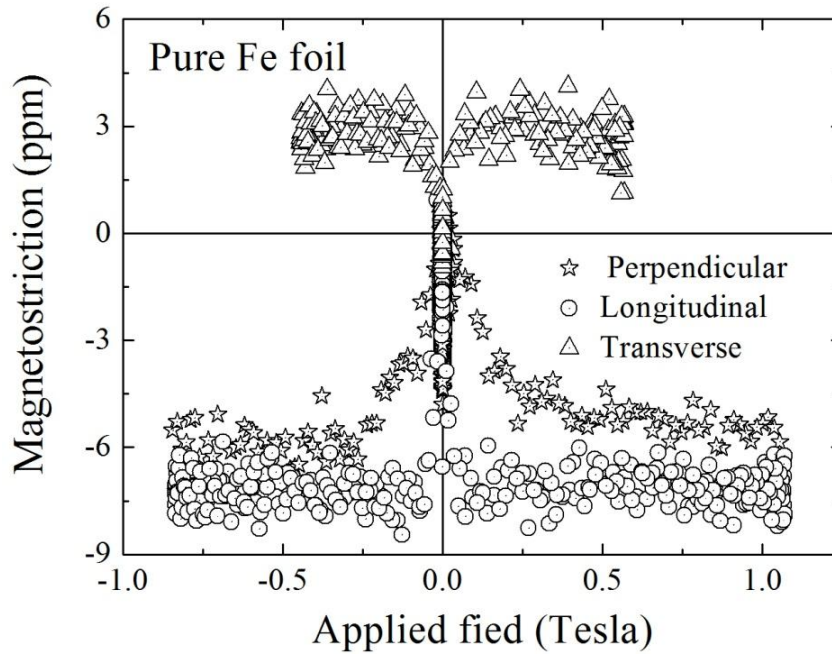
Figure 4.89: Magnetostrictions measured on a pure Fe foil from Good fellows.
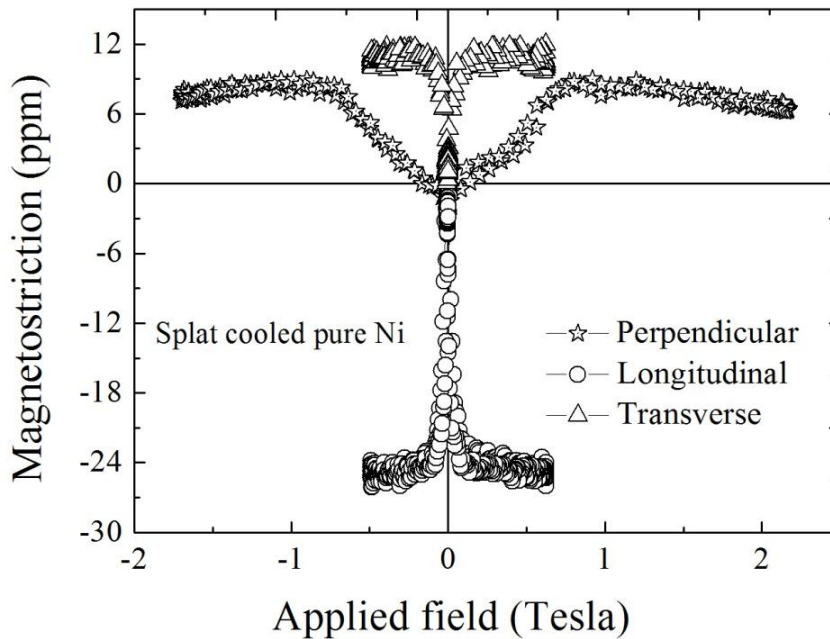
Figure 4.90: Magnetostrictions measured on as-produced splat cooled pure Ni.

fellows) and also a splat cooled pure Ni with thickness of about 100 μm The samples were cut to have a similar geometry as that of the ribbons. These measurements are shown in Figures 4.89 and 4.90.

The values of longitudinal and transverse magnetostrictions fits rather well to those of polycrystalline pure Fe and Ni materials, mainly for the pure Fe from Good fellows, where the internal stress must be small. These results suggest that the magnetostriction along the ribbons are comparable to the magnetostriction of bulk polycrystalline Fe-Ga [134],
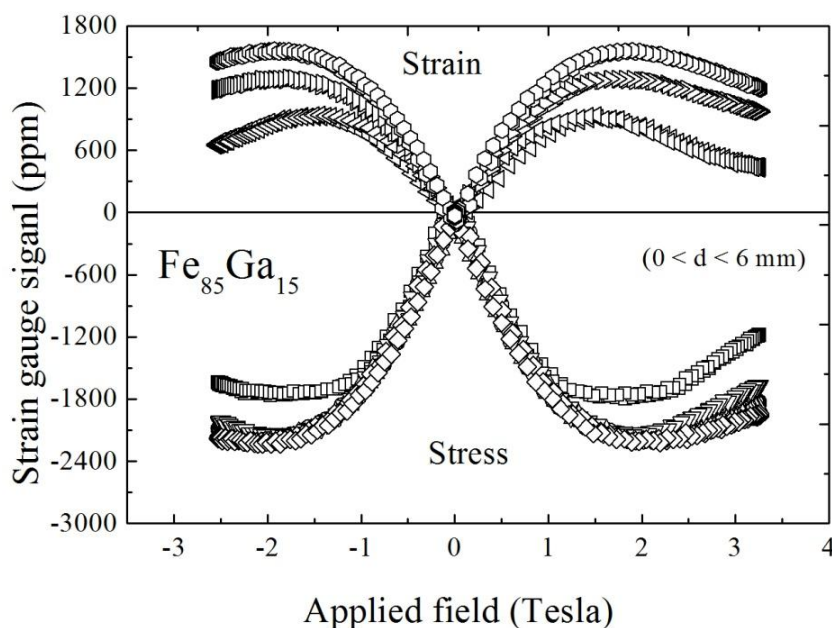
Figure 4.91: Strain and stress distortions as function of d measured on the $Fe_{85}Ga_{15}$ ribbon at room temperature at perpendicular geometry. The strain gauge signal increases with increasing d.

even applying a magnetic field perpendicular to the ribbon plane. However, we cannot decide if the magnetostrictions values obtained by gluing a strain gauge and additional gluing the sample on a plastic plate are reliable values due to the possibility of glue induced mechanical stresses.

On the other hand, for measurements using strain gauges on ribbons and applying the external field perpendicular to the plane of the ribbon, if the samples are partially free from an external stress (besides strain gauge glue) bending of the sample can occur (Figure 4.79). Therefore in this work we also investigate how the strain gauge signals change as function of the distance of the part of the ribbon sample left free, which in Figure 4.79 is indicated by the parameter d, applying a magnetic field perpendicular to the ribbon plane. The length of the strain gauge is of 6 mm. These measurements were carried out on Fe-Ga alloys (see Figures 4.91, 4.92 and 4.93) as well as on pure Fe-foil (see Figure 4.94) for various values of d ($0 \leq d \leq 6$ mm).

The strain gauge signals obtained for d = 0 are similar to those results found for samples glued on the plastic plate. However, a strong increase of signal was detected with increasing d. For the Fe-Ga alloys, a "giant" strain gauge signal up to ± 2200 ppm was found (negative values when the magnetic field is applied in the direction perpendicular to the ribbon plane as indicated in Figure 4.79 causing a stress in the strain gauge and, positive when the field is applied in opposite direction resulting thus a strain). It is rather sure that this occurs due to bending of a part of the sample. In fact, the special shape of the curve can also be understood because at field values larger than the demagnetizing field the magnetization
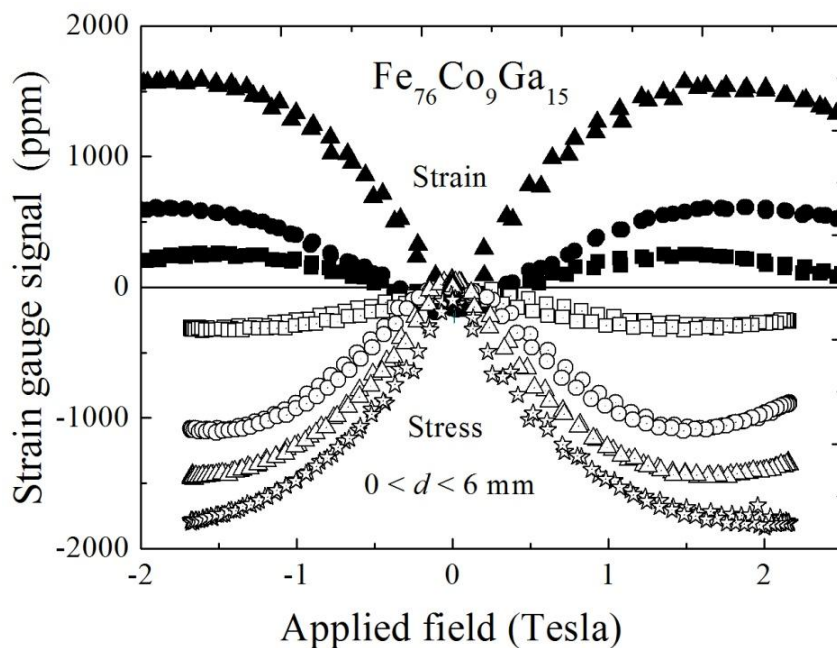
Figure 4.92: Strain and stress distortions as function of d measured on a $Fe_{76}Co_9Ga_{15}$ ribbon at perpendicular geometry. The strain gauge signal increases with increasing d.
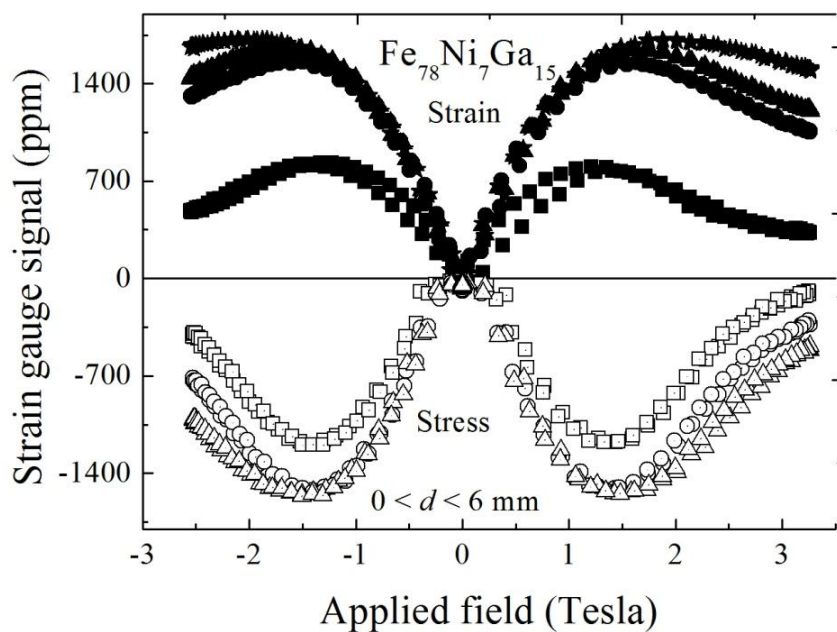
Figure 4.93: Strain and stress distortions as function of d measured on a $Fe_{78}Ni_7Ga_{15}$ ribbon at perpendicular geometry. The strain gauge signal increases with increasing d.
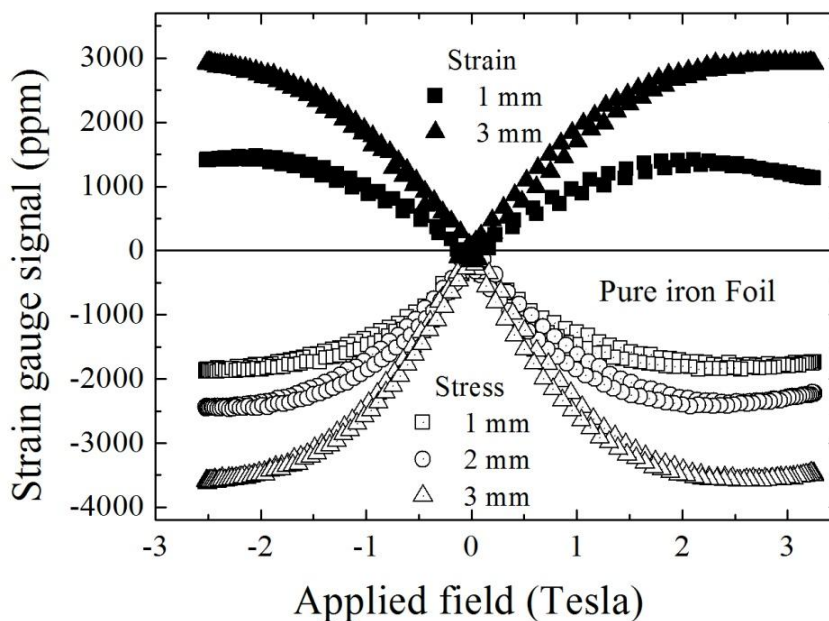
Figure 4.94: Strain and stress distortions as function of d measured on the pure Fe foil (from Good fellows) at perpendicular geometry. The strain gauge signal increases with increasing d.

starts to rotate out of the plane parallel to the external field, and thus torque decreases, consequently reducing the bending. This behavior was observed for all samples including the pure Fe foil, where the highest value of bending effect ($\pm$ 3200 ppm) was obtained (see Figure 4.94). This high value occurs for pure Fe because pure Fe exhibits the highest saturation magnetization and additionally the thickness of the foil was thinner, which makes the bending effect to become easier.

4.12   Magnetostriction Investigations in $Fe_{82.5}Ga_{17.5}$ Melt Spun Ribbons as a Function of Quenching Rate [135]

Comparison between magnetostriction (λ) obtained on bulk material with that measured on ribbons gave hints that the degree of disorder may support a high λ in these materials [11]. Cheng et al. found a maximum λ value of about 130 ppm in $Fe_{83}Ga_{17}$ ribbon [11]. However the finding of magnetostriction values higher than 2000 ppm in Fe-Ga (see e.g. [56]) was later demonstrated by us may be due to a measuring problem [58].

Liu et al. found in $Fe_{81}Al_{19}$ ribbon a magnetostriction value high as 700 ppm using a strain-gauge [15]. However to perform accurate magnetostriction measurements on a single ribbon using the strain-gauge technique is extremely difficult [58]. Due to the fact that the magnetostrictive behavior of ribbons seems of technological interest, especially in combination with a [100] texture along the ribbon length.

High purity Fe and Ga (99.99%) were high frequency melted in Ar atmosphere using a water cooled Cu-crucible. Ribbons of nominal compositions $Fe_{81}Al_{19}$ were prepared by varying the wheel speed, WS, from 7.5 up to 25 m/s. The average width of the ribbons is about 3 mm and the thickness, d, varies from 36 to 80 μm. The concentration of Ga for all ribbons was determined via EDAX at five different points of the samples. For all samples, the average concentration of Ga found was of (17.5$\pm$0.7) at % Ga.

In this work, magnetostriction of $Fe_{82.5}Ga_{17.5}$ ribbons with different quenching rates, QR, were investigated using a capacitance cell method [121].

4.12.1   Microstructure

The microstructure of the $Fe_{82.5}Ga_{17.5}$ ribbons obtained at different wheel velocities, WS, is shown in Figure 4.95. Usually, quenching rate, QR, is proportional to the WS. As can be seen, generally, columnar particles perpendicular to the surface of the ribbons are formed. During the quenching procedure a strong temperature gradient appears over the thickness of the ribbon. The melted material first will crystallize at the surface which is on border to the copper wheel forming many small grains and when they touch each other the crystals start to grow in columns along the temperature gradient. Due to the fast transport of the ribbon by the rotating wheel also a tangential component causes a bowing of the columns.

4.12.2   XRD Data Analysis

All $Fe_{82.5}Ga_{17.5}$ ribbons exhibit a disorder bcc A_2 structure, XRD pattern shown in Figures 4.96 and 4.97. The average grain size and lattice constant as a function of the
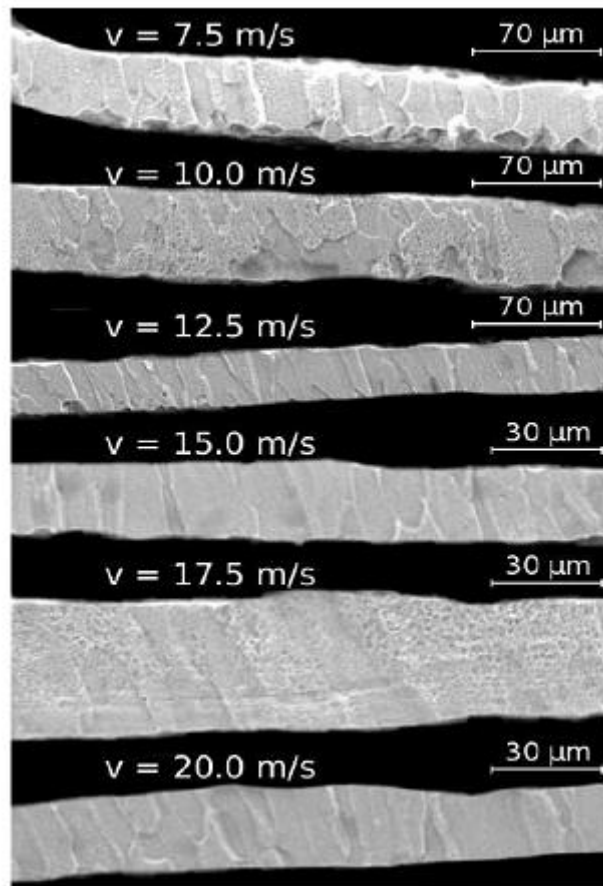
Figure 4.95: Micrograph of Fe$_{82.5}$Ga$_{17.5}$ ribbons melt-spun at different velocities and magnification as indicated in the figure.

wheel speed are shown in Figures 4.98 and 4.99, respectively. The values of D (crystallite size) and a (lattice constant) were determined for both wheel and free side of the surface of the ribbons.

As can be seen, the D and a values are almost independent of the surface side indicating that the average grain size and lattice constant along the thickness can be considered almost constant. However, both D and a value fluctuate with increase of the WS.

This result suggests that, in these experiments, the proportionality between WS and QR does not hold. The texture degree (i.e. a number that represents the percentage of a certain texture existing in the sample, which "1" corresponding to 100 % of this certain texture) was refined based on intensity analysis using XRD diffraction data. Only an average texture and grain size can be refined by this method. Statistical distribution was verified by measuring the ribbons under different diffraction angles between source and ribbon and on rotating the sample. The intensities did not differ significantly. An average texture behavior can be calculated from diffraction data (TOPAS 4.1, allowing 2 texture settings on one sample). Figure 4.100 shows a strong (100) and a weak (310) texture degree as a function of wheel speed obtained for Fe$_{82.5}$Ga$_{17.5}$ ribbons.
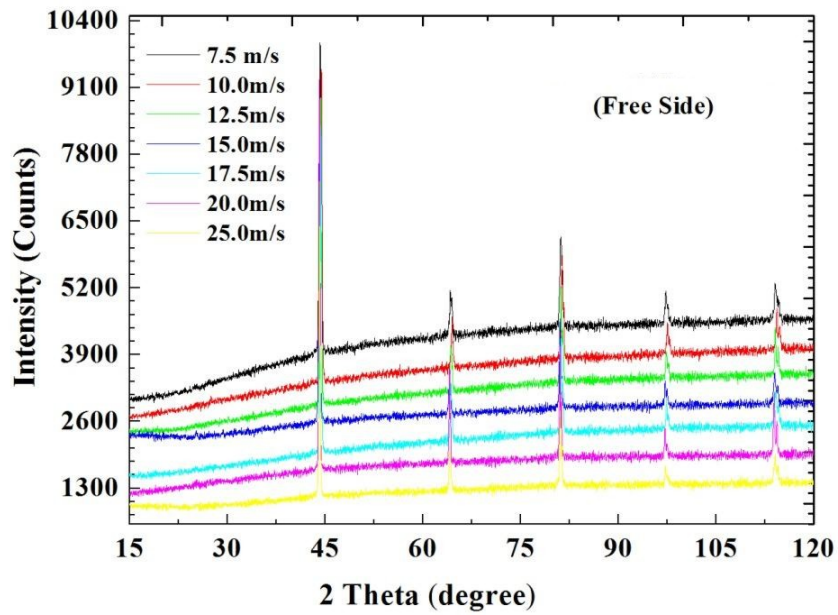
Figure 4.96: X-ray diffraction pattern (Cu- Kα radiation) of free side of Fe$_{82.5}$Ga$_{17.5}$ melt spun ribbons.
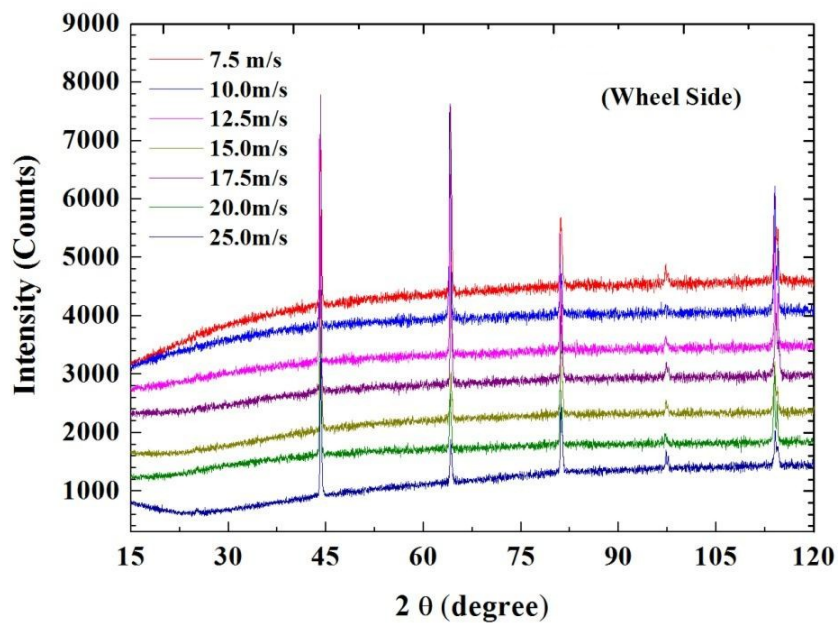
Figure 4.97: X-ray diffraction pattern Cu- Kα radiation) of wheel side of Fe$_{82.5}$Ga$_{17.5}$ melt spun ribbons.
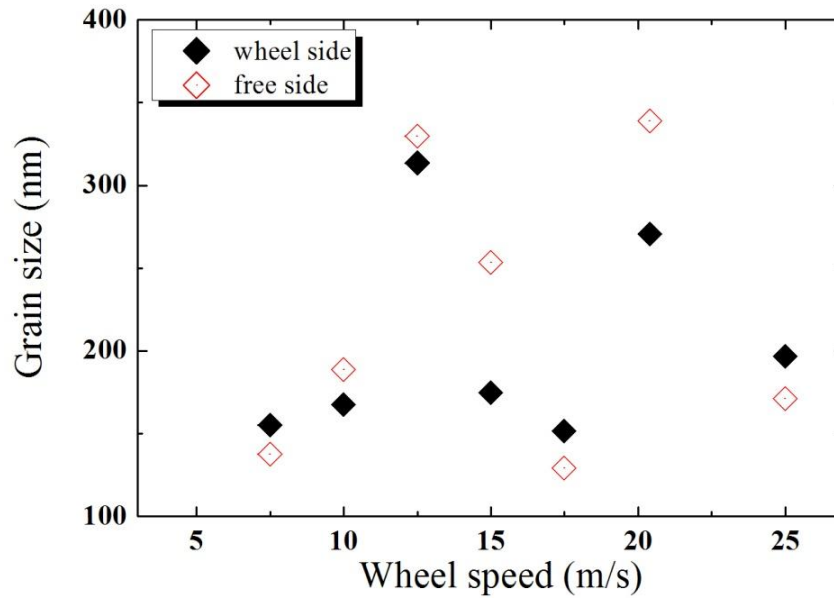
Figure 4.98: The dependence of the average grain size D on wheel speed obtained for Fe$_{82.5}$Ga$_{17.5}$ melt spun ribbons.
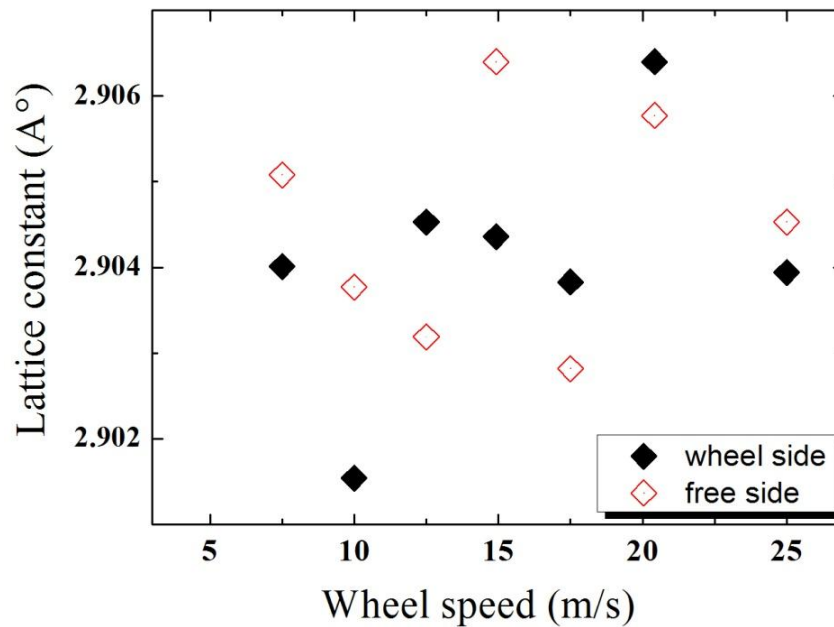
Figure 4.99: The dependence of the lattice constant a on wheel speed obtained for Fe$_{82.5}$Ga$_{17.5}$ melt spun ribbons.
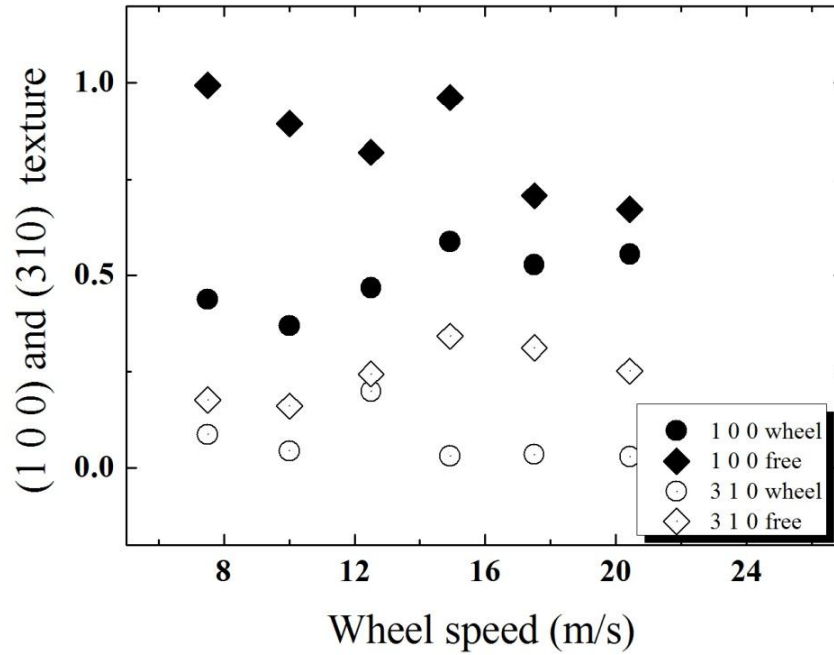
Figure 4.100: The (100) and (310) texture degree as a function of wheel speed obtained for wheel and free side of $Fe_{82.5}Ga_{17.5}$ melt spun ribbons.

The texture degree on both sides of the sample is different, may be due to the different cooling situation on the two surfaces which influences the nucleation [11]. Within the ribbon, the columns might bend under this growth conditions giving two different textures on both sides. Diffracted intensities are therefore different and can be associated with the average texture of the sample.

4.12.3 Magnetization Measurements

At room temperature, the saturation magnetization of $Fe_{82.5}Ga_{17.5}$ obtained from the hysteresis measurement is 174 emu/g.

4.12.4 Magnetostriction Measurements

Figure 4.101 shows selected magnetostriction data of different ribbons of $Fe_{82.5}Ga_{17.5}$, produced at different WS, indicating a large variation in λ_{long}, and λ_{trans} values and also in the character of the field dependence of the magnetostriction. In this work, the ribbon produced with 15 m/s gave the maximum longitudinal magnetostriction value. The λ_{long} and λ_{trans} values are 116 ppm and around zero, respectively (see Figure 4.101 and Figure 4.102). The λ_{long} value is comparable with those reported in [11] , which are 98 and 130 ppm for $Fe_{79}Ga_{21}$ melt spun at 50 m/s and $Fe_{83}Ga_{17}$ melt spun at 15 m/s, respectively.
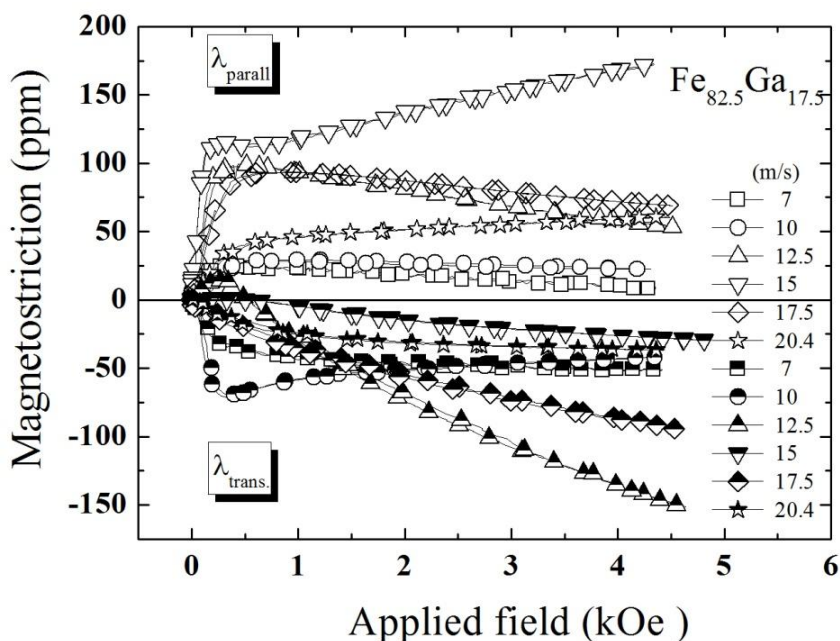
Figure 4.101: Room temperature longitudinal and transverse magnetostriction, λ_{long} and λ_{trans}, of Fe$_{82.5}$Ga$_{17.5}$ melt spun ribbons, produced by different WS.
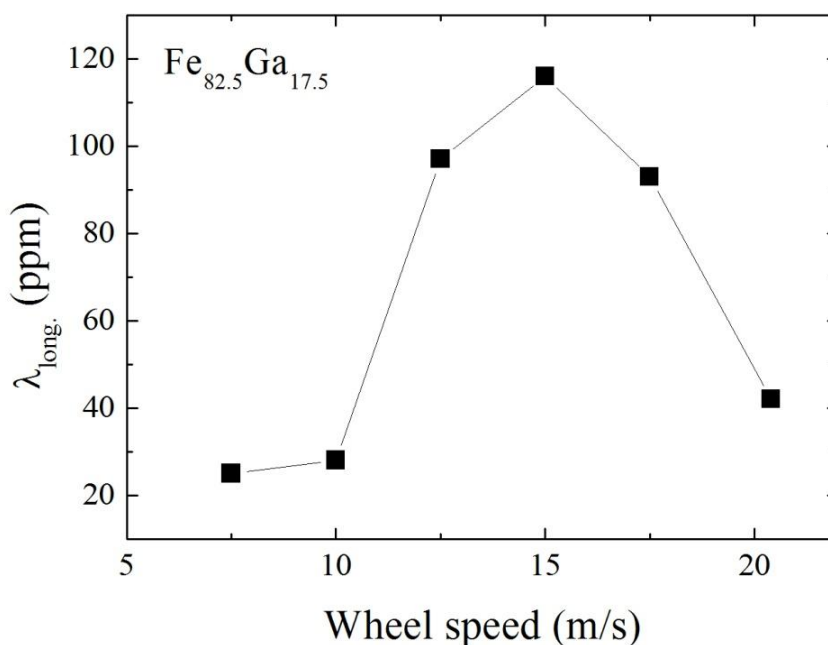
Figure 4.102: The longitudinal magnetostriction as a function of the wheel speed found in Fe$_{82.5}$Ga$_{17.5}$ ribbons.

The high longitudinal magnetostriction value may be related to the (100) texture degree. XRD on wheel and free side gave hints how the texture develops through the thickness of the ribbons. The texture on the free side is stronger (average (100) texture degree = 0.85) than that of the wheel side. As can be seen in Figure 4.100, the texture degree changes with wheel velocity showing the highest (100) texture degree (both wheel and free side) for

the sample produced at WS of 15 m/s, where the longitudinal magnetostriction reaches the highest value. However additional effects such as fluctuations in the local composition (the magnetostriction in Fe-Ga alloys is very sensitive to the Ga content [6]) as well as-quenched in stresses may also influence the longitudinal and transverse magnetostriction, as can be seen in Figure 4.101. It is worth to observe that the sample with highest magnetostriction shows a linear increase of the longitudinal magnetostriction after the magnetization is saturating. This effect can be originated due to the forced volume magnetostriction, however it is also possible that a contribution due to the (310) texture occurs.

4.13 Magnetostriction Investigations in Fe-Al Melt Spun Ribbons [136]

Rapid quenching by melt spinning technique can produce samples with different structural properties, such as disordered structure, grain size, lattice constant and texture. In this work an investigation of the influence of quenching rate on magnetostriction and structural properties was performed on a set of $Fe_{100-x}Al_x$ (x = 14.3, 18.7 and 22.3) ribbons. Ingots of compositions $Fe_{85.7}Al_{14.3}$, $Fe_{81.3}Al_{18.7}$ and $Fe_{77.7}Al_{22.3}$ were prepared using Fe and Al of high purity (> 99.9%) in an induction furnace under argon atmosphere. The concentrations of Fe and Al for ingots and all ribbons were determined via EDAX at five different points of the samples. The average concentrations of constituent elements of ingots and ribbons (obtained from these ingots) presented similar compositions, within of 2 %. The measurements of magnetization as a function of the applied field were performed using a pulsed field magnetometer. Longitudinal, λ_{long} , and transverse, λ_{trans}, magnetostriction measurements at room temperature ,RT, were performed on ribbons in the shape of discs using a special capacitance device [121] . All measurements were performed at room temperature.

4.13.1 Microstructure and XRD Analysis

The XRD analysis of the $Fe_{100-x}Al_x$ ribbons showed that $Fe_{85.7}Al_{14.3}$ and $Fe_{81.3}Al_{18.7}$ exhibit a disorder bcc A_2 structure $Im\bar{3}m$ with a statistical substitution of Fe by Al, whereas for $Fe_{77.7}Al_{22.3}$ superlattice lines according to the DO_3 phase $Fm\bar{3}m$ were found (see detailed line of the inset in Figure 4.103). Figure 4.103 shows XRD patterns obtained for $Fe_{85.7}Al_{14.3}$, $Fe_{81.3}Al_{18.7}$ and $Fe_{77.7}Al_{22.3}$ ribbons melt spun at 15 m/s. In the inset is plotted the strongest line with enlarged 2 Theta axis showing the line detail. Similar XRD patterns were obtained for all other melt spun ribbon samples.

The texture degree (i.e., a number that represents the percentage of a certain texture existing in the sample, which "1" corresponding to 100 % of this certain texture) was refined based on intensity analysis using XRD diffraction data. Only an average texture and grain size can be refined by this method. Statistical distribution was verified by measuring the ribbons under different diffraction angles between source and ribbon and on rotating the sample. The intensities did not differ significantly. An average texture behavior can be calculated from diffraction data (TOPAS 4.1, allowing 2 texture settings on one sample). However, contrary to $Fe_{82.5}Ga_{17.5}$ ribbons where strong texture and columnar particles were formed [135], on $Fe_{100-x}Al_x$ ribbons a significant texture was not detected. Additionally, columnar particles along the ribbon thickness of all samples were not formed as shows an example in the micrograph for $Fe_{81.3}Al_{18.7}$ in Figure 4.104. It is important to mention that the shape and size of particles vary along the ribbon and also differ from one sample to another one. However, for all samples, the particles are distributed randomly, without for-
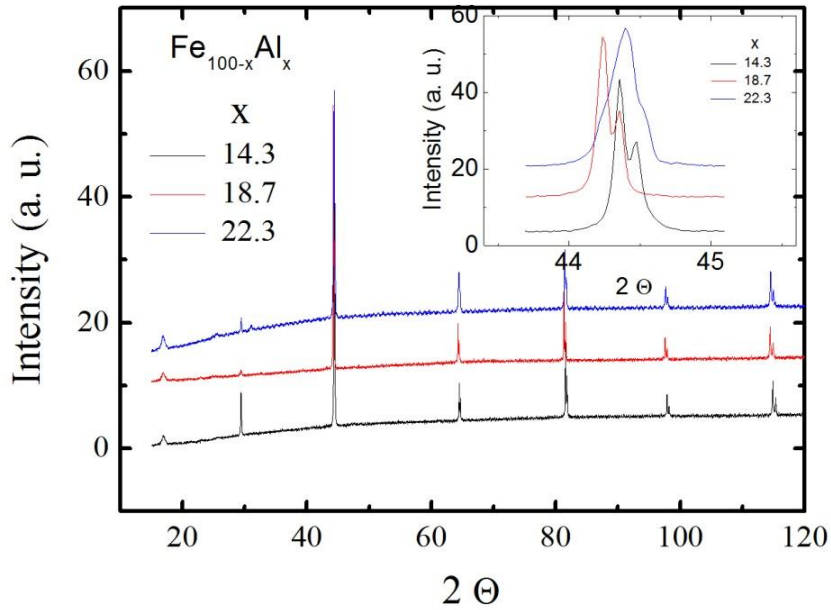
Figure 4.103: XRD patters obtained for $Fe_{85.7}Al_{14.3}$, $Fe_{81.3}Al_{18.7}$ and $Fe_{77.7}Al_{22.3}$ ribbons melt spun at 15 m/s. In the inset is represented strongest lines from patterns with an enlargement of the 2 Theta axis is presented.
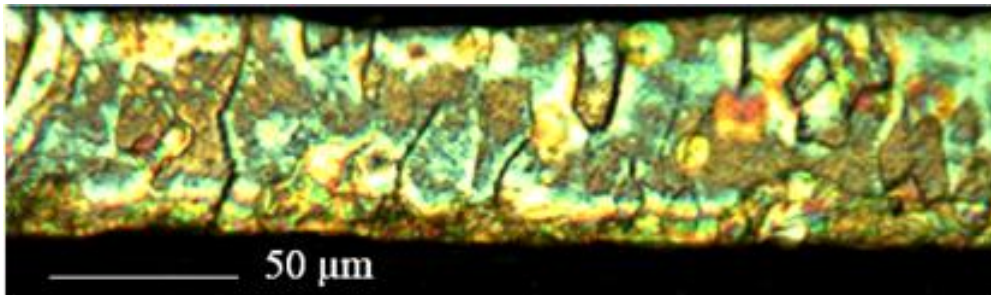
Figure 4.104: Micrograph of $Fe_{81.3}Al_{18.7}$ ribbon melt-spun at velocity 15 m/s and magnification indicated in the figure.

mation of columnar particles as was found for $Fe_{82.5}Ga_{17.5}$ ribbons [135]. For this reason, the study of XRD on Fe-Al ribbons was performed only on the wheel side of the ribbon. Table 4.12 lists the values of the ribbons thickness, t, ribbons width, d, the crystallite size, D, and the lattice constant, a, obtained for samples produced with different wheel speed, WS. Generally, the ribbon thickness and crystallite size decrease with increase of the wheel speed. However our ribbons present thickness and width, additionally crystallite size, varying almost arbitrary with the wheel speed as shows Table 4.12.

However, it is well known that in $Fe_{100-x}Al_x$ alloys the structural disorder causes a change of the lattice parameter in relation to the ordered structure in bulk and powdered alloys [137] as well as in alloys produced by Facing Target type DC sputtering [138]. In ribbons, our results also showed various values of lattice constants in samples produced with different wheel velocity, which may have caused different degree of structural disor-
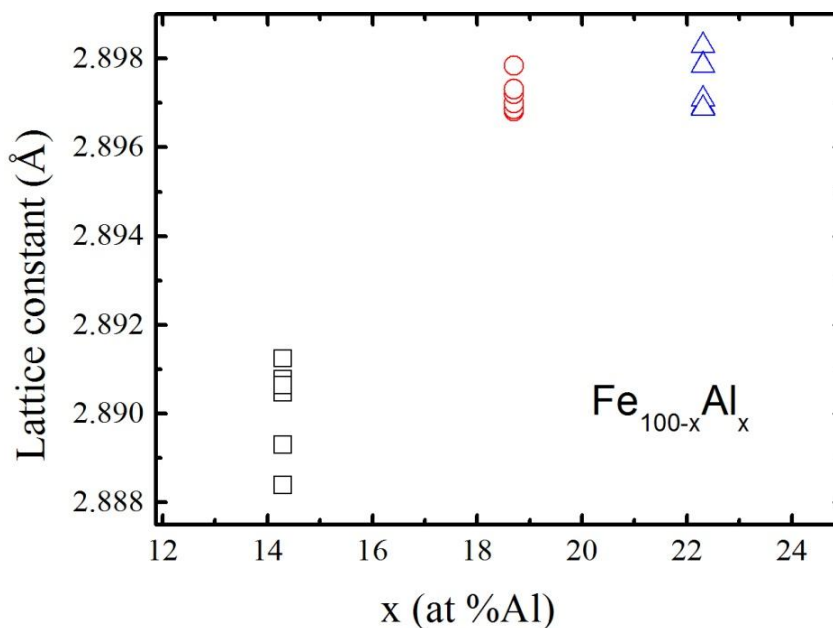
Figure 4.105: Lattice constant as a function of Al concentration in $Fe_{85.7}Al_{14.3}$, $Fe_{81.3}Al_{18.7}$ and $Fe_{77.7}Al_{22.3}$ ribbons obtained with various wheel speeds.

%Al	WS (m/s)	t (μm)	d mm	Space group	a (Å)	D (nm)
14.3	10	110	1.8	$Im\bar{3}m$	2.8908	204(52)
14.3	12.5	85	2.7	$Im\bar{3}m$	2.8884	147(53)
14.3	15	60	2.4	$Im\bar{3}m$	2.8905	248(50)
14.3	17.5	70	4.0	$Im\bar{3}m$	2.8906	112(12)
14.3	20.4	50	2.9	$Im\bar{3}m$	2.8912	408(12)
14.3	25	50	1.2	$Im\bar{3}m$	2.8893	56(10)
18.7	10	90	1.9	$Im\bar{3}m$	2.8968	191(40)
18.7	12.5	70	2	$Im\bar{3}m$	2.8969	153(30)
18.7	15	75	2	$Im\bar{3}m$	2.8971	384(10)
18.7	17.5	70	2.5	$Im\bar{3}m$	2.8972	238(68)
18.7	20.4	40	2.3	$Im\bar{3}m$	2.8973	168(30)
18.7	25	60	1.9	$Im\bar{3}m$	2.8978	573(30)
22.3	10	100	3	$Fm\bar{3}m$	2.8969	110(13)
22.3	12.5	40	2.5	$Fm\bar{3}m$	2.8983	408(12)
22.3	15	60	5	$Fm\bar{3}m$	2.8971	87(92)
22.3	17.5	40	1.8	$Fm\bar{3}m$	2.8977	538(26)
22.3	20.4	30	1.7	$Fm\bar{3}m$	2.8978	546(15)
22.3	25	60	2.5	$Fm\bar{3}m$	2.8969	208(30)

Table 4.12: Values of the average thickness and width of the ribbons, lattice constant, average crystallite size and space group determined for the wheel side of the ribbons produced with different wheel speed. Esd's in brackets.
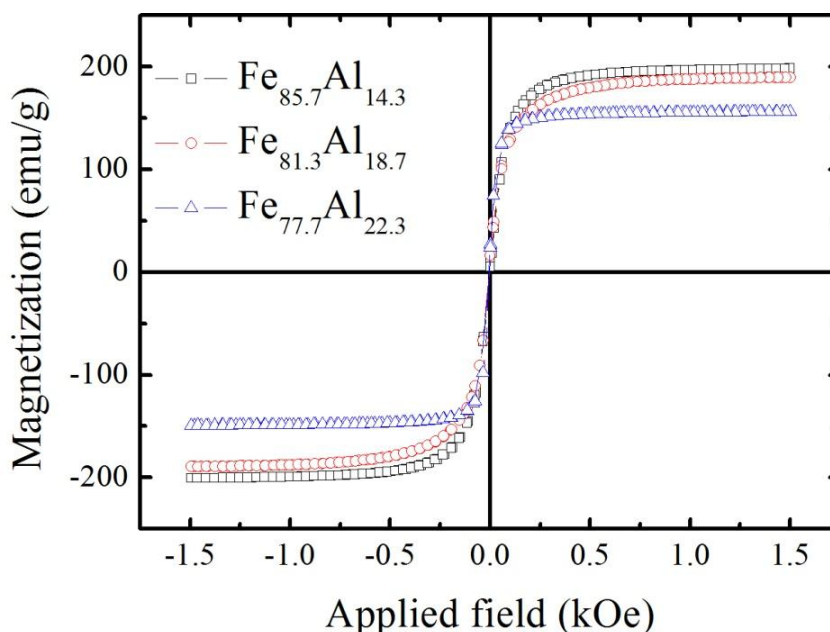
Figure 4.106: Magnetization curves measured on $Fe_{100-x}Al_x$ (x = 14.3, 18.7 and 22.3) samples

der. Figure 4.105 shows the dependence of the lattice constants versus Al concentration in $Fe_{85.7}Al_{14.3}$, $Fe_{81.3}Al_{18.7}$ and $Fe_{77.7}Al_{22.3}$ ribbons produced with different wheel speed. It can be seen that our results are in agreement with those values reported in [137, 138]. In our investigations, the error (3.esd's) of the lattice constant is less than 0.0001(Å).

4.13.2   Magnetization and Magnetostriction Measurements

The magnetization as a function of the applied field measured on $Fe_{100-x}Al_x$ (x = 14.3, 18.7 and 22.3) samples is shown in Figure 4.106. Each curve represents from the average data measured on six samples of same composition but melt spun at different WS. The saturation magnetization decreases with increase of the Al concentration. The saturation magnetization values found for $Fe_{85.7}Al_{14.3}$, $Fe_{81.3}Al_{18.7}$ and $Fe_{77.7}Al_{22.3}$ are 198 emu/g, 189 emu/g and 153 emu/g, respectively, with a deviation of 2 %.

As was mentioned before, the magnetostriction value of bulk Fe-rich $Fe_{100-x}Al_x$ alloys is also not unique for a given alloy (see e.g. Figure 4.103 and ref [122]) but depends on the production method, thermal and mechanical treatment, quenching from high temperature process of the sample studied, which results in different structural properties. In this work we could show that also for ribbons produced with different quenching rates result in different structural properties. Consequently, it is expected also for the ribbons produced at different WS obtaining different magnetostriction values. In fact, as shown in Figures 4.107, 4.108 and 4.109, where data from longitudinal and transverse magnetostriction of $Fe_{85.7}Al_{14.3}$, $Fe_{81.3}Al_{18.7}$ and $Fe_{77.7}Al_{22.3}$, respectively, are plotted the magnetostriction is depending on the wheel speed.
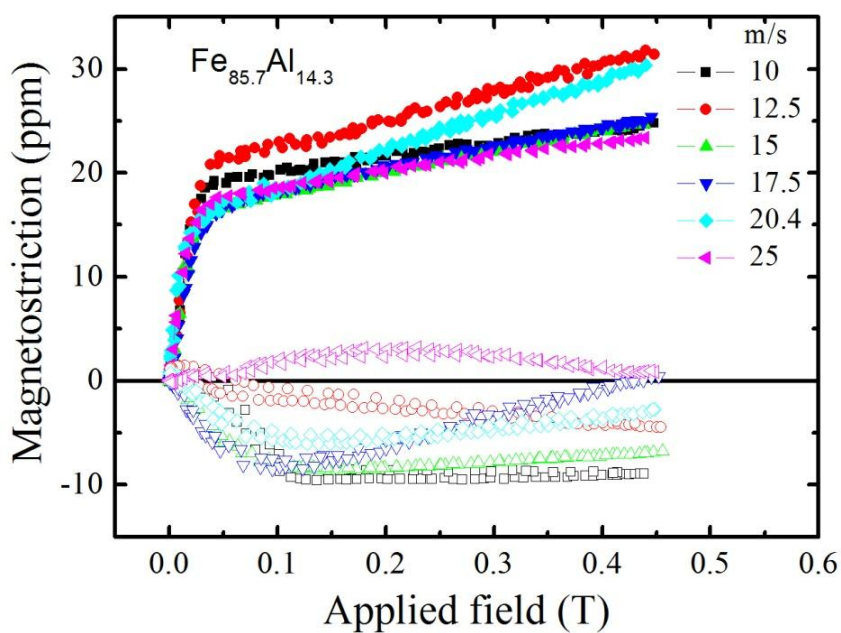
Figure 4.107: Room temperature λ_{long} and λ_{trans} of $Fe_{85.7}Al_{14.3}$ ribbons produced with different wheel speed. Full symbols represent λ_{long} and corresponding open symbols represents λ_{trans}.
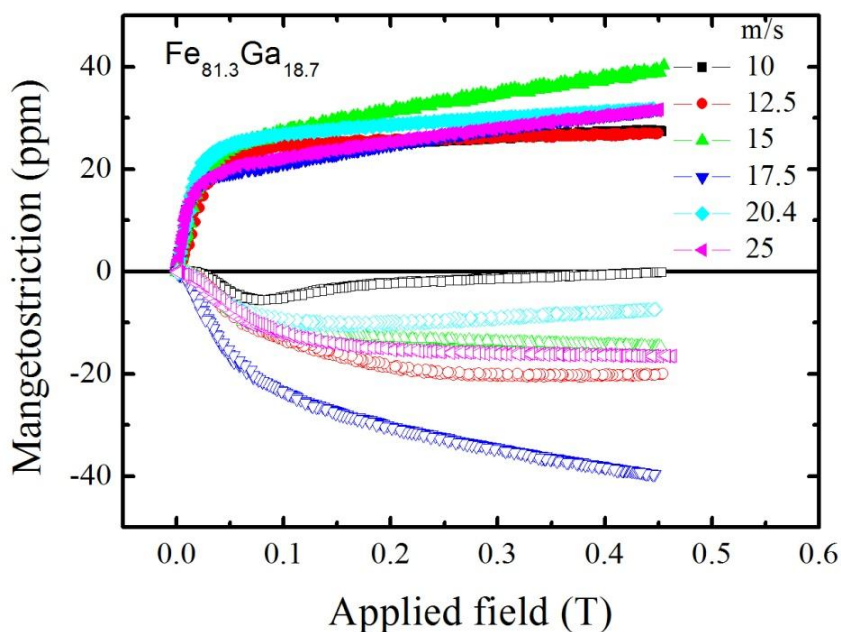
Figure 4.108: Room temperature λ_{long} and λ_{trans} of $Fe_{81.3}Al_{18.7}$ ribbons produced with different wheel speed. Full symbols represent λ_{long} and corresponding open symbols represents λ_{trans}.
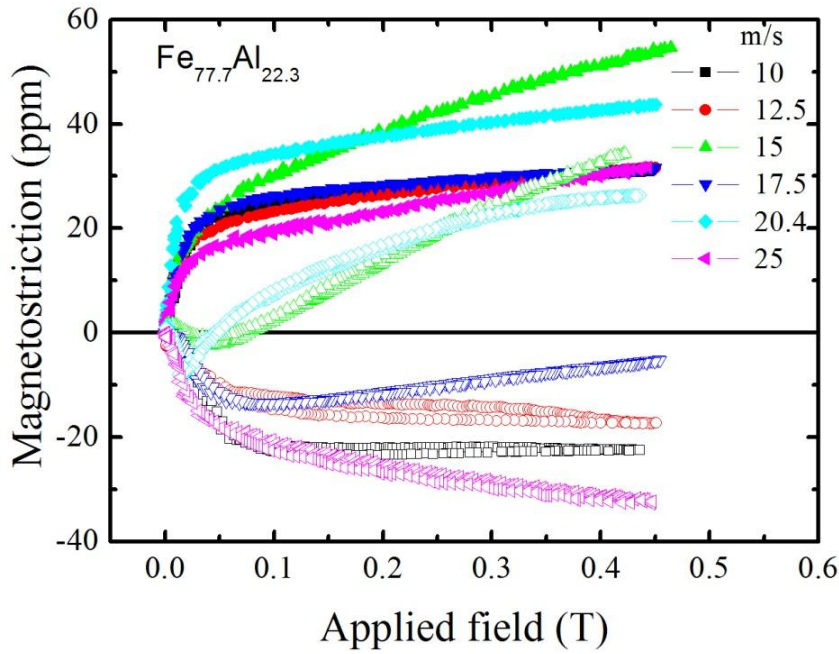
Figure 4.109: Room temperature λ_{long} and λ_{trans} of $Fe_{77.7}Al_{22.3}$ ribbons produced with different wheel speed. Full symbols represent λ_{long} and corresponding open symbols represents λ_{trans}.

For the longitudinal magnetostriction, the magnitude is dependent on the WS, however the behavior of λ_{long} vs. applied field is similar for all three alloys. On the other hand, for the transverse magnetostriction, both behavior and magnitude are strongly dependent on the wheel speed. These results indicate that due to preparation technique of ribbons by rapid quenching, different degree of stresses are frozen, which influences the domain state of the samples, consequently result in different magnetostriction behavior. The transverse magnetostriction reflects also stresses perpendicular to the ribbon axis, however the samples exhibit stronger stresses in this direction (may be, due to relatively small ribbon width!), which may cause positive or negative contribution to the transverse magnetostriction. Therefore, in our ribbons the relation $\lambda_{\text{long}} = -2\lambda_{\text{trans}}$ seldom was found, as in stress-free polycrystalline isotropic materials. Figure 4.110 shows the longitudinal and transverse magnetostriction as a function of Al concentration obtained on samples produced at different WS. The maxima λ_{long} and λ_{trans} were found for $Fe_{77.7}Al_{22.3}$, which values were 34 x 10^{-6} and -23 x 10^{-6}, respectively, which values are smaller if compared with those found for textured polycrystalline bulk materials [122] and much smaller comparing with those reported in [15] may be due to a different measuring technique [58].

It is well known that Fe-rich Fe-Al alloys exhibit forced volume magnetostriction effect (dipole magnetostriction which depends of the sample and on the demagnetization factor) which increases with increase of Al concentration showing a maximum value around a critical concentration [139]. The volume magnetostriction, λ, can be determined adding the longitudinal magnetostriction to twice the transverse magnetostriction, i.e, $\omega = \lambda_{\text{trans}} + 2\lambda_{\text{trans}}$.
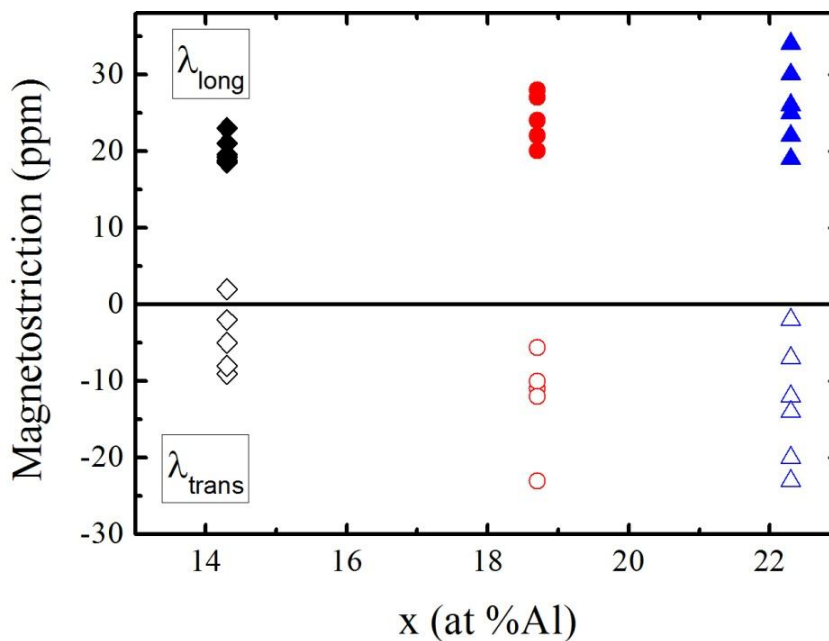
Figure 4.110: Scattered longitudinal and transverse magnetostriction obtained for $Fe_{100-x}Al_x$ (x = 14.3, 18.7 and 22.3) ribbons. The values of magnetostriction were taken at field where the linear behavior starts (at around 0.1 T).

As can be seen from Figure 4.107, Figure 4.108 and Figure 4.109, in fact, the volume magnetostriction effect becomes more frequent with increasing Al concentration.

Chapter 5

Conclusions

5.1 Fe-Ga Alloys

Severe plastic deformation (SPD) process has no significant effects on magnetostriction of $Fe_{81}Ga_{19}$ alloy. For higher deformation rates magnetostriction decreases and is larger across the solidification directions as compared to along severe plastic deformation direction. For sample deformed at higher temperature there is small increase in magnetostriction but it is not so trivial. The most important outcome was a decrease in the magnetostriction of SPD $Fe_{81}Ga_{19}$ sample as compared to coarse grain sample. $Fe_{81}Ga_{19}$ samples needs due to induced stress higher magnetic field for saturation as compared to coarse grain samples.The main problem here is possible a complicated texture due to the SPD procedure.

5.2 Fe-Al Alloys

Substituting Fe by Al increases the magnetostriction significantly. The highest value of $\lambda_{long} = 62$ ppm could be obtained for the annealed sample of 19 at% Al, where the material is almost isotropic and presents a disordered A_2 structure, with larger and more regular domains. The available magnetostriction value depends significantly on the phases A_2, B_2 or DO_3 as well as on the degree of disorder as achieved applying different heat treatments. The total magnetostriction $3/2 \, \lambda_S$ should be the same for one Al concentration (assuming an isotropic polycrystalline situation). The fact that λ_{total} varies significantly with the heat treatment can be explained in different ways: different structures or preferential alignment of crystals or a change of the stressed state. Here, especially the very high values of λ_{total} for 19 and 25 at% Al should be considered. These results suggest further experiments such as stress or field annealing of Fe–Al, which may be the methods to achieve a significant enhancement of the technically usable magnetostriction.

5.3   Fe-Mn Alloys

The addition of Mn in Fe results in an increase in magnetostriction but Fe-Mn samples requires very high magnetic field to get saturation, even samples are not saturated at field 5.2 Tesla, which makes it difficult to use Fe-Mn for practical applications in sensors and actuators. These may be a consequence of an antiferromagnetic order in Fe-Mn compounds. All the magnetostriction values measured on Fe-Mn alloys were negative irrespective of heat treatment conditions and solidification direction.

5.4   Ni-Ga Alloys

The addition of Ga in Ni does not significantly enhance the magnetostriction and for higher values of Ga addition magnetostriction decreases. This shows that the magnetostriction of Ni behaves completely different by substituting with the nonmagnetic element Ga. The fact that Fe crystallizes bcc but Ni, fcc seems to be crucial.

5.5   Sm-Fe Alloys

The cubic Laves phases $TbFe_2$ and $SmFe_2$ are the well known materials with the highest magnetostriction at room temperature. Polycrystalline $SmFe_2$ sample exhibit after heat treatment a longitudinal magnetostriction about ∼-1040 ppm at a magnetic field of 4 Tesla. The main problem here is only that $SmFe_2$ needs a rather high external field in order to develop the high magnetostriction which is a consequence of the high magnetocrystalline anisotropy of this material. Here steps to reduce the anisotropy, such as alloying or producing the material in a nanocrystalline state - are necessary in order to obtain a technically useful magnetostrictive material.

5.6   Steel Samples

All pipeline steels investigated here exhibit about 2% non-iron elements such as Mn, Si and C. Consequently the saturation magnetization shows a value which is 2% below that of pure Fe. The microstructure exhibits an average grain size between 10 and 20 μm. For the material X-52 the grains are elongated in the L-direction indicating a texture whereas for the samples X-56 and X-60 no texture is visible in the microstructure. EDX shows an inhomogeneous distribution of the additive elements. Especially carbon is found at the grain boundaries. The domains are smaller than the average grain size; they are several micrometers in size, which is typical for a soft magnetic material. The hysteresis loops as measured in a magnetically closed loop indicate clearly the longitudinal texture in these steel samples. The texture is most pronounced for the steel X-52. The shape of the

loop can be understood considering the generally higher magnetostriction in the transversal direction, which couples with the texture.

5.7   Polymer Composites

Contrary to results reported in references [107, 108], our polymer composite samples has no magnetostriction measured by bonding strain gauge on sample in Hirst pulse field magnetometer. The investigations has to be required in a static field.

5.8   Cobalt Ferrite ($CoFe_2O_4$)

Several technique (sol gel, combustion and mechanical alloying) have been used to produce polycrystalline Co-ferrite. Measurements of the longitudinal magnetostriction λ were performed and also analyzed with respect to a high sensibility of magnetostriction to applied field. The maximum magnetostriction achieved with the methods here described was 126 ppm, which are even slightly higher than the expected value compared with 2/5 of λ_{100} of a single crystal λ_{100} = -250 ppm. However for sensor applications as well as for magnetoelectric composites based on Co-ferrite, the factor $\lambda.d\lambda/dH$ is more important. A sufficient long heat treatment of the material produced by ball milling or the citrate-sol-gel method delivers the highest values of $\lambda.d\lambda/dH$ for $CoFe_2O_4$.

Microstructure, lattice constant, crystallite size, magnetization, coercivity and magnetostriction of $CoFe_2O_4$ produced by sol-gel method strongly depend on the annealing temperature.The lattice constant, crystallite size and saturation magnetization of increases with increase in sintering temperature. The coercivity of the sample decreases with increase in crystallite size and increase in annealing temperature. Saturation magnetization increases with increase in crystallite size. Magnetostriction increases gradually with increase in annealing temperature. Higher magnetostriction -124 ppm was obtained for samples annealed at 1100°C and for sample annealed at 1300°C magnetostriction decreases to value of -114 ppm.

Glycine-nitrate combustion method of synthesis is a simple, convenient and fast method for the synthesis of nanosized single phase spinel oxides. Particle size can be easily controlled by adjusting the fuel/oxidizer ratio. Almost uniform sized nano particles can be easily synthesized. The nanocrystalline particles can be sintered at high temperatures without considerable grain growth. Sintered ferrite from combustion synthesized nanocrystallites show exceptional properties. Longitudinal magnetostriction value -147 ppm was measured for sample having glycine to nitrate ratio 1.3:1 with strain derivative of 564 ppm/T.

5.9   Fe-Ga Melt Spun Ribbons and Splat Cooled Foils

Magnetostriction measurements performed on rapidly quenched ribbon-shaped samples applying the external field perpendicular to the ribbon plane using strain gauges needs special care in order to avoid bending effects. Due to the large demagnetizing factor the ribbons tend to bend into the field direction thus causing an unrealistic high magnetostriction. This can also not be avoided by gluing several ribbons to a stack-shaped sample together. Gluing ribbons together can change the magnetostriction values due to stresses induced by the glue. This can also cause hysteresis effects in magnetostriction experiments on glued samples. There are hints that in rapidly quenched material due to high disorder as well as due to a preferential crystallization perpendicular to the ribbon plane large magnetostriction values (up to more than 400 ppm) in this direction are possible. Possibly a production process (as e.g. field annealing) which leads to a preferential orientation parallel to the ribbon plane makes this high magnetostriction values technically usable.

In $Fe_{82.5}Ga_{17.5}$ ribbons, a strong dependence of the longitudinal and transverse magnetostriction on quenching rates was found. We observed a formation of (100) textured columnar grains in the temperature gradient direction, which (100) texture degree is higher at the free surface side of the ribbon. The highest value of longitudinal magnetostriction (116 ppm) was found for the ribbon exhibiting the highest (100) texture, which ribbon was obtained with wheel velocity of 15 m/s.

5.10   Fe-Al Melt Spun Ribbons

Fe-Al The ribbons produced with different solidification rate exhibit different structural properties such as grain size and lattice constant and also different magnetostriction values. Although our ribbons do not present columnar particles and texture, the relation $\lambda_{long}=-2\lambda_{trans}$, which is typical relation for the polycrystalline materials, was not fulfilled almost for all samples.

5.11   Conclusion-Highlights

- No significance increase in magnetostriction values occurred in $Fe_{81}Ga_{19}$ alloy due to SPD phenomenon.

- The highest longitudinal magnetostriction was measured in slow cooled $Fe_{81}Al_{19}$ ($\lambda_{long} \approx 62$ ppm) and strong dependence magnetostriction on heat treatment was found.

- Bulk $SmFe_2$ has magnetostriction value of -1040 ppm at very high field 4 Tesla.

- The addition of Ga in Ni does not significantly enhance the magnetostriction and as in case of Ga addition in Fe.

- The addition of Mn in Fe results in an increase in magnetostriction, however requires very in high magnetic field (more than 5T) for the saturation.

- Polymeric composite containing nano and micro carbon fiber, shows zero magnetostriction, in pulse field.

- Pipeline steels exhibit a texture in the direction of the tube axis. The saturation magnetization is about 210 emu/g which is 2% below that of pure Fe. The shape of the loop agrees well with the microstructure and the magnetostrictive behavior. This is in agreement with magnetostriction measurements which also show higher values in the transversal direction.

- $CoFe_2O_4$ sample, prepared by combustion method have longitudinal magnetostriction value of -147 ppm.

- For applying external field perpendicular to the ribbons plane it is demonstrated that bending effects can occur, which leads to large signals in the strain gauge of more than $\pm$ 3000 ppm, in our case magnetostriction in ribbon samples were found to be consistent with bulk materials.

- For $Fe_{82.5}Ga_{17.5}$ alloy magnetostriction values strongly depends on the quenching rate. The dependence of the longitudinal magnetostriction with wheel speed exhibits a maximum of about 116 ppm at 15 m/s ribbons.

- The magnetostriction in Fe-Al melt spun ribbons only found to be only up to 34 ppm, approx. four time less as compared to Fe-Ga alloys ribbons.

Bibliography

[1] A.E. Clark. *Magnetostrictive rare earth-Fe2 Compounds (Ferromagnetic Materials: A Handbook on the Properties of Magnetically Ordered Substances)*, volume 1. North-Holland Publishing Company, 1980.

[2] J.L. Butler. Application manual for the design of etrema Terfenol-D magnetostrictive transducers. Technical report, Etrema Poducts, Inc. Ames, Iowa, 1988.

[3] A.E. Clark, M. Wun-Fogle, J.B. Restorff, and T.A. Lograsso. Magnetic and magnetostrictive properties of Galfenol alloys under large compressive stresses. In *International Symposium on Smart Materials-Fundamentals and System Applications, Pacific Rim Conference on Advanced Materials and Processing (PRICM-4) Honolulu, Hawaii*, 2001.

[4] A.E. Clark, M. Wun-Fogle, J.B. Restorff, T.A. Lograsso, and J.R. Cullen. Effect of quenching on the magnetostriction of Fe1-xGax(0.13 < x < 0.21). *IEEE Transactions on Magnetics*, 37(4 I):2678–2680, 2001. cited By (since 1996) 80.

[5] J.R. Cullen, A.E.Clark, M. Wun-Fogle, J.B. Restorff, and T.A Lograsso. Magnetoelasticity of Fe-Ga and Fe-Al alloys. *Journal of Magnetism and Magnetic Materials*, 226-230 (Part-1):948–949, 2001.

[6] E.M. Summers, T.A Lograsso, and M. M. Wun-Fogle. Magnetostriction of binary and ternary Fe-Ga alloys. *Journal of Materials Science*, 42(23):9582–9594, 2007. cited By (since 1996) 7.

[7] R.A Kellogg, A.B. Flatau, A.E. Clark, M. Wun-Fogle, and T.A Lograsso. Texture and grain morphology dependencies of saturation magnetostriction in rolled polycrystallineFe83Ga17. *Journal of Applied Physics*, 93(10 3):8495–8497, 2003. cited By (since 1996) 14.

[8] R.A. Kellogg. *Development and Modeling of Iron-Gallium alloys*. PhD thesis, Engineering Mechanics, Lowa State University, Ames, Iowa, 2003.

[9] R.A Kellogg, A.M. Russell, T.A. Lograsso, A.B. Flatau, A.E. Clark, and M. Wun-Fogle. Tensile properties of magnetostrictive Iron-Gallium alloys. *Acta Materialia*, 52(17):5043–5050, 2004. cited By (since 1996) 21.

[10] N. Srisukhumbowornchai and S. Guruswamy. Large magnetostriction in directionally solidified FeGa and FeGaAl alloys. *Journal of Applied Physics*, 90(11):5680–5688, 2001. cited By (since 1996) 67.

[11] S.F. Cheng, B.N. Das, M. Wun-Fogle, P. Lubitz, and A.E. Clark. Structure of melt-spun Fe-Ga-based magnetostrictive alloys. *IEEE Transactions on Magnetics*, 38(5 I):2838–2840, 2002. cited By (since 1996) 21.

[12] M.C. Zhang, X.X. Gao, H.L. Jiang, J. Zhu, S.Z. Zhou, X.P. Hao, , and B.Y. Wang. Atomic vacancies in Fe81Ga19 ribbons and its effect on the magnetostrictions. *Journal of Alloys and Compounds*, 450(1-2):28–30, 2008. cited By (since 1996) 0.

[13] R.C. Hall. Magnetostriction of aluminum-iron single crystals in the region of 6 to 30 atomic percent Aluminum. *Journal of Applied Physics*, 28(6):707–713, 1957. cited By (since 1996) 18.

[14] R.C. Hall. Single crystal anisotropy and magnetostriction constants of several ferromagnetic materials including alloys of NiFe, SiFe, AlFe, CoNi, and CoFe. *Journal of Applied Physics*, 30(6):816–819, 1959. cited By (since 1996) 35.

[15] Z.H. Liu, G.D Liu, M. Zhang, G.H Wu, F.B Meng, H.Y Liu, L.Q Yan, J.P Qu, and Y.X. Li. Large magnetostriction in Fe100-xAlx (15<x<30) melt-spun ribbons. *Applied Physics Letters*, 85(10):1751–1753, 2004. cited By (since 1996) 6.

[16] O. Caltun, I. Dumitru, M. Feder, N. Lupu, and H. Chiriac. Substituted cobalt ferrites for sensors applications. *Journal of Magnetism and Magnetic Materials*, 320(20):e869–e873, 2008. cited By (since 1996) 0.

[17] D.C. Jiles. *Introduction to Magnetism and Magnetic Materials*. Chapman and Hall, 1991.

[18] Tetsuya; Smith Leslie M. (Eds.) Czichos, Horst; Saito, editor. *Springer Handbook of Materials Measurement Methods*. Springer Berlin Heidelberg, 2006.

[19] M.J. Dapino. *Magnetostrictive materials: their use in smart structure applications*. Encyclopedia of Smart Materials. John Wiley & Sons, Inc., New York, 2000.

[20] S. Chikazumi. *Physics of Magnetism*. John Wiley and Sons, Inc.,, 1964.

[21] J. Atulasimha. *Characterization and modeling of the magnetomechanical behavior of Iron-Gallium alloys*. PhD thesis, Faculty of the Graduate School of the University of Maryland, 2006.

[22] A.G. Olabi and A.Grunwald. Design and application of magnetostrictive materials. *Materials & Design*, 29(2):469–483, 2008.

[23] K. Honda and S. Kaya. On the magnetization of single crystals of Iron. *Sci. Rep.Tohoku Univ*, 15, 1926.

[24] S. Kaya. On the magnetization of single crystals of Nickel. *Sci. Rep.Tohoku Univ*, 1928.

[25] M. Getzlaff. *Fundamentals of Magnetism*. Springer, 2007.

[26] G. Engdahl. *Handbook of giant magnetostrictive materials*. Academic Press, 2000.

[27] J.R Cullen. Materials with large magnetostrains. *Scripta Metallurgica et Materialia Proceedings of an Acta Metallurgica Meeting on Novel Magnetic Structures and Properties*, 33 (10-11):1849–1867, 1995.

[28] J.P. Joule. On a new class of magnetic forces. *Ann. Electr. Magn*, Chem. 8, 1842.

[29] J.P. Joule. On the effects of magnetism upon the dimensions of iron and steel bars. *Phil. Mag.*, pages 76–87 and 225–241, 1847.

[30] N.S. Akulov. Uber die anwendungen des gesetzes ferromagnetischer anisotropie zur berechnung der eigenschaften polykristallinischen eisens, 1930.

[31] K.H.J. Buschow and F.R. de Boer. *Physics of Magnetism and Magnetic Materials*. Kluwer Academic Publishers, 2004.

[32] N.B. Ekreem, A.G Olabi, T. Prescott, A. Rafferty, and M.S.J. M.SJ. Hashmi. An overview of magnetostriction, its use and methods to measure these properties. *Journal of Materials Processing Technology*, 191(1-3):96–101, 2007. cited By (since 1996) 2.

[33] A.E Clark. Structural Fe-based alloys with high magnetostriction. Galfenol Workshop, 2004. Presentation.

[34] D. C. Jiles. Theory of the magnetomechanical effect. *Journal of Physics D: Applied Physics*, 8:1537, 1995.

[35] M.J. Dapino, R.C. Smith, F.T. Calkins, and A.B. Flatau. A coupled magnetomechanical model for magnetostrictive transducers and its application to villari-effect sensors. *Journal of Intelligent Material Systems and Structures*, 13(11):737–747, 2002. cited By (since 1996) 6.

[36] E. A. Lindgren, S. Haroush, J. C. Poret, A. D. Mazzatesta, M. Rosen, M. Wun-Fogle, J. B. Restorff, A. E. Clark, and J. F. Lindberg. Development of Terfenol-D transducer material. volume 83, pages 7282–7284. AIP, 1998.

[37] R.M. Bozorth. *Ferromagnetism*. D. Van Nostrand, Inc., 1968.

[38] E. Du Tremolet de Lacheisserie. *Magnetostriction : theory and applications of magnetoelasticity*. CRC Press, 1993.

[39] E.W. Lee. Magnetostriction and magnetomechanical effects. *Reports on Progress in Physics*, 18(1):184–229, 1955.

[40] W. C Thoburn, S. Legvold, and F.H Spedding. Magnetic properties of Terbium metal. *Physical Review (American Physical Society)*, 112, 1958.

[41] D.R. Behrendt, S. Legvold, and F.H. Spedding. Magnetic properties of Dysprosium single crystals. *Physical Review (American Physical Society)*, 109 (5):1544, 1958.

[42] D. Gignoux E.du.T.de Lacheisserie and and M. Schlenker, editors. *Magnetism: Materials and Applications*. Springer (Grenoble Sciences), 2005.

[43] A.E. Clark, , M. Wun-Fogle, J.B. Restorff, T.A.Lograsso, and G.Petculescu. Magnetostriction and elasticity of body centered cubic Fe100 - xBe x alloys. *AIP*, 95:6942–6944, 2004.

[44] J.B. Restorff, M. Wun-Fogle, A.E. Clark, T.A. Lograsso, A.R. Ross, and D.L. Schlagel. Magnetostriction of ternary Fe-Ga-X alloys (X = Ni,Mo,Sn,Al). *Journal of Applied Physics*, 91(10 III):8225, 2002.

[45] L. Dai, J. Cullen, M. Wuttig, T T. Lograsso, and E. Quandt. Magnetism, elasticity, and magnetostriction of FeCoGa alloys. *Journal of Applied Physics*, 93 (10):8627–8629, 2003.

[46] J.G. Benatar. FEM implementations of magnetostrictive-based applications. Master's thesis, Faculty of the Graduate School of the University of Maryland, College Park, 2005.

[47] E. Tatsumoto and T. Okamoto. Temperature dependence of the magnetostriction constants in Iron and Silicon Iron. *J. Phys. Soc. Jpn.*, 14:1588–1594, 1959.

[48] H.B. Callen and E.R. Callen. Theory of high-temperature magnetostriction. *Physical Review*, 132(3):991–996, 1963. cited By (since 1996) 2.

[49] Landolt-Börnstein. New series ii. *Landolt-Börnstein*, 1961.

[50] R.C. Hall. Single-crystal magnetic anisotropy and magnetostriction studies in iron-base alloys. *Journal of Applied Physics*, 31(6):1037–1038, 1960. cited By (since 1996) 16.

[51] A.E. Clark, J.B. Restorff, M. Wun-Fogle, T.A Lograsso, and D.L. Schlagel. Magnetostrictive properties of body-centered cubic Fe-Ga and Fe-Ga-Al alloys. *IEEE Transactions on Magnetics*, 36(5 I):3238–3240, 2000. cited By (since 1996) 142.

[52] O. Ikeda, R. Kainuma, I. Ohnuma, K. Fukamichi, and K. Ishida. Phase equilibria and stability of ordered b.c.c. phases in the Fe-rich portion of the Fe-Ga system. *Journal of Alloys and Compounds*, 347(1-2):198–205, 2002. cited By (since 1996) 50.

[53] A.E. Clark, K.B Hathaway, M. Wun-Fogle, J.B. Restorff, T.A. Lograsso, V.M. Keppens, G. Petculescu, and R.A. Taylor. Extraordinary magnetoelasticity and lattice softening in bcc Fe-Ga alloys. *Journal of Applied Physics*, 93(10 3):8621–8623, 2003. cited By (since 1996) 88.

[54] Y. Furuya, C. Saito, and T. Okazaki. Large magnetostriction in Fe-Ga rapid-solidified alloy. *Nippon Kinzoku Gakkaishi/Journal of the Japan Institute of Metals*, 66(9):901–904, 2002. cited By (since 1996) 8.

[55] M. Zhang, X. Gao, H. Jiang, J. Zhu, and S. Zhou. Magnetostriction and microstructure of the melt-spun Fe83Ga17 alloy ribbons. *Frontiers of Materials Science in China*, 1(1):54–58, 2007. cited By (since 1996) 0.

[56] M.C. Zhang, X.X. Gao, H.L Jiang, Y. Qiao, and S.Z. Zhou. Effect of Ga content on the magnetostriction and microstructure of Fe-Ga ribbons. *Journal of Alloys and Compounds*, 431(1-2):42–44, 2007. cited By (since 1996) 7.

[57] G.D Liu, B.L Liu, Z.H. Liu, M. Zhang, J.L. Chen, J.Q Li, G.H Wu, Y.X. Li, J.P Qu, and T.S. Chin. Giant magnetostriction on Fe85Ga15 stacked ribbon samples. *Applied Physics Letters*, 84(12):2124–2126, 2004. cited By (since 1996) 25.

[58] R. Grössinger, R. Sato Turtelli, N. Mehmood, S. Heiss, H. Müller, and C. Bormio-Nunes. Giant magnetostriction in rapidly quenched Fe-Ga? *Journal of Magnetism and Magnetic Materials*, 320 (20):2457–2465, 2008.

[59] L. Libao, F. Shiyou, L. Guodong, W. Guangheng, S. Xiudong, and L. Jianqi. Transmission electron microscopy study on the microstructure of Fe85Ga15 alloy. *Physica B: Condensed Matter*, 365(1-4):102–108, 2005. cited By (since 1996) 2.

[60] S. Pascarelli, M.P. Ruffoni, R. Sato Turtelli, F. Kubel, and R. Grossinger. Local structure in magnetostrictive melt-spun Fe80 Ga20 alloys. *Physical Review B - Condensed Matter and Materials Physics*, 77(18), 2008. cited By (since 1996) 0.

[61] R. Grössinger, R. Sato Turtelli, and N. Mehmood. Magnetostriction of Fe-X (X =Al,Ga,Si, Ge) intermetallic alloys. *IEEE Transactions on Magnetics*, 44(11):3001–3004, 2008.

[62] H.J. Leamy, E.D. Gibson, and F.X. Kayser. The elastic stiffness coefficients of iron-aluminum alloys-i experimental results and thermodynamic analysis. *Acta Metallurgica*, 15(12):1827–1838, 1967. cited By (since 1996) 58.

[63] J.M Cook and A.S. Pavlovic. Magnetostriction and thermal expansion of single crystal and polycrystalline alloys of iron and aluminum in the vicinity of Fe3Al. *Journal of Applied Physics*, 55(2):499–502, 1984. cited By (since 1996) 2.

[64] A.E. Clark, J.B. Restorf, M. Wun-Fogle, D. Wu, and T.A. Lograsso. Temperature dependence of the magnetostriction and magnetoelastic coupling in Fe100-x Alx (x=14.1,16.6,21.5,26.3) and Fe50 Co50. *Journal of Applied Physics*, 103(7), 2008. cited By (since 1996) 0.

[65] R.Gersdorf. *On Magnetostriction of Single Crystals of Iron and Some Dilute Iron Alloys*. PhD thesis, The University of Amsterdam., 1961.

[66] A. Fairweather, F.F. Roberts, and A.J.E. Welch. Ferrites. *Reports on Progress in Physics*, 15(1):142–172, 1952. cited By (since 1996) 4.

[67] Jr William D. Callister. *Materials Science and Engineering: An Introduction*. John Wiley & Sons, Inc,, 2003.

[68] N. Spaldin. *Magnetic materials: Fundamentals and device applications*. Cambridge University press, 2003.

[69] D.S Mathew and R.S. Juang. An overview of the structure and magnetism of spinel ferrite nanoparticles and their synthesis in microemulsions. *Chemical Engineering Journal*, 129(1-3):51–65, 2007. cited By (since 1996) 7.

[70] C.R. Vestal and Z.J. Zhang. Magnetic spinel ferrite nanoparticles from microemulsions. *International Journal of Nanotechnology*, 1(1-2):240–263, 2004. cited By (since 1996) 19.

[71] K.J Davies, S. Wells, R.V. Upadhyay, S.W. Charles, K. O'Grady, M. El Hilo, and S. Mrup T. Meaz. The observation of multi-axial anisotropy in ultrafine Cobalt Ferrite particles used in magnetic fluids. *Journal of Magnetism and Magnetic Materials*, 149(1-2):14–18, 1995. cited By (since 1996) 54.

[72] V. Pillai and D.O. Shah. Synthesis of high-coercivity cobalt ferrite particles using water-in-oil microemulsions. *Journal of Magnetism and Magnetic Materials*, 163(1-2):243–248, 1996. cited By (since 1996) 108.

[73] J.W.D Martens, W.L. Peeters, H.M. Van Noort, and M. Erman. Optical, magneto-optical and mossbauer spectroscopy on co3+ substituted cobalt ferrite Co2+Fe2-xCo3+ xO4(0 < x < 2). *Journal of Physics and Chemistry of Solids*, 46(4):411–416, 1985. cited By (since 1996) 38.

[74] S.N. Okuno, S. Hashimoto, and K. Inomata. Preferred crystal orientation of cobalt ferrite thin films induced by ion bombardment during deposition. *Journal of Applied Physics*, 71(12):5926–5929, 1992. cited By (since 1996) 44.

[75] F. Bodker, S. Morup, and S. Linderoth. Surface effects in metallic iron nanoparticles. *Physical Review Letters*, 72(2):282–285, 1994. cited By (since 1996) 258.

[76] C.V. Gopal Reddy, S.V. Manorama, and V.J Rao. Preparation and characterization of ferrites as gas sensor materials. *Journal of Materials Science Letters*, 19(9):774–778, 2000. cited By (since 1996) 8.

[77] Dennis K.W. Jiles D.C. Snyder J.E. Chen Y.H. McCallum, R.W. Composite magnetostrictive materials for advanced automotive magnetomechanical sensors. *Low Temperature Physics*, 27(4):266–274, 2001. cited By (since 1996) 15.

[78] D.C. Jiles and C.C.H. Lo. The role of new materials in the development of magnetic sensors and actuators. *Sensors and Actuators, A: Physical*, 106(1-3):3–7, 2003. cited By (since 1996) 18.

[79] Y. Chen, J.E. Snyder, K.W. Dennis, R.W. McCallum, and D.C Jiles. Temperature dependence of the magnetomechanical effect in metal-bonded cobalt ferrite composites under torsional strain. *Journal of Applied Physics*, 87(9 II):5798–5800, 2000. cited By (since 1996) 17.

[80] J.A Paulsen, A.P. Ring, C.C.H Lo, J.E. Snyder, and D.C. Jiles. Manganese-substituted cobalt ferrite magnetostrictive materials for magnetic stress sensor applications. *Journal of Applied Physics*, 97(4):044502–1–044502–3, 2005. cited By (since 1996) 27.

[81] S.D. Bhame and P.A. Joy. Enhanced magnetostrictive properties of Mn substituted cobalt ferrite $Co_{1.2}Fe_{1.8}O_4$. *Journal of Applied Physics*, 99(7), 2006. cited By (since 1996) 9.

[82] S.D. Bhame and P.A. Joy. Tuning of the magnetostrictive properties of $CoFe_2O_4$ by Mn substitution for Co. *Journal of Applied Physics*, 100(11), 2006. cited By (since 1996) 7.

[83] Y.Ghen, J.E. Snyder, C.R. Schwichtenberg, and K.W. Dennis. Metal-bonded Co-Ferrite composites for magnetostrictive torque sensor applications. *IEEE Transactions on Magnetics*, 35(5 PART 2):3652–3654, 1999. cited By (since 1996) 35.

[84] A. Goldman. *Modern Ferrite Technology*. Van Nostrand Reinhold, 1990.

[85] T. Nakamura. Low-temperature sintering of Ni-Zn-Cu ferrite and its permeability spectra. *Journal of Magnetism and Magnetic Materials*, 168(3):285–291, 1997. cited By (since 1996) 107.

[86] F. Cheng, Z. Peng, C. Liao, Z. Xu, S. Gao, C. Yan, D. Wang, and J. Wang. Chemical synthesis and magnetic study of nanocrystalline thin films of cobalt spinel ferrites. *Solid State Communications*, 107(9):471–476, 1998. cited By (since 1996) 33.

[87] Z.H. Zhou, J. M. Xue, J.Wang, H.S.O Chan, T. Yu, and Z.X. Shen. $NiFe_2O_4$ nanoparticles formed in situ in silica matrix by mechanical activation. *Journal of Applied Physics*, 91(9):6015, 2002. cited By (since 1996) 40.

[88] J. Gwak, A. Ayral, V. Rouessac, L. Cot, J.C. Grenier, and J.H. Choy. Synthesis and characterization of porous ferrimagnetic membranes. *Microporous and Mesoporous Materials*, 63(1-3):177–184, 2003. cited By (since 1996) 5.

[89] L.A. Garcia-Cerda, V.A. Torres-Garcia, J.A. Matutes-Aquino, and O.E. Ayala-Valenzuela. Magnetic nanocomposites: Preparation and characterization of Co-Ferrite nanoparticles in a silica matrix. *Journal of Alloys and Compounds*, 369(1-2):148–151, 2004.

[90] C.H. Yan, Z.G. Xu, F.S. Cheng, Z.M Wang, S.S Liao L.D Sun, and J.T Jia. Nanophased $CoFe_2O_4$ prepared by combustion method. *Solid State Communications*, 111(5):287–291, 1999. cited By (since 1996) 48.

[91] S.Li, L. Liu, V.T. John, C.J. O'Connor, and V.G. Harris. Cobalt-ferrite nanoparticles: Correlations between synthesis procedures, structural characteristics and magnetic properties. *IEEE Transactions on Magnetics*, 37(4 I):2350–2352, 2001. cited By (since 1996) 18.

[92] X. Li and C. Kutal. Synthesis and characterization of superparamagnetic $Co_xFe_{3-x}O_4$ nanoparticles. *Journal of Alloys and Compounds*, 349(1-2):264–268, 2003. cited By (since 1996) 32.

[93] S.M Montemayor, L.A. Garcia-Cerda, and J.R. Torres-Lubian. Preparation and characterization of Cobalt Ferrite by the polymerized complex method. *Materials Letters*, 59(8-9):1056–1060, 2005. cited By (since 1996) 13.

[94] T. Pannaparayil, S. Komarneni, R. Marande, and M. Zadarko. Subdomain zinc ferrite particles: Synthesis and characterization. *Journal of Applied Physics*, 67(9):5509–5511, 1990. cited By (since 1996) 11.

[95] G.B Ji, S.L. Tang, S.K. Ren, F.M. Zhang, B.X . Gu, and Y.W Y.W. Simplified synthesis of single-crystalline magnetic CoFe2O 4 nanorods by a surfactant-assisted hydrothermal process. *Journal of Crystal Growth*, 270(1-2):156–161, 2004. cited By (since 1996) 26.

[96] S.S Hayrapetyan and H.G. Khachatryan. Porosity appearance in Cobalt Ferrite and changes under the thermal treatment of co-precipitated iron(ii) and cobalt(ii) oxalates. *Microporous and Mesoporous Materials*, 72(1-3):105–110, 2004. cited By (since 1996) 4.

[97] S.Arul Antony, K.S. Nagaraja, and O.M. Sreedharan. Preparation of 15 molpolymeric gel-combustion method. *Journal of Nuclear Materials*, 295(2-3):189–192, 2001. cited By (since 1996) 8.

[98] Z.X. Yue, J.H. Shan, X.W. Qi, X.H. Wang, J. Zhou, Z.L. Gui, and L.T.Li. Synthesis of nanocrystalline manganite powders via a gel auto-combustion process for NTC thermistor applications. *Materials Science and Engineering B: Solid-State Materials for Advanced Technology*, 99(1-3):217–220, 2003. cited By (since 1996) 5.

[99] L.A. Chick, L.R.Pederson, G.D. Maupin, J.L. Bates, L.E.Thomas, and G.J Exarhos. Glycine-nitrate combustion synthesis of oxide ceramic powders. *Materials Letters*, 10(1-2):6–12, 1990. cited By (since 1996) 503.

[100] H.C. Yi and J.J. Moore. Self-propagating high-temperature (combustion) synthesis (SHS) of powder-compacted materials. *Journal of Materials Science*, 25(2):1159–1168, 1990.

[101] V. Hlavacek. Combustion synthesis: A historical perspective. *Ceram. Bull.*, 70(2):240–243, 1991.

[102] T. Ye, Z. Guiwen, Z. Weiping, and X. Shangda. Combustion synthesis and photoluminescence of nanocrystalline Y2O3:Eu phosphors. *Materials Research Bulletin*, 32(5):501–506, 1997. cited By (since 1996) 168.

[103] C. Suryanarayana. Mechanical alloying and milling. *Progress in Materials Science*, 46(1-2):1–184, 2001. cited By (since 1996) 1312.

[104] C.C.H Lo, A.P. Ring, J.E Snyder, and D.C Jiles. Improvement of magnetomechancial properties of Cobalt Ferrite by magnetic annealing. *IEEE Transactions on Magnetics*, 41(10):3676–3678, 2005. cited By (since 1996) 7.

[105] J.A Paulsen, C.C.H Lo, J.E. Snyder, A.P. Ring, L.L Jones, , and D.C. Jiles. Study of the curie temperature of cobalt ferrite based composites for stress sensor applications. *IEEE Transactions on Magnetics*, 39(5 II):3316–3318, 2003. cited By (since 1996) 7.

[106] O. Caltun, G.S.N. Rao, B. K.H.Parvatheeswara Rao, I. Dumitru, C.O Kim, and C. Kim. The influence of Mn doping level on magnetostriction coefficient of cobalt ferrite. *Journal of Magnetism and Magnetic Materials*, 316(2 SPEC. ISS.):e618–e620, 2007. cited By (since 1996) 7.

[107] D. Nai-Xiu and Z. Mao-Sheng. Magnetostrictive properties of carbon black filled polypropylene composites. *Polymer Testing*, 23(5):523–526, 2004. cited By (since 1996) 1.

[108] D. Nai-Xiu, D.M Sheng, and Z.P.X Wang. Magnetostrictive properties of carbon fiber filled polypropylene composites. *Polymer Testing*, 24(5)(5):635–640, 2005. cited By (since 1996) 1.

[109] J.M Makar and B.K. Tanner. Effect of plastic deformation and residual stress on the permeability and magnetostriction of steels. *Journal of Magnetism and Magnetic Materials*, 222(3):291–304, 2000. cited By (since 1996) 24.

[110] R. Grössinger, F. Keplinger, N. Mehmood, J.H. Araujo, Espina-Hernandez, C. Eisenmenger, K. Poppenberger, and J.M. Hallen. Magnetic and microstructural investigations of pipeline steels. *Magnetics, IEEE Transactions on*, 44(11):3277–3280, 2008.

[111] H. Kronmuller and M. Fahnle. *Micromagnetism and the Microstructure of Ferromagnetic Solids.* Cambridge University Press, 2003.

[112] E. Kneller. Ferromagnetismus. *NA*, page 512, 1962.

[113] W.Y. Peng and J.H. Zhang. Magnetostriction studies in an antiferromagnetic polycrystalline Mn42Fe58 alloym. *Applied Physics Letters*, 89(26), 2006. cited By (since 1996) 2.

[114] M. Yan, J. Zhang, T. Ma, and Y. Xu. Magnetostriction studies on antiferromagneticMnxFe100-x (30<x<55) alloys. In *Intermag Madrid, Spain*, 2008.

[115] Mario Faleschini. *Severe Plastic Deformation of Tungsten Alloy and its Influence on Fracture Behavior.* PhD thesis, Erich Schmid Institute of Materials Science, Austrian Academy of Sciences Department of Materials Physics, 2006.

[116] R. Grössinger, N. Mehmood, G. Senbaslar, M. Atif, R. Sato Turtelli, W. Linert, and F. Kubel. Co-ferrite: A material with high magnetostriction produced by different methods. In *REPM08, Rare Earth Permanent Magnets and Applications (Creta Greece)*, 2008.

[117] H.G. Jiang, M. Rühle, and E.J. Lavernia. On the applicability of the X-ray diffraction line profile analysis in extracting grain size and micro-strain in nanocrystalline materials. *Journal of Materials Research*, 14(2):549–559, 1999.

[118] R. Grössinger. Hirst pulsed field magnetometer. Technical report, Institute of Solid State Physics, Vienna University of technology, Austria.

[119] E.W. Lee. *Experimental Magnetism*. John Wiley and Son, 1979.

[120] M. Rotter, H. Muller, E. Gratz, M. Doerr, and M. Loewenhaupt. A miniature capacitance dilatometer for thermal expansion and magnetostriction. *Review of Scientific Instruments*, 69(7):2742–2746, 1998. cited By (since 1996) 46.

[121] G. Vlasak. Direct measurement of magnetostriction of rapidly quenched thin ribbons. *Journal of Magnetism and Magnetic Materials*, 215:479–481, 2000.

[122] N. Mehmood, R. Sato Turtelli, R. Grossinger, and M. Kriegisch. Magnetostriction of polycrystalline Fe100-xAlx (x=15, 19, 25). *Journal of Magnetism and Magnetic Materials*, In Press, Corrected Proof:–, 2009.

[123] A.E. Clark and H.S. Belson. Giant room-temperature magnetostrictions in TbFe2 and DyFe2. *Physical Review B (American Physical Society)*, 5 (9):3642, 1972.

[124] M.A. Anjanappa and J. Jie. Modeling, design, and control of embedded Terfenol-D actuator. In *Proc. SPIE Vol. 1917, p. 908-918, Smart Structures and Materials : Smart Structures and Intelligent Systems, Nesbitt W. Hagood; Ed.*, 1993.

[125] J.W. Xie, D. Fort, and J.S Abell. The preparation, microstructures and magnetostrictive properties of Samfenol-D. *Journal of Alloys and Compounds*, 366(1):241–247, 2004.

[126] API specifcations 5L specification for line pipes.

[127] E45-05 standard test method for determining inclusion in steels.

[128] M. Atif. Measurements were performed by Muhammad Atif., 2008.

[129] M. Rozman and M. Drofenik. Sintering of nanosized MnZn ferrite powders. *Journal of the American Ceramic Society*, 91 (7):1757–1764, 1988.

[130] A.E. Berkowitz and W.J. Schuele. Magnetic properties of some ferrite micropowders. *Journal of Applied Physics*, 30:134–135, 1959.

[131] T. Okazaki, Y. Furuya, C. Saito, T. Watanabe, and M. Wuttig. New development of rapid-solidified Fe-Ga sensor/actuator alloy. In *Stormining Media /(http://www.dtic.mil/cgi-bin/)*, 1998.

[132] K.H.J. Buschow, P.G. van Engen, and R. Jongebreur. Magneto-optical properties of metallic ferromagnetic materials. *Journal of Magnetism and Magnetic Materials*, 38(1):1–22, 1983. cited By (since 1996) 138.

[133] S. Heiss. Measurements were performed by Stephen Heiss., 2006.

[134] C. Bormio-Nunes, R. Sato Turtelli, H.Muller, R. Grossinger, H. Sassik, and M.A. Tirelli. Magnetostriction and structural characterization of Fe-Ga-X (X=Co,Ni, Al) mold-cast bulk. *Journal of Magnetism and Magnetic Materials*, 290-291 PART 2:820–822, 2005. cited By (since 1996) 3.

[135] N. Mehmood, G. Vlasak, F. Kubel, R. Sato Turtelli, R. Grossinger, M. Kriegisch, H.Sassik, and P. Svec. Magnetostriction of rapidly quenched Fe-X (X = Al, Ga) ribbons as function of the quenching rate. *IEEE Transactions on Magnetics (Accepted)*, Intermag 2009 Sacramento, California, USA, 2009.

[136] R. Sato Turtelli, G. Vlasak, F. Kubel, N. Mehmood, M. Kriegisch, R. Grossinger, and H. Sassik. Effect of rapid solidification on magnetostriction and microstructure in melt-spun Fe-Al ribbons. *IEEE Transactions on Magnetics (Submitted)*, 19th Soft Magnetic Materials Conference IEEE Transactions on Magnetics (Submitted), 2009.

[137] E. P. Yelsukov, E. V. Voronina, and V.A. Barinov. Mossbauer study of magnetic properties formation in disordered Fe-Al alloys. *Journal of Magnetism and Magnetic Materials*, 115(2-3):271–280, 1992.

[138] K. Sumiyama and Y. Nakamura Y. Hirose and. Structural and magnetic properties of nonequilibrium disordered Fe-Al alloys produced by facing target type DC sputtering. *Journal of the Physical Society of Japan*, 59(8):2963–2970, 1990.

[139] Y. Muraoka, H. Wada, M. Shiga, and Y. Nakamura. Magnetovolume effects around critical concentration. *Physica B+C*, 119(1-2):174–179, 1983. cited By (since 1996) 0.

Curriculum Vitae:

Nasir Mehmood

Mohallah: Melad Nagar
City: New Khanpur
Tehsil and District: Haripur (Hazara)
N.W.F.P, Pakistan
e-mail: nasirifp@gmail.com
Phone: +92-995-640361

Personal:

Birth: 04 Apr 1974
Nationality: Pakistan
Sex: Male
Family Status: Married

Education:

since Nov 2006: working for PhD in Institut für Festkörperphysik, TU Wien.
Oct 1997: Master of Science (M.Sc.) Physics, University of Peshawar Paksitan.
Dec 1994: Bachelor of Science (B.Sc.) Physics and Math, University of Peshawar Pakistan.
Oct 1992: Intermediate Examination (F.Sc.) BISE Abbottabad Pakistan.
Aug 1990: Secondary School Exam (S.Sc.)BISE Peshawar Pakistan.

Award:

PhD Scholarship in Austria, from Higher Education Commission (HEC) of Pakistan, currently in progress.

Employment:

Apr 1999- Nov 2006: Quality Assurance- Advanced Computing & Engineering Solutions (Pvt) Ltd (ACES) Pakistan.

Research Interest:

Hard and Soft Magnetic Materials

Publications:

1. R. Grossinger, F. Keplinger, N. Mehmood, and R.Sato Turtelli. Magnetic characterization of soft and hard magnetic material. *In 3rd International Conference on Magnetism and Metallurgy* (WMM' 08) Ghent-Belgium, 2008.

2. R. Grössinger, N. Mehmood, G. Senbaslar, M. Atif, R. Sato Turtelli, W. Linert, and F. Kubel. Co-ferrite: A material with high magnetostriction produced by different methods. In *REPM08, Rare Earth Permanent Magnets and Applications (Creta Greece), 2008.*

3. R. Grössinger, R. Sato Turtelli, N. Mehmood, S. Heiss, H. Müller, and C. Bormio-

Nunes. Giant magnetostriction in rapidly quenched Fe-Ga? *Journal of Magnetism and Magnetic Materials*, 320 (20):2457–2465, 2008.

4. R. Grössinger, R. Sato Turtelli, and N. Mehmood. Magnetostriction of Fe-X (X = Al,Ga,Si, Ge) intermetallic alloys. *IEEE Transactions on Magnetics,* 44(11):3001–3004, 2008.

5. R. Grössinger, F. Keplinger, N. Mehmood, J.H. Araujo, Espina-Hernandez, C. Eisenmenger, K. Poppenberger, and J.M. Hallen. Magnetic and microstructural investigations of pipeline steels. *IEEE Transactions on Magnetics,* 44(11):3277–3280, 2008.

6. N. Mehmood, R. Sato Turtelli, R. Grossinger, and M. Kriegisch. Magnetostriction of polycrystalline $Fe_{100-x}Al_x$ (x = 15, 19, 25). *Journal of Magnetism and Magnetic Materials*, In Press, Corrected Proof:–, *(Accepted)*, 2009.

7. N. Mehmood, G. Vlasak, F. Kubel, R. Sato Turtelli, R. Grossinger, M. Kriegisch, H.Sassik, and P. Svec. Magnetostriction of rapidly quenched Fe-X (X = Al, Ga) ribbons as function of the quenching rate. *IEEE Transactions on Magnetics (Accepted)*, 2009.

8. R. Sato Turtelli, G. Vlasak, F. Kubel, N. Mehmood, M. Kriegisch, R. Grossinger, and H. Sassik. Effect of rapid solidification on magnetostriction and microstructure in melt-spun Fe-Al ribbons. *IEEE Transactions on Magnetics (Accepted)*, 2009.

Academic References:

1. Univ.Prof. Dr.techn. Roland Grössinger

   Institut für Festkörperphysik, TU Wien, Wiedner Hauptstraße 8-10, A 1040 Wien, Austria Tel: +43-1-58801-13801 | Fax: +43-1-58801-13899

2. Dr. Reiko Sato Turtelli

   Institut für Festkörperphysik, TU Wien, Wiedner Hauptstraße 8-10, A 1040 Wien, Austria Tel: +43-1-58801-13801 | Fax: +43-1-58801-13899